Universiteit Gent
Faculteit Wetenschappen
Vakgroep Fysica en Sterrenkunde

Development and application of a highly accurate polychromatic X-ray microtomography simulator

Jelle Dhaene

Proefschrift ingediend tot het behalen van de graad van
Doctor in de wetenschappen:
fysica
Academiejaar 2016-2017

Universiteit Gent
Faculteit Wetenschappen
Vakgroep Fysica en Sterrenkunde

Promotor:	Prof. dr. Luc Van Hoorebeke
Examencommissie:	Prof. dr. Jan Ryckebusch (voorzitter) Dr. ir. Manuel Dierick (secretaris) Prof. dr. Luc Van Hoorebeke (promotor) Dr. Mathieu Plamondon Prof. dr. ir. Bart Nicolai Prof. dr. Laszlo Vincze Dr. Loes Brabant

Universiteit Gent
Faculteit Wetenschappen

Vakgroep Fysica en Sterrenkunde
Proeftuinstraat 86, B-9000 Gent, België

Proefschrift ingediend tot het behalen van de graad van
Doctor in de wetenschappen: fysica
Academiejaar 2016-2017

Dankwoord

Vier jaar geleden begon ik met volle moed aan mijn doctoraat. Onderzoek sprak me echt aan en met ups en downs heb ik dit werk tijdens de laatste vier jaar kunnen verwezelijken. Alleen ging mij dit echter nooit gelukt zijn, dus daarom wil ik hier ook even de tijd nemen om enkele mensen te bedanken.

Eerst en vooral zou ik Luc willen bedanken. Bedankt dat je mij 4 jaar geleden de kans gegeven hebt om aan dit doctoraat te starten. Wat het uiteindelijke resultaat hiervan zou worden, was voor geen van ons op dat moment echt duidelijk, maar ik denk dat we na 4 jaar beiden meer dan tevreden kunnen zijn met het behaalde resultaat. Jij was ook de persoon bij wie ik altijd terecht kon om de fysica achter de vele simulaties beschreven in dit werk te bespreken en te bediscussiëren. Bedankt voor de vele leerrijke (fysische) discussies die we samen gehad hebben, om mijn doctoraat zo zorgvuldig na te lezen, je gevoel voor humor en alle steun die je mij geboden hebt de voorbije jaren.

Verder wil ik ook mijn collega's en ex-collega's bedanken voor zowel leerrijke als ontspannende momenten. Bert en Denis, bedankt voor al het werk dat jullie besteed hebben aan het bouwen van de beschikbare scanners op het UGCT. Zonder jullie zou dit onderzoek niet mogelijk geweest zijn. Manu, bedankt voor alle begeleiding die ik in het begin van jou gekregen heb. Zonder jou zou ik niet de kennis hebben die ik vandaag heb, en dan bedoel ik niet alleen de kennis opgedaan in de context van ons onderzoek. Loes, Matthieu, Elin, ook jullie waren reeds werkzaam op het UGCT toen ik begon met mijn doctoraat en bedankt voor alle begeleiding die jullie me in de begindagen gegeven hebben. Bedankt om me te leren kickeren en dat niks te gek is om in onze scanners te plaatsen en het te visualiseren. Pieter, jij ook bedankt om steeds klaar te staan om scans te doen als dat nodig was. Alhoewel je gemist wordt denk ik dat Ivan een waardige opvolger voor je zal zijn. Thomas, we zijn samen gestart aan ons doctoraat en in het begin liep de samenwerking soms wat stroef, maar ik denk dat we uiteindelijk beiden een mooi resultaat bereikt hebben en dat onze neuzen uiteindelijk toch in dezelfde richting wezen. Amélie, jij kwam er later bij en ik kon altijd op jouw hulp rekenen. Ook bedankt voor de vele ping pong spelletjes welke de laatste tijd helaas niet meer aan bod komen, maar daar moet dringend terug verandering in komen! Jeroen, je werkte even bij ons en ik was blij te zien wat je bereikt hebt in je onderzoek gedurende dat jaar. Ik doe mijn uiterste best om jouw ontwikkelde techniek verder

uit te werken en wens je veel succes in je zoektocht naar een nieuwe job. Marjolein, Frederic en Abhishek, ook jullie kwamen er later bij en ik kijk ernaar uit om verder met jullie samen te werken. Ook bedankt aan alle geologen voor alle hulp die ik van jullie gehad heb en om mij te voorzien van samples wanneer dat nodig was. Ook jij, Jan VDB wil ik bedanken voor jouw eeuwige enthousiasme voor alles wat we doen. Dit werkt echt aanstekelijk en heeft mij toch vaak belet om bepaalde dingen op te geven, en zie met welk resultaat... Ook bedankt dat ik Nanowood steeds tot men beschikking kreeg als ik dat nodig achte. En bedankt aan alle collega's en mensen die ik hier vergeten vermelden ben.

Ook zou ik de volledige examencommissie willen bedanken voor het lezen van dit werk en de interessante discussie die we gevoerd hebben tijdens de interne verdediging. Met behulp van jullie opmerkingen en suggesties kon ik de kwaliteit van dit werk drastisch verbeteren.

Verder zou ik ook het Agentschap voor Innovatie door Wetenschap en Technologie (IWT, SBO project 120033 'TomFood') willen bedanken voor hun financiele steun. Zoder hen ging dit doctoraat niet mogelijk geweest zijn. Ik zou ook de collega's met wie ik hierin samengewerkt heb willen bedanken. Eerst en vooral Pieter en Bart, bedankt om het project te leiden en verschillende onderzoeksgroepen uit Vlaanderen samen te brengen in een project dat als doel had het ontwikkelen en verbeteren van X-stralen CT als inspectietool voor de voedselproductie. Ook bedankt aan Jan, Sofie en Barbara van ILVO, Johan en Maria van Thomas More Lab4Food, Bart, Pieter en Mattias van Mebios van de KU Leuven en aan Jan, Vincent en Eline van UAntwerp voor de samenwerking en de interessante wetenschappelijke discussies de laatste 4 jaar.

Bedankt Dimi, Lisa, Klaas, Julie, Dieter, Eline, Bram, Emma, Karel, Evi, Thomas, Frank, Filipe, Jasmien en zovele anderen voor alle onstpannende avonden, etentjes en (Gentse) feesten - Baudelo Podium Links - die we de afgelopen jaren samen beleefd hebben. Deze momenten waren de afgelopen jaren zeer welkom om de stressvolle thesismomenten even te vergeten. Ik weet dat ik de laatste maanden jullie allemaal minder gezien heb, maar dat zullen we proberen goedmaken in de (zonnigere) maanden die volgen! Bedankt voor alle leuke momenten samen.

Ik zou ook mijn ouders willen bedanken omdat ze mij 9 jaar geleden de kans gegeven hebben om Fysica te gaan studeren en mij hierin altijd gesteund hebben. Na 5 jaar behaalde ik hierdoor mijn masterdiploma, waarna ik aan dit doctoraat kon beginnen en met trots presenteer ik het eindresultaat vandaag aan jullie. Mémé, Oma, Opa, ik weet dat jullie mij de laatste maanden zelden gezien hebben, maar nu dit werk geschreven is zullen jullie mij terug vaker zien. Ook bedankt aan alle familie en schoonfamilie voor alle steun de afgelopen jaren.

Tenslotte wil ik ook mijn fantastisch lieve vriendin, Elin, bedanken. Ik weet dat we de laatste maanden niet veel tijd samen hebben kunnen doorbrengen door ons drukke leven, maar ik kijk er echt naar uit om wat meer tijd samen te hebben nu onze beide doctoraten erop zitten. Ondanks jouw drukke leven ben je er wel altijd voor mij als het nodig is en je staat altijd aan mijn zij om mij te steunen. Bedankt hiervoor, lieve schat.

Gent, 2017
Jelle Dhaene

English summary

In 1895, The German Physicist, Wilhelm Conrad Röntgen, discovered X-rays. Since then, these are widely used in different research domains to visualise the internal structure of objects. Furthermore these are also used in various spectroscopy, diffraction and scattering experiments providing a multitude of physical and chemical information next to the internal structure. Visualising the internal structure can either be done by two-dimensional (2D) imaging in which a radiograph is taken or by obtaining a complete three-dimensional (3D) representation with the use of computed tomography (CT). Since the late 1970's it is possible, with the use of CT, to get a 3D representation of the internal organs and skeletal structure of a patient by taking a series of radiographic projections. During the eighties, the technological progress led to the development of high resolution CT or μCT. This allowed to obtain a complete 3D representation with a resolution in the few tens of micrometre range. High resolution CT has evolved to an omnipresent research technique in various research domains. Nowadays, resolutions of less than a micrometre can be obtained at laboratory based X-ray CT scanners.

The developments presented in this work were obtained at the Centre for X-ray Tomography of Ghent University (UGCT), more specifically in the radiation physics group (RP) which is part of UGCT. Within UGCT the RP group develops state-of-the-art μCT scanners as well as new methods and software for reconstruction, 3D analysis and imaging simulation. Nowadays, UGCT has four CT scanners available and a fifth scanner was developed together with the X-ray Microspectroscopy and Imaging group (XMI) of the Department of Analytical Chemistry. This last scanner combines CT and X-ray Fluorescence (XRF) imaging.

In this thesis, new developments in the research of X-ray μCT are presented and discussed. The developments presented in this work focus on the modelling of a μCT scanner, the accurate simulation of radiographs and the application of these realistic simulations. Finally, it is shown how these simulations can be used to characterise materials inside a reconstructed volume.

Before discussing the results, a historical overview of X-ray CT is given and the scanners available at UGCT are discussed. After this overview, the physical processes and properties of μCT scanners are discussed in chapter 3. An overview

of the interaction mechanisms between electrons and matter is given. These processes play an important role in the production of X-rays in conventional X-ray tubes used in laboratory-based X-ray CT. Afterwards, the interaction mechanisms between photons and matter are discussed. These interaction mechanisms are important for the attenuation that an X-ray beam will undergo when it travels through a sample and for the detection of X-rays in an X-ray detector. Furthermore, physical properties of X-ray CT scanners such as X-ray flux, spot size, heel effect, detector unsharpness, detector ghosting and beam hardening, which need to be taken into account when one wants to simulate an X-ray CT scanner in a realistic way, are discussed.

In chapter 4, the modelling of the polychromatic behaviour of X-ray tubes and detectors is discussed. These models play an import role in the simulation of accurate X-ray CT radiographs because the polychromatic behaviour of the tube and detector have a major influence on these simulations. The software package BEAMnrc, based on a Monte Carlo technique, was used for the simulation of the tubes and detectors present at UGCT and is described briefly. Furthermore, the geometric models of the tubes and detectors available at UGCT are shown as well as the results of the Monte Carlo simulations. The generated spectra of the X-ray tubes and generated efficiencies for the X-ray detectors are discussed. These generated spectra are used in chapter 5 for the developed projection simulator, Arion, and in chapter 6, for the developed dual-energy CT (DECT) method. Also, a method is described to model the secondary spot, present in one of the transmission tubes available at UGCT. For one of the detectors, the Perkin Elmer detector, a model for the Line spread functions (LSF) is determined.

In chapter 5, the development of a realistic projection simulator, Arion, is described. First, the geometry used by the simulator to describe a CT scan is discussed. This geometry is important for describing the relative movement of the source, sample and detector during the simulation of a CT acquisition. The theoretical background of the program, which is based on a ray-tracing technique, is discussed together with a method for including beam filtration and a method to reduce the computation time by efficiently binning the spectrum used during the simulations without too much loss of spectral information. Additionally, the graphical user interface (GUI) is discussed. Besides the simulator, some other components of Arion are discussed. The Material Creator allows the user to create attenuation coefficients for ‘new’ materials, compositions or solutions which can later be used during the CT simulations. The Image Handler is a program which allows the user to perform elementary image operations such as adding, subtracting, dividing and multiplying images or image folders. Furthermore, this program can be used to include a secondary spot effect or the effect of an MTF in the simulated projection images. The chapter ends with a comprehensive comparison between real and simulated data for different scanners present at UGCT. In general, deviations between the real and simulated data of a few percent are found.

These results are good enough to perform an optimisation procedure with the use of Arion for X-ray CT. Some examples in which this optimisation was successfully applied are shown. Some of these results were obtained in the framework of the IWT/SBO TomFood project whose purpose was to develop novel techniques for inspection and engineering of food (micro)structure based on X-ray computed tomography. The chapter is concluded with a benchmark and an outlook for future improvements.

Chapter 6 describes how the developed simulator can be used to obtain chemical information of the materials present in a sample by using DECT. First, a historical overview of DECT is given and the DECT method which is already used at UGCT is discussed. Afterwards, a new method is presented which makes it possible to determine the composition and density of a material in a voxel of a reconstructed 3D volume by using DECT. This is done by using a priori knowledge of the physical properties of the tube and detector provided by the Monte Carlo simulations described in chapter 4. Because the polychromatic properties and parameters of the sources and detector available at UGCT are well known, it is possible to reconstruct a set of unambiguous parameters, i.e. composition and density, for each voxel instead of the reconstructed linear attenuation coefficients for the two volumes without the need of a calibration of the scanner used. This method was successfully applied on virtual and real data. The method is also applied to determine densities in samples of which the composition is known. An example of densitometry on a wood sample is presented. For doing this, it is sufficient that the sample is scanned at a single energy, or spectrum, because the composition of the material is known. Nowadays, this method is still a post reconstruction method, but it should be possible to implement it in an iterative reconstruction algorithm in the near future. In this way it should be possible to reconstruct a set of parameters inside each voxel which represents physical parameters of the material present in each voxel. Further, such implementation in an iterative reconstruction algorithm, in which Arion can be used as a forward projection simulator, will lead to a strong reduction of beam hardening artefacts.

In the last chapter a conclusion of the whole work presented in this thesis is given.

Nederlandse samenvatting

In 1895 ontdekte de Duitse fysicus Wilhelm Conrad Röntgen X-stralen. Sindsdien worden deze in verschillende onderzoeksdomeinen onder andere gebruikt om de interne structuur van objecten te bestuderen. Verder kunnen deze ook gebruikt worden in spectroscopie, diffractie en verstrooiings experimenten waaruit fysische en chemische informatie gehaald kan worden naast de interne structuur. De interne structuur kan gevisualizeerd worden door twee-dimensionale (2D) beeldvorming door middel van radiografie of een complete 3-dimensionale (3D) voorstelling kan gemaakt worden door middel van computertomografie (CT). Sinds de late jaren 1970 is het mogelijk om met behulp van X-stralen CT een CT representatie te krijgen van het inwendige van een patiënt met behulp van een serie projectiebeelden die opgemeten worden. In de jaren '80 leidde de technologische vooruitgang tot de ontwikkeling van hoge resolutie CT of μCT. Dit liet toe om een complete 3D representatie te bekomen met een resolutie van enkele tientallen micrometer. Hoge resolutie CT is doorheen de jaren sterk geëvolueerd tot een allomtegenwoordige onderzoekstechniek in verscheidene onderzoeksdomeinen. Tegenwoordig kunnen resoluties van minder dan een micrometer gehaald worden.

De ontwikkelingen gepresenteerd in dit werk werden uitgevoerd aan het Centrum voor X-stralen Tomografie van de Universiteit Gent (UGCT), meer bepaald in de Stralingsfysica groep (RP) die deel is van UGCT. De RP groep werkt binnen het UGCT aan zowel de ontwikkeling van hoge resolutie CT scanners en de ontwikkeling van nieuwe methodes en software rond reconstructie, 3D analyse en simulatie van de beeldvorming. Op de dag van vandaag beschikt UGCT over 4 CT scanners plus een scanner die samen met de X-ray Microspectroscopy and Imaging groep (XMI) van de vakgroep Analytische Chemie werd gebouwd. Deze laatste scanner combineert CT en X-stralen Fluorescentie (XRF) beeldvorming.

In deze doctoraatsthesis worden enkele nieuwe ontwikkelingen binnen het domein van X-stralen μCT behandeld. De ontwikkelingen die hier beschreven worden focussen op het modelleren van een μCT scanner, het zo accuraat mogelijk simuleren van radiografieën en de toepassingen van deze realistische simulaties. Uiteindelijk wordt ook getoond hoe deze simulaties gebruikt kunnen worden om materialen in een gereconstrueerd volume te karakteriseren.

Vooraleer de resultaten besproken worden, wordt er een overzicht gegeven van de historiek van X-stralen CT en worden de X-stralen scanners beschikbaar in het Centrum voor X-stralen Tomografie van de Universiteit Gent (UGCT) voorgesteld. Na dit overzicht worden in hoofdstuk 3 de fysische processen en eigenschappen van CT scanners behandeld. Er wordt een overzicht van de interactiemechanismen tussen elektronen en materie gegeven. Deze processen spelen een belangrijke rol in de productie van X-stralen in conventionele X-stralenbuizen die gebruikt worden in laboratoriumomgevingen. Hierop volgend wordt de interactie tussen fotonen en materie besproken, die een belangrijke rol speelt in het beeldvormingsproces tijdens X-stralen CT. Deze interactiemechanismen spelen zowel een rol voor de attenuatie die de X-stralen zullen ondergaan als ze doorheen het sample passeren als voor de detectie van X-stralen fotonen in X-stralendetectoren. Verder worden ook fysische eigenschappen eigen aan X-stralen CT-scanners besproken zoals X-stralen flux, spotgrootte, heel effect, onscherpte van detectoren, *detector ghosting* en *beam hardening* waarmee rekening dient gehouden te worden indien men een realistische simulatie van een X-stralen CT scanner wil bekomen.

Vervolgens wordt in hoofdstuk 4 het modelleren van het polychromatisch gedrag van X-stralenbuizen en detectoren besproken. Deze modellen zijn nodig om accurate CT beelden te kunnen simuleren omdat het energie afhankelijk gedrag van zowel bron als detector in de vorming van deze beelden een grote rol zullen spelen. Het software pakket BEAMnrc, gebaseerd op een Monte Carlo techniek, wordt gebruikt voor de simulaties van de bronnen en detectoren aanwezig op het UGCT. Verder worden er geometrische modellen getoond van de bronnen en detectoren beschikbaar op het UGCT en worden de resultaten van de Monte Carlo simulaties getoond. De gegenereerde spectra voor de beschikbare X-stralenbuizen en de detectorefficiënties worden later in hoofdstuk 5 gebruikt in de ontwikkelde projectiesimulator, Arion, en in de nieuwe *Dual-Energy CT* (DECT) methode besproken in hoofdstuk 6. Verder wordt ook een methode beschreven hoe een model voor een secundaire spot, aanwezig in één van de transmissiebuizen op het UGCT gemodelleerd kan worden. Verder werd ook voor één van de detectoren een model voor de Line Spread function (LSF) bepaald aan de hand van opgemeten transmissies.

Hoofdstuk 5 beschrijft de ontwikkeling van een realistische projectiesimulator, Arion. Als eerste wordt de geometrie gebruikt om een CT scan te beschrijven besproken. Deze geometrie is belangrijk om de relatieve beweging van de bron, sample en detector te beschrijven gedurende de CT acquisitie. De theoretische achtergrond van het programma, dat gebaseerd is op een *ray-tracing* techniek wordt besproken samen met methodes om filtratie van de X-stralen bundel te bekomen en een methode om de rekentijd te reduceren aan de hand van het efficiënt *binnen* van X-stralen spectra zonder al te veel spectrale resolutie te verliezen. Bovendien wordt ook de grafische gebruikersinterface van Arion besproken. Naast de simulator zelf worden nog enkele andere onderdelen van Arion behandeld. De Material Creator laat de gebruiker bijvoorbeeld toe om zelf atten-

uatiecoeficiënten van “nieuwe” materialen, composities of oplossingen te creëren die later tijdens een simulatie gebruikt kunnen worden. De Image Handler is een programma dat de gebruiker toelaat om radiografieën gemakkelijk te bewerken en er eenvoudige operaties op uit te voeren, zoals beelden optellen, delen, aftrekken en vermenigvuldigen. Verder kan dit programma ook gebruikt worden om het effect van een secundaire spot in de gesimuleerde beelden te genereren of om het effect van de MTF op gesimuleerde beelden toe te passen. Het hoofdstuk eindigt met een uitvoerige vergelijking tussen echte en gesimuleerde data voor verschillende scanners aanwezig op het UGCT. Afwijkingen van enkele procenten werden gevonden tussen de gesimuleerde en echte data. Deze resultaten zijn zeker goed genoeg om optimalisatie van scanparameters uit te voeren. Enkele voorbeelden van optimalisaties die succesvol toegepast werden worden getoond. Enkele van deze resultaten werden behaald in het kader van het IWT/SBO TomFood project dat tot doel had om nieuwe technieken voor inspectie en ontwikkeling van voedsel te ontwikkelen door gebruik te maken van X-stralen CT. Het hoofdstuk wordt afgesloten met een *benchmark* en een vooruitzicht op toekomstige verbeteringen.

Hoofdstuk 6 beschrijft hoe de ontwikkelde simulator gebruikt kan worden om chemische informatie van materialen in een sample te bekomen door gebruik te maken van DECT. In dit hoofdstuk wordt eerst een historisch overzicht gegeven van DECT en de techniek die reeds gebruikt wordt aan het UGCT wordt besproken. Daarna wordt een nieuwe methode voorgesteld die het mogelijk maakt om de compositie en densiteit van een materiaal te bepalen in een voxel van een gereconstrueerd 3D volume aan de hand van DECT. Dit is mogelijk door gebruik te maken van de fysische voorkennis van de bron en detector die gehaald wordt uit de Monte Carlo simulaties beschreven in hoofdstuk 4. Omdat de polychromatische eigenschappen en parameters van de bronnen en detectoren aanwezig op het UGCT zo goed gekend zijn is het mogelijk om deze set van ondubbelzinnige parameters, compositie en densiteit, te gaan reconstrueren in plaats van de gereconstrueerde lineare attenuatiecoefficiënten in de voxels van de twee gereconstrueerde volumes. Dit alles kan zonder dat de scanner hiervoor dient gecalibreerd te worden. De methode werd met succes toegepast op virtuele en echte data. Verder wordt de methode ook gebruikt om densiteiten te bepalen van samples waarvan de compositie gekend is. Een voorbeeld waar densitometrie op houtsoorten gedaan kan worden wordt getoond. Hiervoor is het echter voldoende om een scan bij één welbepaalde energie, of spectrum, uit toe voeren aangezien de compositie van het materiaal gekend is. Op de dag van vandaag is deze methode nog steeds een post-reconstructie methode, maar het zou mogelijk moeten zijn om deze te implemenenteren in een iteratief reconstructiealgoritme zodanig dat een set van parameters gereconstrueerd kan worden in iedere voxel. Verder zou de implementatie van deze methode in een iteratief reconstructiealgoritme, waarin Arion als een voorwaartse projectiesimulator gebruikt wordt, ook aanleiding geven tot een sterke reductie van *beam hardening* effecten.

In het laatste hoofdstuk wordt een conclusie van dit volledige werk gegeven.

Table of Contents

List of Figures

List of Tables

1 Introduction

Since their discovery more than a century ago, X-rays have been used to visualise the internal structure of various objects [1–4]. Contrary to 2D radiography, X-ray computed tomography (CT) offers a solution to unambiguously determine the internal morphology of an object in 3D. CT is well known from its application in the medical sciences, but is certainly not limited to this field. For non-medical imaging, high-resolution X-ray CT or μCT is commonly used. Currently, very high resolution X-ray CT scanners can achieve a resolution below one micrometre and are significantly valuable instruments in various scientific and industrial applications.

The Centre for X-ray Tomography of Ghent University (UGCT) was founded in 2006 and is specialised in research on and the use of high-resolution X-ray CT. To overcome the limitations of a commercial system, UGCT developed its first high-resolution X-ray CT scanner in 2005-2006. Nowadays, there are four complementary home-built X-ray CT setups available for various purposes. A fifth system was built in cooperation with the X-ray Microspectroscopy and Imaging group (XMI) of the Department of Analytical Chemistry. In addition to the development of hardware, a great deal of research on X-ray CT acquisition, reconstruction and analysis methodology has been performed at UGCT by the Radiation Physics group in which this work was performed. Octopus, a reconstruction package which includes both analytical and iterative reconstruction, was developed as well as Morpho+, an analysis software package nowadays called Octopus Analysis. During recent years, a simulation program called Arion was also developed,

which creates a virtual environment in which X-ray CT data sets can be simulated with very high correspondence to the experimental images.

UGCT acts as a user facility and cooperates with a large number of research groups both within Ghent University and from other universities, in various scientific fields such as geology, plant sciences, biological sciences, medical sciences and much more. As such, a great variety of samples is being scanned, and the optimal scanner setting are very sample dependent. The ability to determine the optimal scanner settings by simulation is a great asset for UGCT. Therefore, during recent years, a simulation program called Arion was developed, which creates a virtual environment in which X-ray CT data sets can be simulated with very high correspondence to the experimental images and which allows to optimise scanning conditions. The use and need of this tool is however, not limited to the optimisation of scanning conditions. Also, new scan geometries for industrial/inline environments can be developed with the tool in which only a limited number of projections and/or a limited angular range are available. By doing this virtually a much larger parameter space can be explored and evaluated at a faster rate and reduced cost than when all these geometries need to be evaluated in real life. Furthermore, because the emphasis of the program is on simulating the underlying imaging physics as accurate as possible, it is particularly useful for developing and testing reconstruction algorithms and their response to physical artefacts and properties because a ground truth is known. Finally, the knowledge of the physics of X-ray CT, particularly the knowledge of the polychromatic behaviour, allows for extracting extra information which can be used for material characterisation by applying a dual-energy CT technique which is described in Chapter 6. Arion has been applied several times in the context of the IWT/SBO TomFood project (IWT SBO 120033) which focuses on novel techniques for inspection and engineering of food (micro)structure based on X-ray computed tomography.

Outline

The research presented in this work focuses on the simulation software developed, Arion. Chapter 1 provides an introduction to the scope of this work and the major achievements, while Chapter 2 explains the basic concepts of X-ray CT.

Chapter 3 presents a theoretical description of the physical processes which play a role in X-ray CT imaging. Understanding these processes is of key relevance in the development of accurate simulations of a complex physical system such as an X-ray μCT scanner. The chapter also takes a detailed look at the interactions between electrons/photons and matter. The interactions between electrons and matter plays a central role in the production of X-rays in X-ray tubes. Photon interactions

with matter, on the other hand, are very important for describing the interaction between the X-ray beam and the sample as well as for modelling the X-ray detector efficiency. Furthermore, the production and detection of X-rays is discussed and the chapter closes with the description of physical properties more specific to laboratory-based μCT. This includes concepts such as X-ray flux, resolution and spot size, the heel effect, detector unsharpness, detector ghosting and beam hardening.

Chapter 4 describes the detailed modelling of the polychromatic behaviour of laboratory-based X-ray CT components, more specifically X-ray tubes and detectors. Modelling of these components needs their geometry as necessary input for accurate Monte Carlo simulations of the spectral behaviour of X-ray tubes and detectors present at UGCT. The chapter starts with a short introduction to BEAMnrc, the Monte Carlo code used, followed by a thorough description of the modelling and simulation of the X-ray tubes and detectors available at UGCT. For all tubes at UGCT, some simulated emission X-ray energy spectra are shown as well as the 3D shape of the primary spot in which the X-rays are generated. For one of the transmission tubes, the secondary spot generated by the inner structure of the tube itself is simulated. Also for the various UGCT detectors, models are presented and their energy dependent efficiency as calculated by the Monte Carlo simulations is shown. The simulated spectra of the X-ray tubes and the simulated energy dependent efficiencies of the X-ray detectors are used in Arion (Chapter 5) and the dual-energy CT technique (Chapter 6) as look-up tables.

Chapter 5 discusses Arion, the X-ray CT simulation program developed at UGCT. The goal of this simulation tool is to include and model the physical behaviour of X-ray imaging as accurate as possible. This includes, but is not limited to, the spectral properties of an X-ray CT scanner. By doing this, the tool has the advantage over other tools that, in general, the physical properties are included unambiguously and that the effects of these properties can be studied accurately. Furthermore by doing this, the simulation tool does not need a calibration to compare the results with real life experiments. The chapter starts by defining a geometry which can be used to describe the relative movement of the source, detector and sample during an X-ray CT acquisition. The theoretical background of the simulation program, which is based on ray-tracing calculations, is explained along with methods to include beam filtration and a method to reduce the computation time by using binned X-ray spectra, without losing too much spectral resolution. Additionally, the features of Arion are described and the graphical user interface (GUI) is presented. The chapter finishes by comparing real and simulated data, and by proposing some applications that explain how the simulator can be used to optimise scanning conditions. Some of these results are obtained in the context of

the IWT/SBO TomFood project. Finally, the chapter lists some benchmarks and an outlook on future improvements.

Chapter 6 outlines how Arion can be used to characterise materials and densities with the use of dual-energy CT. A method is presented which makes it possible to identify the material and determine its density in each voxel in the reconstructed 3D volume by using the prior knowledge on the spectral behaviour of the components of the scanner used. Because the physical properties such as spectrum produced by the X-ray tube, spectral attenuation in the sample and spectral detector efficiency are very well known for the systems present at UGCT, it is possible to reconstruct a set of unambiguous parameters rather than the average attenuation coefficient which is prone to spectral effects. It is shown how the 3D volumes containing the reconstructed linear attenuation coefficients for both CT scans can be converted to two volumes containing a material and a density in each voxel, without calibration of the scanner. Nowadays, this method is still a post-reconstruction method. However, it should be possible to implement the method in an iterative reconstruction algorithm, such that the result of the reconstruction is a set of parameters (e.g. material and density) inside each voxel.

Finally, chapter 7 presents a summary and conclusion of this work.

Main contributions

The main contributions of the author to the field of high resolution X-ray CT which are presented in this work are:

- Further improvement of the modelling of the polychromatic behaviour of X-ray sources and detectors available at UGCT.
- Proposing a method to model a secondary spot and heeling of an X-ray tube and Line spread function of a detector.
- Development of a GPU based highly accurate polychromatic projection simulator, Arion.
- Validation of Arion by extensively testing it for different scanners at UGCT.
- Proposing a method for optimising X-ray μCT by using simulated data of Arion and verifying the results by comparing them with real data.
- Application of the developed optimisation technique in the context of the IWT/SBO TomFood project.

- Development of a new DECT method with which it is possible to characterise materials in a reconstructed volume of a sample.
- Validation of the new DECT method by testing it on virtual and real data.

References

[1] W. C. Röntgen. *On a new kind of rays*. Würzburg Physical and Medical Society, 1895.

[2] J. Radon. *Über die Bestimmung von Funktionen durch ihre Integralwerte längs gewisser Mannigfaltigkeiten*. Berichte des Schsischen Akademie der Wissenschaften, 69:262–277, 1917.

[3] A. M. Cormack. *Representation of a Function by Its Line Integrals, with Some Radiological Applications*. Journal of Applied Physics, 34:2722–2727, September 1963.

[4] A. M. Cormack. *Representation of a Function by Its Line Integrals, with Some Radiological Applications. II*. Journal of Applied Physics, 35:2908–2913, October 1964.

2

X-ray Computed Tomography

For a long time, visible light was the only electromagnetic radiation that could be observed by mankind. Researchers tried for centuries to develop techniques to visualise all kinds of objects invisible to the human eye. The scale of these objects ranged from the tiniest particles such as quarks inside a proton or neutron, to stars and galaxies far, far away. This quest to unravel the mysteries of the universe led to the development of numerous different devices to visualise these objects. An essential element in such devices is the detection of electromagnetic waves. The wavelength of these electromagnetic waves is directly correlated with the smallest distinguishable features that can be observed, as shown in Figure 2.1.

One of these techniques is X-ray Computed Tomography (CT). This is a non-invasive technique which was originally developed for medical applications. Because X-ray CT is non-destructive, it is an ideal technique to visualise the internal structure of the human body. Apart from the medical field, the technique can also be used for non-medical applications. It is possible to visualise the inner structure of an object without opening the object, which opens up many possibilities for scientific research.

This chapter starts with a short historical overview of medical and high-resolution CT. The CT workflow and reconstruction algorithms are also discussed. Finally, the software and hardware available at the Centre for X-ray Tomography of Ghent University is described. While this chapter gives a general overlook on X-ray CT,

in the next one a more detailed overview of the physics that play a role in X-ray μCT is given.

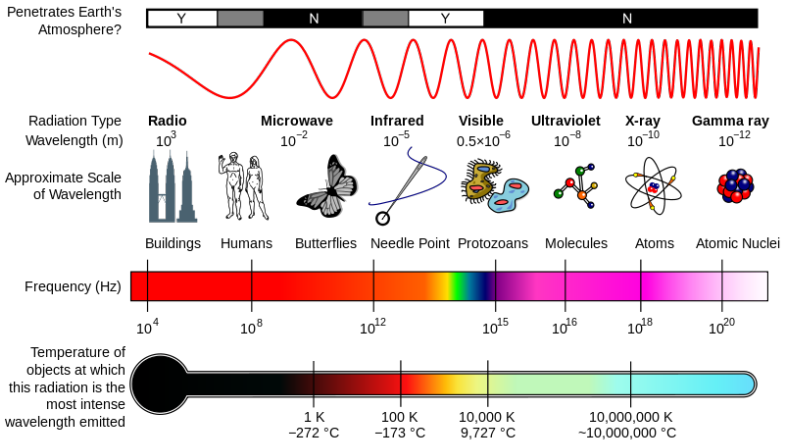

Figure 2.1: Electromagnetic waves of different energies and wavelengths can be used to study different objects. [1]

2.1 History

2.1.1 Radiography

In 1895, the German physicist Wilhelm Conrad Röntgen discovered X-rays. This discovery was made while he was experimenting with vacuum tubes in his lab, and was published in the paper 'Uber eine neue art von Strahle' ('On a new kind of rays') [2]. Shortly after their discovery, X-rays were already beginning to be used in medicine and industry. Today, this type of radiation is still the basis of an important imaging technique and is accompanied by other techniques such as fluoroscopy, nuclear medicine, ultrasound and magnetic resonance imaging. Furthermore, for his discovery, Röntgen received a Nobel Prize in Physics in 1901.

A radiograph, also called a projection image later on, is an image that contains information about the integrated attenuation of X-rays along their path from the source through an object to the detector. It is a two-dimensional (2D) representation of a three-dimensional (3D) volume.

2.1.2 Tomography

In Computed Tomography (CT) a complete three-dimensional representation of the scanned object is acquired by taking a series of projection images at different

angles. In medical CT, this is done by rotating the source and detector around the patient. The mathematical foundation for tomography was proposed by the Austrian mathematician Johann Karl August Radon in 1917 [3]. This could only be put into practice when sufficient computer power was readily available. Allan Mac Lead Cormack, an American physicist, published two papers on the theoretical foundations for CT in 1963 and 1964 [4, 5]. These papers led to the development of the first CT scanner by Sir Godfrey Newbold Hounsfield in 1972. Both Cormack and Hounsfield were awarded a Nobel Prize in Physiology or Medicine for their work on tomography.

A first generation of clinical CT scanners was manufactured in 1974. This first generation used a source generating a pencil beam and a single detector to measure the transmitted X-rays. These scanners used a translate-rotate method; this involved translating the source and detector simultaneously across the patient for every projection angle until a range of 180° was covered. With this projection data, a single cross-section of the patient's body could be reconstructed. This process could be repeated to obtain several cross-sections and could take hours to complete.

In a second generation of CT scanners, the source generated a fan-shaped beam. The same scanning method as in the first generation was used, but this fan beam decreased the scanning time drastically. These scanning times were further reduced below 10 seconds per cross-section in a third generation of scanners where an array of detectors was used.

The fourth generation of medical CT scanners used a fixed ring of detectors that completely surrounded the patient. This concept had the advantage that only the source needed to be rotated. The complexity of the design was thus greatly reduced. However, scan times remained limited because the X-ray tube was still interfaced by cable and always needed to turn back to its initial position after rotating in a full circle. This problem was solved by introducing slip ring technology. With this technology the ring, source and detector system can spin non-stop, and this enables the use of helical CT. In this case the table with the patient moves smoothly through the scanner while the gantry rotates continuously around it. Modern CT scanners also use multiple rows of detectors to further reduce the scan time and thus the dose deposited in the patient. Some scanners even use multiple X-ray tubes for additional reductions in scanning time. The fastest CT scanner nowadays can scan a patient in real time; this means that acquisition and reconstruction is performed almost instantly.

2.1.3 High resolution CT

Outside of the medical field, X-ray CT was also quickly used in industrial settings for quality control and non-destructive testing. With the use of high-voltage X-ray sources and high-energy sensitive detectors, it is possible to look inside large objects such as cars, airplane components and turbine blades.

Both medical and industrial CT are used to study relatively large objects at a limited resolution. However, the scientific community realised that the technique could also have potential on a smaller scale. The development of CT with a resolution within the micrometre scale caught the attention of researchers in fields such as geology, biology, palaeontology, bone research, material sciences and many more. To them, tomography had the advantage that it could be used to make a complete 3D representation of their objects in a non-destructive way. When the resolution of a CT system is in the order of micrometres it is called microCT or μCT. The term nanoCT is used when the resolution is even better than a micrometre, although the term submicroCT is more suitable. Both types of CT are referred to as high-resolution CT in this work.

Eliot and Dover built the first high-resolution X-ray CT scanner in the early 1980s [6]. This scanner used the same scanning method as the first medical scanners and had a resolution of around 50 μm. This made the acquisition for a complete scan very slow, taking from several hours up to a day to complete a scan of an object. A newer generation of high-resolution scanners used a fan-beam geometry, but it was only with the arrival of a third generation of cone-beam scanners that high-resolution CT became a practically feasible technique. These scanners combined an X-ray tube with a small focal spot size with a 2D detector. The flux of these cone beam sources is rather low, but because a projection of the complete 3D volume could be measured by a single radiograph, the scan time was significantly reduced. Furthermore, the use of this cone-beam geometry allows the user to magnify the object by moving it closer to the source. Nevertheless, it was only after Feldkamp, David and Kress presented their algorithm for fast and efficient reconstruction of CT data [7] that cone-beam CT could actually be put into practice.

Just as in medical CT, the use of a helical cone-beam geometry can provide several advantages and is therefore used more and more in X-ray research facilities like UGCT. High-resolution CT can also be conducted at certain synchrotron beamlines. These offer advantages such as a tunable monochromatic source, a much higher X-ray flux, a coherent beam and much better resolution. However,

such an installation is considerably more expensive and not as easily accessible as laboratory-based X-ray CT.

2.2 CT workflow

The process to obtain a CT scan consists of two main steps: the acquisition and the reconstruction. During the acquisition a series of projection images is taken, and during the reconstruction a virtual 3D representation of the scanned object is calculated. This 3D volume obtained can then be visualised, processed and analysed further.

2.2.1 Acquisition

The first step in performing a 3D scan is acquiring the necessary projections. If a high-resolution scanner is used, this involves a setup which typically looks like that shown in Figure 2.2. This setup consist of a source, a sample, which rotates, and a detector. The voltage of the tube and the filtration of the X-ray beam can be altered to optimise the scanning conditions for a certain sample. These optimal conditions will depend on the size, composition and density of the sample, as well as the information the user wants to extract from the scanned object.

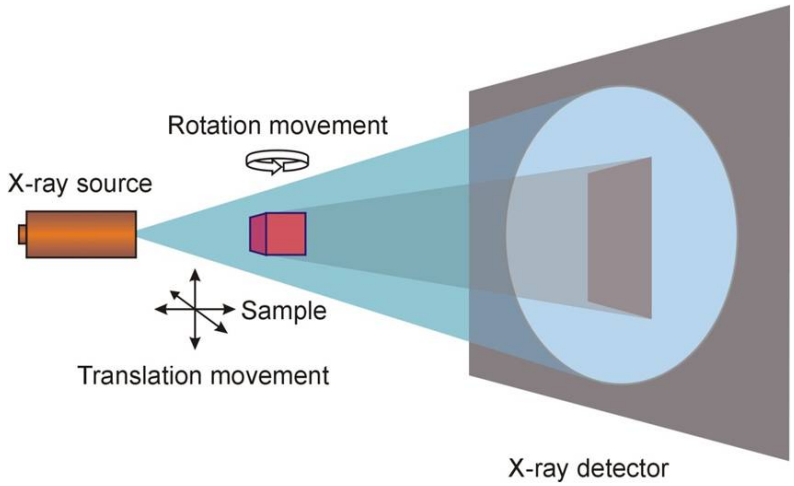

Figure 2.2: A schematic representation of the setup during an X-ray CT acquisition. [8]

During the acquisition process the following images are acquired:

- **Dark fields:** These images are taken when the X-ray source is turned off. As such, the contribution of the dark current in the detector and the pixel

offsets are measured. The exposure time of these images is best taken equal to that of the projection images for optimal results. Multiple dark images can be averaged to obtain a better result.

- **Flat fields:** These images are acquired when the tube is turned on, but when the sample is removed from the beam. It is unlikely that every pixel has the same sensitivity. These images are thus used to measure and correct for inhomogeneities in the detector response. Just as for the dark fields, these images need to be taken with the same exposure time as the projection images and multiple images can be averaged to obtain a better result.

- **Projection images:** A number of projections are taken while the X-ray tube is on and the sample is present in the beam. These images are generally acquired in regular angular intervals while the sample rotates over 360° in case of a full scan.

These images can be used to obtain the normalised projection images that represent the transmitted fraction of the X-rays in a pixel:

$$N_{ij} = \frac{P_{ij} - D_{ij}}{F_{ij} - D_{ij}}, \tag{2.1}$$

in which N_{ij} represents the transmitted fraction in pixel (i, j) and D, F and P represent the dark field, flat field and projection image, respectively.

2.2.2 Reconstruction

The normalised images can be used to reconstruct a 3D volume that consists of voxels. These voxels in the reconstructed volume contain a value that represents the X-ray linear attenuation coefficient in that voxel. This linear attenuation coefficient is a measurement of the degree to which X-rays are attenuated per unit of length travelled through the material. These reconstructed attenuation coefficients can be obtained by solving the following equation:

$$\int_L \mu(x, y, z) ds = -\ln(I/I_0), \tag{2.2}$$

in which s represents the 3D Cartesian coordinates (x, y, z) and I/I_0 is the normalised projection image and $-\ln(I/I_0)$ the projected attenuation. This equation can be solved by using analytical or iterative reconstruction algorithms. A short overview of these algorithms is presented in the next section.

2.3 Reconstruction algorithms

Analytical reconstruction algorithms are still the fastest and most frequently used reconstruction method for X-ray CT. The basic principles of analytical reconstruction and different geometries are discussed below.

2.3.1 Analytical reconstruction

In general, the projection data from an object are a set of measurements of integrated values of a parameter of the object, the local linear attenuation coefficient. These integrations occur along straight lines in the object and are referred to as line integrals. The key to reconstructing the 3D object from these measured line integrals is the Fourier Slice Theorem. In what follows, the line integrals of projections are discussed and the Fourier Slice Theorem is derived. Furthermore, as the reconstruction algorithm depends on the type of source geometry that is used, the reconstruction algorithms for each common source geometry type are briefly described.

Projections and Line integrals

Consider a 2D object that can be modelled by a 2D distribution function $f(x, y)$. In X-ray CT, this distribution corresponds to the distribution of the X-ray linear attenuation coefficients inside the object. The projection of this distribution along the line

$$t = x\cos\theta + y\sin\theta \tag{2.3}$$

is given by

$$P_\theta(t) = \int_{-\infty}^{\infty} f(x, y)ds. \tag{2.4}$$

where θ is the projection angle under which the projected attenuation $P_\theta(t) = -\ln(I/I_0)$ is calculated and t is the position on the detector. The function $P_\theta(t)$ is also known as the Radon transform of the function $f(x, y)$. Figure 2.3 shows how such a projection is formed by combining a set of line integrals.

Fourier Slice Theorem

The Fourier Slice Theorem can be derived by taking the one-dimensional Fourier transform of a parallel projection. First, consider the two-dimensional Fourier transform of the object function $f(x, y)$

$$F(u, v) = \int_{-\infty}^{\infty} f(x, y)e^{-i2\pi(ux+vy)}dxdy \tag{2.5}$$

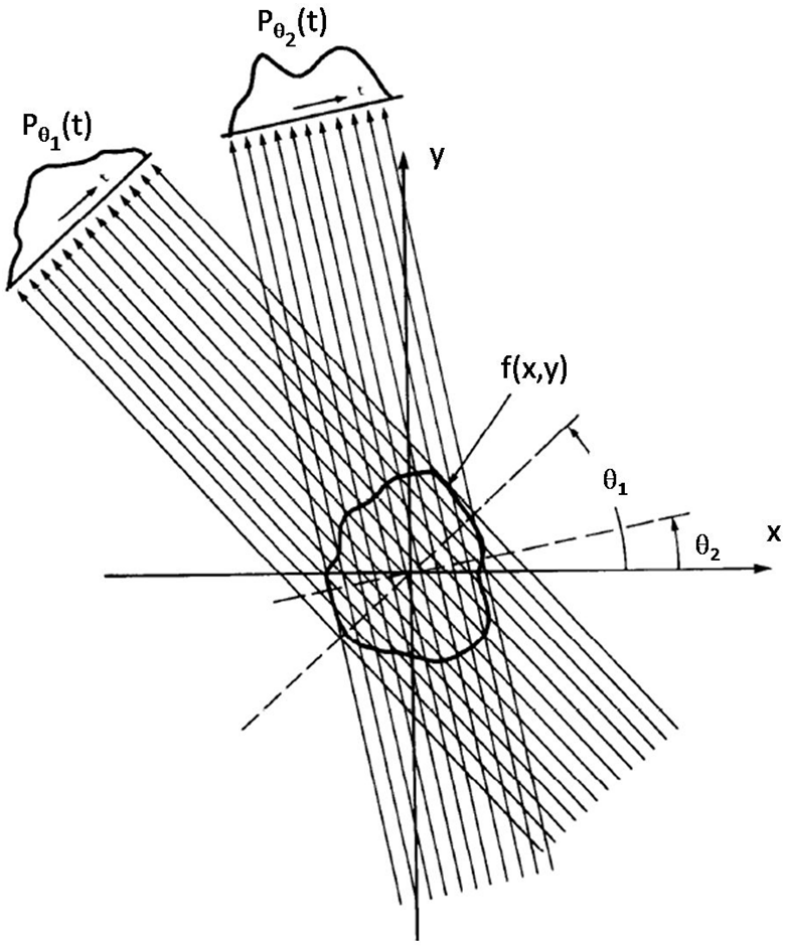

Figure 2.3: The projection of an object with distribution function $f(x, y)$ formed by combining a set of line integrals. [9]

and the Fourier transform of the Radon transform

$$S_\theta(w) = \int_{-\infty}^{\infty} P_\theta(t) e^{-i2\pi wt} dt. \tag{2.6}$$

Consider the Fourier transform of the object along the line in the frequency domain were $v = 0$. This is the simplest example of the Fourier Slice Theorem at $\theta = 0$. The Fourier transform simplifies to

$$F(u, 0) = \int_{-\infty}^{\infty} \left[\int_{-\infty}^{\infty} f(x, y) dy \right] e^{-i2\pi ux} dx \tag{2.7}$$

and by substituting Equation 2.4 into this

$$F(u,0) = \int_{-\infty}^{\infty} P_{\theta=0}(x) e^{-i2\pi ux} dx. \tag{2.8}$$

This equation shows that the one-dimensional Fourier transform of the projection $P_{\theta=0}$ is related to the two-dimensional Fourier transform of the object function:

$$F(u,0) = S_{\theta=0}(u). \tag{2.9}$$

This can be extended to all θ. Consider a rotation of the (x,y) coordinate system over an angle θ.

$$\begin{bmatrix} t \\ s \end{bmatrix} = \begin{bmatrix} \cos\theta & \sin\theta \\ -\sin\theta & \cos\theta \end{bmatrix} \begin{bmatrix} x \\ y \end{bmatrix} \tag{2.10}$$

In this new coordinate system, a projection along a line of constant t is given by

$$P_\theta(t) = \int_{-\infty}^{\infty} f(t,s) ds. \tag{2.11}$$

By using Equation 2.3, which is the new coordinate t expressed as a function of the old coordinates, we retrieve the Fourier transform of the Radon transform

$$S_\theta(w) = \int_{-\infty}^{\infty} \int_{-\infty}^{\infty} f(x,y) e^{-i2\pi w(x\cos\theta + y\sin\theta)} dx dy. \tag{2.12}$$

The two-dimensional Fourier transform at a spatial frequency $(u = w\cos\theta, v = w\sin\theta)$ is represented in the right-hand side of this equation:

$$S_\theta(w) = F(u,v) \tag{2.13}$$

This leads to the Fourier Slice Theorem [10]:

The one-dimensional Fourier transform of a parallel projection of a two-dimensional object function $f(x,y)$ at an angle θ with respect to the x-axis, gives a slice of the two-dimensional Fourier transform $F(u,v)$ of the function $f(x,y)$ at an angle θ with respect to the u-axis.

Filtered back projection

Figure 2.4 illustrates the Fourier Slice Theorem and shows the Fourier transform of the projections of the object $f(x,y)$ at different angles θ. The function $F(u,v)$ can thus be determined along radial lines. However, this function is only

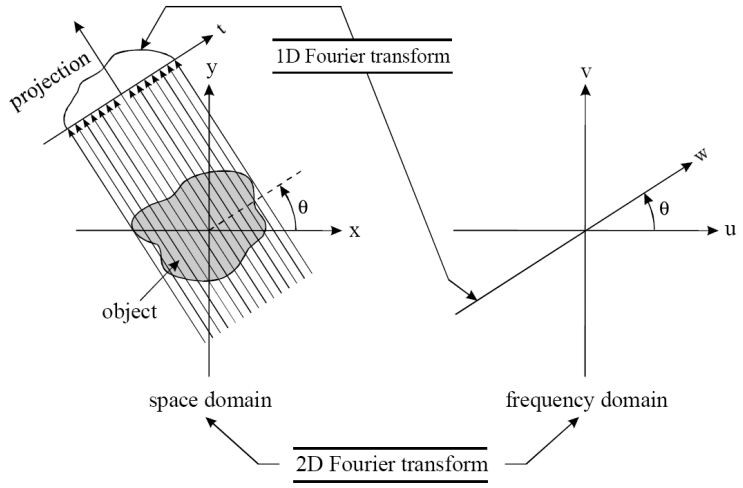

Figure 2.4: The Fourier Slice Theorem states that the Fourier transform of a projection is related to the Fourier transform of the object function along a radial line. [9]

known along a finite number of radial lines. This leads to the fact that the higher frequencies will always be under-sampled relative to the lower frequencies, and results in a blurry reconstruction as shown in Figure 2.5(b) . This can be solved by applying a filter in the frequency domain. Figure 2.6(a) shows the ideal sampling of one projection in the frequency domain and Figure 2.6(b) shows the actual sampling along a single line. By applying a filter (Fig. 2.6(c)) the ideal situation can be approximated. By using this filter and then back-projecting the object, a better result can be achieved as is seen in Figure 2.5(d). This method is called filtered back projection (FBP) and manages to obtain a much better reconstruction of the object.

Parallel

Parallel beam geometry was mostly used in the first generation of medical and high-resolution CT scanners. Nowadays, it is still widely used with synchrotron beamlines, but not in laboratory or medical CT. The inverse Fourier transform of the object function $f(x, y)$ can be expressed as

$$f(x,y) = \int_{-\infty}^{\infty}\int_{-\infty}^{\infty} F(u,v)e^{i2\pi(ux+vy)}dudv. \tag{2.14}$$

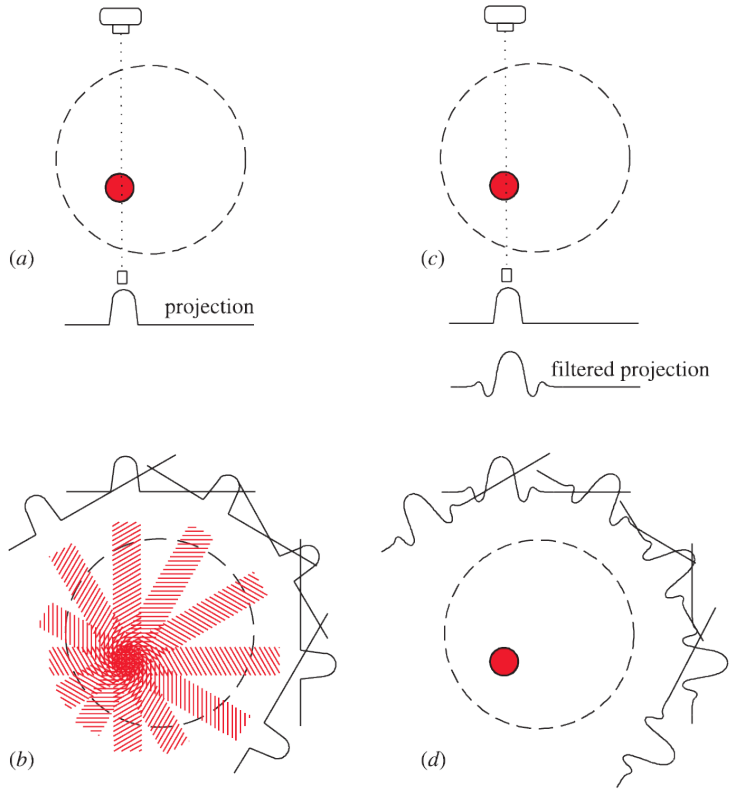

Figure 2.5: A schematic visualisation of the principle of Filtered Back Projection in the case of a parallel beam geometry. A single attenuation line profile can be back-projected along the incident X-ray path (a). Many line profiles can be recorded and thus back-projected from different directions (b). This simple back projection, however, induces a starburst pattern and blurry edges. To overcome this effect a filter is applied (c). The filter induces negative values along the line profiles which cancel out the starburst pattern (d). [11]

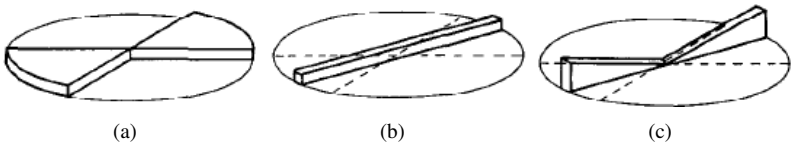

Figure 2.6: A schematic representation of the data available in the frequency domain from one projection. (a) shows the ideal situation and (b) shows the actual situation. The ideal situation is approximated by weighing the data as given in (c). [9]

Switching to a polar coordinate system (w, θ) with

$$\begin{aligned} u &= w\cos\theta \\ v &= w\sin\theta \end{aligned} \tag{2.15}$$

the inverse Fourier transform can be rewritten as

$$f(x,y) = \int_0^{\pi} \left[\int_{-\infty}^{\infty} F(w,\theta)|w|e^{i2\pi wt} dw \right] d\theta \tag{2.16}$$

with

$$t = x\cos\theta + y\sin\theta. \tag{2.17}$$

The Fourier Slice Theorem states that the 2D Fourier transform $F(w,\theta)$ can be replaced by the Fourier transform $S_\theta(w)$ at a projection angle θ. The object function can thus be reconstructed by using the following set of line integrals:

$$f(x,y) = \int_0^{\pi} Q_\theta(t) d\theta, \tag{2.18}$$

$$Q_\theta = \int_{-\infty}^{\infty} S_\theta(w)|w|e^{i2\pi wt} dw, \tag{2.19}$$

$$S_\theta(w) = \int_{-\infty}^{\infty} P_\theta(t) e^{-i2\pi wt} dt. \tag{2.20}$$

The last equation represents the 1D Fourier transform of the projection data at an angle θ. The second equation represents a filtering operation on the Fourier transform of the projection data. The frequency response is given by $|w|$ but other filters may be used as well. The first equation is the back-projection of the filtered projections. This process of first filtering the projections is called filtered back projection, as explained before.

In a realistic CT scan it is impossible to obtain an infinite number of projections. The set of integrals presented above can be rewritten for a set of K projections at projection angles θ_k. The line integrals of the projection data $P_\theta(t)$ are sampled at positions $n\Delta t$ with Δt the detector pitch and $n = -(N-1)/2, ..., (N-1)/2$, where N is the number of pixel columns in the detector. The projection data is represented by $P_{\theta_k}(n\Delta t)$. Furthermore, it is safe to assume that above a certain frequency the Fourier transform component will be negligible; the projection data is thus band limited. The maximum frequency contained in the projection data is given by the Nyquist frequency $W = 1/2\Delta t$. The Fourier transform of the projection $S_\theta(w)$ can be sampled at the frequencies $m\Delta w$ where $w = 2W/N$ and $m = -(N-1)/2, ..., (N-1)/2$. The Fourier transform of the projection data can thus be represented by $S_{\theta_k}(m\Delta w)$. By using this discretisation and Fourier

transform of the projected data, the following practical sampling scheme can be obtained:

$$f(x,y) = \frac{\pi}{K} \sum_{k=1}^{K} Q_{\theta_k}(x\cos\theta_k + y\sin\theta_k), \tag{2.21}$$

$$Q_{\theta_k}(n\Delta t) = \Delta w \sum_{m=-\frac{N-1}{2}}^{\frac{N-1}{2}} S_{\theta_k}(m\Delta w)|m\Delta w| e^{i2\pi mn\Delta w\Delta t}, \tag{2.22}$$

$$S_{\theta_k}(m\Delta w) = \Delta t \sum_{n=-\frac{N-1}{2}}^{\frac{N-1}{2}} P_{\theta_k}(n\Delta t) e^{-i2\pi mn\Delta w\Delta t}. \tag{2.23}$$

Fan

A fan-beam geometry can be achieved by using a point source of X-rays and a planar or circular line detector. This modification in geometry will require a change in the back-projection algorithm. Moreover, the use of a planar or circular detector will also change the algorithm for reconstructing the back-projections (Fig. 2.7). By using a planar detector, the detector pixels are placed equidistant on a straight line. For a circular detector, the detector pixels are placed equiangular on an arc with its centre at the X-ray source. In [9] a derivation of the reconstruction method for both geometries is given. Here, the result of a fan-beam geometry with a planar detector is given:

$$f(x,y) = \int_0^{2\pi} \frac{R^2}{U(x,y,\theta)^2} Q_\theta(t) d\theta, \tag{2.24}$$

$$Q_\theta = \int_{-\infty}^{\infty} S_\theta(w)|w| e^{i2\pi wt} dw, \tag{2.25}$$

$$S_\theta(w) = \int_{-\infty}^{\infty} \frac{R}{\sqrt{R^2+t^2}} P_\theta(t) e^{-i2\pi wt} dt, \tag{2.26}$$

with

$$U(x,y,\theta) = R - x\sin\theta + y\cos\theta, \tag{2.27}$$

$$t = R\frac{x\cos\theta + y\sin\theta}{R - x\sin\theta + y\cos\theta}. \tag{2.28}$$

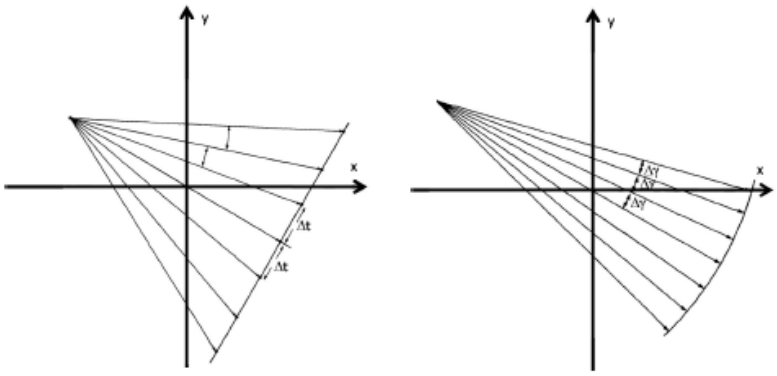

(a) Planar detector (b) Circular detector

Figure 2.7: When a fan-beam geometry is used, the rays can either be sampled at equidistant (a) or equiangular (b) intervals. [12]

Cone

The algorithms described previously are developed to reconstruct a single slice. However, to reconstruct a 3D volume, this process must be repeated slice by slice. During the acquisition, the projection data for every slice is easier and much faster to obtain when a 2D detector is used (Fig. 2.8). The projection data $P_\theta(t, r)$ will thus be a function of the projection angle θ and the horizontal and vertical detector positions t and r.

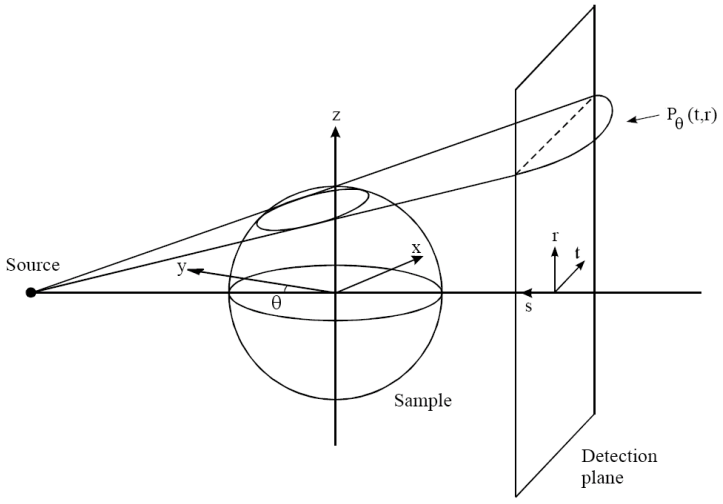

Figure 2.8: When using a cone-beam geometry, a 2D detector is used to measure the projections and thus line integrals across the object. [9]

The object function $f(x, y, z)$ can exactly be reconstructed by defining the 3D Radon transform [13]:

> Consider a plane defined by its normal $\vec{n}$ and at a distance s to the origin. The 3D Radon transform $Rf(\vec{n}, s)$ is the integral of $f(x, y, z)$ over this plane.

Each plane can thus be represented by the value of the Radon transform $Rf(\vec{n}, s)$ which defines a unique point in object space. The Fourier Slice theory can be extended to three dimensions:

> The 1D Fourier Transform $FRf(\vec{n}, s)$ of the Radon values with respect to s is equal to a central slice at direction $\vec{n}$ of the 3D Fourier transform $Ff(x, y, z)$ of the object function.

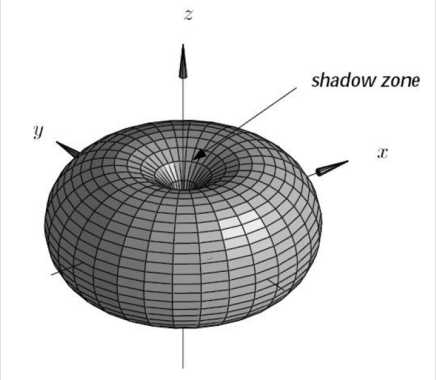

Figure 2.9: This figure represents the values of the 3D Radon transform of the object function that can be retrieved when using a cone-beam geometry. [14]

The 3D Fourier transform of the object can thus be calculated if the 3D Radon values in the object space are available. Theoretically, the 3D Radon values of a plane through an object can be obtained by integrating the projection data over the intersection between the detector and the plane. An exact reconstruction is only possible when the Tuy-Smith condition [15] is satisfied. This condition states that an exact reconstruction is only possible when all planes intersecting the object intersect the source trajectory at least once. For most of the planes, this condition will be satisfied in a circular cone-beam geometry. However, for planes parallel to the circular trajectory of the source, this condition will not be valid. This results in missing data, so the Radon data are confined to a torus which is shown in Figure 2.9. This zone with missing data is referred to as the shadow zone.

Although exact reconstruction is therefore not possible for cone-beam CT as described above, the induced errors are rather small. An extension of the filtered

back projection algorithm for cone-beam CT was proposed by Feldkamp, David and Kress (FDK) [7]. This is the most commonly used analytic reconstruction algorithm for cone-beam CT data and is described by the following set of equations:

$$f(x,y) = \int_0^{2\pi} \frac{R^2}{U(x,y,\theta)^2} Q_\theta(t) d\theta, \tag{2.29}$$

$$Q_\theta = \int_{-\infty}^{\infty} S_\theta(w)|w| e^{i2\pi wt} dw, \tag{2.30}$$

$$S_\theta(w) = \int_{-\infty}^{\infty} \frac{R}{\sqrt{R^2+t^2+r^2}} P_\theta(t) e^{-i2\pi wt} dt, \tag{2.31}$$

with

$$U(x,y,\theta) = R - x\sin\theta + y\cos\theta, \tag{2.32}$$

$$t = R\frac{x\cos\theta + y\sin\theta}{R - x\sin\theta + y\cos\theta}, \tag{2.33}$$

$$r = z\frac{R}{R - x\sin\theta + y\cos\theta}. \tag{2.34}$$

Here R is the distance between the source and origin. $U(x,y,\theta)$ is the distance from the source to the point (x,y) projected on the central ray. $P_\theta(t,r)$ represents the projection data at an angle θ of the pixel at a position (t,r) in the detector plane.

Helical

As mentioned previously, there is an incomplete sampling of the Radon space in cone-beam geometry; as a result, this does not allow for an exact reconstruction. A helical cone-beam geometry can be used as an alternative. By introducing an additional translation along the axis of rotation between the projections as shown in Figure 2.10, it is possible to allow for exact reconstruction. Furthermore, this geometry has the advantage that object size does not necessarily limit the resolution of the scan. The object can be larger in size than the detector in the dimension that coincides with the translation axis of the helical setup.

The technical requirements needed for helical cone-beam geometry are relatively high because the vertical movement of the sample must be very precise. A high resolution requires a high level of accuracy of the vertical translation axis while a helical CT scan is performed. This is the standard technique used in medical CT and is being used more and more for high-resolution CT. The reconstruction algorithms are complex due to the trajectory of the system, but different exact

analytic reconstruction methods exist [14]. The algorithm used at UGCT is the Katsevich algorithm [16].

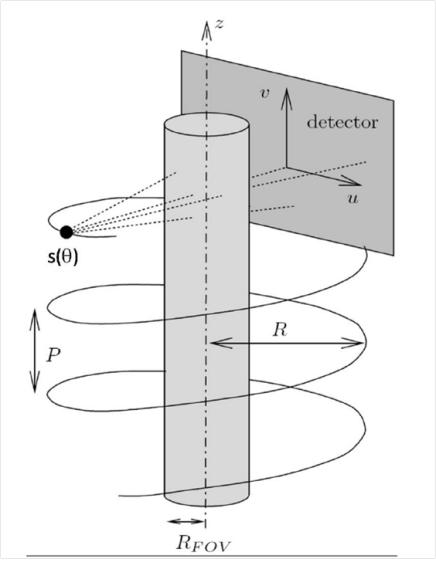

Figure 2.10: The geometry used in helical cone-beam. [17]

2.3.2 Iterative reconstruction

All reconstructions shown in this work are performed with the analytical reconstruction methods present in Octopus [18, 19]. In the scope of this work, iterative reconstruction algorithms are not addressed. A thorough discussion of iterative reconstruction algorithms can be found in [20, 21].

2.4 UGCT

The Centre for X-ray Tomography of Ghent University (UGCT) was founded in 2006. It was initially a collaboration between the Radiation Physics (RP) group of the Department of Physics and Astronomy and the Sedimentary Geology and Engineering Geology group, nowadays called PProGRess, of the Department of Geology and Soil Science. Later, in 2009, the Laboratory of Wood Technology of the Department of Forest and Water Management joined this collaboration. In addition, two spinoff companies originated from UGCT. The first, Inside Matters - formerly called inCT - was founded in 2008. This company focuses on the further development and commercial distribution of the Octopus Imaging Software and offers X-ray services to companies (www.insidematters.eu). In 2011, a second

spinoff company called X-ray Engineering (XRE) was founded. XRE offers conceptual and complete solutions for X-ray imaging, and works together with UGCT to further develop the acquisition software Acquila (www.xre.be).

The research of the Radiation Physics group, in which this work was performed, focuses on the development and application of state-of-the-art high-resolution CT scanners. The scanners present at UGCT are modular, and improvements or modifications can be applied if necessary. For example, pressure cells or climate chambers can be mounted on the scanners when scientific experiments require this. Furthermore, the development of acquisition, reconstruction, analysis and simulation software is also a part of the research performed by the RP group. All software and scanners developed at UGCT are listed below.

2.4.1 Software

Acquila

A software platform for controlling the CT scanners present at UGCT was developed in Labview ® [22]. The scanners differ in their physical implementations but the basic functionalities are the same. For example, each scanner will have a tube and will be able to take projections. The acquisition software is designed in such a way that each software component of a motor, tube or detector can be added quite easily to the main component of the program. Software components of add-on modules for the scanners can be integrated as well. This makes this acquisition software very useful in a research facility like UGCT, where components can and will often be installed at different scanners and when a large amount of peripheral equipment is used.

Octopus Reconstruction

Octopus Reconstruction was originally developed at UGCT [18, 19]. This reconstruction software package combines the reconstruction of parallel, fan, cone and helical cone-beam data with advanced artefact reducing methods. The reconstruction performance of the package can be optimised by using multiple CPU cores or a graphic processing unit (GPU). In addition, an iterative SART method is also available in the package.

Octopus Analysis

For analysis of reconstructed 3D volumes, the software package Morpho+ was developed at UGCT [8, 19, 23]. This package is currently called Octopus Analysis. The software package can process large datasets, and provides several parameters and routines which are applicable in a variety of scientific fields.

Arion

Arion is a fast GPU based X-ray CT simulator. The program was recently developed at UGCT and is discussed extensively in Chapter 5.

2.4.2 Scanners

Nanowood

Nanowood is a versatile multi-resolution X-ray CT scanner [24]. It is located at the Laboratory for Wood Technology and is nowadays, since the refurbishment of the original 2006 scanner, the 'oldest' system at UGCT. The system is equipped with two separate X-ray tubes and two different X-ray detectors. The first tube is a directional tube with a maximum high voltage of 130 kV that allows a focal spot size down to 5 μm. The second tube has a tungsten transmission target and can reach a high voltage of 100 kV and achieve a minimum spot size of 400 nm. The first detector is a Si flat panel with a CsI scintillator and has a good efficiency from about 20 to 130 keV, while the second detector has a Gadox scintillator and has an efficiency that peaks around 10 keV and drops fast for photons above 20 keV. This combination of sources and detectors, together with the way they are mounted (Fig. 2.11), ensures that small samples can be scanned with a resolution below 1 μm while samples up to 35 cm can also be scanned, albeit with a lower resolution.

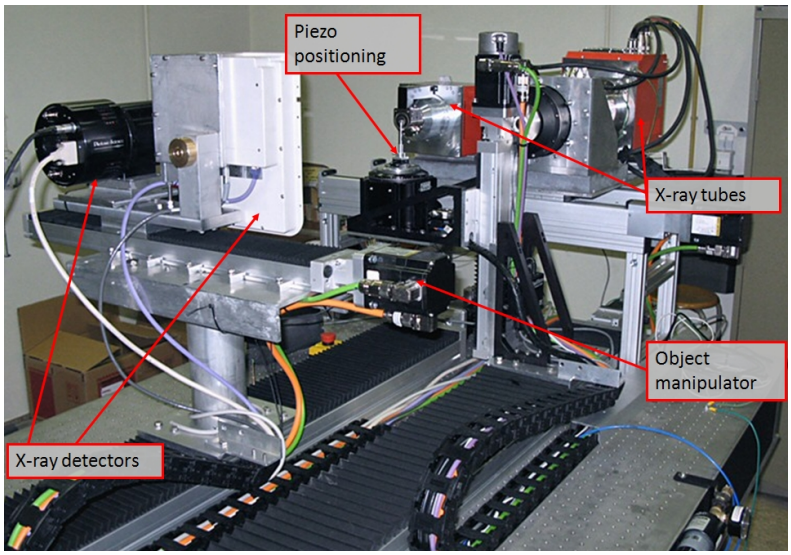

Figure 2.11: The Nanowood scanner, located at the Laboratory of Wood Technology.

HECTOR

The High-Energy CT system Optimized for Research, or HECTOR [25], is the current workhorse of UGCT (Fig. 2.12). This system can be used for a wide range of applications due to its modularity and voltage range covered. The tube voltage can be adjusted from 20 kV up to 240 kV with a minimum spot size of 4 μm at a tube power of 10 W. For applications that require more flux, such as dense concrete cylinders, the power can be set as high as 280 W. The detector is a Perkin Elmer flat panel detector with dimensions of 40 by 40 cm, but this detector can be moved so that by tiling a field of view of 80 by 80 cm can be achieved. The detector uses a CsI scintillator and is still sensitive for energies above 200 keV.

Samples weighing up to 80 kg and measuring 1 m long and 80 cm in diameter can be mounted on the rotation stage. The scanner can thus be used to investigate the microstructure of small objects as well as large dense objects such as concrete cores. Furthermore, the source detector distance can be varied from 30 cm up to 2 m depending on the requirements for the scanned objects. The complete system is installed in a large concrete bunker and leaves room to equip the scanner with peripheral equipment such as compressing stages.

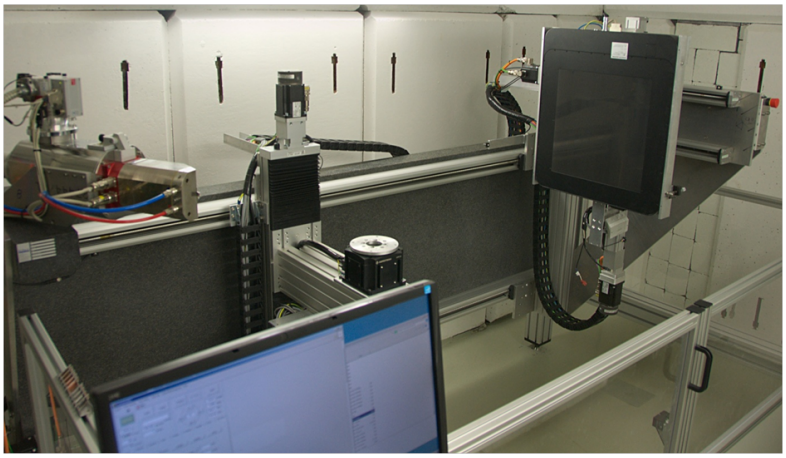

Figure 2.12: The High-Energy CT system Optimized for Research (HECTOR) at the UGCT.

EMCT

The Environmental Micro-CT (EMCT) system [24] is a rather unique system for high-resolution CT (Fig. 2.13). The system is gantry based just like a medical CT scanner, but is mounted horizontally. The sample remains stationary and the source

and detector move around the sample. Contrary to a medical CT scanner, the source object distance and thus magnification can be adapted and the best possible resolution can be as low as 5 μm. Moreover, this arrangement is ideal for installing add-on modules on the stage such as flow cells, pressure stages and temperature stages. The system can perform five full rotations per minute, which makes it ideal for visualising changing processes such as crystallisation of salt inside rocks [26].

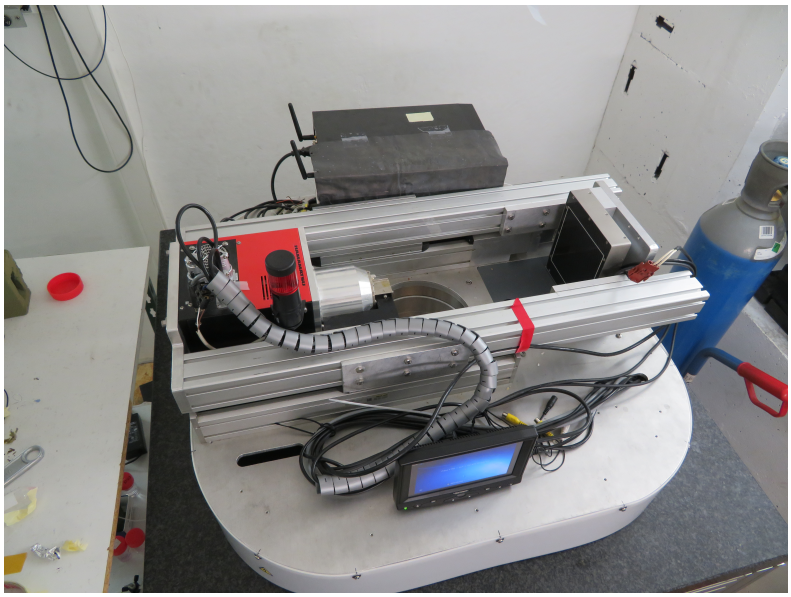

Figure 2.13: EMCT scanner at UGCT.

The source and detector are installed on a linear motorised stage and can be used to control the magnification. This stage which is mounted on a goniometer has a positional accuracy better than 5 μm. The vertical translation motor is centred in a 190-mm hole in the goniometer. To assure the required precision during the scanning process, the entire system is mounted on a granite base and uses slip ring technology to enable continuous scanning. The source is a directional source with a maximum tube voltage of 130 kV and a minimum spot size of 5 μm, and can achieve a maximum power of 39 W. The detector is a CMOS detector with a CsI scintillator and a field of view measuring 14 by 14 cm.

Medusa

The very high-resolution scanner Medusa is a refurbishment of the first high-resolution scanner built at UGCT in 2005 [27]. Similar to the Nanowood scanner,

it combines the same type of detectors together with a transmission tube with a minimum spot size of 700 nm (Fig. 2.14). Both detectors are mounted on a linear motorised stage and can be switched very fast. The combination of both detectors allows the user to scan both extremely small biological low-density materials as well as high-density geomaterials.

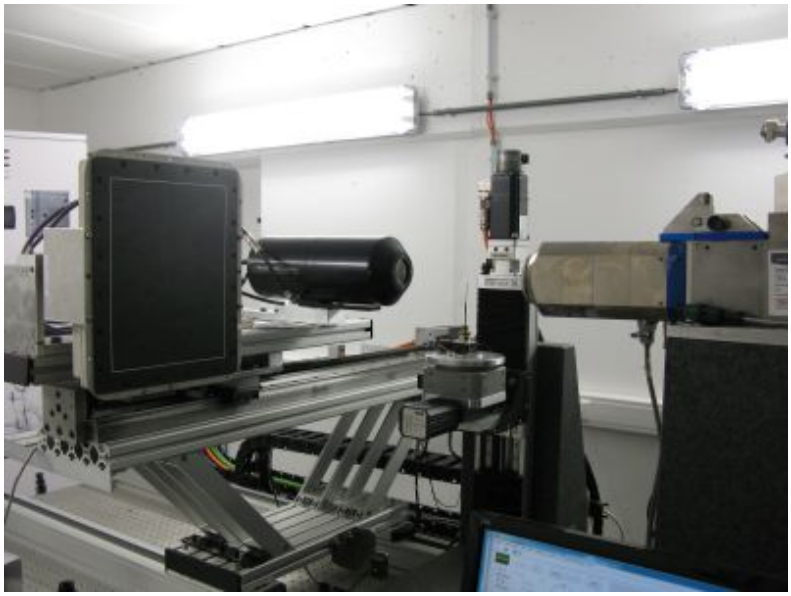

Figure 2.14: Medusa scanner at UGCT.

Herakles (XMI-UGCT)

Herakles is a system involving three scanning stages that combines micro-CT and micro-XRF (Fig. 2.15). The development and construction of this setup was made possible by the collaboration between the X-ray Microspectroscopy and Imaging Group (XMI) of the Department of Analytical Chemistry and the radiation physics group. Two micro-XRF stages and one high-resolution CT stage are mounted on the scanner. These three stages are linked with an air-beared positioning system which offers 10-μm precision over a range of 80 cm. This is necessary for the correlation between the CT and XRF images. The scanner is in the final stages of construction and can soon be used for state-of-the-art research.

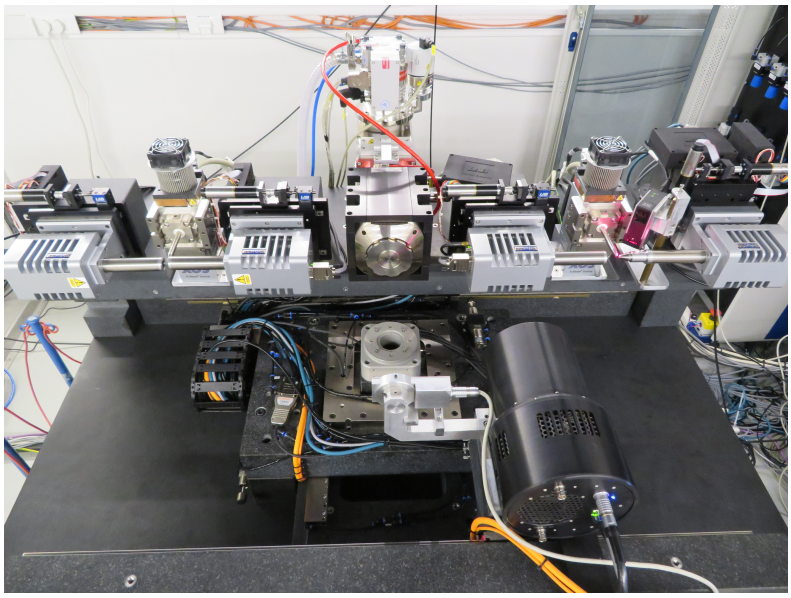

Figure 2.15: Herakles scanner (XMI-UGCT).

References

[1] *http://en.wikipedia.org/wiki/Electromagnetic_spectrum#/media/File:EM_Spectrum_Properties_edit.svg*.

[2] W. C. Röntgen. *On a new kind of rays*. Würzburg Physical and Medical Society, 1895.

[3] J. Radon. *Über die Bestimmung von Funktionen durch ihre Integralwerte längs gewisser Mannigfaltigkeiten*. Berichte des Schsischen Akademie der Wissenschaften, 69:262–277, 1917.

[4] A. M. Cormack. *Representation of a Function by Its Line Integrals, with Some Radiological Applications*. Journal of Applied Physics, 34:2722–2727, September 1963.

[5] A. M. Cormack. *Representation of a Function by Its Line Integrals, with Some Radiological Applications. II*. Journal of Applied Physics, 35:2908–2913, October 1964.

[6] J.C. Elliot and S.D. Dover. *X-ray microtomography*. Journal of Microscopy, 126(2):211–213, 1982.

[7] L.A. Feldkamp, L.C. Davis, and J.W. Kress. *Practical cone-beam algorithm*. Journal of the Optical Society of America A, 1(6):612–619, 1984.

[8] J. Vlassenbroeck. *Advances in laboratory-based X-ray microtomography*. Phd dissertation, Ghent University, 2009.

[9] A. C. Kak and M. Slaney. *Principles of Computerized Tomographic Imaging*. IEEE Press, New York, 1988.

[10] S. Haykin, J. H. Justice, N. L. Owsley, J. L. Yen, and A. C. Kak. *Array signal processing.* IEEE Press, 1985.

[11] G. Michael. *X-ray computed tomography*. Physics Education, 36(6):442, 2001.

[12] A. Rosenfeld and A. C. Kak. *Digital Picture Processing*. Academic Press, New York, 1982.

[13] A. Averbuch, R. Coifman, M. Israeli, I. Sedelnikov, and Y. Shkolnisky. *Advances in signal transforms: theory and application*. Hindawi Publishing Corporation, New York, 2007.

[14] H. Turbell. *Cone-beam reconstruction using filtered backprojection*. Phd dissertation, Linköping University, 2001.

[15] H. Tuy. *An inversion formula for cone-beam reconstruction*. SIAM Journal of Applied Mathematics, 43(3):546–552, 1983.

[16] A. Katsevich. *Analysis of an exact inversion algorithm for spiral cone-beam CT*. Physics in Medicine and Biology, 47(15):2583–2597, 2002.

[17] H. Kudo, T. Rodet, F. Noo, and M. Defrise. *Exact and approximate algorithms for helical cone-beam CT*. Physics in Medicine and Biology, 49(13):2913–2931, 2004.

[18] M. Dierick, B. Masschaele, and L. Van Hoorebeke. *Octopus, a fast and user-friendly tomographic reconstruction package developed in LabView*. Measurement Science and Technology, 15(7):1366–1370, 2004.

[19] J. Vlassenbroeck, M. Dierick, B. Masschaele, V. Cnudde, L. Van Hoorebeke, and P. Jacobs. *Software tools for quantification of X-ray microtomography*. Nuclear Instruments and Methods in Physics Research A, 580(1):442–445, 2007.

[20] Y. De Witte. *Improved and practically feasible reconstruction methods for high resolution X-ray tomography*. Phd dissertation, Ghent University, 2010.

[21] L. Brabant. *Latest developments in the improvement and quantification of high resolution X-ray tomography data*. Phd dissertation, Ghent University, 2013.

[22] M. Dierick, D. Van Loo, B. Masschaele, M. Boone, and L. Van Hoorebeke. *A LabVIEW® based generic CT scanner control software platform*. Journal of X-Ray Science and Technology, 18(4):451–461, 2010.

[23] L. Brabant, J. Vlassenbroeck, Y. De Witte, V. Cnudde, M.N. Boone, J. Dewanckele, and L. Van Hoorebeke. *Three-Dimensional Analysis of High-Resolution X-Ray Computed Tomography Data with Morpho+*. Microscopy and Microanalysis, 17(2):252–263, 2011.

[24] M. Dierick, D. Van Loo, B. Masschaele, J. Van den Bulcke, J. Van Acker, V. Cnudde, and L. Van Hoorebeke. *Recent micro-CT scanner developments at UGCT*. Nuclear Instruments and Methods in Physics Research, Section B, 324(0):35–40, 2014.

[25] B. Masschaele, M. Dierick, D. Van Loo, M. N. Boone, L. Brabant, E. Pauwels, V. Cnudde, and L. Van Hoorebeke. *HECTOR: A 240kV micro-CT setup optimized for research*. Journal of Physics: Conference Series, 463, 2013.

[26] Tom Bultreys, Marijn A. Boone, Matthieu N. Boone, Thomas De Schryver, Bert Masschaele, Luc Van Hoorebeke, and Veerle Cnudde. *Fast laboratory-based micro-computed tomography for pore-scale research: Illustrative experiments and perspectives on the future*. Advances in Water Resources, pages –, 2015.

[27] B. Masschaele, V. Cnudde, M. Dierick, P. Jacobs, L. Van Hoorebeke, and J. Vlassenbroeck. *UGCT: new x-ray radiography and tomography facility*. Nuclear Instruments and Methods in Physics Research, Section A, 580(1):266–269, 2007.

3

Physics of X-ray CT

This chapter starts with an extended description of interactions between electrons and matter, followed by interactions between photons and matter. An understanding of these two interaction types is not only crucial to performing accurate simulations of X-ray tubes and detectors (chapter 4), but it is also important in simulating the complete CT scan process (chapter 5). In addition to these two physical interaction mechanisms, the production of γ-rays by radioactive decay and X-rays by synchrotron facilities and X-ray tubes is discussed. Further, a brief summary of the most commonly used X-ray detectors is given. Finally, some physical properties of laboratory-based X-ray systems are discussed.

3.1 Interactions of electrons with matter

Charged particles lose energy when they penetrate matter. However, electrons and positrons behave differently from heavy particles such as alpha particles. Both collide with electrons in the atomic shells, but a heavy charged particle can only transfer a small amount of its energy, and its deflection in the collision is negligible. These particles thus travel in an almost straight line through matter while losing energy continuously. In some cases, however, these particles can undergo a substantial deflection due to scattering off of an atomic nucleus, as demonstrated by Rutherford's scattering experiments [1].

Electrons and positrons also lose energy almost continuously while travelling through matter. However, the mass of these particles is equal to the mass of the shell electrons with which they collide. This can result in large energy transfers and deflections of the electrons and positrons. Furthermore, these particles can also be scattered at large angles by nuclei. Thus, in contrast to heavy charged particles, electrons and positrons do not generally travel through matter in straight lines. Because of the context of this work, only electron interactions are described further in this section.

There are two main interactions between electrons and the penetrated material that cause the electrons to lose their energy. The first interaction is when the penetrating electrons collide with the shell electrons. The second type, also known as bremsstrahlung, occurs when the electron emits electromagnetic radiation when it is deflected in the electric field of the nucleus and electrons in the material. The loss of energy can be described by the stopping power, which is material-dependent and defined as the energy loss of the penetrating electron per unit path length travelled through the material:

$$S(E) = -\frac{dE}{dx}. \tag{3.1}$$

The stopping power can be divided into two components: collisional and radiative stopping power, depending on the process by which the electrons lose their energy.

Collisional stopping power

As mentioned above, an electron can lose a large fraction of its initial energy when it collides with an electron in an atomic shell and can also undergo a large deflection. Therefore, it is difficult to distinguish between the incident and the struck electron. The electron with the highest energy after the collision is considered to be the initial particle in the calculation of the stopping power. The collisional stopping power of an electron is given by [2]:

$$\left(-\frac{dE}{dx}\right)^{-}_{col} = \frac{4\pi k_0^2 e^4 n}{m_e c^2 \beta^2}\left(\ln\frac{m_e c^2 \tau\sqrt{\tau+2}}{\sqrt{2}I} + F(\beta)^{-}\right), \tag{3.2}$$

with

$$F(\beta)^{-} = \frac{1-\beta^2}{2}\left(1 + \frac{\tau^2}{8} - (2\tau+1)\ln 2\right). \tag{3.3}$$

Here $m_e c^2$ is the rest energy of the electron and $\tau = T/m_e c^2$ is the kinetic energy T in multiples of the particle's rest energy, n the number of electrons per unit volume in the medium, $\beta = v/c$ the velocity of the particle relative to c and I the mean excitation energy of the medium.

Radiative stopping power

A charged particle that is accelerated in an electromagnetic field loses energy by radiating photons. When electrons strike a target material, for example in an X-ray tube, they can be deflected in the electric fields of the nuclei and electrons. This results in the emission of bremsstrahlung. If the electron passes near a nucleus, it is accelerated by the bare Coulomb field of the nucleus. If it passes at a greater distance from the nucleus, the nucleus is partially screened by the atomic electrons. This screening effect depends on how close or far the electron passes from the nucleus. Further, the screening and subsequent energy loss are also dependent on the energy of the initial electron. Logically, the energy of the emitted radiation cannot be greater than the kinetic energy of the incident electron.

Unlike for the collisional stopping power, no analytic formula exists for calculating the radiative stopping power. However, based on numerical methods to obtain values for the radiative stopping power, [2] follows that the efficiency of bremsstrahlung in elements varies with $Z(Z+1)$, and the collisional stopping power is proportional to n (Eq. 3.2) and hence to Z. Furthermore, the radiative energy loss rate is nearly linear with the energy E of the electron, while the collisional rate increases only logarithmically at high energies. At high energies the radiative energy loss is thus dominant. An approximation for the ratio between the radiative and collisional stopping power can be given by

$$\frac{(-dE/dx)^{-}_{rad}}{(-dE/dx)^{-}_{col}} \cong \frac{ZE}{800}, \tag{3.4}$$

for high energies, with E the energy in MeV. This formula shows that for tungsten, a typical target material for X-ray tubes, the two rates of energy loss are equal and around 10.8 MeV.

Total stopping power

The total stopping power of a particle is the sum of the collisional and radiative stopping powers:

$$\left(-\frac{dE}{dx}\right)^{\pm}_{tot} = \left(-\frac{dE}{dx}\right)^{\pm}_{col} + \left(-\frac{dE}{dx}\right)^{\pm}_{rad} \tag{3.5}$$

Figure 3.1 shows the collisional, radiative and total stopping powers of tungsten. As mentioned before, at low energies below 1 MeV the collisional stopping power is dominant, and at energies higher than 10 MeV the radiative stopping power becomes the dominant source of energy loss for materials with a high atomic number such as tungsten.

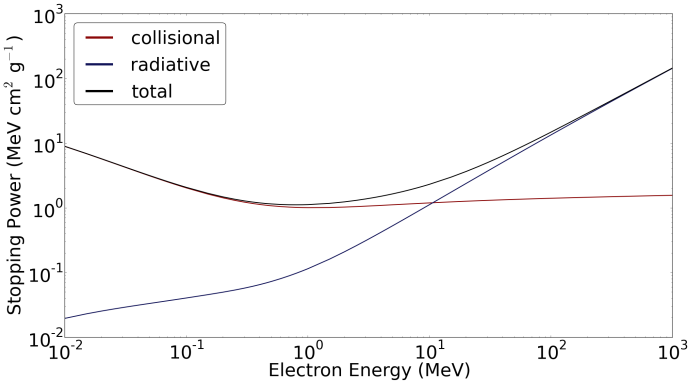

Figure 3.1: Stopping power of tungsten (Z = 74). Data obtained from NIST(ESTAR) [3].

Radiation yield

The radiation yield is the average energy fraction of the initial energy an electron loses by radiation as it slows down in a medium. The radiation yield increases with increasing energy, as the radiative stopping power becomes more important at higher energies. Further, for an electron with a given energy it also increases with increasing atomic number of the medium. An estimate of the radiation yield for a high-energy electron with kinetic energy T (MeV) and atomic number Z is given by [4]:

$$Y \cong \frac{6 \times 10^{-4} ZT}{1 + 6 \times 10^{-4} ZT}. \tag{3.6}$$

Figure 3.2 shows a more accurate value for the radiation yield over a broader energy range for tungsten (W) and molybdenum (Mo). For example, a 100 keV electron loses a fraction of 0.0103 of its total energy by bremsstrahlung in tungsten.

Range

The range of a charged particle is defined as the distance it penetrates through a medium before it comes to rest. The range can be expressed as

$$R(T) = \int_0^T \left(-\frac{dE}{dx} \right)^{-1} dE. \tag{3.7}$$

This definition assumes that the particle loses energy continuously as it travels through the medium. The average range that an electron travels before it is fully stopped can thus be calculated by this equation. Figure 3.3 shows the range of an electron penetrating tungsten. For example, the range of a 100 keV electron

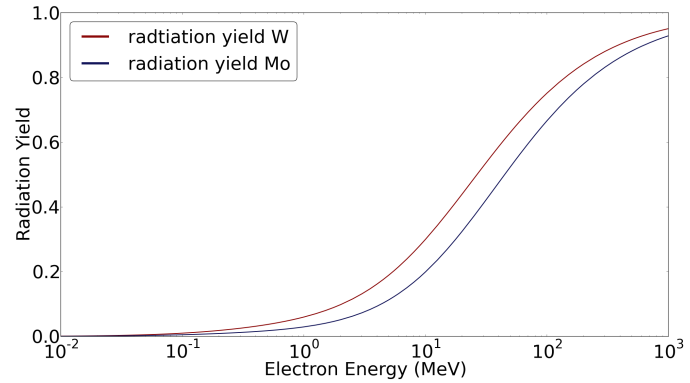

Figure 3.2: Radiation yield for an electron in tungsten ($Z = 74$) and molybdenum ($Z = 42$). Data obtained from NIST(ESTAR) [3].

in tungsten is 15.4 μm. Note that only a few of such particles will actually reach this depth inside a tungsten medium. This is because the particle can be scattered when it loses energy and it will thus not travel in a straight path.

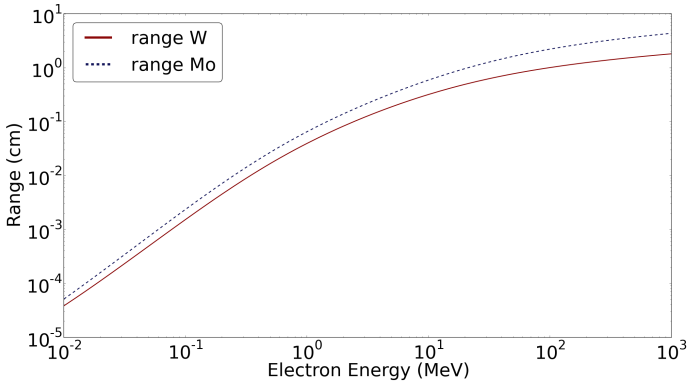

Figure 3.3: Range of an electron in tungsten ($Z = 74$, $\rho = 19.3$ g/cm^3) and molybdenum ($Z = 42$, $\rho = 10.25$ g/cm^3). Data obtained from NIST(ESTAR) [3].

3.2 Interaction of photons with matter

Unlike electrons, photons are electrically neutral and do not continuously lose energy while travelling through a medium. They can instead travel some distance in the medium before they interact. The mean free path of a photon between interactions is determined by the medium traversed and the photon energy. Upon

interaction, the photon can be absorbed or scattered with or without losing energy. In this section, different interactions between photons and matter are discussed.

3.2.1 Photoelectric absorption

During the photolectric absorption process, a photon interacts with a shell electron and transfers all its energy to that electron. When a photon has sufficient energy to ionise an atom, an electron of one of its shells can escape. The kinetic energy of an escaping electron is equal to the energy of the incident photon minus the binding energy of the electron:

$$E_{e^-} = E_\gamma - B \tag{3.8}$$

in which E_{e^-} is the energy of the electron, E_γ the energy of the incident photon and B the binding energy of the escaped electron.

The photoelectric absorption of a photon by an atom is always followed by secondary events. The ejection of a photoelectron leaves a vacancy in the absorber. If this vacancy is in one of the lower shells, it can be filled by the transition of an electron from a higher shell, resulting in the emission of a fluorescence or characteristic X-ray with an energy equal to the difference in the binding energy between the two shells. Alternatively, an Auger electron can be created. This occurs when the vacancy is filled with an electron from a higher energy level, but instead of emitting a photon, the energy is transferred to a higher shell electron that is emitted from the atom. The fluorescence yield of a shell is the probability that a photoelectric interaction is followed by the emission of a characteristic X-ray. For heavy elements (high Z), the K-fluorescence yield is close to 1, while the L-fluorescence yield is significantly lower.

Although these secondary effects do not influence the X-ray imaging process, they can be important for the dose deposited inside a sample during a CT scan. Further, in X-ray detectors this dose deposited in the scintillator determines the observed intensity in the X-ray image.

The photoelectric absorption is the main interaction process between photons and matter for X-rays of relatively low energy and remains the dominant process at higher energies as the atomic number of the absorber increases. Photoelectric absorption is only possible if the energy of the photon is above the binding energy of a shell electron. This results in discontinuities called edges in the photoelectric absorption curve. Figure 3.4 shows the mass attenuation coefficient (see section 3.2.6) for oxygen (O), aluminium (Al) and iron (Fe). The K-edges, at which a photon can knock an electron out of the K shell of the atom, of Al and Fe are

clearly seen. The presence of these edges makes it impossible to determine an analytic function for the photoelectric absorption cross section inside a material. Nevertheless, the following approximation can be used:

$$\tau \cong k\frac{Z^l}{E^m}, \tag{3.9}$$

where τ is the atomic cross section (cm^2/atom), Z is the atomic number of the material, E is the photon energy, and k is a constant. m and l are only constant over a limited range of energy values. For energies typically used in X-ray imaging, Equation 3.9 can be approximated as

$$\tau \propto \frac{Z^4}{E^3}, \tag{3.10}$$

From this equation it can be seen that the photoelectric attenuation of a photon in a material is strongly dependent on both atomic number and photon energy. The photoelectric attenuation coefficient is much higher for a given photon energy for heavy elements than for lighter elements.

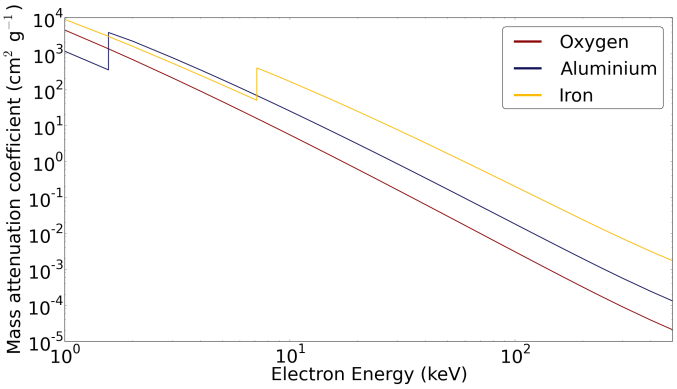

Figure 3.4: The mass attenuation coefficient for the photoelectric absorption for oxygen, aluminium and iron. Data obtained from NIST(XCOM) [5].

3.2.2 Compton effect

The Compton effect is the inelastic scattering between a photon and an electron. The photon is deflected through an angle θ with respect to its original direction and loses energy.

Consider X-rays with a wavelength λ that are scattered at a target (Arthur Compton used graphite in 1922 [Fig. 3.5]. The scattered wavelength λ' can be measured

at an angle θ. If the wavelength of the scattered photons at a given angle is measured, two peaks are visible (Fig. 3.6). The first peak is at the same wavelength λ as the incident photons. This scattered radiation is known as Rayleigh scattering in which the photon interacts coherently with all electrons in the electron cloud of the atom (section 3.2.5).

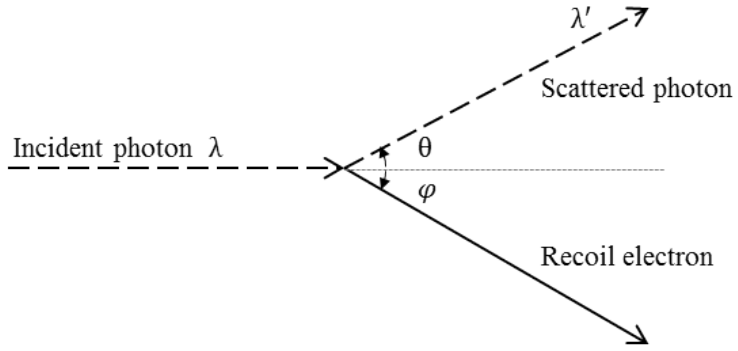

Figure 3.5: Compton scattering at a graphite target. The scattered photon wavelength λ' can be measured at an angle θ. The recoil electron makes an angle φ with the incident photon.

A second peak in the measured wavelength can be seen at a longer wavelength $\lambda^{'}$. This shift in wavelength is called the Compton shift

$$\Delta\lambda = \lambda' - \lambda \tag{3.11}$$

and is only dependent on θ and not on the incident wavelength of the photon. This shift can be explained by the quantum model in Figure 3.5. $h\nu$ and $h\nu'$ are the energy of the photon before and after interaction, respectively. $m_e c^2$ is the rest energy of the electron, and E' and P' are its total energy and impulse after the interaction. Conservation of energy and momentum yields

$$h\nu + m_e c^2 = h\nu' + E', \tag{3.12}$$

$$h\nu/c = h\nu'/c\cos(\theta) + P'\cos(\varphi). \tag{3.13}$$

$$0 = h\nu'/c\sin(\theta) - P'\sin(\varphi), \tag{3.14}$$

Combining these three equations results in

$$h\nu' = \frac{h\nu}{1 + (h\nu/m_e c^2)(1 - \cos(\theta))}. \tag{3.15}$$

For small scattering angles θ, the energy loss of the scattered photon is negligible, and for the extreme scattering angle $\theta = \pi$, the scattered photons have a minimal energy.

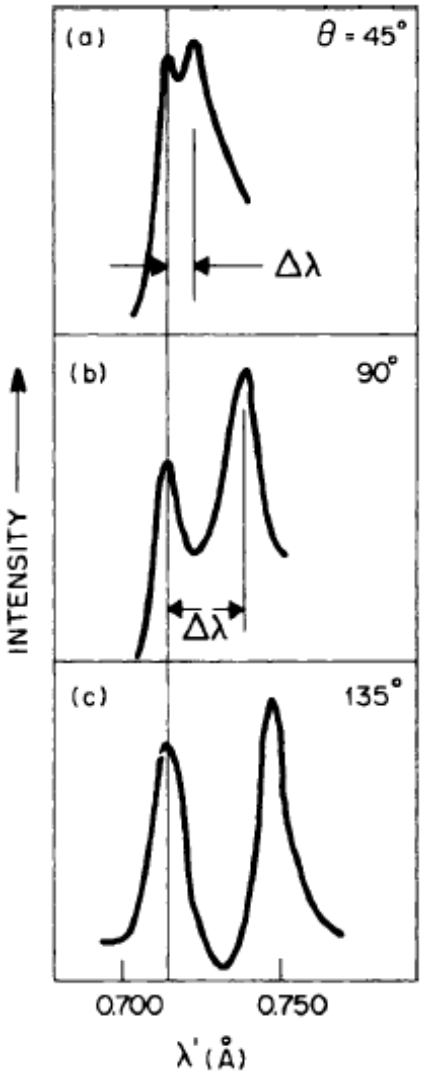

Figure 3.6: Intensity and wavelength of photons scattered at different angles [2].

The probability of Compton scattering in a material depends on the electron density in that material and thus on the atomic number Z. Figure 3.7 shows the mass attenuation coefficient for Compton interaction, which is proportional to the interaction probability for oxygen, aluminium and iron. The Klein-Nishina for-

mula gives an analytic expression for the differential cross section [6, 7]:

$$\frac{d\sigma}{d\Omega} = Zr_0^2 \left(\frac{1}{1+\alpha(1-\cos\theta)} \right)^2 \left(\frac{1+\cos^2\theta}{2} \right) \times \left(1 + \frac{\alpha^2(1-\cos\theta)^2}{(1+\cos^2\theta)(1+\alpha(1-\cos\theta))} \right) \tag{3.16}$$

The cross section is strongly dependent on the scattering angle θ. Figure 3.8 shows the angular dependency of this cross section at various incident photon energies. For photon energies typically used in X-ray CT, Compton scattering can be considered to be roughly isotropic. The atomic cross section for the Compton effect σ can be written as

$$\sigma \propto Zf(E) \tag{3.17}$$

in which $f(E)$ is the Klein-Nishina formula (Eq. 3.16) integrated over the solid angle.

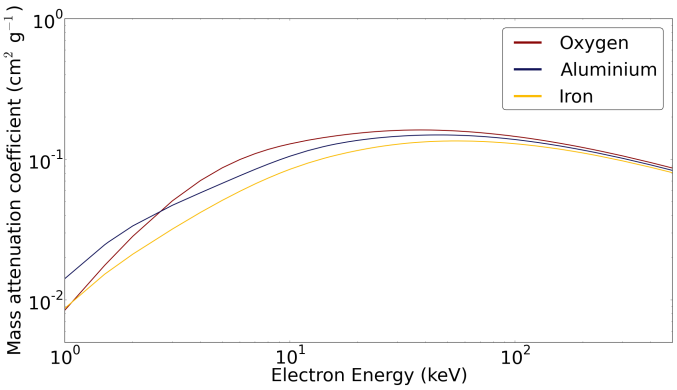

Figure 3.7: Mass attenuation coefficient for the Compton effect for oxygen, aluminium and iron. Data obtained from NIST(XCOM) [5].

3.2.3 Pair production

At photon energies above 1.022 MeV, the photon energy is larger than two times the rest energy of an electron/positron. Above these energies the photon can produce an electron-positron pair. This process, however, is only possible when a third particle is present. To prove this, consider the conservation of energy for a pair production by a photon in empty space:

$$h\nu = E_{kin,+} + E_{0,+} + E_{kin,-} + E_{0,-}, \tag{3.18}$$

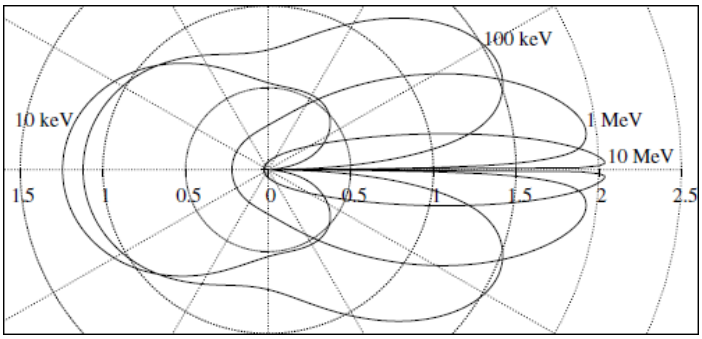

Figure 3.8: Polar representation of Compton scattering angular distribution for iron [8].

where + and - indicate the positron and electron, respectively. Inserting the relativistic formula for the kinetic energy of both particles results in

$$h\nu = [m_e c^2 \gamma_+ - m_e c^2] + m_e c^2 + [m_e c^2 \gamma_- - m_e c^2] + m_e c^2 \tag{3.19}$$

and further in

$$h\nu = m_e c^2 [\gamma_+ + \gamma_-]. \tag{3.20}$$

In addition to energy conservation, the conservation of momentum gives

$$p_{y,+} = p_{y,-} \tag{3.21}$$

$$m_e v_+ \gamma_+ \sin(\alpha) = m_e v_- \gamma_- \sin(\beta) \tag{3.22}$$

in the y direction and

$$h\nu/c = m_e v_+ \gamma_+ \cos(\alpha) + m_e v_- \gamma_- \cos(\beta) \tag{3.23}$$

$$h\nu = m_e c v_+ \gamma_+ \cos(\alpha) + m_e c v_- \gamma_- \cos(\beta) \tag{3.24}$$

in the x direction. Again, both equations use the relativistic formulas of the momentum of the electron and positron. If both energy and momentum need to be conserved, this would result in

$$v_+ \cos(\alpha) = v_- \cos(\alpha) = c \tag{3.25}$$

which is impossible because $\cos(\alpha) <= 1$, and the speed of the created electrons cannot reach or exceed the speed of light.

A third particle is needed to take part in the conservation of momentum and energy. The pair production can thus occur in the field of an atomic nucleus. Some of the momentum and energy is transferred to the nucleus during the annihilation, which recoils with negligible energy. The energy of the photon in excess of the

rest energy of the electron-positron pair is transferred to the kinetic energy of the two particles, which ranges from zero to a maximum of $h\nu - 2m_e c^2$. Furthermore, this pair production becomes more likely when the photon energy increases, and the probability depends on the atomic number approximately as Z^2. The pair production can also occur in the field of an atomic electron, but the probability is much smaller, and the energy threshold is $4m_e c^2$. As opposed to the nucleus, the electron in whose field the annihilation occurs receives a large amount of kinetic energy and suffers a large recoil.

The created positrons can then annihilate in flight or can slow down and form positronium or annihilate. This is a bound system between an electron and positron that orbit their mutual centre of mass. This state only exists for around 10^{-10} seconds before the electron and positron annihilate.

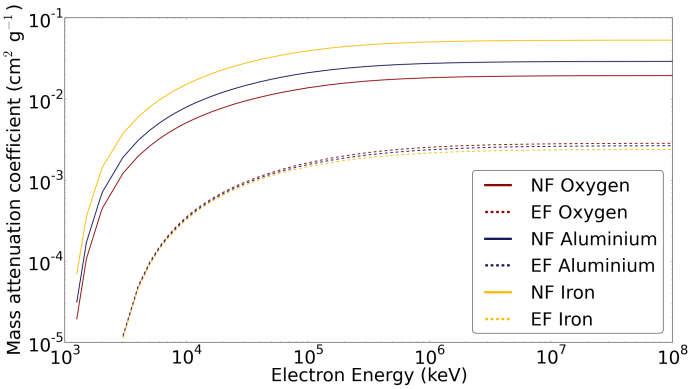

Figure 3.9: Mass attenuation coefficient of pair production in the nuclear and electron field for oxygen, aluminium and iron. Data obtained from NIST(XCOM). [5]

3.2.4 Nuclear reactions

A high-energy photon can interact with a nucleus and emits a nucleon or nucleon cluster. To do this, the photon must have enough energy to overcome the binding energy of the ejected nucleon. Like many other interaction mechanisms, this can only occur above a certain threshold energy typically ranging from a couple MeV to a dozen or more MeV, depending on the nucleus. The kinetic energy of the emitted nucleon (cluster) is equal to the incident photon energy minus the binding energy of the nucleon and the recoil energy. Further, the probability of this effect occurring is much smaller than the photoelectric effect, the Compton effect or pair production. It is also possible that the nucleus emits a proton in addition to a neutron. However, the threshold energy to emit a proton is often higher than the

threshold energy to emit a neutron because the proton has to overcome a repulsive Coulomb barrier.

Other photonuclear reactions such as the knock-out of two neutrons, a neutron-proton couple or an alpha particle from the nucleus are also possible. Finally, fission of heavy nuclei can also occur as a result of the absorption of a high-energy photon. All these nuclear reactions often lead to nuclei that are radioactive after losing one or more nucleons. Therefore, bombarding materials with high-energy photons can lead to the activation of the material. However, in laboratory-based X-ray CT, the photon energies used are much lower than the threshold energies (a couple of MeV) needed to induce these nuclear reactions. Thus, activation of a scanned sample cannot appear in conventional laboratory-based CT.

3.2.5 Rayleigh scattering

As mentioned before (section 3.2.2), Rayleigh scattering can occur when the photon interacts coherently with all electrons in the electron cloud of the atom. This type of scattering can neither excite nor ionise an atom, and no energy is transferred to it. The relative significance of Rayleigh scattering increases at low photon energies and in atoms with a higher atomic number. In the latter case, the scattering angle can be up to 10° but is usually very small in CT [8–10] (Fig. 3.11). Figure 3.10 shows the mass attenuation coefficient of the Rayleigh interaction for oxygen, aluminium and iron. Comparing this figure with Figure 3.4 and 3.7, it can be seen that the probability of Rayleigh scattering occurring is much smaller than for photoelectric absorption or Compton scattering in the energy range used in X-ray CT.

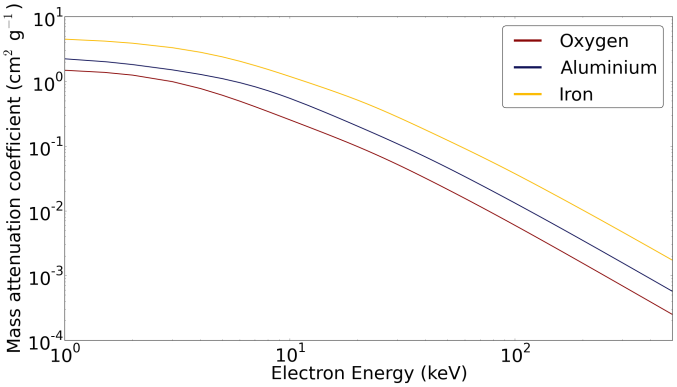

Figure 3.10: Mass attenuation coefficient of Rayleigh scattering for oxygen, aluminium and iron. Data obtained from NIST(XCOM) [5].

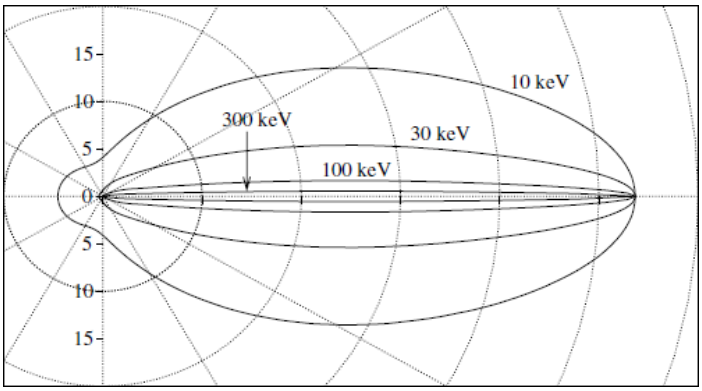

Figure 3.11: Polar representation of the Rayleigh scattering for iron [8].

3.2.6 Attenuation coefficients

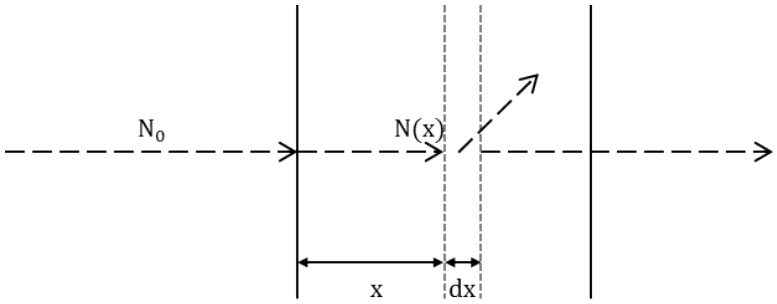

Figure 3.12: A monochromatic beam N_0 strikes a slab with attenuation coefficient μ. The number of original photons that reach a depth x is given by $N(x) = N_0 e^{-\mu x}$.

Linear attenuation coefficient

The linear attenuation coefficient is the probability per unit distance travelled that a photon will interact with the medium it travels through. Figure 3.12 shows a monochromatic photon beam with an initial number of N_0 photons that penetrates a slab with a linear attenuation coefficient μ. After the beam penetrates a distance x in the material, only $N(x)$ original photons are left in the beam. The number of photons that interact, and thus are lost from the original beam, in the next travelled distance dx is

$$dN = -\mu N dx. \tag{3.26}$$

Integrating this differential equation leads to the Beer-Lambert law:

$$N(x) = N_0 e^{-\mu x}. \tag{3.27}$$

After having travelled a certain distance d through a uniform material, a fraction $e^{-\mu d}$ has not undergone any kind of interaction with the material. Note that some of the original interacted photons are not completely absorbed because some interactions cause the photons to scatter in the material. These photons are removed from the beam and may have lost some energy, but they are not absorbed by the material.

The linear attenuation coefficient for photons of a given energy and target material is the sum of all linear attenuation coefficients of all interaction mechanisms between the photons and the material. For conventional X-ray CT, the energies range from a few keV to 200/300 keV. In this energy range only photoelectric absorption and Compton scattering have a significant effect. Thus, the linear attenuation coefficient can be written as

$$\mu = (\tau(\text{photoelectric}) + \sigma(\text{Compton}))N = \mu_\tau + \mu_\sigma \tag{3.28}$$

in which N represents the atom density. The units corresponding with μ are thus 1/cm. Note that Rayleigh scattering can make a small contribution to the interactions between the X-ray photons and the material in X-ray CT, but these photons do not lose any energy and are not deflected from their original path, or this deflection is minimal. Thus, Rayleigh scattering must not be taken into account as a part of linear attenuation coefficient.

Additionally, Equation 3.27 is only valid for a monochromatic beam of photons. Conventional X-ray tubes, however, produce a polychromatic X-ray spectrum $N_0(E)$. The Beer-Lambert law for a polychromatic beam can be written as

$$N_d = \int_0^{E_{Max}} \frac{dN_0(E)}{dE} e^{-\mu(E)d} dE, \tag{3.29}$$

in which dN_0/dE is the initial amount of photons in an infinitesimal small energy bin dE and N_d is the total number of original photons that have travelled through a material with thickness d.

Mass attenuation coefficient

The linear attenuation coefficient depends on the material and its density ρ being traversed. By using the mass attenuation coefficient μ/ρ, the density dependence of the material can be eliminated. This mass attenuation is thus independent of the density of the material and is solely dependent on the atomic number (or combination of it for molecules and composites) of the material and energy of the X-ray photon. Furthermore, this quantity represents the probability of interactions

between the photon and the material in $g\ cm^{-2}$ of material traversed. The attenuation data found in the NIST XCOM [5] database are the mass attenuation coefficients of atoms and molecules.

Mass energy-absorption coefficient

Equation 3.27 shows how many photons are left in an initial monochromatic photon beam that impinge on the material. However, not all the energy of the removed photons is completely absorbed by the material. The total intensity in the initial monochromatic beam is given by I_0 and is expressed in Wm^{-2}. After this monochromatic beam has traversed a slab of material with thickness d, the measured intensity is

$$I_d = I_0 e^{-\mu_{en} d}, \tag{3.30}$$

in which μ_{en} is the energy-absorption coefficent. I_d includes scattered and other photons such as bremsstrahlung and fluorescence. This decrease in beam intensity is logically less than the one described by the linear attenuation coefficient. The difference between I_0 and I_d is the energy absorbed in the material in units $Js^{-1}m^{-2}$. Just as the mass attenuation coefficient, the mass energy-absorption coefficient is dependent on the photon energy. The polychromatic version of Equation 3.30 then becomes

$$I_d = \int_0^{E_{Max}} \frac{I_0(E)}{dE} e^{-\mu_{en}(E) d} dE. \tag{3.31}$$

The mass energy-absorption coefficient can be subdivided into three components: a photoelectric part, a Compton part and a pair production part. Of course, the latter does not contribute to the energy deposited in samples during X-ray CT. For the photoelectric absorption, the fraction of energy transferred to electrons can be written as

$$1 - \frac{\delta}{h\nu}, \tag{3.32}$$

with δ the average energy emitted by characteristic radiation following the photoelectric absorption in the material. The mass energy-transfer coefficient can be written as

$$\frac{\mu_{\tau_{tr}}}{\rho} = \frac{\mu_\tau}{\rho} \left(1 - \frac{\delta}{h\nu}\right), \tag{3.33}$$

and is different from the mass energy-absorption coefficient for the photoelectric effect because any subsequent energy loss from bremsstrahlung is not taken into account in the energy transfer. Further, the energy-transfer coefficient for Compton scattering can be written as

$$\frac{\mu_{\sigma_{tr}}}{\rho} = \frac{\mu_\sigma}{\rho} \frac{T_{avg}}{h\nu}, \tag{3.34}$$

with $T_{avg}/h\nu$ the average fraction of the incident energy converted to kinetic energy of the Compton electrons. Just like for the photoelectric effect, this energy-transfer coefficient takes no subsequent bremsstrahlung into effect. A high-energy photon can produce an electron-positron pair with a kinetic energy of $h\nu - 2m_e c^2$. The pair production transfer coefficient can thus be written as

$$\frac{\mu_{\kappa_{tr}}}{\rho} = \frac{\mu_\kappa}{\rho}\left(1 - \frac{2m_e c^2}{h\nu}\right). \tag{3.35}$$

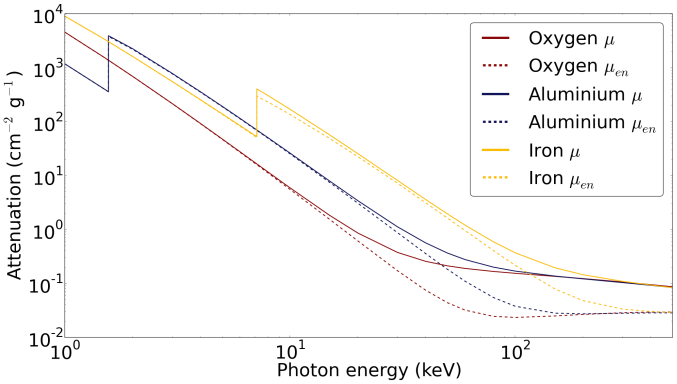

Figure 3.13: Mass attenuation and mass energy-absorption coefficient for oxygen, aluminium and iron [11].

The total mass energy-transfer coefficient μ_{tr}/ρ can thus be written as

$$\frac{\mu_{tr}}{\rho} = \frac{\mu_\tau}{\rho}\left(1 - \frac{\delta}{h\nu}\right) + \frac{\mu_\sigma}{\rho}\frac{T_{avg}}{h\nu} + \frac{\mu_\kappa}{\rho}\left(1 - \frac{2m_e c^2}{h\nu}\right). \tag{3.36}$$

As mentioned, this coefficient does not take any subsequent bremsstrahlung radiation into effect. If g represents the average fraction of the transferred energy that is emitted as bremsstrahlung, the mass energy-absorption coefficient can be written as

$$\frac{\mu_{en}}{\rho} = \frac{\mu_{tr}}{\rho}(1 - g). \tag{3.37}$$

Figure 3.13 compares the mass attenuation and mass energy-absorption coefficients of oxygen, aluminium and iron.

3.2.7 Wave effects

The previously described interactions assume that the X-ray photons are particles that travel along straight paths from source to detector. However, like any form

of electromagnetic radiation, X-rays also manifest themselves as waves propagating through a medium. Each electromagnetic wave is characterised by its phase, amplitude and frequency. The amplitude of a wave changes when it traverses a medium because of the attenuation process described above. A change in the phase of the wave occurs due to a difference between the propagation velocity of the wave through the given medium and another medium (such as air or a vacuum, for example). The part of the wave that traverses the medium gains on the un-affected part that does not travel through the medium. This causes a perturbation of the wavefront at the edge of the medium. Due to the refraction of X-rays at the edge between two materials, these edges become enhanced in images (Fig. 3.14). Along the line of the border, the transmission appears lower because many X-rays are removed by this refraction. In the same way, the refracted X-rays induce an increased intensity just outside the borders of an object. The change in amplitude and phase shift is determined to a large extent by the refraction index of the medium

$$n(\lambda) = 1 - \delta(\lambda) + i\beta(\lambda). \tag{3.38}$$

Here β is related to the linear attenuation coefficient of the medium, and δ corresponds to the phase shift per unit length of the electromagnetic wave.

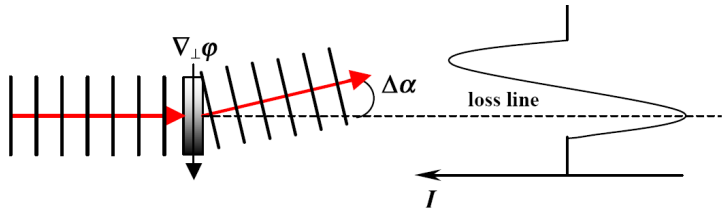

Figure 3.14: Angular deflection of an incident ray due to a phase shift [5].

Polychromatic source

The propagation in space of the original X-ray wave can be described by the propagation vector $\vec{k}(x, y, z)$, which is perpendicular to the local wavefront. This propagation becomes perturbed by an object through a phase shift and results in a vector $\vec{k_\theta}(x, y, z)$. The difference between these two propagation vectors can be represented by $\vec{\kappa}$, and it can be proven that [12]:

$$|\vec{\kappa}| \propto \lambda^2. \tag{3.39}$$

From this dependency it follows that diffraction decreases rapidly with photon energy. This relationship has an influence on edge enhancement when a polychromatic X-ray source is used in CT, as shown in Figure 3.15. As previously discussed, the phase shift causes a sharp minimum on the detector along the line

in which the photons disappear. But contrary to the effect when using monochromatic sources, polychromatic sources allow the maximum to be spread out due to the dependence of the diffraction angle (and phase shift) for different wavelengths.

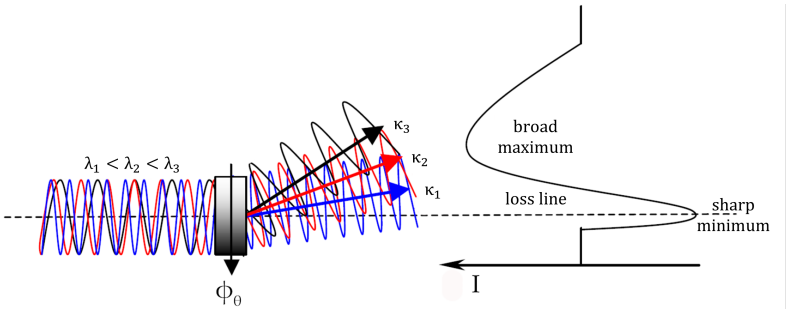

Figure 3.15: The effect of a polychromatic source on the refraction angle [13].

Phase contrast imaging

The enhancing of the edges induced by the phase effect can be used to one's advantage. Very small structures that otherwise would not be visible or very difficult to distinguish in a high resolution CT can become visible by this effect [14, 15] (Fig. 3.16). Despite the benefits for visualisation in radiographs, the edge-enhancement effect can hinder the visual interpretation of reconstructed images in CT. Indeed, in reconstructed images the edges of structures can be enhanced. Figure 3.17 shows a reconstructed slice of a cake. Here also, the edges of the holes present in the cake are clearly enhanced ans thus show a false increased attenuation, but some brighter spots also appear in the reconstructed slice. These can falsely be misinterpreted as dense structures in the cake. However, these are the visible enhanced edges at the top or bottom of a hole just above or below the specific slice.

A proper treatment for coping with these unwanted phase effects is thus necessary for a correct interpretation, analysis or segmentation of the reconstructed CT data. Different methods exist to mitigate these effects. Depending on the algorithm, a correction can either be performed before [16, 17] or after reconstruction [18].

Figure 3.16: A high-resolution mixed phase-and-amplitude image of a fly [12].

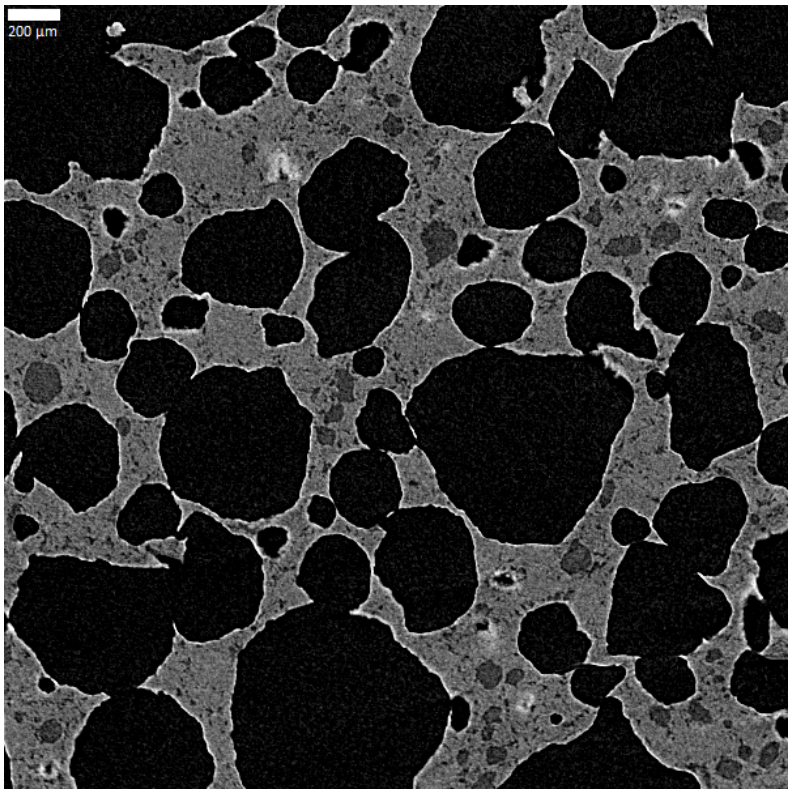

Figure 3.17: A part of a reconstructed slice of a cake. Artificial white spots are visible due to top or bottom edges of air holes.

3.3 Production of X-rays

In this section, three methods for the production of X/γ-rays are discussed. The first is the production of photons by radioactive decay, which are also called gamma radiation or γ-rays. The second method uses the fact that accelerated electrons lose energy and is applied to produce synchrotron radiation. As a third method, the production of X-rays in conventional X-ray tubes, which is the most common method for laboratory-based and industrial X-ray CT, is discussed.

3.3.1 Radiation isotope (gamma) sources

Radioactive decay in the forms of α- and β-decay are the most well-known types of radioactive decay. Often the nucleus is left in an excited state after emitting an α or β particle. In order to decay to a stable energy level, the nucleus emits energy in the form of a photon with an energy equal to the difference between the energies of the unstable and stable states of the nucleus. These photons typically have an energy between a couple of keV and a couple of MeV. The term gamma rays is used when the photon is produced in nuclear or annihilation processes.

Gamma sources can be used as an alternative to X-ray tubes. They produce a high-energy monochromatic beam, but since radioactive isotopes emit their radiation uniformly in space, some collimation of the beam to a point source is necessary and the flux is rather low. Further, the sources need to be shielded heavily. Because of the low flux and safety issues, such sources are limited to industrial CT.

3.3.2 Synchrotron

As mentioned earlier, charged particles such as electrons emit highly energetic photons when accelerated. In a synchrotron, this principle is used to produce high-energy photons or X-rays. The electrons are accelerated to an extreme high energy and are then injected into a large circular storage ring, which contains bending magnets to keep the electrons in a circular orbit. When synchrotron radiation was first discovered, it was considered to be a nuisance because of the unwanted energy loss of the electrons. But soon it became clear that the emitted X-rays could be used for varying purposes.

The first generation of synchrotrons were developed for particle physics experiments and the synchrotron radiation was used only in a parasitic mode. This resulted in the creation of radiation with a wide spectral distribution. Crystalline monochromators could be added to the emitted beam to obtain a beam of monochromatic photons, of course with a reduced flux. A second generation of synchrotrons

were dedicated to produce synchrotron radiation. In the current third-generation synchrotron facilities, devices are inserted on the straight sections of the storage ring that are specially designed to produce higher photon fluxes and/or monochromatic radiation with higher energy. The most commonly used devices are undulators and wigglers. Both of these use a series of dipole magnets to produce electromagnetic radiation. While undulators are specially developed to produce an almost monochromatic photon beam, wigglers produce a beam with a broader spectrum but of high intensity.

Because of its unique properties, synchrotron radiation offers some advantages for X-ray CT. The flux emitted is much higher than the flux produced in an X-ray tube and the beam is nearly parallel which makes it particularly suited for CT and imaging can be done far from the source. Furthermore, a synchrotron is, contrary to an X-ray tube, able to produce a tuneable and almost monochromatic beam that can be very useful for applications such as K-edge imaging or Dual-Energy Computed Tomography (DECT) in general. X-ray optics can also be applied much easier on such a monochromatic beam which makes it possible to create very small spot sizes with which a much higher resolution can be achieved compared to laboratory based X-ray CT. Furthermore the emitted radiation in a synchrotron is also spatially coherent, which makes it particularly useful for imaging wave-related effects, as the beam can be used to increase the resolution and contrast of these effects. The downside of a synchrotron is that it is a large and expensive system, and thus there are few available, which makes the accessibility of these systems limited. In addition, complex X-ray optics are needed in order to obtain a magnification.

3.3.3 X-ray tubes

Laboratory-based X-ray CT uses traditional X-ray tubes, and their working principles are discussed here. A more detailed description of the tubes present at UGCT can be found in the next chapter, where the modelling and simulation of X-ray tubes is also discussed.

Tube design

The design of a sealed (Coolidge) X-ray tube is shown in Figure 3.18. Electrons are emitted from a hot filament (cathode) and accelerated towards a target (anode) by an electric field. A small focal spot on the anode can be created by using simple electrostatic focusing. These tubes, however, are limited in the minimal focal spot size that they can achieve. No spots with a size smaller than 5 μm can be produced. This limitation can be overcome by using an open X-ray tube, which are tubes that can actually be openend. Figure 3.19 shows the design of such an open tube.

Similar to a closed X-ray tube, electrons are created by a heated filament through thermionic emission. An additional electromagnetic focusing mechanism results in further reduction of the diameter of the electron beam and thus in a smaller spot size on the target. The tube must be continuously evacuated by a vacuum system, as an open tube is never completely air-tight. It also has the advantage that components such as the filament and target can easily be replaced on failure or depending on the needs of the application. Even the head of the tube can be exchanged for certain purposes.

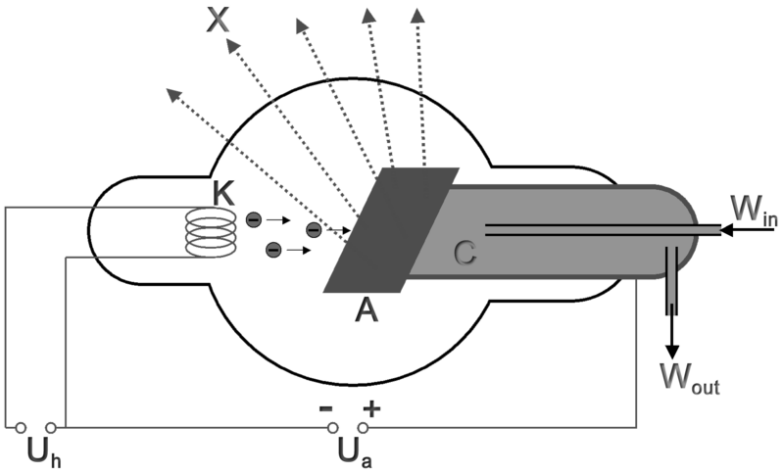

Figure 3.18: Design of the Coolidge tube [19].

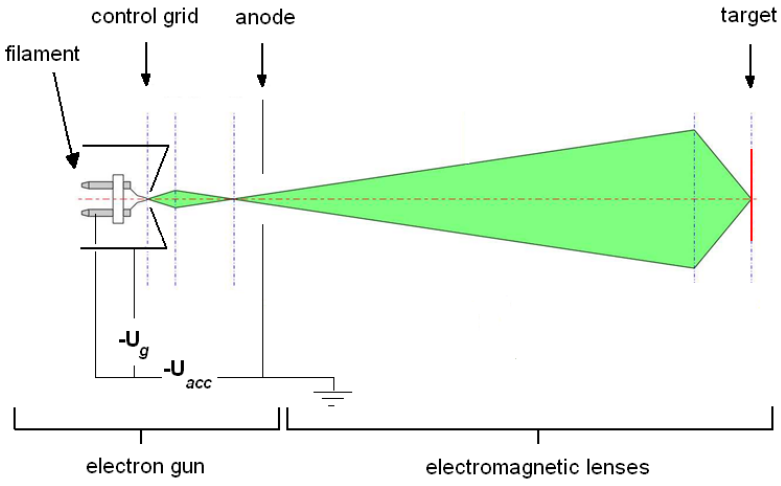

Figure 3.19: Schematic view of an open X-ray tube [9].

Electron gun

The electron guns of an open and closed tube are almost identical. A current is sent through a filament, typically tungsten, which becomes heated to a temperature above 2700 K. At this temperature, thermionic emission of electrons from the filament occurs. These electrons are then accelerated towards the anode, which is positively charged with respect to the filament by a potential U_{acc}. Around the filament, a control grid at a negative potential $-U_g$ is present. This grid serves two purposes. First, the electrons are decelerated by the negatively charged grid, which allows for control of the electron flux emitted by the electron gun. Secondly, the electrons are forced towards the central hole in the grid and thus to the axis of the gun.

The number and the focusing of the electrons produced by the electron gun can be controlled by adjusting the filament current I_f and the grid voltage U_g. A large current I_f results in a higher temperature of the filament and an increased yield of electrons that will be emitted by it. The current of the electron gun is thus higher, but the lifetime of the filament is reduced because of evaporation of the filament material at high temperatures. On the other hand, a higher grid voltage U_g stops more electrons and reduces the electron current produced by the electron gun. Furthermore, the increase of the grid voltage enhances the focusing of the electrons towards the centre of the electron gun, and thus an electron beam with a lower divergence is created. A low divergence of electrons is necessary for optimal performance of the electromagnetic lensing system in an open tube type.

Electromagnetic lensing and focusing

A sub-micrometre focal spot size on the target can only be obtained by an additional electromagnetic focusing mechanism. Sometimes multiple lenses can be used not only to obtain a higher focusing of the electron beam, but also to add to the flexibility of the system.

A coil of conductive winding, typically copper, surrounded by an iron shielding can be used as an electromagnetic lens in an X-ray tube (Fig. 3.20). This lens produces a magnetic field with a longitudinal (B_z) and radial (B_r) component. The Lorentz force

$$\vec{F} = -e(\vec{v} \times \vec{B}) \tag{3.40}$$

causes the electrons to undergo a force perpendicular to their velocity and the magnetic field. While in a uniform magnetic field an electron follows a helical trajectory, in a non-uniform magnetic field an electron also undergoes a radial force that drives it towards the optical axis to the next circular movement around the axis.

This is a result of the combination of the radial and longitudinal components of the magnetic field generated by the conductive coil.

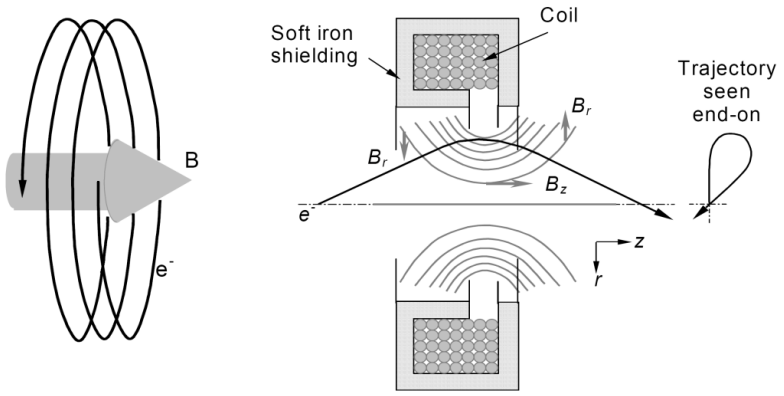

Figure 3.20: Schematic view of an electron trajectory in a uniform magnetic field (left) and in a non-uniform magnetic field (right) [9].

Due to the rotational symmetry, the helical trajectory can be discarded. Electrons close to the optical axis are approximately all focused towards the same point. By using this approximation, the paraxial approximation of optical lenses can be used, and an electromagnetic lens can thus be modelled as a thin lens with a clearly defined focal distance f.

Photon production in the target

The surface of the target material is placed at the focal point of the electromagnetic lensing system. The collisional and radiative stopping powers of the electrons cause the electrons to lose their energy and emit part of it as X-ray radiation, as discussed in section 3.1. The collisions of the electrons with the target material will lead to excited atoms in the target of the tube which will lead to the production of characteristic X-rays. The radiative stopping power will lead to bremsstrahlung, which will thus produce a continuous spectrum. Figure 3.21 shows an example of an X-ray spectrum generated by a tungsten target. The characteristic lines and the continuum produced by the bremsstrahlung are clearly seen. The direction and the energies at which these X-rays are emitted depend heavily on the inner structure of the tube. Detailed modelling and a simulation of the spectra of different X-ray tubes is discussed in chapter 4.

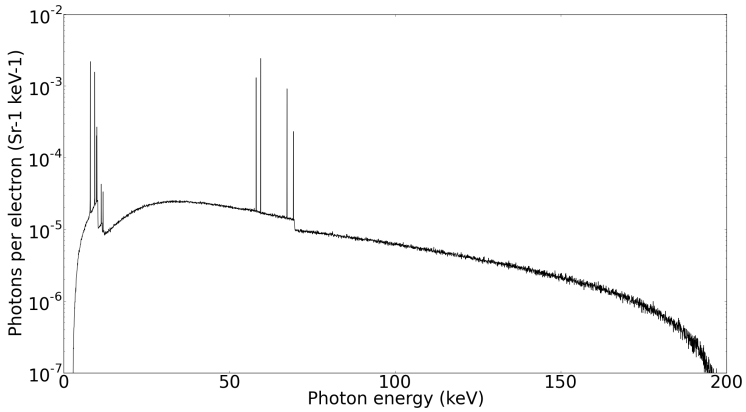

Figure 3.21: An example of a spectrum generated by an X-ray tube.

3.4 Detection of X-rays

X-rays can either be detected in a direct or indirect manner. The basic principles are discussed briefly in this section. A more detailed description of the simulation and modelling of X-ray detectors present at UGCT is discussed in chapter 4.

The working principle of a direct detector is shown in Figure 3.22. An incoming X-ray photon interacts in the depleted region in the detector device and creates electron-hole pairs. This depletion layer is divided into different areas (pixels). The deposited charge in such a pixel can be integrated or digitised for each photon interaction event. Thus, it is possible to count single photons and derive their energy based on the deposited charge in a pixel.

Despite the advantage that photon counting is possible with a direct detector, some practical issues exist. First, the deposited charge of an incoming photon needs to be read out before a second event takes place. The flux of the incoming photons thus must be sufficiently low to match the frame rate of the CCD-based direct detector. Second, the X-ray photon needs to interact through photoelectric absorption in order to deposit all its energy when the energy information of the photon needs to be obtained. Only low-energy X-rays can be detected this way since most detectors of this type are composed of silicon. Last, when the detector is pixellated, the deposited charge needs to be contained in one pixel. Otherwise, an interaction can be interpreted as two events in different pixels of photons with a lower energy. Today, some of these limitations can be overcome [20].

Figure 3.23 shows a schematic representation of an indirect detector. The incident photons interact with a scintillator, where the deposited energy is converted to

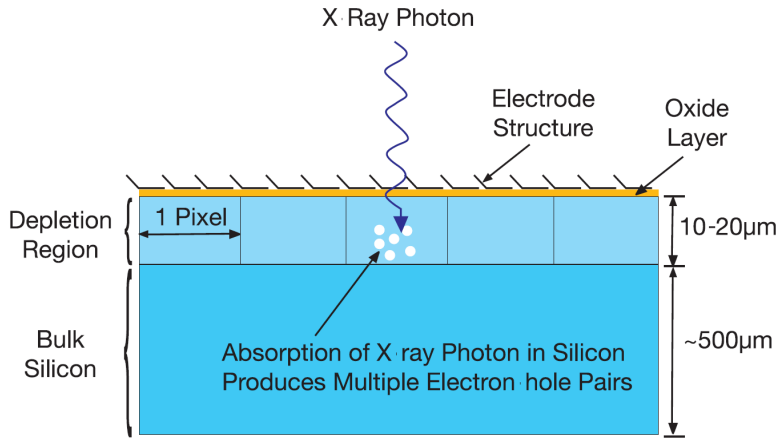

Figure 3.22: Principle of direct X-ray detection [9].

visible light. The light is then guided to a CCD or CMOS sensor through an optic fibre and converted to an electric signal. This signal is approximately proportional to the deposited energy in the scintillator and thus contains information about the X-ray intensity. The spectral information is typically lost in indirect, integrating X-ray detectors. Further, the imaging resolution is limited due to scattering inside the scintillator.

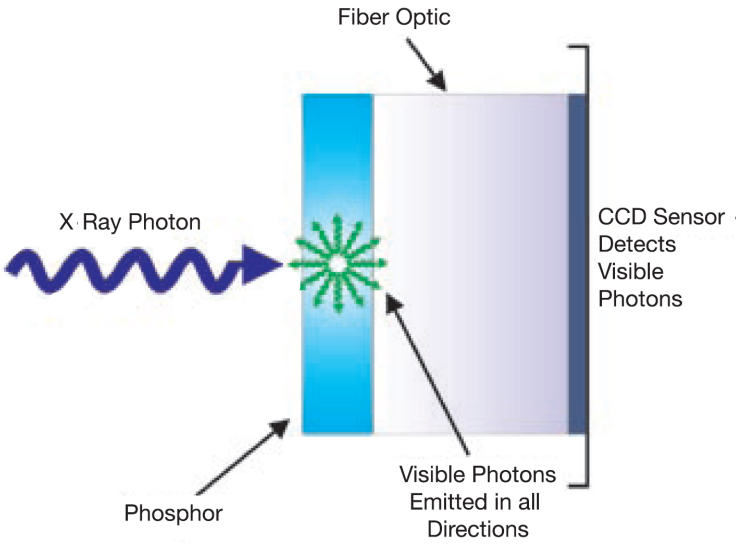

Figure 3.23: Principle of indirect X-ray detection [9].

These indirect detectors are widely used in laboratory-based X-ray CT because they have a number of advantages. For example, the energy response of such detectors can be tuned by varying the scintillator material and thickness. Further, visible light detectors are widely available, and the optimal detector with the best-suited sensor with optimal pixel size, sensitivity and noise characteristics can be chosen. Moreover, high X-ray tube voltages can be used because X-rays that do not interact with the scintillator are stopped in the optical fibres and thus cannot damage the detector sensor.

3.5 Physics of X-ray components

In this section, a number of physical effects present in laboratory-based X-ray CT scanners are discussed. First, some physical properties of X-ray tubes are discussed, such as the flux, finite spot size and heel effect in a directional X-ray tube. Further, some detector issues are discussed, and finally the beam-hardening effect that occurs in laboratory-based X-ray CT is described.

3.5.1 X-ray flux

The X-ray flux of the beam can be defined as the number of photons per unit area per unit time. The flux can thus be expressed as photons per second per centimetre squared. This is an important quantity of the X-ray tube as it determines how many photons can be detected by the detector in a certain amount of time, and it thus correlates directly to the statistical information in the projection images. The advantage of having a higher flux is either obtaining an improved signal-to-noise ratio for a scan or allowing a shorter scan time to obtain similar statistical information. Compared to that of a synchrotron, the flux of an X-ray tube is very low. When a small X-ray spot is created in an X-ray tube, the electron flux needs to decrease to prevent the melting of the target which will result in a lower X-ray flux. An additional constraint is the filament, which can be damaged when a too high current is applied to it. Due to thermal limits, scanning times in μCT are thus much longer than in medical or industrial CT.

For a conical X-ray beam, the distance between the detector and the X-ray source also plays a role in the amount of flux that passes through the detector. The flux through a pixel is proportional to $1/r^2$ with r the distance between the source and pixel. Let $\vec{n}$ be the normalised normal vector on the plane of the pixel and $\vec{u}$ the normalised vector that gives the direction between the source and detectorpixel. The solid angle of such a pixel with a pitch a can be written as:

$$\Delta\Omega_{pixel} \approx \frac{a^2\vec{n}\cdot\vec{u}}{r^2} = \frac{a^2 cos(\theta)}{r^2}, \tag{3.41}$$

with θ the angle between the two vectors. Multiplying this solid angle by the photons emitted per steradian by the X-ray tube in a certain amount of time yields the time integrated number of photons hitting the detectorpixel

3.5.2 Resolution and spot size

In high resolution CT, the sample is placed on a rotation stage that can be moved closer to or farther away from the source. When a conical X-ray beam is used, the positioning of the sample in the beam also determines the magnification of the sample. By moving a small object closer to the X-ray source, the magnification increases. Large objects can be positioned closer to the detector in order to capture the complete object in a single projection. Their magnification is thus smaller. The magnification M of the object is given by

$$M = \frac{SDD}{SOD}, \tag{3.42}$$

were SOD is the distance between the source and object and SDD the distance between the source and detector. In high resolution CT, the order of magnification is typically between 10 and 1,000. Theoretically, the resolution R of the CT scan is then given by

$$R = p/M, \tag{3.43}$$

with p the pixel pitch of the detector.

In most cases, the magnification and resolution are determined by the size of the sample. The smaller the sample, the higher the magnification that can be achieved, leading to a better resolution. Nevertheless, the limiting factor for the resolution is not always the sample size. The spot created inside the target by the accelerated electrons from which the photons are emitted has a finite dimension called the spot size F of the tube. Together with the object, this spot size is also enlarged in a projection and causes an unsharpness on the detector (Fig. 3.24). The best achievable resolution on a detector is therefore given by

$$R = \frac{p}{M} + F\left(1 - \frac{1}{M}\right). \tag{3.44}$$

For large magnifications, which are the case in high resolution CT, $R \approx F$. The resolution of an X-ray CT scan is thus determined and limited by the spot size at which the X-ray photons are produced in the target of the X-ray tube. Further, this geometrical unsharpness becomes negligible for smaller magnification and thus has a lower resolving power. In this case, the second term in Equation 3.44 can be neglected, and the source can be treated as a point source.

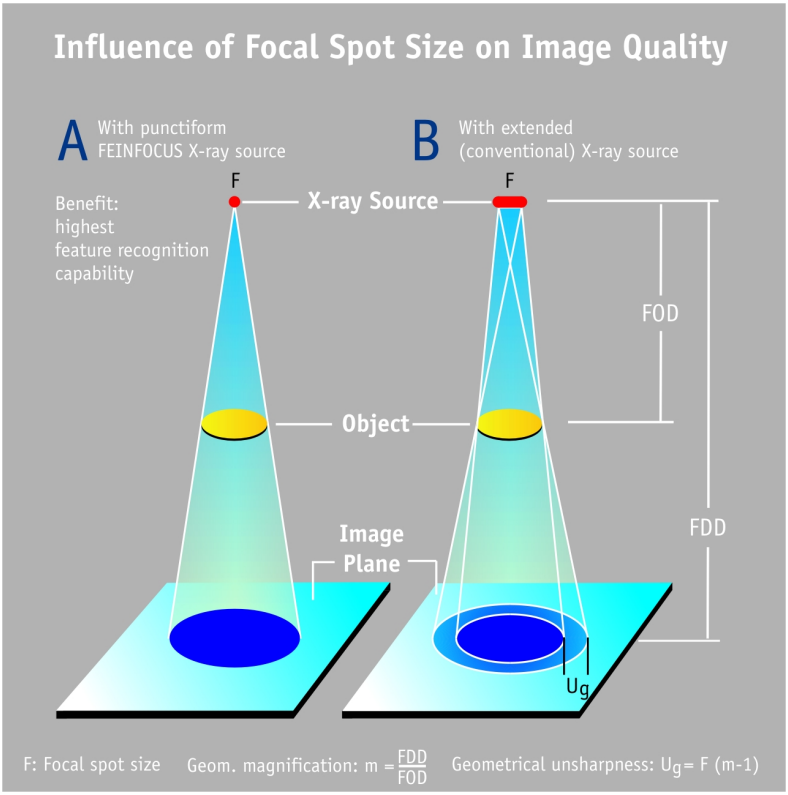

Figure 3.24: Image unsharpness caused by a finite focal spot size [9].

3.5.3 The heel effect

The heel effect can occur in directional X-ray sources. It is caused by a non-perpendicular incident angle of the electron beam on the target. The distance a produced X-ray photon travels through the target before escaping depends on the place where it was created. X-ray beams that travel a greater distance through the target material have a higher mean energy than a beam that needs to travel less distance. When a directional tube is used, the spectrum emitted by the tube has a directional dependency.

Different factors cause the heel effect to be less or more present during an X-ray scan. Of course, the angle at which the electron beam impinges on the target plays a role. However, the distance of the source to the object (SOD) also has an influence on this effect. A larger SOD results in a bigger distance over which the X-ray beam can diverge. The heel effect becomes seemingly larger in this case.

3.5.4 Detector unsharpness

The sharpness of detectors plays an important role in the process of X-ray imaging and differs from system to system. Unsharpness is partially caused by the scintillator screen for indirect X-ray detection, the readout sampling (pixel size) and electronics.

Partial volume effect

Partial pixel coverage in a radiograph can be caused by arbitrary placing of the object on the rotation stage of an X-ray system. Consider a perfect X-ray detector of which a part is covered by an object absorbing all X-rays that impinge on it. If the edge of the object is perfectly aligned with the edge of a pixel, the uncovered pixels measure all radiation and the covered ones measure none. In a realistic case, however, the edge of such an object never perfectly aligns with the edge of a detectorpixel, resulting in pixels that are partially covered. Depending on the part of the pixel that is covered, a radiation value between the completely covered and uncovered pixels is measured. These partially covered pixels cannot be distinguished from pixels with full coverage that detect partial attenuation. This can hinder the determination of the unsharpness of a system.

A similar effect is present in tomography. During a CT reconstruction, the distribution of linear attenuation coefficients is calculated in a voxelised 3D volume. The grey value in each voxel of this reconstructed volume represents the average attenuation coefficient in the voxel. In the reconstruction of a binary object, which consists only of air and a certain material, intermediate values can thus occur when a voxel is only partially filled. This is called the partial volume effect. This effect is inherent in pixelated data, which is the case in 2D (radiography) and 3D (tomography) imaging. This effect must thus be taken into account when a tomographic dataset is analysed or interpreted.

Modular Transfer Function (MTF)

In a perfect detection system with infinite sampling and finite pixel size, the line profile of a straight edge that is perfectly aligned with the edge of a pixel is a perfect step function. If the imaging system has a finite resolution (but infinite sampling), an edge appears as a smooth curve. The width of this curve determines the resolution p/M of the imaging system. This effect can be caused by using an X-ray tube with a spot size much larger than the achievable resolution of the setup. But even when the spot size is small enough, the scintillator screen of the detector can also cause a smooth curve.

The edge response is a parameter that can be used to characterise this behaviour. This parameter is a measure for the distance between the points where 10% and 90% of the transition magnitude is reached (Fig. 3.25(b)). However, these points are not easy to detect in noisy data or when the resolution is close to the sample rate of the detector. In that case, interpolation has to be used to determine a value for the parameter. Further, the derivative of the edge response can be calculated. This derivative is called the line spread function (LSF) and represents a one-dimensional Dirac delta function in the ideal case, with infinite resolution and sampling. At a finite resolution, the LSF is close to a Gaussian distribution that can be characterised by its full width at half maximum (FWHM) (Fig. 3.25(a)).

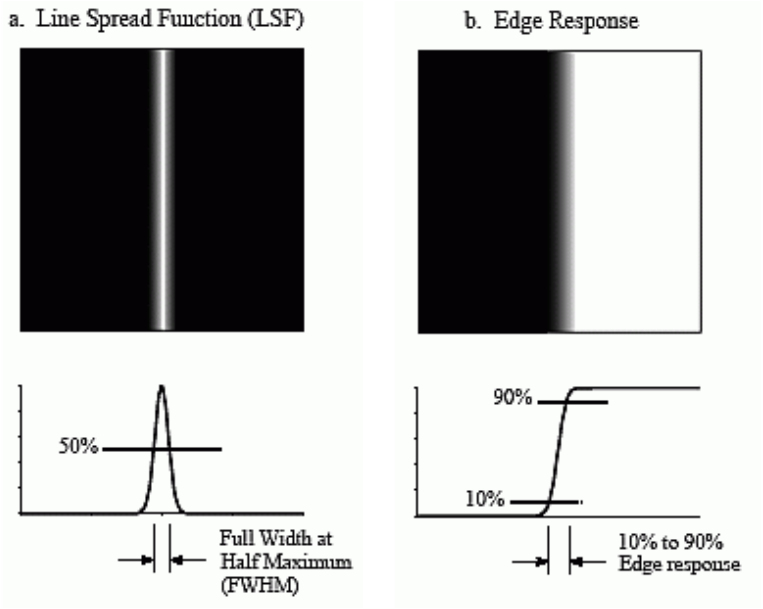

Figure 3.25: Edge response (b) and line spread function (a) of an image with finite resolution but infinite sampling [21].

In real imaging systems, the sample rate is finite due to the discrete pixels. The resolution on the detector is typically close to this pixel size. In an ideal detector system with finite pixel size, the resolution is limited by the sampling and is exactly one pixel wide. In real systems, the resolution depends on the position of the edge and the finite sampling. The Modular Transfer Function (MTF) can account for this finite sampling. This function is the modulus of the Fourier Transfer of the LSF and indicates which spatial frequencies can or cannot be resolved. The

MTF_{50} can be defined as the spatial frequency at which the MTF drops below 50% of its maximum value achieved at zero frequency. This results in a value expressed in line pairs per pixel. The maximum value that is achievable is 0.5 lp/pixel as two edges should be separated from each other by at least one pixel.

3.5.5 Detector Ghosting

Ghosting is a process that can occur in a detector when not all accumulated charges are read out during the image acquisition or by scintillator afterglow. A part of the charges can be left in the pixels or visible light photons can still be present in the scintillator after readout. This can influence the next image taken by the detector ans thus cause ghost images. The effect can be mitigated by illuminating the detector with a uniform (X-ray) light source or by reading the detector out at the highest frame rate. Further, flatfield and darkfield corrections ensure that the reconstructed images do not suffer noticeable artefacts caused by this effect.

3.5.6 Beam hardening

In laboratory- based X-ray CT, X-ray tubes produce a polychromatic beam in the energy range between zero keV and the tube energy. Of course, as mentioned before, the attenuation in a sample depends on the energy of the incident photons. When a monochromatic beam is attenuated by 50% by an aluminium slab of thickness d, then an aluminium slab of thickness $2d$ attenuates 75% of the beam. However, if a polychromatic beam is used, this is no longer the case. Figure 3.26 shows how a polychromatic beam is affected after travelling through slabs of aluminium of thicknesses of 1 mm and 2 mm. The mass attenuation coefficients for the lower-energy X-rays are much higher than those for the high-energy X-rays. The low-energy photons are thus eliminated from the beam much faster than the high-energy photons. This causes the mean energy of the beam to increase when it travels through a slab. The beam thus hardens as it travels through the slab, and the effect is called beam hardening. This effect increases with increasing density and atomic number of the material.

Conventional reconstruction algorithms are based on the Beer-Lambert law (Equation 3.27) and assume a monochromatic beam when calculating a reconstructed volume. When heavy (high Z) or dense materials are present in the sample, the algorithms fail significantly and artefacts become visible in the reconstructed images. Most reconstruction software includes a beam hardening correction [22, 23].

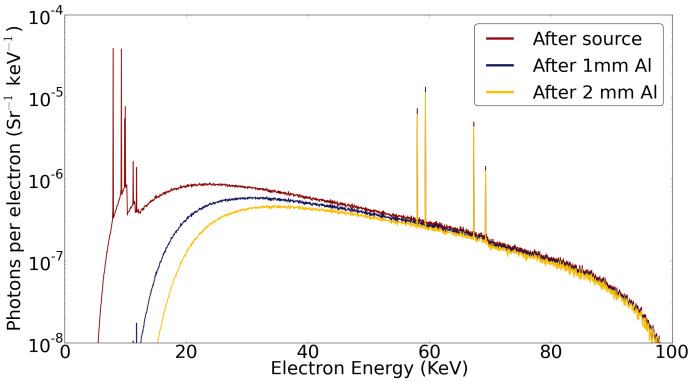

Figure 3.26: Change in beam spectrum before and after travelling through 1- and 2-mm aluminium.

References

[1] E. Rutherford. *The scattering of alpha and beta particles by matter and the structure of the atom*. Phil. Mag. Ser.6, 21:669–688, 1911.

[2] J. E. Turner. *Atoms, radiation, and radiation protection*. Wiley-Interscience, New York, 1995.

[3] `http://physics.nist.gov/PhysRefData/Star/Text/ESTAR.html`.

[4] H. W. KOCH and J. W. MOTZ. *Bremsstrahlung Cross-Section Formulas and Related Data*. Reviews of Modern Physics, 31:920–955, Oct 1959.

[5] `http://www.nist.gov/pml/data/xcom/`.

[6] G.F. Knoll. *Radiation Detection and Measurement*. Wiley, 2000.

[7] O. Klein and T. Nishina. *Über die Streuung von Strahlung durch freie Elektronen nach der neuen relativistischen Quantendynamik von Dirac*. Zeitschrift fur Physik, 52:853–868, November 1929.

[8] N. Freud, P. Duvauchelle, S. A. Pistrui-Maximean, J.-M. Letang, and D. Babot. *Deterministic simulation of first-order scattering in virtual X-ray imaging*. Nuclear Instruments and Methods in Physics Research, Section B, 222(1-2):285–300, 2004.

[9] J. Vlassenbroeck. *Advances in laboratory-based X-ray microtomography*. Phd dissertation, Ghent University, 2009.

[10] Lynn Kissel, R. H. Pratt, and S. C. Roy. *Rayleigh scattering by neutral atoms, 100 eV to 10 MeV*. Physical Review A, 22:1970–2004, Nov 1980.

[11] `http://physics.nist.gov/PhysRefData/XrayMassCoef/tab3.html`.

[12] M. Boone. *New imaging modalities in high resolution X-ray tomography*. Phd dissertation, Ghent University, 2013.

[13] N. Kardjilov. *Further developments and applications of radiography and tomography with thermal and cold neutrons*. Phd dissertation, Technischen Universität München, 2003.

[14] S. W. Wilkins, T. E. Gureyev, D. Gao, A. Pogany, and A. W. Stevenson. *Phase-contrast imaging using polychromatic hard X-rays*. Nature, 384(6607):335–338, November 1996.

[15] A. Snigirev, I. Snigireva, V. Kohn, S. Kuznetsov, and I. Schelokov. *On the possibilities of x-ray phase contrast microimaging by coherent high-energy synchrotron radiation*. Review of Scientific Instruments, 66:5486–5492, 1995.

[16] Andrei V. Bronnikov. *Reconstruction formulas in phase-contrast tomography*. Optics Communications, 171(4 - 6):239 – 244, 1999.

[17] D. Paganin, S. C. Mayo, T. E. Gureyev, P. R. Miller, and S. W. Wilkins. *Simultaneous phase and amplitude extraction from a single defocused image of a homogeneous object*. Journal of Microscopy, 206(1):33–40, 2002.

[18] Erik L. G. Wernersson, Matthieu N. Boone, Jan Van den Bulcke, Luc Van Hoorebeke, and Cris L. Luengo Hendriks. *Postprocessing method for reducing phase effects in reconstructed microcomputed-tomography data*. Journal of the Optical Society of America A, 30(3):455–461, Mar 2013.

[19] `https://en.wikipedia.org/wiki/X-ray_tube`.

[20] R. Ballabriga, M. Campbell, E.H.M. Heijne, X. Llopart, and L. Tlustos. *The Medipix3 Prototype, a Pixel Readout Chip Working in Single Photon Counting Mode With Improved Spectrometric Performance*. IEEE Transactions on Nuclear Science, 54(5-2):1824 – 1829, 2007.

[21] Steven W. Smith. *The Scientist and Engineer's Guide to Digital Signal Processing*. California Technical Publishing, San Diego, CA, USA, 1997.

[22] Jiang Hsieh, Robert C. Molthen, Christopher A. Dawson, and Roger H. Johnson. *An iterative approach to the beam hardening correction in cone beam CT*. Medical Physics, 27(1):23–29, 2000.

[23] L. Brabant, E. Pauwels, M. Dierick, D. Van Loo, M.A. Boone, and L. Van Hoorebeke. *A novel beam hardening correction method requiring no prior knowledge, incorporated in an iterative reconstruction algorithm*. NDT and E International, 51(Complete):68–73, 2012.

4

Modelling of the polychromatic behaviour of laboratory-based X-ray CT components

An important step in predicting the performance of an X-ray CT scanner is to model and simulate the polychromatic performance of its different components as accurately as possible. Semi-analytical [1–3] and analytical [4] models for X-ray tubes are available, but these often do not include secondary effects such as the heel effect [5]. More recently, Monte Carlo simulations have been widely used to predict spectra produced in X-ray tubes [6–9]. The X-ray tubes and detectors present at UGCT are simulated by using the EGSnrc package [10, 11]. A Monte Carlo method is preferred over a (semi-)analytical method, as the former allows for the inclusion of many more details about the inner structure of the tube. Furthermore, effects like a secondary spot can easily be well described by these Monte Carlo simulations [12].

The results of the Monte Carlo simulations described in this Chapter are later on used in Chapter 5 to simulate accurate radiographic projections and in the dual-energy CT method proposed in Chapter 6.

In this chapter, the EGSnrc simulation package, which was used for the Monte Carlo simulations, is discussed. More specifically, the BEAMnrc code present in the package was used. Then, the modelling of the X-ray tubes used at UGCT and

the results of the simulations are discussed. Finally, this chapter also examines the detectors present at UGCT. Note that this simulation method is not limited to tubes or detectors at UGCT, but can easily be expanded to other sources and detectors as long as their necessary characteristics are known. For the Perkin Elmer detector, for example, a model for the MTF is created by using measurements performed at HECTOR.

4.1 EGSnrc

The Electron-Gamma Showers (EGS) package is a general-purpose package for Monte Carlo simulations of electron and photon interactions. The package was initially developed for high-energy physics (MeV range) but was later adapted for the simulation of low-energy (1 keV-100 keV) electron and photon transport and interactions in complex geometries [10, 11].

4.1.1 BEAMnrc

The simulation package, EGS, is a set of FORTRAN codes rather than a stand-alone simulation program. These codes can be adapted to model any necessary geometry. A macro language, MORTRAN, was developed to implement a geometric model for the simulations. Further, different codes were created to reduce the work for creating a model. In this work, the BEAMnrc code is used [13]. This code was initially created to calculate the dose deposition of electrons in radiotherapy, but can be used for the problems discussed in this chapter.

BEAMnrc allows a user to create a geometric model for Monte Carlo simulations; the process is divided into two parts. First, an 'accelerator' needs to be built. This is a geometrical model composed of a set of non-overlapping component modules (CMs). These CM units contain geometric shapes such as slabs, conical filters and target configurations. These accelerator structures can be built into an executable file. Second, an input file needs to be created that contains all parameters for the simulation. These parameters contain information such as the initial particles (photons or electrons), their energy and the size, position and composition of the CMs. Further, the parameters that influence the physical interactions during the simulation can be chosen (cross-sectional data, electron step size, etc.).

An output file can be generated after passing each CM. These files contain information on the fluence of the different particles. Additionally, a phase space file is generated. This file contains information about the position of the last interaction site, energy and particle type for each particle. An extra output file can optionally

be generated that contains all coordinates of the last interaction sites of the particles. This information can be used in the simulation of X-ray tubes and detectors. The spectra produced by an X-ray tube and the efficiency and deposited energy in an X-ray detector can be extracted from the phase space file. The extra output file can be very useful in determining the position of where X-rays are produced in a tube. This yields information about the size and shape of the primary (and secondary) spot of the X-ray tube.

4.1.2 Electron transport simulation

The simulation of the behaviour of electrons inside a medium is crucial for the accuracy of the obtained data and thus spot size estimations. Electrons undergo multiple collisions inside a target, and in most collisions only a minimal amount of energy is lost or a minimal deflection is undergone. Sampling all these individual interactions would drastically increase the calculation time. Therefore, a condensed history approach is used during the simulations to condense a large number of the electron interactions in a single simulation step. Further, secondary particle creation events are still treated in a discrete and explicit manner. This is done to provide an accurate estimation of the energy and of the trajectory of the new particle. In the simulations described in this chapter, the created secondary particles are bremsstrahlung photons and secondary electrons (delta particles). The latter are created in ionisation reactions with atomic electrons, where an atomic electron is knocked out of its shell and has enough kinetic energy to ionise other atoms.

Transporting electrons from one discrete interaction site to the next can be implemented by a condensed history algorithm while condensing the whole trajectory between both sites in a single step. The electron undergoes a large number of interactions in reality, both elastic and inelastic. All energy loss below a certain bremsstrahlung threshold E_γ and delta particle creation threshold E_δ needs to be taken into account when this single step is simulated.

Instead of sampling and simulating the path length to the next interaction, each step between two interactions of an electron with initial energy E_i is accompanied by an energy loss ΔE. EGSnrc samples the resulting energy loss according to the following cumulative distribution:

$$P(\Delta E) = \exp\left(-\int_{E_i-\Delta E}^{E_i} dE \sum_E (E)\right) = \eta. \tag{4.1}$$

Here η is a random value between 0 and 1 and $\sum_E(E)$ is the interaction cross section per unit energy loss:

$$\sum_E(E) = \frac{\sum(E)}{L(E, E_\gamma, E_\delta)}, \tag{4.2}$$

with $\sum(E)$ the total macroscopic particle production cross section (cm^{-1}) and $L(E, E_\gamma, E_\delta)$ the stopping power (MeV/cm).

When this approach is used, the step size between two simulated interactions equals the electron path length corresponding to the energy loss. Further, the corresponding scattering angle and interaction position can be calculated. These calculations, however, are only reliable if several assumptions are made. The first assumption is that the fractional energy loss $\Delta E/E$ is a single step and cannot be too large. If this were not the case, errors would be introduced in the energy loss calculations and the corresponding path length. To avoid this, a maximum value for this fractional energy loss is set to 0.25, which is sufficient for most calculations. Second, the scattering angle calculated from the energy loss uses an approximation that is only valid if the scattering angle is not too large. Therefore, a restriction of the XImax parameter can be set in EGSnrc. This parameter is related to the maximum scattering angle. A default value of 0.5 is used, which corresponds to a maximum scattering angle during the step in the order of 1 radian.

The simulations of the electron interactions in EGSnrc can be summarised as follows. The energy-loss appearing after the production of a bremsstrahlung photon or delta particle takes place is sampled by Equation 4.1. The path length and scattering angle corresponding to this energy loss is determined. The fractional energy loss and scattering angle cannot exceed threshold values. If these thresholds are violated, the trajectory is broken down into smaller steps. The electron is then transported to the correct location. The secondary particles are created in this final location, and position, direction cosines and energy of the original and secondary particle(s) are calculated.

Additionally, atomic relaxations can be taken into account in the simulations. When a shell electron is removed from an atom, the vacancy is filled with an electron from a higher shell and a characteristic X-ray photon is produced.

The screened Rutherford cross section data [14] are used for the multiple elastic electron scattering approach in EGSnrc. For the inelastic scattering, the Møller cross section [15] is used, in which the binding effect of atomic electrons is disregarded. However, because characteristic X-rays are of crucial importance for

the simulations in this chapter, EGSnrc offers an electron impact ionisation option. This option is mentioned in several articles [16] dealing with the accurate simulation of X-ray tubes. This option is thus enabled for the work described here.

4.2 Modelling of X-ray tubes

Modelling of X-ray tubes at UGCT has been comprehensively described in the past [17]. This section describes the current geometric models and simulations of all available X-ray tubes at UGCT. Two main schematic models for the tubes are used: a transmission and a directional tube geometry (Fig. 4.1). Further, the results of the simulations are also shown in this section. They include the produced spectra corresponding to the transmission and directional tube geometries, as well as the visualisation of the primary and secondary, if present, spot size. For each tube, a Monte Carlo simulation was performed for a range of tube voltages from 10 kV to the maximum tube voltage in steps of 5 kV. Only part of the results of these simulations is shown here.

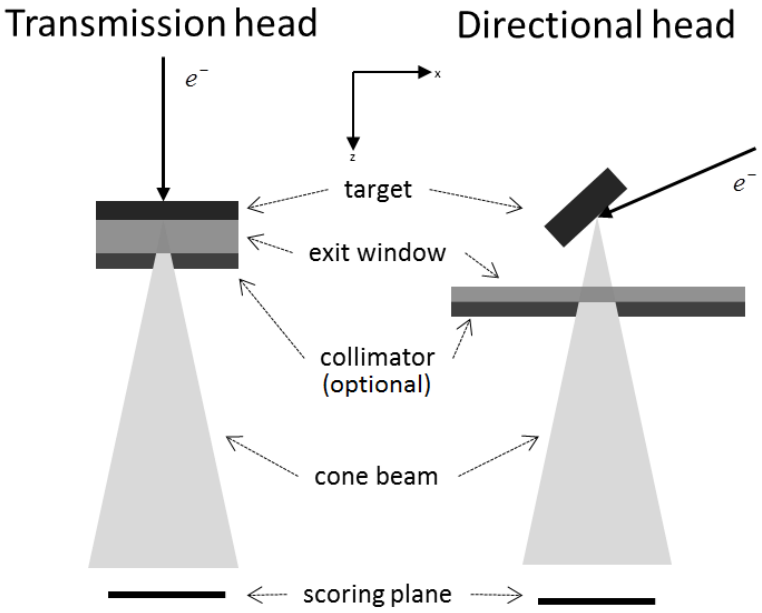

Figure 4.1: Schematic models of a transmission tube head and a directional tube head used during the Monte Carlo simulation performed for the X-ray tubes present at UGCT. During the simulations, the energies of the photons that hit the scoring plane are stored.

4.2.1 XWT-240-SE microfocus directional tube

The first tube discussed is the X-ray tube mounted on the current workhorse of UGCT, HECTOR. This directional tube can reach a voltage of 240 kV with a maximal target power of 280 W. The minimal spot size that can be achieved with this tube is around 4 μm.

Geometric model

A schematic model of this tube is given in Figure 4.2. The tube consists of a tungsten target that is tilted around 15° relative to the z-axis. The angle of the incident beam with the positive x- and z-axis is 45° and 135°, respectively; hence the beam impinges at 30° on the target. The vacuum of the tube is shielded by a beryllium exit window with a thickness of 1 mm. Behind this exit window, there is a drift section of 5 cm, followed by a scoring plane of 1cm^2. The photons that strike this plane are 'scored' and stored in an output file. The solid angle covered by such a plane is given by [18]

$$\Delta\Omega_{source} = 4 \arccos\left(\sqrt{\frac{1+2\alpha^2}{(1+\alpha^2)^2}}\right), \tag{4.3}$$

with $\alpha = a/2d$, where a is the length of the side of the square scoring plane and d is the distance from the scoring plane to the source of the photons.

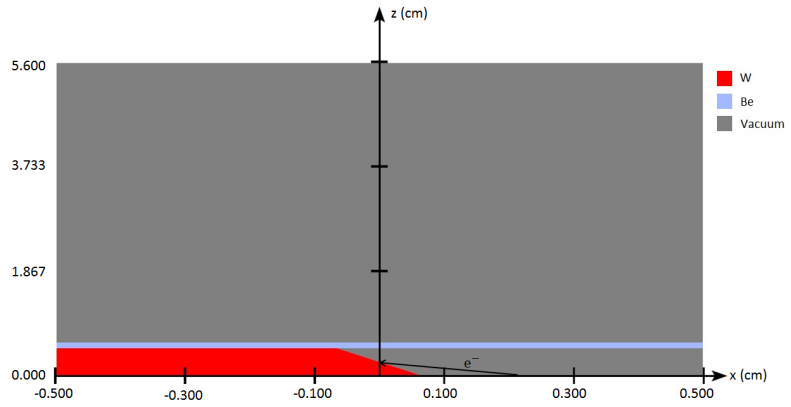

Figure 4.2: Schematic model of the XWT-240-SE microfocus directional tube. Note the different scaling for both axes.

Spectrum

The energy of the particles scored at the scoring plane during the simulation can be used to create the spectrum of the beam created by the tube at a certain volt-

age. Figure 4.3 shows such a spectrum of the XWT-240-SE microfocus directional tube at a voltage of 200 kV. This spectrum is expressed as the number of photons produced per electron per steradian per keV Equation 4.3 is used to determine the solid angle spanned by the scoring plane.

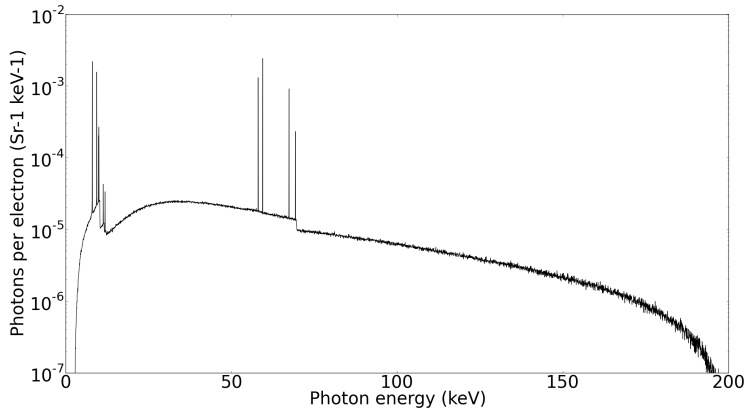

Figure 4.3: Simulated spectrum of the XWT-240-SE tube at a tube voltage of 200 kV.

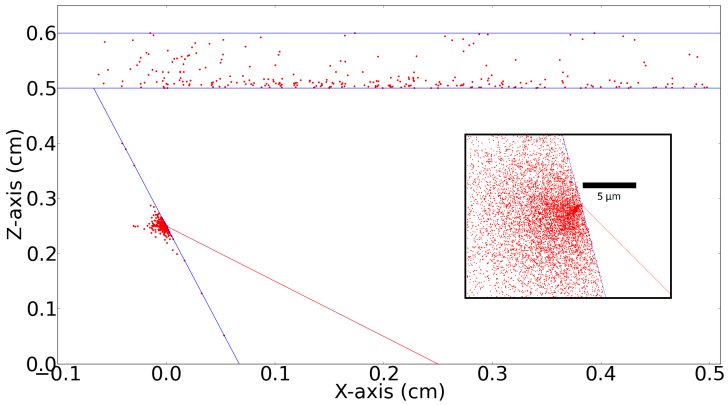

Figure 4.4: Site of last interaction of the photons that struck the scoring plane during the simulations. All positions are projected in the xz plane for the simulated spectrum of the XWT-240-SE tube at a tube voltage of 200 kV. Between $z = 0.5\ cm$ and $z = 0.6\ cm$ the exit window can be seen.

As discussed in chapter 3, X-rays originate inside a target mainly from electron impact ionisation and bremsstrahlung. Further, a large portion of the created X-rays is absorbed by the target material through the photoelectric effect. This process also results in the emittance of fluorescent characteristic X-rays. Note that

both mechanisms produce characteristic X-rays with the same energies, although the creation process is different.

Whereas the characteristic radiation originating from the tungsten (W) target is clearly visible in the simulated spectra, there is a small difference between the simulated and 'expected' energies based on tabulated values in literature [19]. The largest deviation is around 0.4 keV, but this is not significant for our applications. The difference in these characteristic energies can be explained by how the atomic relaxation is modelled in EGSnr. The exact modelling that causes these differences is not explained here but can be found in [17].

Table 4.1: Characteristic X-rays in simulated spectra and the expected photon energies.

Line	Simulated energy E (keV)	Expected energy E (keV)
$L_{\alpha,i}$	7.92	8.40 - 8.34
$L_{\beta,i}$	9.27 - 9.82 - 9.93	9.35 - 9.67 - 9.82 - 9.96
$L_{\gamma,i}$	11.23 - 11.77	11.28 - 11.68
$K_{\alpha,i}$	57.98 - 59.32	57.98 - 59.32
$K_{\beta,i}$	67.28 - 69.22	66.95 - 67.24 - 69.10

Spotsize

In addition to the energy of the scored particles, the position of the last interaction can also be extracted from the output files. Figure 4.4 shows these positions for the tube as described above at a voltage of 200 kV. The x- and z-axis are the same as in Figure 4.2. Most photons originate from a small spot where the original electron beam (red line) impinges on the tungsten target. However, some electrons can penetrate further into the tungsten or are scattered and interact in the beryllium (Be) exit window or even not at all. The last interaction point of the latter is not displayed in the figure. Also note that the figure is a 2D plot of a 3D simulation. All y-values are set to zero, and thus the points of last interaction are projected in the xz plane.

Heel effect

An effect that is typical for directional X-ray tubes is the heel effect, which is caused by the geometry of the tube. The photons emitted and striking the scoring plane in the positive x-direction have an easier time leaving the target, as they have to travel through less tungsten than the photons that strike the scoring plane in the negative x-direction. The absorption of photon in the target will depend on the pathlength travelled through the target and the energy of the photons. Therefore, the spectrum detected at the scoring plane (in the simulations) or the detector (in a

real scan) varies along the x-axis. Figure 4.5 shows the spectrum for four different positions along the x-axis on the scoring plane. The values along the y-axis are averaged. The yield of the spectrum is clearly higher on the positive x side and the spectrum is softer. Further, in Figure 4.6, the variation of photon yield is given as a function of the position along the x- and y-axis. This confirms that the effect seen is the heel effect, as it is not present in the y-direction.

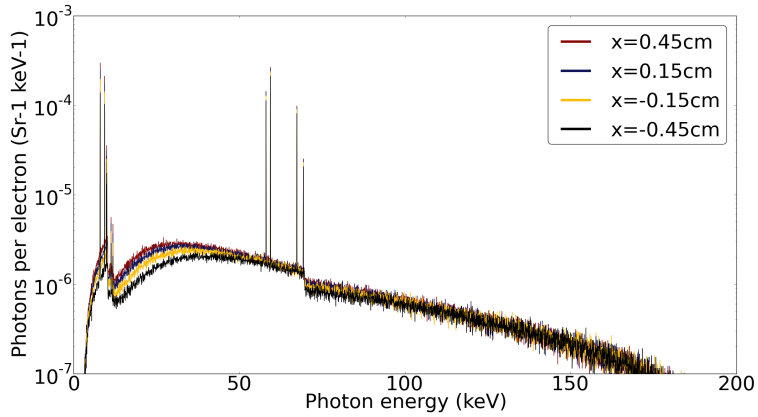

Figure 4.5: Simulated spectra along different positions at the scoring plane in the x-direction for the XWT-240-SE tube at 200 kV. The spectra become harder for lower x values due to the heel effect.

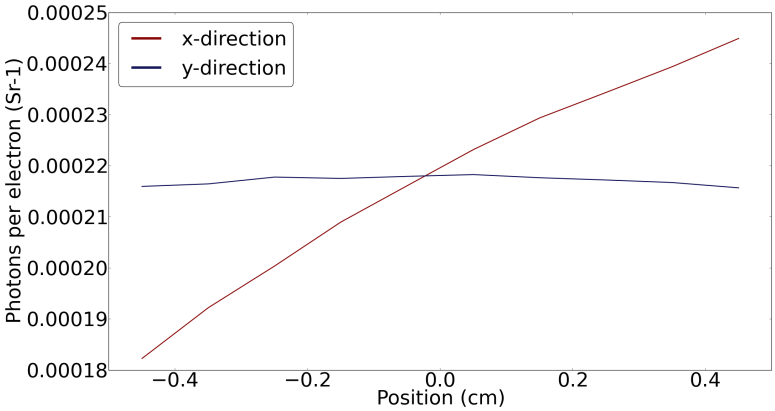

Figure 4.6: Variation in photon yield of the simulated spectra in the x- and y-direction for the XWT-240-SE tube at 200 kV.

4.2.2 130-kV Hamamatsu directional tube

The Hamamatsu directional tube can reach a tube voltage of 130 kV with a maximum power of 39 W. The minimum achievable spot size is around 5 μm. Two such tubes are available at UGCT and are mounted on the EMCT and Nanowood scanners.

Geometric model

Figure 4.7 shows a schematic geometric representation of the tube as simulated with BEAMnrc. The inclination angle between the tungsten target and the z-axis is 20°. The angle between the incident electron beam and the positive x-axis is 150°. The beam thus impinges on the target at an angle of 40°. Furthermore, the X-ray tube contains an iron (Fe) structure and collimator. The tube is shielded by a beryllium exit window with a thickness of 0.5 mm. Between the collimator and the scoring plane of 1cm^2, a drift section of 5 cm is present.

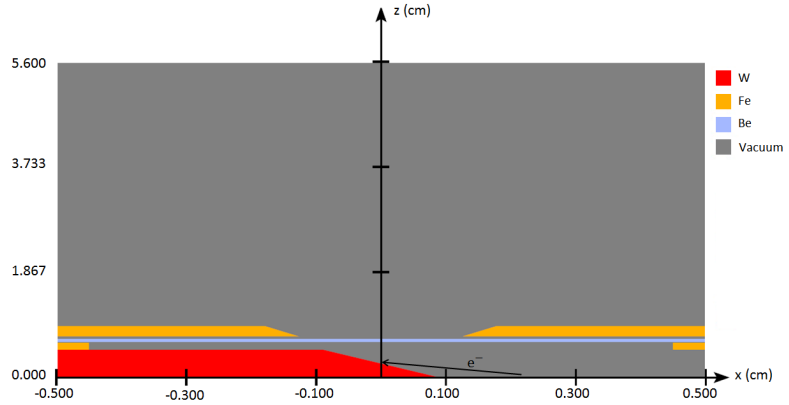

Figure 4.7: Schematic geometric model of the 130-kV Hamamatsu directional tube.

Spectrum

Figure 4.8 shows a spectrum of the Hamamatsu directional tube at a voltage of 100 kV. Again, the characteristic radiation emitted by the tungsten target is clearly visible.

Spotsize

Figure 4.9 shows the positions of last interactions of the photons that reached the scoring plane. For photons, this last interaction place is the position where the

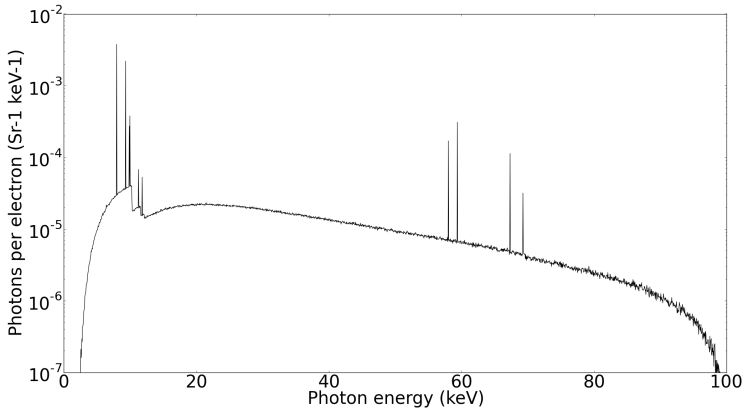

Figure 4.8: Simulated spectrum of the 130-kV tube at a tube voltage of 100 kV.

creation process of the photon takes place. Note that the collimator is a symmetrical cylinder and all positions are projected on the xz plane. The positions that are seemingly located in the vacuum are thus actually positions on the collimator with a y-value different from zero.

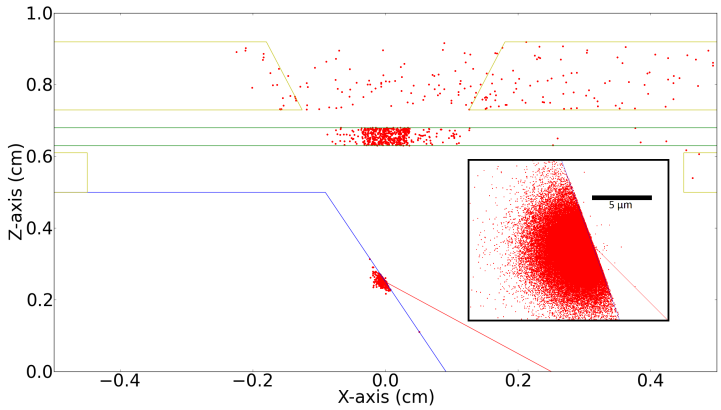

Figure 4.9: Site of last interaction of the photons that struck the scoring plane during the simulations. All positions are projected in the xz plane for the simulated spectrum of the 130-kV tube at a tube voltage of 100 kV.

Heel effect

Just as in the case of the XWT-240kV tube, this tube is a directional tube, and thus a heel effect is present at the position of the scoring plane or detector. Figure 4.10 shows the spectrum for four different x-positions on the scoring plane. All positions are projected in the xz plane for the simulated spectrum of the 130-kV

tube at a tube voltage of 100 kV. The yield of the spectrum is clearly higher and the spectrum is softer on the positive x side. Further, in Figure 4.11, the variation in photon yield is given in function of the position along the x- and y-axis.

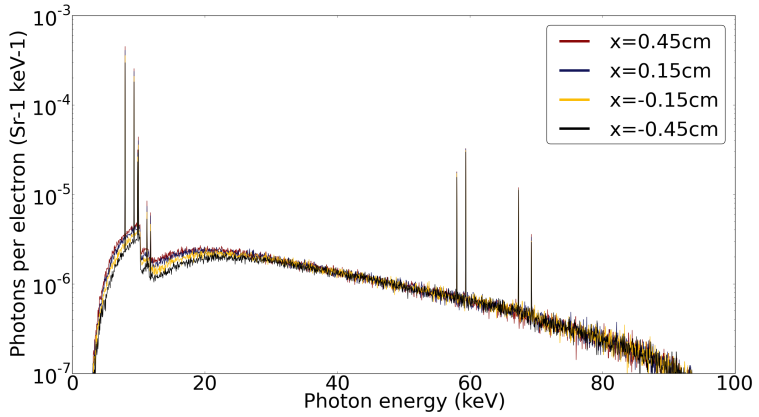

Figure 4.10: Simulated spectra along different position in the x-direction for the 130-kV Tube at 100 kV. The spectra become harder for lower x values which is due to the heel effect.

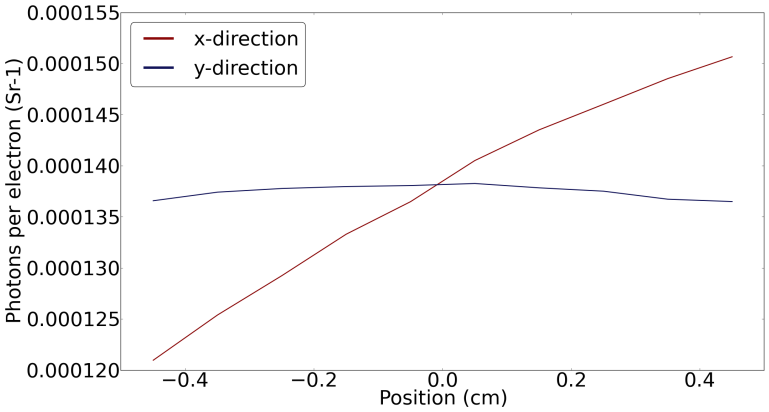

Figure 4.11: Variation of the simulated spectra in the x- and y-direction for the 130-kV Tube at 100 kV.

4.2.3 160-kV FeinFocus transmission tube

The FeinFocus transmission tube was originally used in the first scanner built at UGCT [20], but is now mounted on the refurbishment of this scanner, MEDUSA. The tube can reach a maximal target power of 1, 3 and 10 W for the nano-focus,

micro-focus and high power modes, respectively. The nano-focus mode of the tube can reach a spot size as low as 0.7 μm.

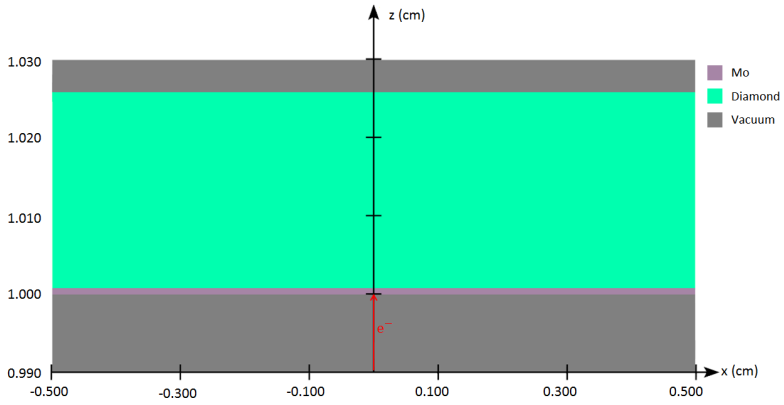

(a) without inner stucture

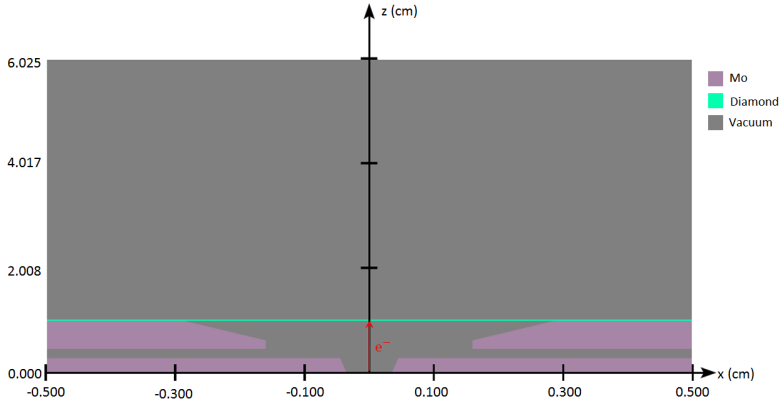

(b) with inner structure

Figure 4.12: A schematic model for the 160-kV FeinFocus transmission tube without (a) and with (b) inner structure. The target of the models shown is the 1 μm thick molybdenum target.

Geometric model

Eight different targets are available for this tube consisting of two materials, tungsten and molybdenum and with a target thickness of 1, 3, 6 and 8 μm. The tube has an inner structure that cannot be neglected since it causes a secondary spot [12]. The simulations for this tube were performed with and without the inner

structure for all eight targets. The geometric models of the tube with and without structure are shown in Figure 4.12.

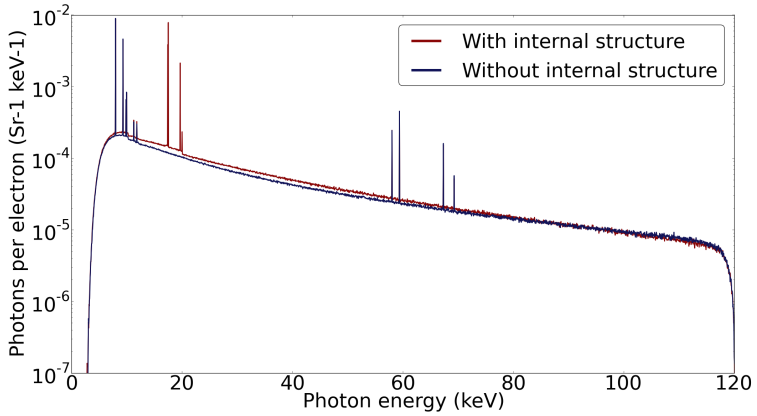

(a) 1μm W target

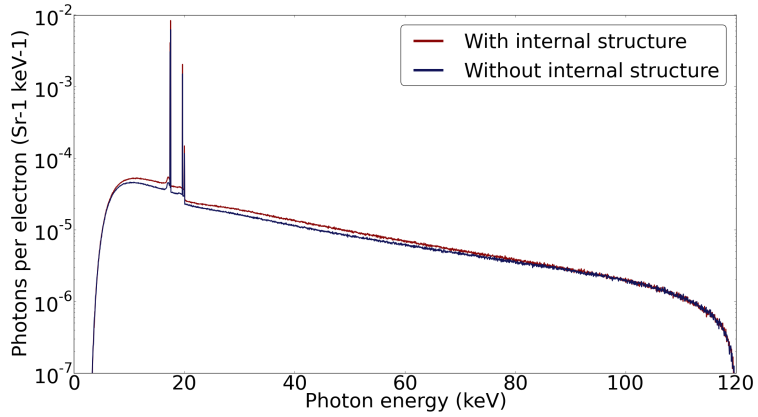

(b) 8μm Mo target

Figure 4.13: Simulated spectrum of the 160-kV transmission tube at a tube voltage of 120 kV for a tungsten target with thickness 1 μm (a) and a molybdenum target with thickness 8 μm (b).

Spectrum

Figure 4.13 shows the spectra of the tube at a voltage of 120 kV with a target thickness of 1 μm tungsten and 8 μm of molybdenum. The characteristic lines of molybdenum below the K-edge of 20.002 keV are clearly visible. Furthermore, there is a clear difference between the yield of the tube depending on the presence of the inner structure. Figure 4.14 shows how much more yield the X-ray tube

produces when the inner structure is taken into account. The increase in production varies between 10 and 26%.

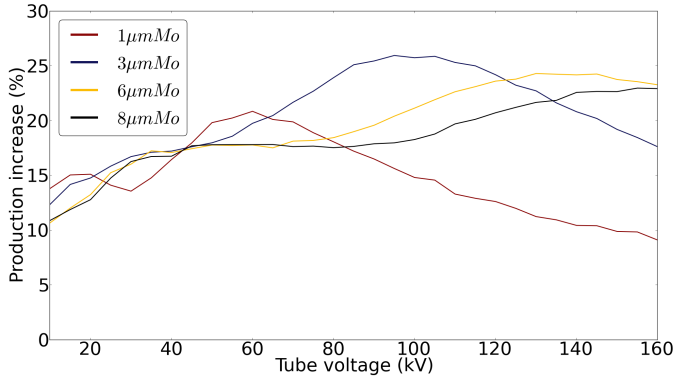

(a) Mo target

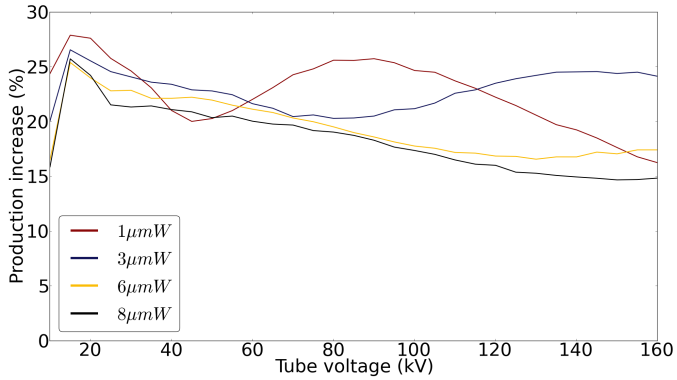

(b) W target

Figure 4.14: Increase in photon production when the inner structure of the tube is taken into account versus when the inner structure is not taken into account during the Monte Carlo simulations for the tungsten (a) and molybdenum (b) targets.

Spotsize and Secondary spot

Figure 4.15(a) shows the position of last interaction in the transmission tube with an inner structure with a target of 3 μm of tungsten at a tube voltage of 90 kV. Note that all positions are projected on the xz-plane and that the inner structure is radially symmetric. Figure 4.15(b) shows a plot of the same positions in the rz-plane, in which $r = \sqrt{x^2 + y^2}$. Here it is clearly visible that a large portion of

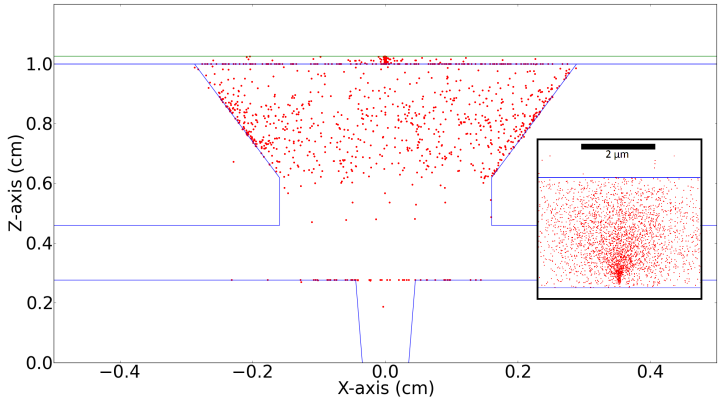

(a)

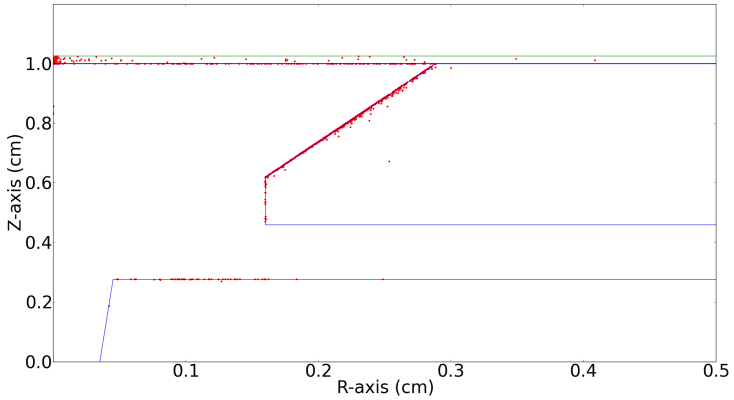

(b)

Figure 4.15: Position of last interaction in the xz-plane (a) and rz-plane (b) for the simulated spectrum of the 160-kV transmission tube at a tube voltage of 90 kV with a tungsten target thickness of 3 µm.

the last interactions occurs on the molybdenum structure in the X-ray tube. The photon production increases in the tube with the inner structure according to the photon production in the tube without the structure. But as can be seen in Figure 4.16, the extra photons do not originate from the primary spot, but from a much larger secondary spot present in the tube.

A fit can be used to model the behaviour of the secondary spot. Three fits are made to model the spot distribution shown in Figure 4.16(b). First, the spot is modelled as a constant value between two radii with the equation given by the fit

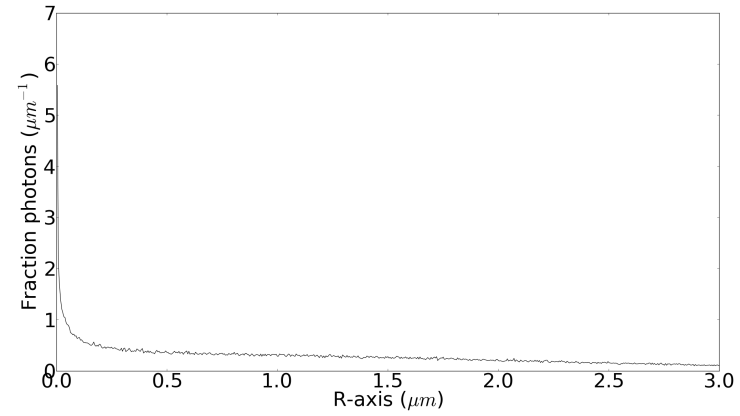

(a) Primary spot

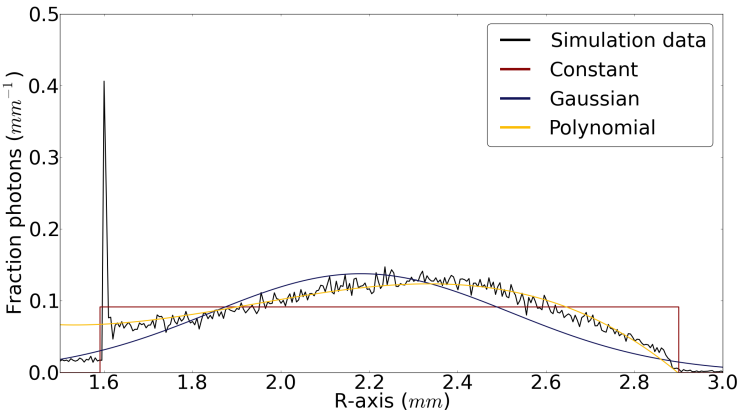

(b) Secondary spot

Figure 4.16: The fraction of photons that is produced at different radii. The presence of a primary (a) and secondary (b) spot can be seen. Note the difference in x-axis scale. Three different models where fitted to the data for the secondary spot.

$F(r)$ in function of the distance r to the central axis (z-axis) of the tube in mm:

$$F(r) = \begin{cases} 0 & \text{if } r \leq 1.6 \\ c & \text{if } 1.6 < r < 2.9 \\ 0 & \text{if } r \geq 2.9 \end{cases} \tag{4.4}$$

with $c = 0.0915$. Furthermore, a Gaussian function can be fitted to the data:

$$F(r) = A \exp\left(\frac{(r - r_0)^2}{2\sigma^2}\right) \tag{4.5}$$

with $A = 0.1380$, $\sigma = 0.1154$ and $r_0 = 2.1807$. Finally, a polynomial fit of third order was performed to obtain a good fit without having too many parameters. The polynomial is given by:

$$F(r) = \begin{cases} 0 & \text{if } r \leq 1.6 \\ a + br + cr^2 + dr^3 & \text{if } 1.6 < r < 2.9 \\ 0 & \text{if } r \geq 2.9 \end{cases} \tag{4.6}$$

with $a = 1.4917$, $b = -2.3810$, $c = 1.2867$ and $d = -0.2218$. These models can by used to make a correction for the secondary spot in simulated radiographs as is done in Chapter 5.

4.2.4 XWT-100-TCHR transmission tube

The XWT-100-TCHR transmission tube is mounted on the Herakles scanner, and a slightly different tube is present on the Nanowood scanner. This tube has a maximum tube voltage of 100 kV, a maximum power of 3 W and can reach a minimum focal spot size of around 700 nm. The target is tungsten and has a thickness of 1 μm, and the exit window of the tube consists of 250 μm of beryllium.

Geometric model

Figure 4.19 shows a schematic view of the tube. No internal structure was taken into account during the simulation, as none is known.

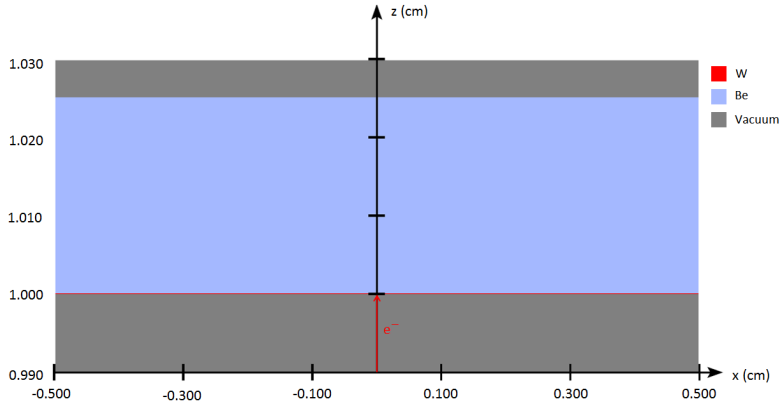

Figure 4.17: A schematic model for the XWT-100-TCHR transmission tube.

Spectrum

A spectrum of the tube produced at 80 kV is given in Figure 4.18. The characteristic L-lines of the tungsten target are dominant to the K-lines because the mean energy of the spectrum is rather low.

Spotsize

Figure 4.19 shows the spatial distribution of the spot size projected in the xz-plane.

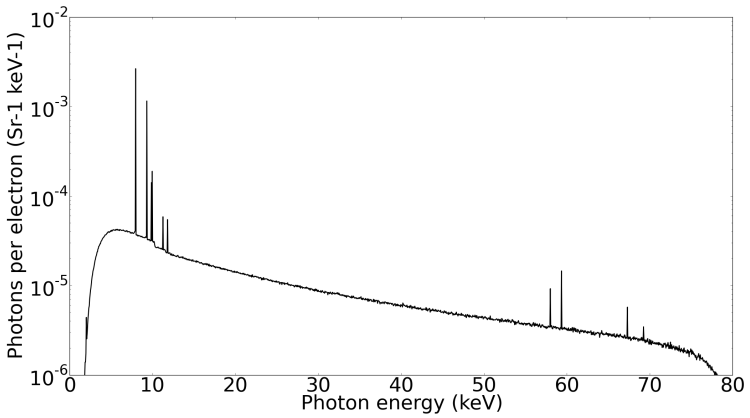

Figure 4.18: Simulated spectrum produced by the XWT-100-TCHR transmission tube at a tube voltage of 80 kV.

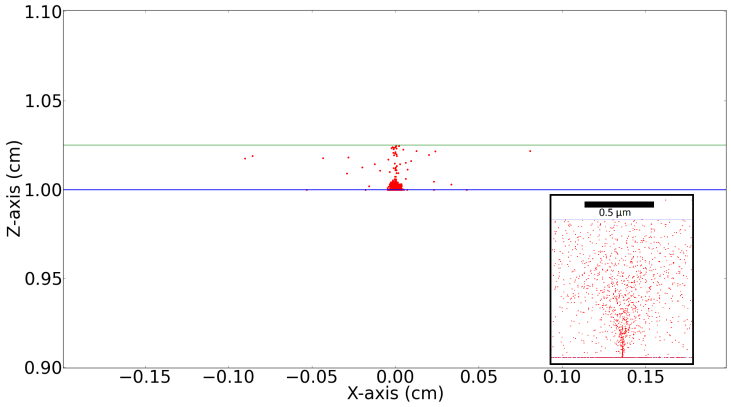

Figure 4.19: Spatial distribution of last interaction projected in the xz-plane for the XWT-100-TCHR tube at 80kV.

4.3 Modelling of X-ray detectors

In this section, the spectral properties of the detectors present at UGCT are discussed.

4.3.1 Varian PaxScan 2520V detector

The Varian PaxScan 2520V is a typical flat panel detector and is composed of an entrance window made of carbon, a thin aluminium foil, a scintillator and an amorphous silicon (aSi) detector layer (Fig. 4.20). The aluminium foil is added to reflect visible light photons created and emitted by the scintillator in the direction of the entrance window. This scintillator is made of caesium iodide (CsI) grown in a columnar structure.

The number of counts per pixel in a radiographic projection is in first order proportional to the deposited energy in the scintillator in front of that pixel. On the other hand, the noise in a radiographic image depends on the number of photons detected per pixel. For accurate simulations, both characteristics should be taken into account.

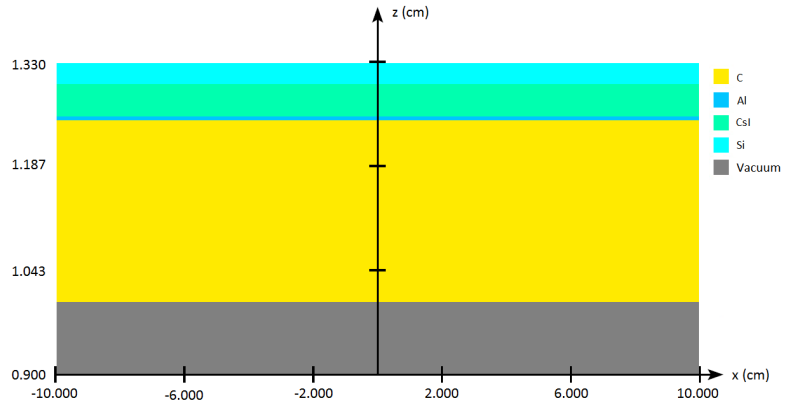

Figure 4.20: Schematic model of the Varian detector. The detector consists of four layers: a carbon entrance window, an aluminium foil a CsI scintillator and an amorphous silicon (aSi) detector layer.

By using BEAMnrc, the spectral sensitivity of the detector can be simulated. The interactions of a pencil beam of mono-energetic photons emitted on the pre-defined detector geometry, as described above, are traced. This allows one to calculate the interaction probability $D_{eff}(E)$ (Fig. 4.22) of these photons and the mean amount of deposited energy per detected $D_d(E)$ (Fig. 4.22) and per incident

$D_{inc}(E)$ (Fig. 4.23) photon as a function of photon energy. The mean amount of deposited energy per incident photon-the photons that reach the detector-is thus what is needed during the simulations described in the next chapter.

The mean deposited energy of an interacting photon shows a nod when the energy of the interacting photon reaches the K-edge of the material. Above this edge, fluorescent K-photons are created which can easily escape the thin scintillator layer without being re-absorbed in it. Above the K-edge, a certain amount of energy is thus able to escape from the scintillator material. For higher energies above the edge, a larger fraction of the incident energy is on average transferred to photoelectrons and Compton scattered photons which can escape the scintillator.

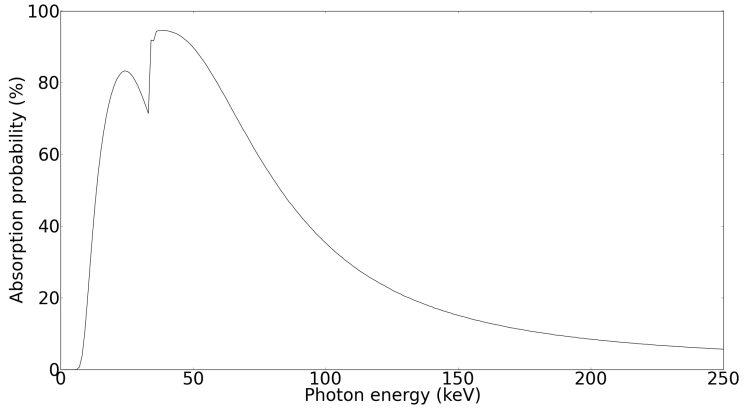

Figure 4.21: Absorption probability in the Varian detector as a function of incident photon energy.

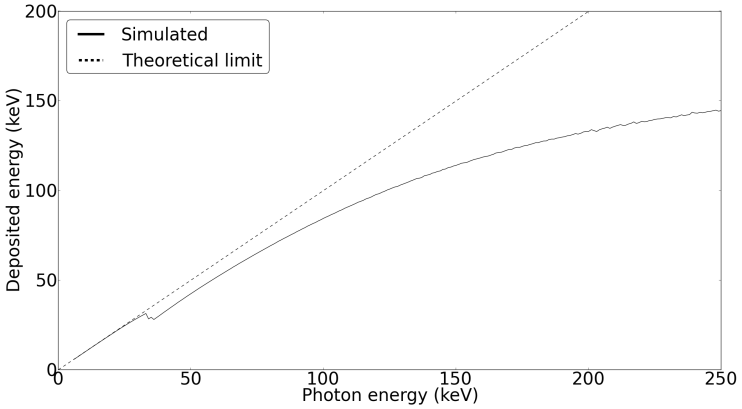

Figure 4.22: Mean deposited energy in the Varian detector for a detected photon as a function of its initial energy.

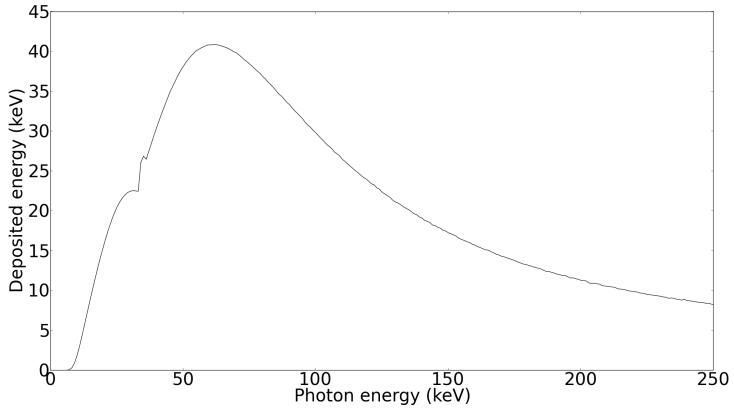

Figure 4.23: Mean deposited energy in the Varian detector per incident photon as a function of its initial energy.

4.3.2 Photonic Science VHR detector

The Photonic Science Very High Resolution (VHR) detector is equipped with a CCD sensor. This detector has a carbon entrance window, but its thickness is not known. Therefore, it is neglected during simulations and can always be introduced as a carbon filter during a simulation of a CT scan. The detector consists of two layers: a Gadox scintillator with a thickness of 13.4 μm and a CCD camera that consists of SiO2. These two layers are connected by a fibre-optic plate. The Gadox layer is deposited directly on the fibre-optic plate, which conducts the visible light photons to the CCD. As the function of the fibre optic is only to guide the visible light photons to the CCD and protect it from radiation damage, this fibre optic is not taken into account during the simulations (Fig. 4.24). Note that because the packing density of the Gadox layer is typically around 50% due to the irregular grain shape, a layer of 6.7 μm of Gadox with the density of pure Gadox (7.44 g/cm^3) is used in the scintillator.

The spectral sensitivity of the Photonic Science VHR is modelled as in the simulations of the Varian detector, . The interaction probability $D_{eff}(E)$ of the X-ray photons is calculated from the simulations (Fig. 4.25) along with the mean amount of deposited energy per detected $D_d(E)$ (Fig. 4.26) and per incident $D_{inc}(E)$ (Fig. 4.27) photon.

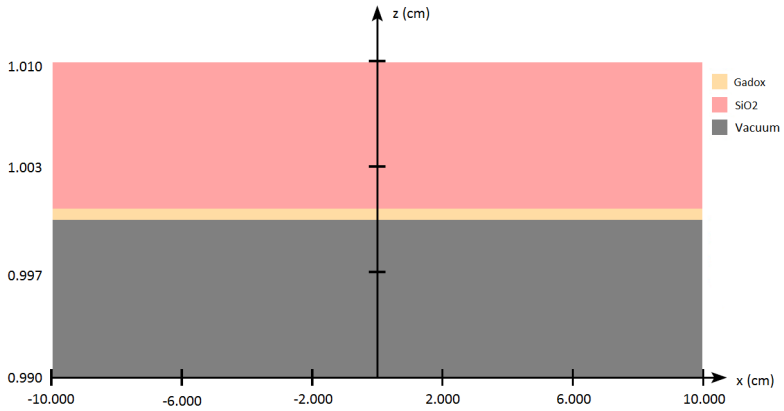

Figure 4.24: Schematic model of the Photonic Science VHR detector. The detector consists of a Gadox entrance window and a SiO_2 scintillator.

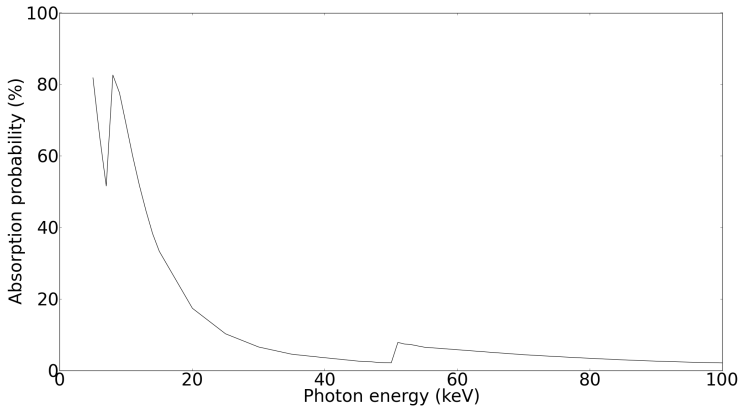

Figure 4.25: Absorption probability of the Photonic Science detector as a function of the incident photon energy

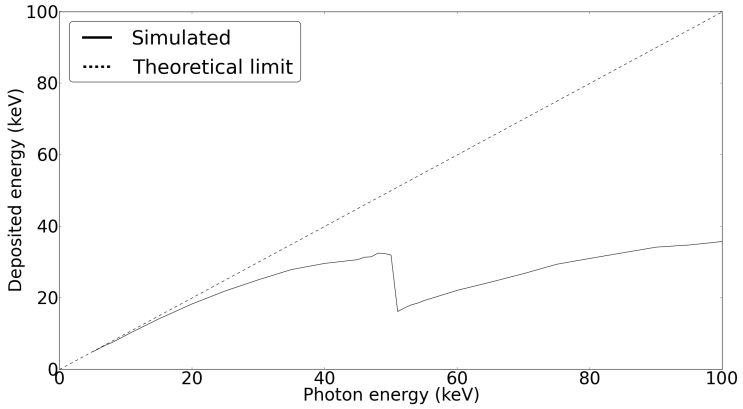

Figure 4.26: Mean deposited energy in the Photonic Science detector for a detected photon as a function of its initial energy.

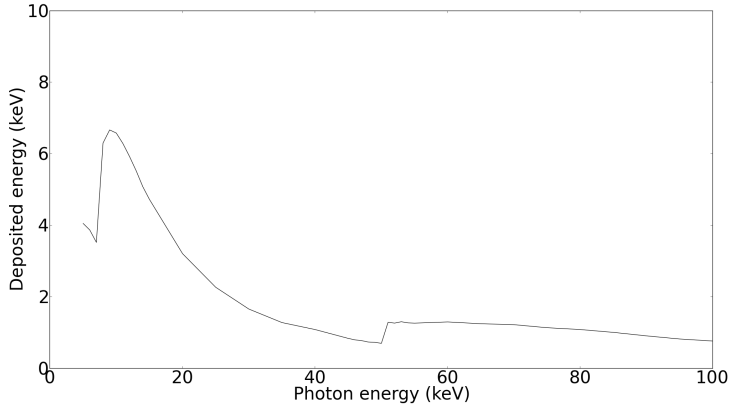

Figure 4.27: Mean deposited energy in the Photonic Science detector per incident photon as a function of its initial energy.

4.3.3 Perkin Elmer XRD 1620 CN3 CS detector

Because the properties of the Perkin Elmer XRD 1620 CN3 CS detector are confidential, the geometric model and spectral efficiency of the detector are not discussed here. Nevertheless, in chapter 5, real scans at HECTOR are compared with simulated scans in which these simulated data are used.

MTF

For the Perkin Elmer detector, the LSF (section 3.5.4) was measured by taking radiographic projections of a copper cylinder with a diameter of 12 cm. A cylinder was used to make sure there was a sharp transition profile measured on the detector. Figure 4.28 shows the measured edge response and its derivative. A Gaussian profile

$$LSF(r) = I \exp\left(\frac{(r - r_0)^2}{2\sigma^2}\right) \tag{4.7}$$

can be fitted to this derivative, and the values for this Gaussian fit are shown in Table 4.2. Of course, when applying such a correction for each pixel in a radiography, $r_0 = 0$ (section 5.3.3).

Table 4.2: Fitted parameters to the Gaussian LSF function shown in Equation 4.7.

Tube voltage	Intensity I	mean r_0	sigma σ
60 kV	0.448	73.805	0.650
120 kV	0.482	74.180	0.564
180 kV	0.474	74.313	0.524

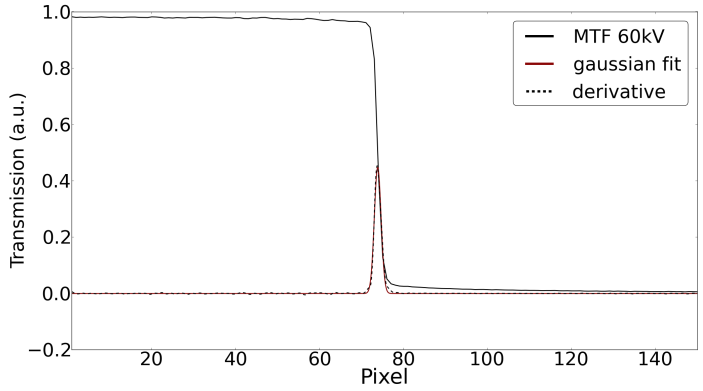

(a)

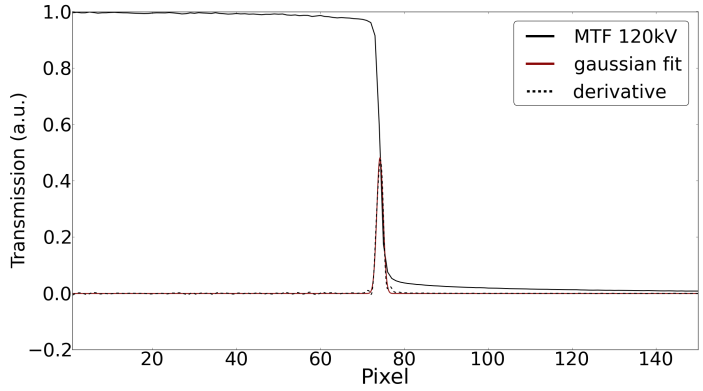

(b)

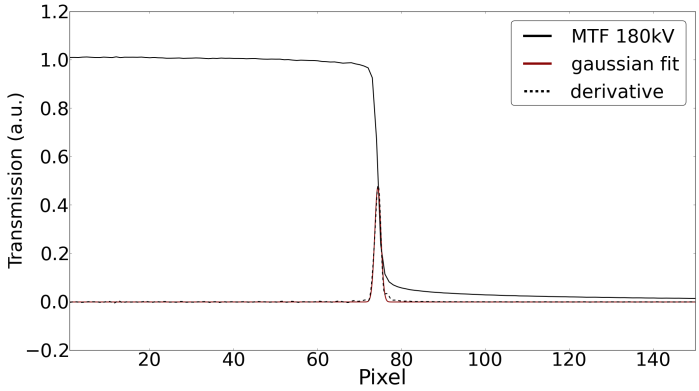

(c)

Figure 4.28: LSF measured for the Perkin Elmer at tube voltages of 60 kV, 120 kV and 180 kV. The XWT-240kV tube was used for the measurement.

4.4 Conclusion

In this chapter it is discussed how the polychromatic properties of an X-ray tube and X-ray detector can be modelled. Next to the polychromatic behaviour, a method to model the heel effect in directional tubes, to model the secondary spot and to model the MTF of the detector are discussed. Particularly the spectra (example in Figure 4.3) and detector efficiencies (example in Figures 4.21, 4.22 and 4.23) are important properties to accurately simulate radiographic projections as discussed in the next chapter. These spectra and efficiencies are available as look-up tables generated from the Monte Carlo simulations data and can easily be used in a program or tool such as Arion.

Furthermore, the correctness of this Monte Carlo simulated data can only be verified by simulating radiographic projections. The spectra cannot be verified separately because a perfect detector, which does not exist, would be needed to do this. On the other hand, for verifying the detector efficiencies, a tuneable monochromatic source which covers the whole energy range to which the detector is sensitive should be needed, which is not available at UGCT.

References

[1] R Birch and M Marshall. *Computation of bremsstrahlung X-ray spectra and comparison with spectra measured with a Ge(Li) detector*. Physics in Medicine and Biology, 24(3):505, 1979.

[2] Douglas M. Tucker, Gary T. Barnes, and Dev P. Chakraborty. *Semiempirical model for generating tungsten target x-ray spectra*. Medical Physics, 18(2):211–218, 1991.

[3] Douglas M. Tucker, Gary T. Barnes, and Xizeng Wu. *Molybdenum target x-ray spectra: A semiempirical model*. Medical Physics, 18(3):402–407, 1991.

[4] John M. Boone and J. Anthony Seibert. *An accurate method for computer-generating tungsten anode x-ray spectra from 30 to 140 kV*. Medical Physics, 24(11):1661–1670, 1997.

[5] Marco Bontempi, Lucia Andreani, Pier Luca Rossi, and Andrea Visani. *Monte Carlo simulator of realistic x-ray beam for diagnostic applications*. Medical Physics, 37(8):4201–4209, 2010.

[6] G. Tirao, C. Quintana, F. Malano, and M. Valente. *X-ray spectra by means of Monte Carlo simulations for imaging applications*. X-Ray Spectrometry, 39(6):376–383, 2010. 718HX Times Cited:2 Cited References Count:41.

[7] M. Guthoff, O. Brovchenko, W. de Boer, A. Dierlamm, T. MÃ¼ller, A. Ritter, M. Schmanau, and H.-J. Simonis. *Geant4 simulation of a filtered X-ray source for radiation damage studies*. Nuclear Instruments and Methods in Physics Research Section A, 675:118 – 122, 2012.

[8] Andrii Sofiienko, Chad Jarvis, and Ådne Voll. *Monte Carlo Simulations of a Scanning System Based on a Panoramic X-Ray Tube with a Conical Anode*. Physics Research International, 2014:9, 2014.

[9] Mohammad M. Nasseri. *Determination of Tungsten Target Parameters for Transmission X-ray Tube: A Simulation Study Using Geant4*. Nuclear Engineering and Technology, 48(3):795 – 798, 2016.

[10] A.F. Bielajew, D.W.O. Rogers, and Kōenerugī Butsurigaku Kenkyūjo (Japan). *History, Overview and Recent Improvements of EGS4: Lecture*. KEK internal. National Laboratory for High Energy Physics, 1994.

[11] I. Kawrakow. *Accurate condensed history Monte Carlo simulation of electron transport. I. EGSnrc, the new EGS4 version*. Medical Physics, 27(3):485–498, 2000.

[12] M. N. Boone, J. Vlassenbroeck, S. Peetermans, D. Van Loo, M. Dierick, and L. Van Hoorebeke. *Secondary radiation in transmission-type X-ray tubes: Simulation, practical issues and solution in the context of X-ray microtomography*. Nuclear Instruments and Methods in Physics Research, Section A, 661(1):7–12, 2012.

[13] D. W. O. Rogers. *BEAM: A Monte Carlo code to simulate radiotherapy treatment units*. Medical Physics, 22, 1995.

[14] Iwan Kawrakow and Alex F. Bielajew. *On the representation of electron multiple elastic-scattering distributions for Monte Carlo calculations*. Nuclear Instruments and Methods in Physics Research, Section B, 134(3-4):325–336, 3 1998.

[15] C. Molller. *Zur Theorie des Durchgangs schneller Elektronen durch Materie*. Luno, 1932.

[16] Ernesto Mainegra-Hing and Iwan Kawrakow. *Efficient x-ray tube simulations*. Medical Physics, 33(8):2683–2690, 2006.

[17] J. Vlassenbroeck. *Advances in laboratory-based X-ray microtomography*. Phd dissertation, Ghent University, 2009.

[18] R. J. Mathar. *Solid angle of a rectangular plate*. `http://www.mpia-hd.mpg.de/~mathar/public/mathar20051002.pdf`, 2014.

[19] Kaye and Laby. *Tables of physical and chemical constants*. `http://www.kayelaby.npl.co.uk/atomic_and_nuclear_physics/4_2/4_2_1.html`, 2016.

[20] B. Masschaele, V. Cnudde, M. Dierick, P. Jacobs, L. Van Hoorebeke, and J. Vlassenbroeck. *UGCT: new x-ray radiography and tomography facility*. Nuclear Instruments and Methods in Physics Research, Section A, 580(1):266–269, 2007.

5

Arion: A realistic projection simulator

This chapter is partly based on the publication: A realistic projection simulator for laboratory based X-ray micro-CT [1]

This chapter describes Arion, which is a realistic projection simulator for laboratory-based X-ray CT developed at UGCT. One of the most important reasons for creating this simulator was to have a tool to optimise image contrast and thus scanning parameters for a CT scan, which are different for each sample. Next to this, it can also be used to expore exotic scan geometries and to test reconstruction algorithms. Realistic simulations have to take various scanning variables into account, including the spectrum emitted by the source, the detector response characteristics, beam filtration and the sample itself. This is necessary in order to define the optimal scanner settings [2]. Several research groups have developed simulation tools for X-ray imaging for different purposes, e.g. ScorpiusXLab [3], VXI [4–8], XRayImagingSimulator [9–11], XRSIM [12], etc. However, in general these tools are developed for the research group's own research and a lot of them use (semi-)analytical models for the X-ray spectra and detector efficiencies, while in Arion the ones calculated with the Monte Carlo method, described in the previous chapter are used. The emphasis of Arion is on modelling and including the X-ray imaging physics as accurate as possible which results in a correct noise prediction in the simulated images and no calibration is needed when simulated data is compared with real data. The intent at UGCT was to create a flexible, fast (GPU-based) and accurate simulation tool which can easily be expanded with physical models such

as including a secondary spot, the heel effect or the MTF of the detector. Furthermore, the previuosly mentioned simulation tools are not readily available and/or have no room for expanding the code and often have no quantitative comparisons between real CT scans and the simulations presented in literature.

First, the implementation of the geometry of the CT setup is described in this chapter. Further, the ray-tracing technique of the simulator is discussed, followed by all the features of Arion and its modules: Material Creator, Setup Optimiser, Arion and Image Handler. Finally, an extensive comparison is made between simulated and real radiographic projections, and reconstructed 3D volumes and methods to optimise scanning conditions are discussed. A variety of samples was scanned at 'optimal conditions' in the context of the IWT/SBO TomFood project. Some of the obtained results are shown.

5.1 Geometry

For an accurate simulation of a complete CT scan, the complete geometry of each component of the scanner should be known, along with the relative positions of the components towards each other. This section describes the geometries used in Arion.

The coordinate system used in the program is defined as shown in Figure 5.1. For each radiography taken during the simulated CT scan, a position and rotation for each of the components can be set. The sample is placed in the main coordinate system $\{\vec{e_x}, \vec{e_y}, \vec{e_z}\}$ and has a position $\vec{r}_{sample}$ in this coordinate system, which is Cartesian and right-handed. The positions of the source and detector in this system are determined by the coordinates $\vec{r}_{source}$ and $\vec{r}_{detector}$, respectively.

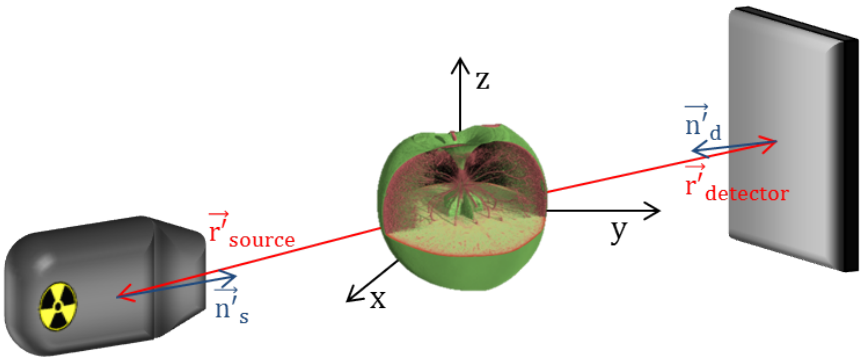

Figure 5.1: Coordinate system as used in Arion. The sample is positioned at the origin and the source and detector make a movement around it.

Besides the positions of each component in the coordinate system, a rotation around the axes can be defined for each component. The initial directions of the source and detectors are determined by the normal vectors:

$$\begin{aligned} \vec{n}_{source} &= (0, 1, 0), \\ \vec{n}_{detector} &= (0, -1, 0). \end{aligned} \tag{5.1}$$

For the sample, the x-, y- and z-axis of the virtual voxelised sample align with the coordinate system in the initial position. The rotation of each component is described by using Tait-Bryan angles (appendix A). These angles describe rotations about the three axes of the coordinate system. The skew (α), tilt (β) and slant (γ) of an object are the rotations around the x-axis, y-axis and z-axis, respectively. By using these angles instead of Euler angles, it is easier for the user to describe the rotation of the sample or detector. The skew, tilt and slant can thus be set for each component. Now, instead of rotating the sample at the position set by the user, a coordinate transformation is performed such that the sample is kept fixed at the origin of the coordinate system. This is for ease of calculation, as it would be computationally difficult to rotate a sample consisting of 500 $\times$ 500 $\times$ 500 voxels during each step of the simulation. It is much easier to keep this whole cube stationary and rotate the positions and orientations of the other components. The rotated position vectors for the source and detector are given by $\vec{r'}_{source}$ and $\vec{r'}_{detector}$ respectively, and the normal vectors by $\vec{n'}_{source}$ and $\vec{n'}_{detector}$. How this coordinate transformation is done exactly can be found in appendix A.

By using these six coordinates, position and orientation, for each component, it is possible to describe every imaginable combination of trajectories. As a result, the simulator can be used to explore new CT setups with non-conventional arrangements, such as a conveyer belt setup, which can be used in an industrial environment [13].

5.2 Ray-tracing calculation

The simulation of a radiographic projection is based on the Beer-Lambert law (Equation 3.27). For a polychromatic beam, this equation can be rewritten as a sum over different energy bins:

$$N = \sum_{i=1}^{n} N_{0,i} \exp(-\mu_i d), \tag{5.2}$$

with n the number of energy bins used, $N_{0,i}$ the initial number of photons emitted by the tube in energy bin i and μ_i the linear attenuation coefficient for the energy corresponding to bin i. The total attenuation along a ray can be calculated by

applying a ray-tracing technique for each energy bin. The total attenuation along the ray-path from source to detector-pixel is calculated using this technique (Fig. 5.2). The resulting number of photons N_i hitting a detector pixel for an energy bin i along such a ray is given by:

$$N_i = N_{0,i} \exp(-\sum_{j=1}^{m} \mu_{i,j} d_j), \tag{5.3}$$

with m the number of materials crossed by the traced ray, μ_{ij} the linear attenuation coefficient in energy bin i of material j and d_j the thickness of the corresponding material crossed by the ray. The number of photons detected by the detector in energy bin i is given by the product of the detector efficiency in energy bin i, $D_{eff,i}$ (section 4.3) with N_i:

$$N_{d,i} = D_{eff,i} \times N_i. \tag{5.4}$$

These detected photons do not deposit all their energy in the pixels but only a certain fraction of it. Multiplying the mean deposited dose per detected photon $D_{d,i}$ for each energy bin results in the total detected energy E_d (section 4.3) in a pixel and is given by:

$$E_d = \sum_{i=1}^{n} E_{d,i} = \sum_{i=1}^{n} D_{d,i} N_{d,i}, \tag{5.5}$$

with $E_{d,i}$ the detected energy per pixel for energy bin i.

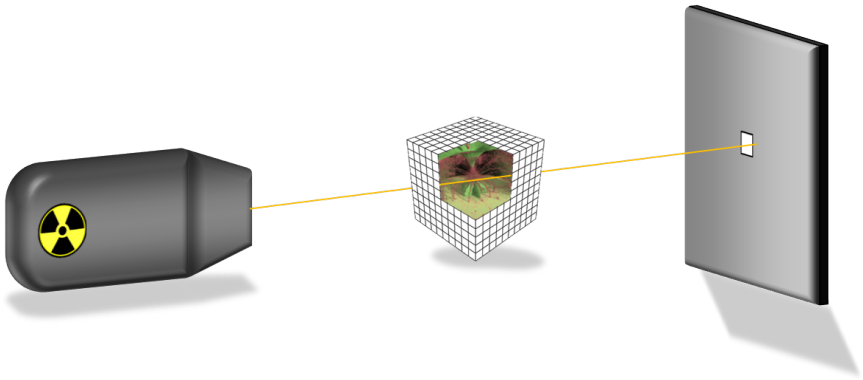

Figure 5.2: Visual representation of the ray-tracing technique used in the projection simulator.

The noise in a simulated image can be calculated by assuming Poisson statistics. The standard deviation on the number of detected photons in an energy bin can be

calculated from the square root of the number of detected photons:

$$\sigma_{N_{d,i}} = \sqrt{N_{d,i}}. \tag{5.6}$$

For a large number of photons per energy bin, a Gaussian error propagation can be assumed. The standard deviation on Equation 5.5 can thus be calculated as follows:

$$\sigma_{E_d} = \sqrt{\sum_{i=1}^{n} \left(\sigma_{E_{d,i}}\right)^2} = \sqrt{\sum_{i=1}^{n} \left(D_{d,i}\sigma_{N_{d,i}}\right)^2}, \tag{5.7}$$

with σ_{E_d} the standard deviation of the detected energy in a pixel for energy bin i.

The only unknown thus far in the calculation of the deposited energy (Equation 5.5) and its standard deviation (Equation 5.7) in a pixel is the number of photons emitted by the tube per bin. This number is related to the tube spectra S_i calculated in section 4.2. The emitted photons $N_{emittedphotons,i}$ in the solid angle of a pixel $\Delta\Omega_{pixel}$ in an energy bin are given by:

$$N_{emitted\ photons,i} = \left(\frac{P\Delta t}{UQ_{e^-}}\right)(\Delta\Omega_{pixel}\Delta E_i S_i'). \tag{5.8}$$

The first factor, $\frac{P\Delta t}{UQ_{e^-}}$, equals the number of electrons hitting the target in the tube during the exposure time of a radiographic projection. In this factor, P represents the tube power, Δt is the exposure time, U the tube voltage and Q_{e^-} the elementary charge. The second factor contains the solid angle of the pixel $\Delta\Omega_{pixel}$, the width of the energy bin ΔE_i and the filtered spectrum $S_i^{'}$ expressed as the number of photons per electron per steradian per keV. Combining Equations 5.4 and 5.8, the number of photons detected in a pixel in energy bin i can be calculated as follows:

$$N_{d,i} = \frac{P\Delta t}{UQ_{e^-}}\Delta\Omega_{pixel}\Delta E_i S_i' D_{eff,i}\exp(-\sum_{j=1}^{m}\mu_{ij}d_j). \tag{5.9}$$

Implementation

Equation 5.9 is evaluated for each pixel of the detector. For all these detector-pixels, the ray is traced from the source to the corresponding pixel. For a ray that crosses the voxelised volume, only the part inside the volume is traced. For the part outside the volume, an attenuation $\mu_{i,air} * d_{air}$ can be added in the summation over the attenuation coefficients inside the voxels of the volume. Furthermore, the step size d_j can be chosen to be much smaller than the voxel size. This is a way to correct for the partial volume effect that can be encountered when applying the ray-tracing method without having to calculate a weight factor for each voxel

during each step. The step size d_j is kept constant during the ray-tracing inside the voxelised volume. Doing this also reduces the computation time because fewer calculations have to be performed. Thus, during the ray-tracing, only the attenuation coefficients encountered during each step are added and they are afterwards multiplied by the step size.

If a ray does not cross the voxelised volume, then the equation is simplified and calculated as follows:

$$N_{d,i} = \frac{P\Delta t}{UQ_{e^-}} \Delta\Omega_{pixel} \Delta E_i S_i' D_{eff,i} \exp(-\mu_{i,air} d_{air}) \tag{5.10}$$

in which d_{air} is the distance from the source to the detector pixel and $\mu_{i,air}$ the attenuation coefficient of air in energy bin i.

Beam Filtration

Just as in a real scan, multiple filters can be added during the simulation of a radiography. Before an actual simulation is performed, the X-ray spectrum can be modified:

$$S_i' = S_i \prod_{j=1}^{l} \exp(-\mu_{ij} d_j), \tag{5.11}$$

with l the number of added filters, and S_i and $S_i^{'}$ representing the unfiltered and filtered spectrum, respectively. Both spectra are expressed as the number of photons per simulated electron per Steradian per keV. The simulation of the spectra S_i in these units is described in section 4.2.

Binning of X-ray Spectra

The simulated spectra shown in section 4.2 are subdivided into energy bins of 50 eV. This energy resolution is sufficiently small to model the peaks originating from characteristic radiation in the spectrum. On the other hand, the continuum can be reproduced with a much larger bin size without the loss of too much spectral information. Therefore, the number of energy bins can be greatly reduced, which results in a significantly shorter computation time. Figure 5.3 shows an example of such a rebinned spectrum, where the number of energy bins (and thus computation time) is reduced by a factor of 20 while still modelling the spectrum accurately. In this rebinned spectrum, not all energy bins have the same width, which is taken into account in Equation 5.9. In the rebinning process, the locations of all edges (K and L) of target material, filtration material, sample material and scintillator material are taken into account to define the limits of the energy bins. This way, the shape of the original spectrum is preserved as well as possible and in this way,

during the calculation the changes in attenuation in a sample or efficiency in the detector will not change drastically in one particular energy bin.

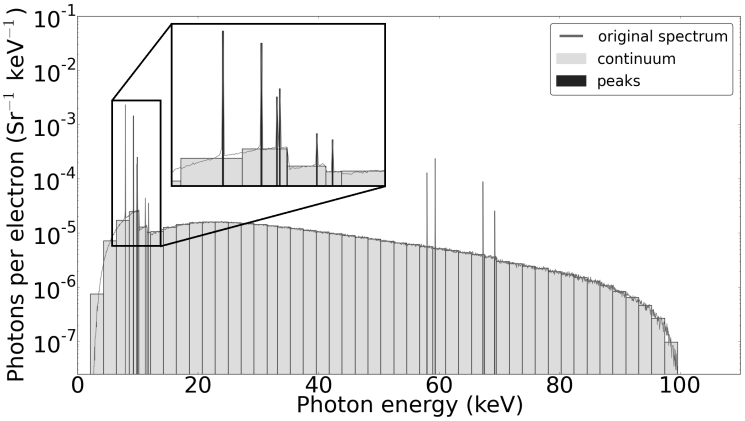

Figure 5.3: Example of a binned spectrum with variable bin size. [1]

GPU-implementation

Over the last decade, GPU development has boomed, mostly due to the gaming industry. In Figure 5.4, the computing power of these devices is compared with central processing units (CPUs) in terms of gigaflops (floating point calculations) per second. In recent years, the gap between these has increased in favour of GPUs. The latest generation of GPUs contain between 2000 and 3000 processing cores combined with 8 to 12 Gb RAM on a single card, which provides a massive amount of parallel processing power. On the other hand, high-end CPUs reach up to 24 cores and are currently available at a price around seven times as expensive as the high-end GPUs. Further, the frequency of CPUs is only up to two times as fast as the newest GPU processing cores. This makes GPUs the preferred devices for parallel computing, which means that many calculations can be performed independently of each other, as in image processing (the primary use for GPUs).

In 2007, Nvidia [14] released its Compute Unified Device Architecture (CUDA), which allows parallel programming on GPUs using a programming interface in C. Further, CUDA is the standard included with each GPU developed by Nvidia, which means it is available on every desktop, laptop or mobile device with an Nvidia GPU. The C implementation also makes it very accessible for programmers. The main component of the simulation program is written in CUDA and C++, and the GUI is implemented with the use of Qt [15].

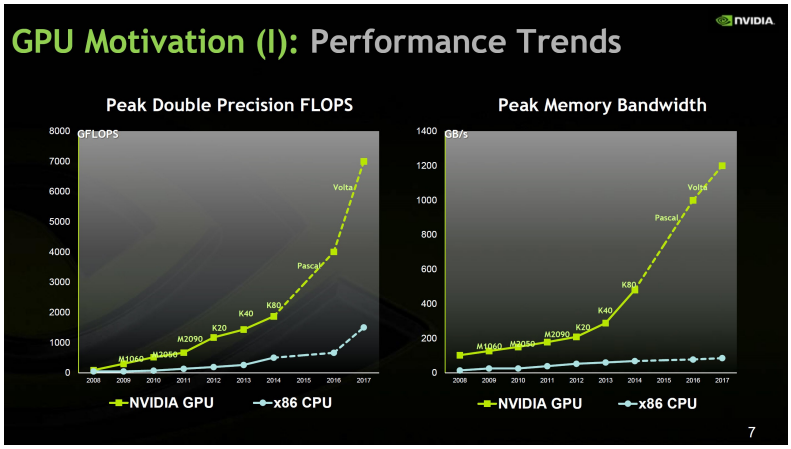

Figure 5.4: Comparison in performance between recent GPUs and CPUs. [16]

5.3 Arion

This section provides an overview of the developed program Arion and its components. In addition to the projection simulator component itself, there are three other components. The first is the Material Creator, which can be used to create tables with the attenuation coefficients of certain materials, compositions or solutions. The second component is the Setup Optimiser, which can be used to calculate an estimation of the transmission coefficients of slabs of materials and can determine optimal signal- and contrast-to-noise ratios. The third component is the Image Handler, which can be used to perform standard image operations such as adding, subtracting, cropping, shifting or rotating images, but it also includes methods to create a (secondary) spot effect on simulated images, create blurring due to the MTF of the detector on simulated images or perform a beam hardening correction.

5.3.1 Material Creator

The Material Creator allows the user to calculate the mass attenuation coefficient of a certain molecule, mixture or solution based on the mass attenuation coefficients of the elements in the periodic table. All mass attenuation coefficients of elements with atomic numbers from 1 to 100 are stored in the program in an energy range from 1 to 500 keV. These coefficients are used by the program to create new tables for the attenuation coefficients of the materials requested by the user. A new material defined by the user can either be defined by a chemical formula or by the mass fractions of atoms in the material. For a solution, the amount of solvent and solute can be entered, and the energy dependency of the mass attenua-

tion coefficients for the solution and the density of the solution can be calculated. The density can always be changed by the user as it is being calculated as if there were no increase in the volume of the solvent. For solutions where the solute is a substantial fraction of the solvent, the calculated density is incorrect and should be entered by the user.

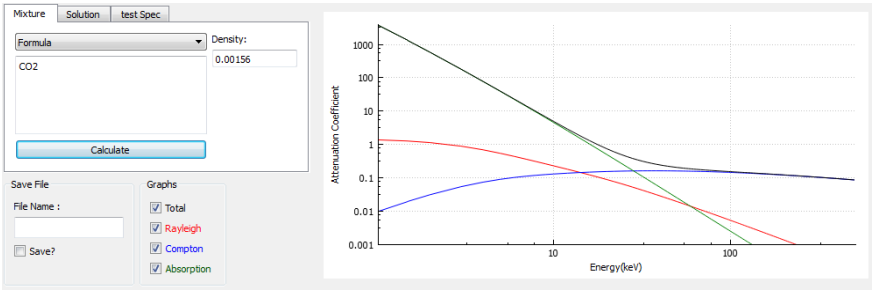

Figure 5.5: Graphical user interface of the Material Creator. Attenuation data for mixtures or solutions can easily be created.

5.3.2 Setup Optimiser

The Setup Optimiser was the predecessor of the projection simulator but can still be used for a broad range of applications. The basic principles of this optimiser are the same as for the projection simulator, and it can be used to calculate energy transmission and energy deposited in the detector through certain slabs of materials by using Equation 5.5, in which $N_{d,i}$ is calculated by using Equation 5.9. The transmission values of an X-ray beam through a slab can be used to provide the user with useful information such as the maximum dose that can be deposited in a sample, the amount of beam hardening, beam hardening profiles and optimised scanning parameters to minimise beam hardening while maintaining an acceptable signal-to-noise ratio (SNR) or contrast-to-noise ratio (CNR). The features of the Setup Optimiser are discussed below. Results from the Setup Optimiser are discussed in section 5.4.

Before discussing all possible features of the Setup Optimiser, the input parameters are mentioned here. As can be seen in Figure 5.6, the components present in a real CT scanner can be found in the GUI of the application. A tube, filter, detector and sample can be chosen.

A tube can be selected in the source box. For each tube, the modelled and simulated tube spectra discussed in section 4.2 are available. Further, a tube voltage and tube power/current can be set for a selected tube. Once the tube voltage has

been defined, either the power or current can be set by the user, as they are dependent on each other. One or more materials can be chosen as filters, which are characterised by material, density and thickness. A detector and its parameters can also be defined. Just as for the tubes, the detectors modelled and simulated in section 4.3 are available. The detectors' binning mode and integration time can be set. Two other parameters, linearity and bit depth, are always the same for a certain detector and can be disregarded in the Setup Optimiser, as they are only needed when calculating an output (greyscale) image. They are used by the projection simulator because the Setup Optimiser only calculates deposited energies or their ratios (transmissions). Effects such as collection efficiency and conversion from visible light to charges in the detector are thus not taken into account. In the projection simulator these effects are bundled in an empirical constant, called linearity, which converts the deposited energy to a greyvalue. Finally, a sample can be added. This sample is defined in a similar way as the filters, by material, density and thickness. Again, multiple slabs can be placed one after another. When the user is only interested in calculating an energy deposition in a detector pixel, it does not matter if a slab is added as a filter or as a sample, as these are treated in the same manner. On the other hand, when one is interested in quantities such as beam hardening or transmission values, it is very important to make a distinction between the filter and sample, as the filter is used during the calculation of the flat field and, logically, the sample is not. The main features of the Setup Optimiser are discussed below.

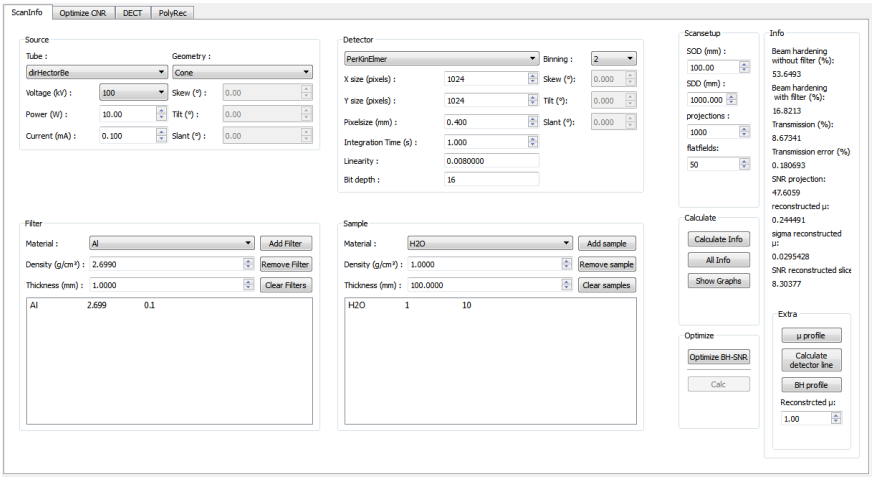

Figure 5.6: Graphical user interface of the Setup Optimiser.

All information

All information for a spectrum that travels through a certain amount of material for a certain scanner setting can be obtained (Fig. 5.7). All scan parameters are listed at the top of the information file. Furthermore, all properties are calculated for the filtered and unfiltered spectrum, detected spectrum without sample and detected spectrum with sample. The emitted spectrum is the spectrum emitted by the source as it would be seen by an ideal detector that detects all photons and all their energy. The three most useful parameters are the detected transmission through a material, the beam hardening factor and the estimate of the reconstructed attenuation coefficient.

The transmission value of a detected spectrum through a number of slabs is given by

$$T = \frac{E}{E_0}, \tag{5.12}$$

where E and E_0 are the energy detected by the central pixel of the detector with and without a sample, respectively. The error for this transmission value is given by

$$\sigma_T = \frac{1}{E_0}\sqrt{\sigma_E^2 + \frac{E^2}{E_0^2}\sigma_{E_0}^2}. \tag{5.13}$$

σ_E and σ_{E_0} are calculated using Equation 5.7. These errors represent the pixel-to-pixel variations that can be found in a real scan and are dictated by Poisson statistics. An estimate for the reconstructed attenuation coefficient can then be calculated as

$$\mu = -\frac{1}{d}\ln(T) \tag{5.14}$$

where d is the thickness of the slab, and the error for this calculated value is given by

$$\sigma_\mu = -\frac{1}{d}\frac{\sigma_T}{T}. \tag{5.15}$$

Note that this is the error on the calculated attenuation coefficient μ and does not represent the statistical error on a CT reconstructed μ in a voxel. This is because the error in the reconstructed attenuation coefficient depends on the used reconstruction algorithm and thus how μ is calculated (section 2.2.2). The beam hardening factor for a sample scanned with a certain scanner setup is defined by

$$BH = 100\left(1 - \frac{\mu}{\mu_{BH}}\right), \tag{5.16}$$

in which μ is the calculated reconstructed attenuation coefficient for the sample, and μ_{BH} is a calculated value for the reconstructed attenuation coefficient for an

Scan Parameters		
Source :	Hector_W	
Detector :	PerKinElmer	
Binning :	2	
SOD (mm) :	400	
SDD (mm) :	1000	
Voltage (kV) :	100	
Power (W) :	10	
Integration Time (s) :	1	
# Projections :	1000	
# Flatfields :	50	
Emitted spectrum	**Without Filter**	**With Filter**
Initial average energy (keV) :	34.0498	44.2261
Average energy after sample (keV) :	53.879	54.7972
Transmission through sample (photons) (%) :	6.04205	8.9985
Transmission through sample (dose) (%) :	9.5607	11.1493
Maximum dose in sample (Gy) :	0.163073	0.125733
Detected spectrum without sample		
Average enery of detected photons (keV) :	35.1622	42.3006
Average energy deposited per incident photon (keV) :	23.8116	30.739
Detected X-ray fraction (%) :	0.766668	0.836566
Total detected counts (photons/second/Sr) :	4.05442e+11	2.67313e+11
Total detected dose (keV/second/Sr) :	1.25924e+13	9.82223e+12
Detected spectrum with sample		
Average enery of detected photons (keV) :	51.2019	52.0505
Average energy deposited per incident photon (keV) :	34.9518	35.2909
Detected X-ray fraction (%) :	0.799837	0.794885
Total detected counts (photons/second/Sr) :	2.55568e+10	2.28557e+10
Total detected dose (keV/second/Sr) :	1.1168e+12	1.01474e+12
Important parameters		
Transmission (%) :	8.86882	10.331
Beam hardening factor (%) :	51.2563	15.2557
μ (1/cm) :	0.242263	0.227002

Exit Save Info

Figure 5.7: All information about the spectrum calculated by the Setup Optimiser for 10 cm of H_2O and a filtration of 1 mm of Al.

infinitesimally thin sample. This value for μ_{BH} deviates from μ because the spectrum is altered more as it propagates through more sample material. The more material the X-ray beam travels through, the lower the attenuation, as the mean energy of the spectrum increases. The beam hardening factor is thus a measurement of how much the beam hardens as it travels through a sample. For a cylindrical sample, the largest attenuation coefficient μ_c is measured at the edge of the cylinder,

and the deviation between μ_c and μ is much smaller than the one between μ_{BH} and μ (Fig. 5.8). However, it can be stated that for a sample with a random geometry, the measured attenuation coefficient always lies between μ_{BH} and μ, where μ is calculated by using the largest straight path length through the material.

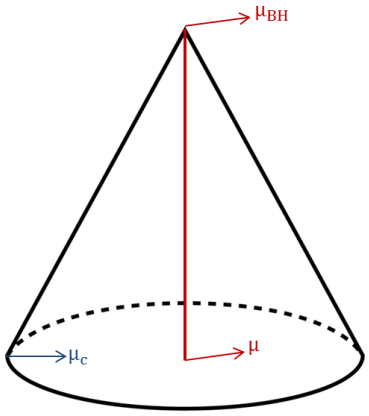

Figure 5.8: Schematic visualisation of how the beam hardening factor is determined.

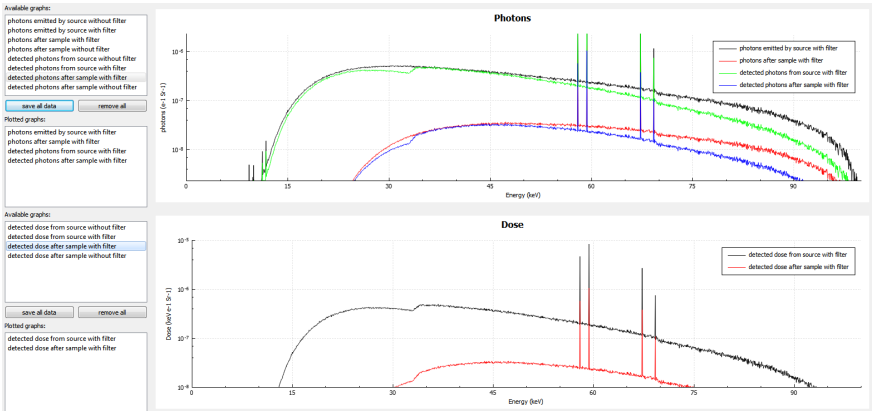

Figure 5.9: Example of graphs generated by the Setup Optimiser that show the photons emitted by the source, the photons detected by the detector and the deposited energy as a function of energy. These graphs can be plotted with or without beam filtration.

Graphs

In addition to all the information described in the previous section, information about altering the spectrum can also be obtained from the Setup Optimiser. Where the average energy of a spectrum is given in the information described above, the graphs provide spectrally dependent information for the user. Beam spectra can be obtained with and without a filter and before and after the sample. In addition, the fraction of these beams' detected photons and their deposited energy can be obtained. This information has proven to be useful when scanner properties need to be optimised. For example, the detector used can have a major effect on detected energy, because when the detector is not sensitive or less sensitive to certain photon energies, it does not matter if they are present in the beam. These detector sensitivities can vary significantly around the K-edges of the scintillator material of which they are made.

Attenuation profiles

Attenuation profiles can also be plotted using this program. In these profiles, an attenuation coefficient and its error are plotted in function of the thickness d of a material. These plotted coefficients correspond with a value found at the centre of a CT reconstruction made of a circular object with diameter d. These graphs represent an estimate for the reconstructed attenuation coefficient on the rotation axis of a cone of this material.

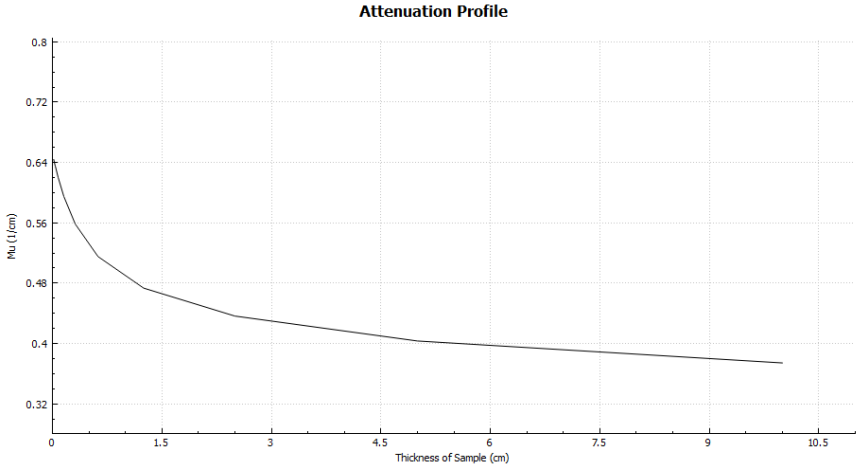

Figure 5.10: Estimated reconstructed linear attenuation coefficients on the rotation axis of a cone C with a certain thickness at HECTOR at 80 kV.

Beam hardening profiles

Most reconstruction algorithms, both analytical and iterative, assume that the radiographic projections used for a 3D reconstruction are taken with a monochromatic beam. They thus assume that the transmission in the normalised projections is proportional to the exponential thickness of the path length through the sample as described by the Beer-Lambert law (Eq. 3.27). As seen for laboratory X-ray CT, however, this cannot be further from the truth. Laboratory-based X-ray tubes produce a polychromatic beam which hardens as it propagates through the sample.

A beam hardening profile can be used to correct a normalised radiographic projection in such a way that the transmission in the projection behaves as if it were taken with a monochromatic source. This profile is created by comparing simulated transmission values through a thickness from zero to the sample thickness with the transmission value through the sample calculated using a constant attenuation μ for all energy bins (Fig. 5.11). The value for this attenuation coefficient can be chosen by the user. The profile is then created by plotting the correction factor, which is the monochromatic transmission divided by the polychromatic transmission, in function of the polychromatic transmission. When a set of radiographic projections is corrected by using this profile, the reconstruction should yield a value μ as set by the user.

The beam hardening profile can thus be used as a look-up table that determines the factor a certain transmission value in a pixel needs to be multiplied by to obtain a 'monochromatic' behaviour. Contrary to conventional beam hardening corrections, which use analytical functions, this profile is determined for a specific scanner and sample. The disadvantage of determining this beam hardening correction based on calculations is that it only takes one material into account. Most samples containing only one material do not really need these corrections, as the difference between the material and the air (for example, in foams) is larger than the deviations between the reconstructed attenuation coefficients in the reconstructed 3D volume of the sample. Nevertheless, this method can be useful in a sample that is dominated by a certain material or in very dense single-material samples, such as copper or lead samples.

Optimising scanner setup

The Setup Optimiser includes two basic methods for optimising X-ray CT scans. The first method can be used for optimising when using samples that consist only of one material, such as foams, or when there is only one material of interest in the sample for the user. The second method optimises the contrast between two certain materials of the user's choice, such as water and butter.

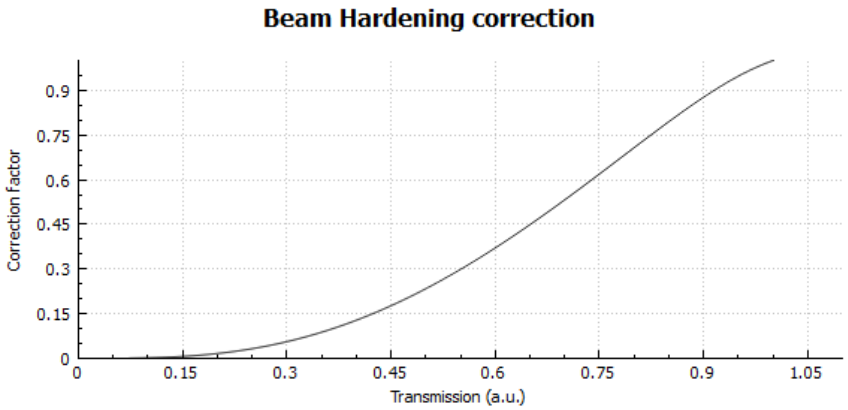

Figure 5.11: Example of a beam hardening correction profile for H_2O.

The first method calculates the SNR of one material present in a sample and the beam hardening factor through the sample. Where the former depends on the material of the sample, the latter is determined by the size of the sample and is calculated by Equation 5.16. The SNR of the material can be determined by

$$SNR = \frac{\mu}{\sigma_\mu}. \tag{5.17}$$

Both parameters, the SNR and Beam Hardening (BH) factor, are calculated for a range of filters and tube voltages for a specific scanner. This way, the optimal scan condition can be determined by the user for a certain sample on a certain scanner.

The second method can be used to optimise the contrast between two materials in a sample and calculates the CNR of these materials. In addition, an estimate for the beam hardening factor is made. The CNR of the materials is determined by

$$CNR = \frac{|\mu_1 - \mu_2|}{\sqrt{\left(\sigma_{\mu_1^2} + \sigma_{\mu_2^2}\right)}}. \tag{5.18}$$

Again, both parameters can be calculated for a range of filters and tube voltages for a certain scanner. Examples of optimising SNR and CNR are shown in section 5.5.

5.3.3 Image Handler

The Image Handler program was developed to handle simulated and real scan data. In addition to some standard image operations, a method for performing beam hardening and spot corrections is included in this tool. Note that the term

spot correction is used here to describe the contribution of the secondary spot of a tube to a simulated radiograph.

Standard image operations

Standard image operations such as subtracting, adding, dividing and multiplying images can be performed. Furthermore, it is possible to shift and rotate images, which is particularly useful when two reconstructed volumes need to be compared, for example for dual energy methods/techniques. Fast methods to resize/crop images and a procedure to normalise scan data are included as well. All these operations can either be performed on single images or on a complete directory containing images.

Beam hardening correction

This tool implements a method to perform a beam hardening correction with the beam hardening profile described in section 5.3.2. The correction curve and normalised radiography directory can be chosen by the user, and the correction is performed automatically.

Spot correction

The last method included in this tool lets the user perform a spot correction or MTF correction. The intensity of each pixel in a radiograph can be corrected using the following equation, which is a convolution of the image and correction functions:

$$I(r) = \sum_{x'=-n/2}^{n/2} \sum_{y'=-n/2}^{n/2} I(r')C(r-r'). \tag{5.19}$$

with $r = \sqrt{x^2 + y^2}$ and $r' = \sqrt{x'^2 + y'^2}$, n the size of the kernel and x and y the pixel coordinates of the radiograph. The correction function $C(r)$ can be either a spot correction, as described in section 4.2 for a secondary spot correction, or the LSF fitted as in section 4.3 for an MTF correction.

5.3.4 Projection Simulator

The Projection Simulator is the core of Arion and consists of two fundamental parts. The first is the Phantom Creator, and the second is the simulation tool itself. The Phantom Creator allows a user to create a virtual 3D phantom that can later be used for the simulation of radiographs.

Phantom Creator

The Phantom Creator lets a user create a virtual 3D phantom. Using one available method, a phantom can be created from a single bitmap file. This file can be stacked as often as the user wants to create a 3D model of the sample. Each colour in the bitmap can be associated with a material with a certain density. A phantom can also be created from a complete stack of different bitmaps that can be loaded into the program instead of stacking one file multiple times. Again, each colour can be associated with a specific material. Using another possible method, a 3D phantom can be created from 'scratch'. The user starts with an empty volume of certain dimensions filled with air and can add different geometrical shapes-cuboids, cubes, cylinders and spheres-into the volume. Each of these shapes represents a material with a certain density. Once the phantom is created, it is saved as a .phantom file, which can later be used by the simulator.

CT-simulations

Figure 5.12 shows a flowchart of the different steps that need to be taken to accomplish a CT scan simulation. The first step, 'Phantom setup', can be performed by using the Phantom Creator described above. The other steps are implemented in the GUI of the Projection Simulator.

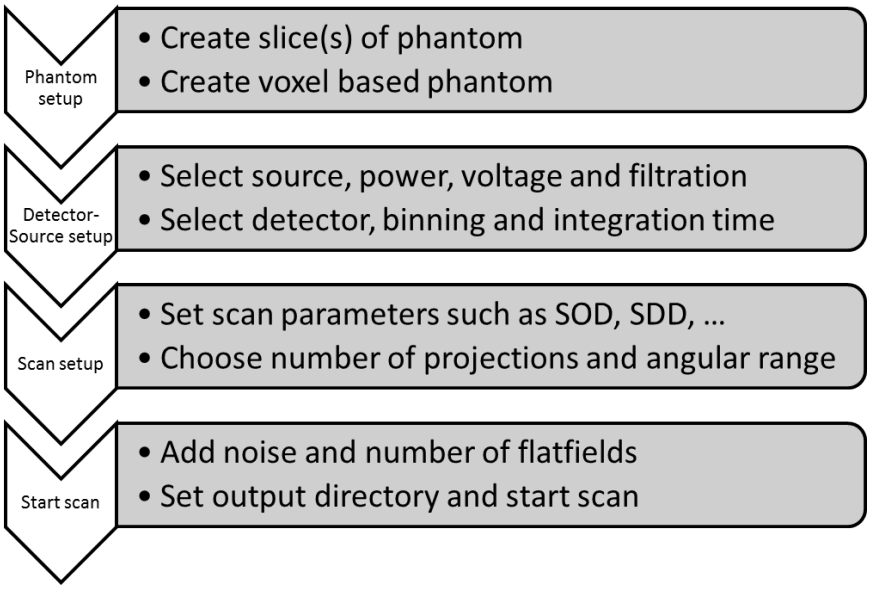

Figure 5.12: Flowchart of the different processes executed to accomplish a CT scan simulation. [1]

When performing a simulation, some standard CT geometries can be selected. The user can choose from the most-used methods, circular and helical CT, but a more exotic conveyer belt geometry is included as well [13]. Besides these three pre-defined geometries, a random CT trajectory can also be performed. In this case, the user needs to provide a data file with all the positions and orientations of the tube, sample and detector for each radiography that needs to be simulated.

Figure 5.13 shows the interface of the simulation part of Arion. A tube and detector can be selected from the dropdown menu, which contains all simulated tubes and detectors described in chapter 4. For both components, the source and detector, a rotation can be added but is kept at zero for all values in all of the pre-defined setups. Further, the power and voltage of the tube can be chosen by the user, as can the binning and integration time of the detector. A virtual phantom can be loaded (and rotated) alongside these components. Furthermore, additional filtration can be chosen, and the scan parameters such as the source object distance and source detector distance can be set. For the helical and conveyer belt setup, the pitch and number of turns can also be set as input parameters. Finally, a radiographic projection can be viewed in the output window as a preview to make sure all parameters are correct. In addition, the user can choose to add noise, calculated as described in section 5.2, and the number of flatfields to be simulated. Rayleigh scattering can either be included or not during the simulation. For high X-ray energies, Rayleigh scattering occurs forward and without a loss of energy, and the scattered photons are thus not removed from the X-ray beam.

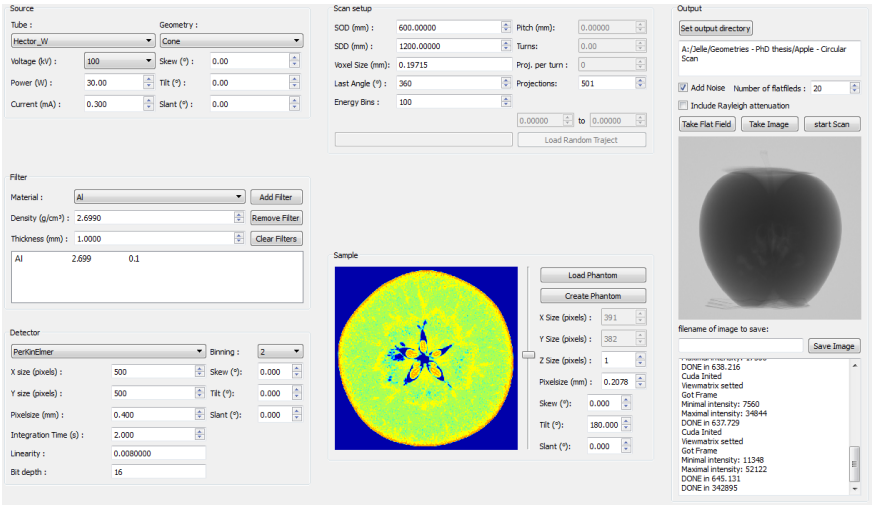

Figure 5.13: Graphical user interface for a circular scan.

Figure 5.14 shows simulated scans of the three pre-defined geometries in Arion. Different positions during the acquisition of the circular, helical and conveyer belt scans are shown.

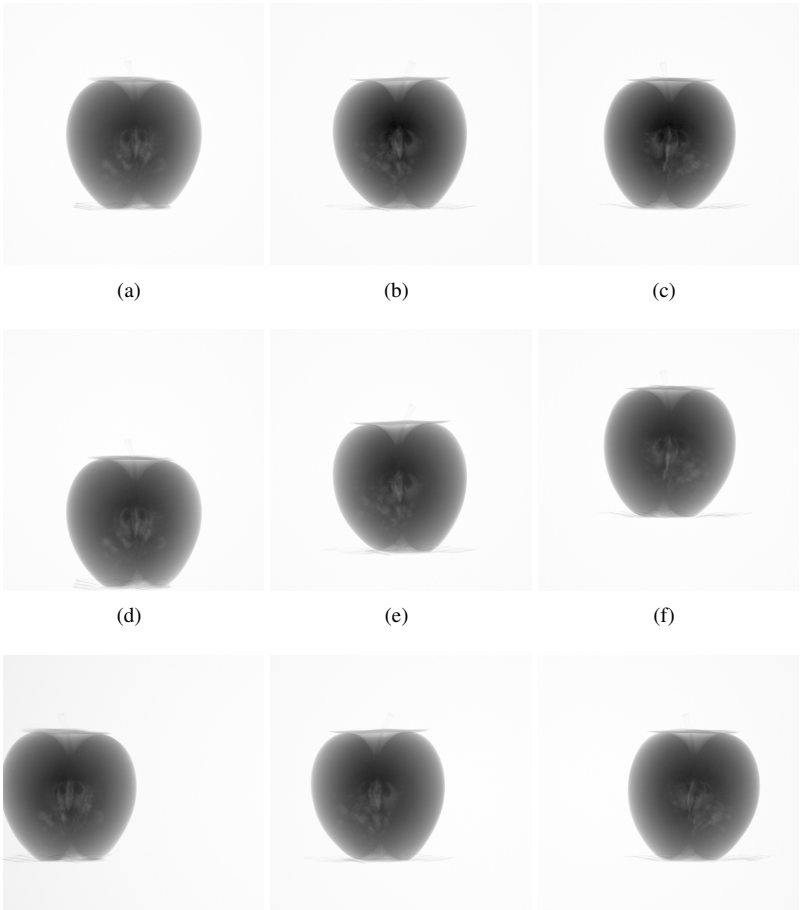

(a) (b) (c)

(d) (e) (f)

(g) (h) (i)

Figure 5.14: Simulated scans of a circular geometry (top row), a helical geometry (middle row) and a conveyer belt geometry (bottom row). For each simulation, a projection is shown at the start (a, d, g), after one-third of the full scan (b, e, h) and after two-thirds of the full scan (c, f, i).

5.4 Results - Comparing simulated and real data

This section compares real and simulated data for the different scan setups present at UGCT: Nanowood, HECTOR and Medusa.

Comparing line profiles

Comparing simulated and real data can easily be done visually, but sometimes this is not sufficient, and a more quantitative way to compare two datasets is needed. This is especially true when a best simulation technique must be determined for simulating the secondary spot, for example. Comparing real r_i and simulated s_i data points can be done using the following equation:

$$ERR = \frac{100}{N} \sum_{i}^{N} \frac{|r_i - s_i|}{r_i}, \tag{5.20}$$

in which N is the number of data points (pixels or voxels). This equation represents the mean deviation of the simulation from the real data as a percentage and is thus a measurement for the simulated data correctness. Note that if the noise signal on the real or simulated data is larger than the deviation between the two sets, this error function actually returns a measurement of the noise level in the data.

Phantoms

Two samples were scanned at different tube voltages in each scanner: an aluminium (Al) sphere with a diameter of 6 mm and a polyoxymethylene (POM) cylinder with a diameter of 1 cm. A virtual phantom was created for these two samples and used to perform the simulations described in this section. These two samples were chosen to represent the bulk of materials present in samples scanned at UGCT and in other research groups or industrial environments. The POM cylinder is a representative sample for organic samples, while the Al sphere represents light metals or geological samples that usually contain light minerals. For the ease of reading, these two samples are referred to as the Al sphere and POM cylinder in this work. Line profiles of the radiographies and reconstructed slices of the simulated and real scans can be found in appendix B.

5.4.1 Radiographies

Transmission values obtained at Nanowood

In order to compare measured and simulated transmission values at Nanowood, two types of tests were performed. For both tests, the directional tube was used in combination with the Varian detector. The first test measured a transmission through a set of filters with different thicknesses. This test was performed at a tube

voltage of 120 kV and a tube power of 3.6 W. The source detector distance was 663.1 mm, and an integration time of 2 s was used. For the second test, radiographs of the Al sphere and POM cylinder were taken at different tube voltages (30 kV, 60 kV, 90 kV and 120 kV). This was done with a tube power of 12 W, an SOD of 19.94 mm and an SDD of 800 mm, and the detector was set at binning 2 with an integration time of 0.5 s.

Table 5.1 shows the measured and simulated transmission values through several filters with different thicknesses for the Nanowood scanner. These filters were placed between the X-ray tube and detector. Projection images of 512 x 512 pixels were obtained. A maximum deviation between the measured and simulated transmission of 1.8% was obtained. It is clear that the deviation is not systematic, as both negative and positive values were found. Furthermore, noise levels were also predicted quite accurately.

Section B.1.1 shows figures that demonstrate the line profiles of radiographs of the Al sphere and the POM cylinder for the real and simulated data. Table 5.2 shows the deviation between the line profiles in the figures. A significant difference in transmission values for the Al sphere only occurred at tube voltages of 30 and 60 kV. All other line profiles correspond quite well in terms of transmission and noise.

Table 5.1: Measured (M) and simulated (S) transmission values and corresponding standard deviations (σ_M and σ_S) at a tube voltage of 120 kV at Nanowood. Deviations (Dev) between real and simulated data are also listed.

Filter	M(%)	S(%)	Dev(%)	σ_M(%)	σ_S(%)
50 μm W	42.3	41.6	-1.7	0.42	0.46
30 μm Mo	70.6	69.3	-1.8	0.55	0.63
150 μm Al	95.5	95.6	0.1	0.34	0.77
68 μm Cu	70.8	71.9	1.6	0.74	0.65
136 μm Cu	58.0	59.0	1.7	0.72	0.58
272 μm Cu	43.7	44.0	0.7	0.61	0.48
544 μm Cu	28.8	28.5	-1.0	0.48	0.38

Transmission values obtained at HECTOR

Two types of tests were performed at HECTOR to compare real and simulated data. First, transmission values through filters were measured and simulated at three different tube voltages (100 kV, 140 kV and 160 kV) at a tube power of 10 W. For this test, the detector was placed at a distance of 1166.7 mm from the source and was used in binning 4 with an integration time of 1 s. During the second test,

Table 5.2: The deviation between the line profiles for Nanowood of the Al sphere and POM cylinder calculated according to Equation 5.20.

Profile	Error (%)
Al sphere @ 30 kV	55.3
Al sphere @ 60 kV	9.60
Al sphere @ 90 kV	3.43
Al sphere @ 120 kV	2.05
POM cylinder @ 30 kV	4.39
POM cylinder @ 60 kV	2.23
POM cylinder @ 90 kV	1.78
POM cylinder @ 120 kV	1.28

radiographs of the Al sphere and POM cylinder were taken at tube voltages ranging from 30 kV to 210 kV in steps of 30 kV at a tube power of 10 W. The samples were placed at an SOD of 23.67 mm (Al sphere) and 37 mm (POM cylinder), and the detector was at an SDD of 1166.7 mm. The detector was set in binning 4 with an integration time of 1 s.

Table 5.3 shows the transmission through different slabs of material in the real and simulated setup at 100 kV. The noise in the measured images is given over a large area σ_M and a small area $\sigma_{M_{sa}}$ of the radiography. A large difference was found between these two because a large heeling effect was present in the directional tube mounted on HECTOR. Thus, the larger area seemingly contains more noise, even though the observed signal is actually a variation of intensity along the detector (Fig. 5.15). A more correct estimate of the pixel-to-pixel variation in the detector is therefore given by the noise measured in a small central area-50 $\times$ 50 pixels-on the detector. This large heeling effect can be a problem in radiographs, but does not cause much trouble when performing a complete CT scan, as the object is turned around 360° and a flatfield correction is performed. Tables 5.4 and 5.5 present the results of the measurements at 140 kV and 160 kV, respectively.

Table 5.3: Measured (M) and simulated (S) transmission values at 100 kV.

Filter	M(%)	S(%)	Dev(%)	σ_M(%)	$\sigma_{M_{sa}}$(%)	σ_S(%)
50 μm W	39.01	38.18	-2.12	0.93	0.15	0.18
30 μm Mo	68.89	64.45	-6.44	0.64	0.11	0.22
150 μm Al	94.33	94.49	0.17	0.32	0.11	0.25
100 μm Pb	33.09	30.57	-7.53	0.77	0.23	0.16
68 μm Cu	66.85	66.54	-0.47	1.06	0.28	0.22
136 μm Cu	53.83	52.88	-1.77	1.08	0.23	0.21
272 μm Cu	39.19	37.89	-3.33	0.85	0.16	0.18
544 μm Cu	24.42	23.23	-4.88	0.57	0.13	0.15

Table 5.4: Measured (M) and simulated (S) transmission values 140 kV

Filter	M(%)	S(%)	Dev(%)	$\sigma_M(\%)$	$\sigma_{M_{sa}}(\%)$	$\sigma_S(\%)$
50 μm W	49.65	46.83	-5.67	0.90	0.14	0.19
30 μm Mo	77.65	72.62	-6.48	0.80	0.13	0.23
150 μm Al	96.98	96.34	-0.66	0.20	0.14	0.25
100 μm Pb	43.25	39.44	-8.82	0.89	0.28	0.18
68 μm Cu	78.45	75.46	-3.81	1.05	0.27	0.23
136 μm Cu	64.82	63.58	-1.91	1.27	0.25	0.22
272 μm Cu	52.21	49.13	-5.89	0.91	0.20	0.20
544 μm Cu	35.62	33.31	-6.49	0.85	0.17	0.17

Table 5.5: Measured (M) and simulated (S) transmission values 160 kV

Filter	M(%)	S(%)	Dev(%)	$\sigma_M(\%)$	$\sigma_{M_{sa}}(\%)$	$\sigma_S(\%)$
50 μm W	49.72	49.67	-0.10	0.81	0.13	0.19
30 μm Mo	78.13	75.04	-3.95	0.63	0.14	0.23
150 μm Al	97.28	96.82	-0.47	0.21	0.17	0.25
100 μm Pb	44.36	42.18	-4.92	0.72	0.28	0.18
68 μm Cu	77.94	78.02	0.10	0.74	0.25	0.23
136 μm Cu	67.59	66.72	-1.28	0.87	0.23	0.22
272 μm Cu	53.58	52.54	-1.95	0.84	0.20	0.20
544 μm Cu	37.62	36.48	-3.04	0.74	0.16	0.17

Table 5.6: The deviation between the line profiles for HECTOR of the Al sphere and POM cylinder calculated according to Equation 5.20.

Profile	Error (%)
Al sphere @ 30 kV	23.84
Al sphere @ 60 kV	5.47
Al sphere @ 90 kV	1.89
Al sphere @ 120 kV	1.69
Al sphere @ 150 kV	1.45
Al sphere @ 180 kV	1.40
Al sphere @ 210 kV	1.60
POM cylinder @ 30 kV	5.07
POM cylinder @ 60 kV	1.40
POM cylinder @ 90 kV	0.87
POM cylinder @ 120 kV	0.72
POM cylinder @ 150 kV	0.64
POM cylinder @ 180 kV	0.60
POM cylinder @ 210 kV	0.63

Section B.1.2 shows figures with the line profiles of a radiograph of the Al sphere and the POM cylinder for the real and simulated data at HECTOR. The deviations between the real and simulated line profiles are shown in table 5.6. The

simulations and real profiles are in general in good agreement with each other. The effect of the heeling can be clearly seen for both the sphere and cylinder only at low tube voltages, where there is a slight deviation between the simulated and real line profiles on the right side of the detector. The photon beam is harder on this side, and thus a larger transmission through the same material thickness is measured, compared to the softer beam on the left side of the detector. As the tube voltage increases, the difference in hardness between the beams becomes smaller, as higher energy photons can more easily escape the directional target of the tube. Nevertheless, traces of the heel effect can still be seen for the Al sphere at the higher tube voltages of 120 kV and 180 kV.

Heel effect at HECTOR

Figure 5.15 shows the normalised radiographic images of four slabs of materials: 50 μm W, 150 μm Al, 68 μm Cu and 136 μm Cu. The heel effect can be seen in the radiographs. The spectra emitted towards the right side of the detector are harder and will cause a higher transmission through the filters. A line profile of these radiographs is shown in Figure 5.16. The simulated profiles, which include a heeling correction as described in section 4.2, are shown next to the measured profiles.

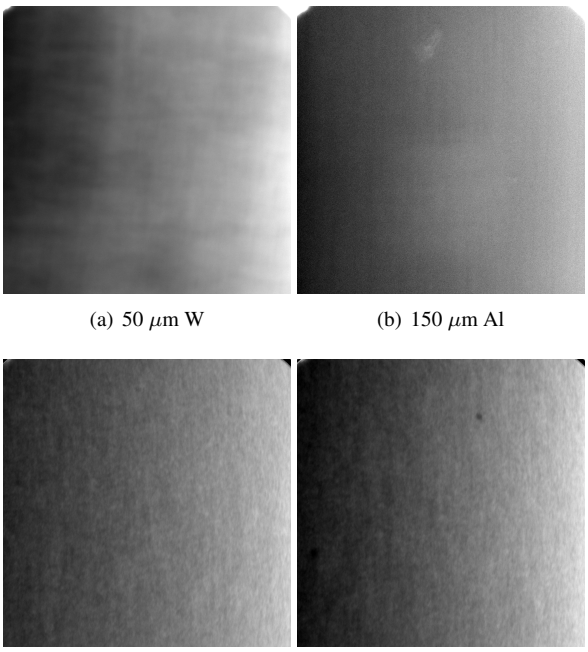

(a) 50 μm W (b) 150 μm Al

(c) 68 μm Cu (d) 136 μm Cu

Figure 5.15: Normalised radiographs of four different filters taken at HECTOR at a tube voltage of 100 kV. The transmission measured at the right side of the detector is clearly higher than the one measured at the left side.

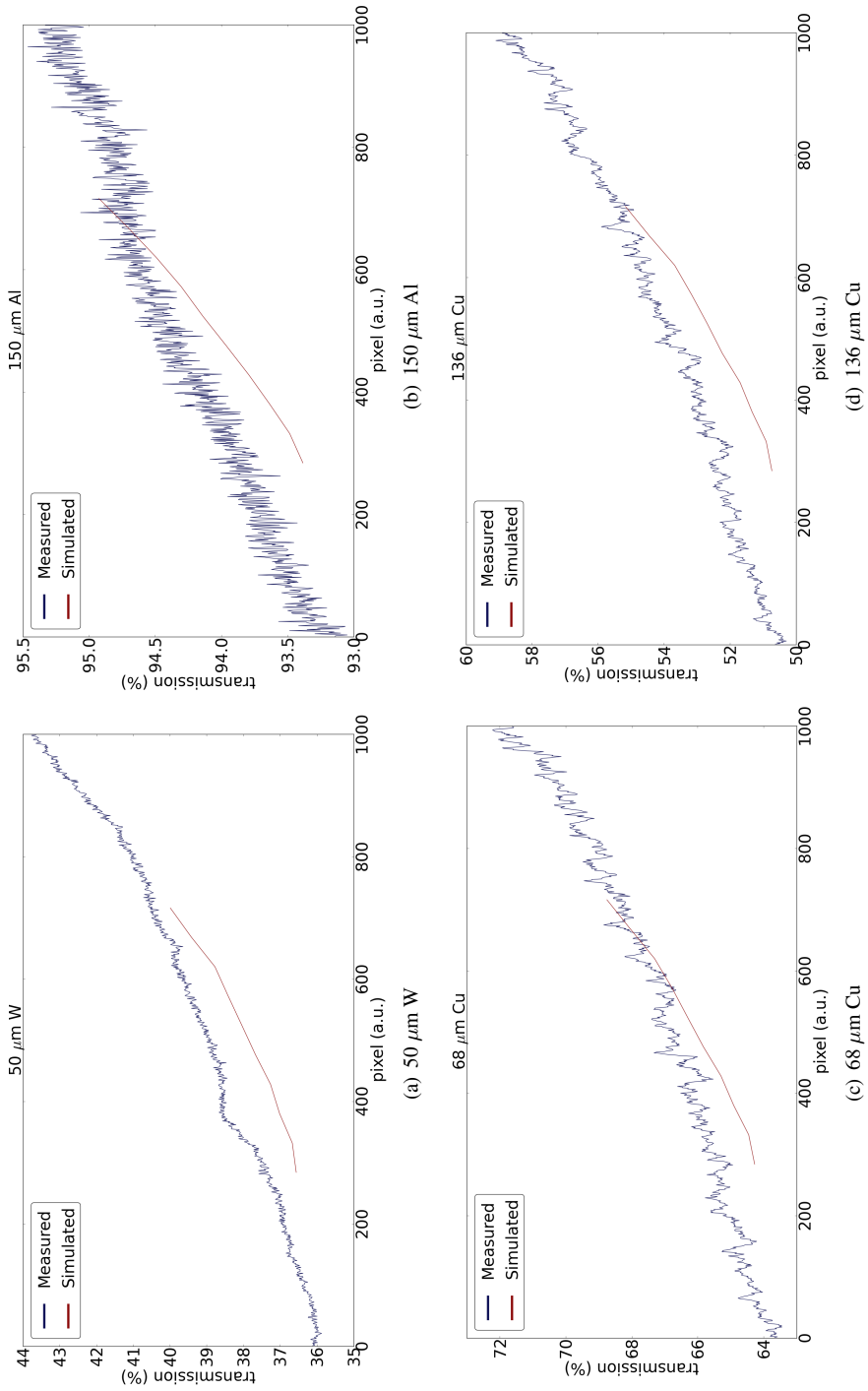

(a) 50 μm W (b) 150 μm Al

(c) 68 μm Cu (d) 136 μm Cu

Figure 5.16: Comparison between line profiles of the real and simulated transmission through a filter. The heel effect is very prominent in both real and simulated data.

Transmission values obtained at Medusa

Figure 5.17(a) shows a radiographic image of the Al sphere taken at Medusa at 90 kV with a tube power of 9 W. A 5 μm tungsten target was used. The SOD was 206.6 mm, and the SDD was 866.7 mm. The detector was set to binning 2 and an integration time of 1 s. A halo is clearly visible around the sphere. This halo was induced by the secondary spot present in the Medusa tube [17]. Figure 5.17(b) shows a simulated radiographic image without any spot correction. The term spot correction is used here for introducing a secondary spot effect in the simulated images. In Figure 5.17(c), the Gaussian spot correction described in section 4.2 is applied. Note that the model fitted to the simulated data in section 4.2 is obtained with a target thickness of 3 μm. Nevertheless, this can be used as a spot correction because the actual target thickness of the transmission tube is unknown and will vary between 1 μm and 5 μm. This is because after prolonged use the target will wear down and holes will appear in the surface of the target material.

The simulation is obtained by splitting the initial spectra generated in the tube into two parts. The first part originates in the primary spot, while the second spectrum originates in the secondary spot. A simulation is then performed by using each of the two spectra. Then, the radiographs obtained using the spectrum of the secondary spot are corrected as described by Equation 5.19. Then the corrected radiographs are added to those obtained using the primary spot and normalised. The simulated halo shows a similar behaviour to the real one. The images shown have the same dimensions and colour scale.

Figure 5.18 shows the transmission along a line profile for the different fits described in section 4.2. Although the corrections show an improvement over the simulated images without correction, the fit is still not optimal. Better fits are obtained if only a fraction of the corrected secondary spot image is added to the original primary spot. Table 5.7 lists the deviation between the simulated and real transmission profiles for the three fits to the secondary spot. Additionally, a smaller fraction of the simulated secondary spot is taken into account for the Gaussian correction.

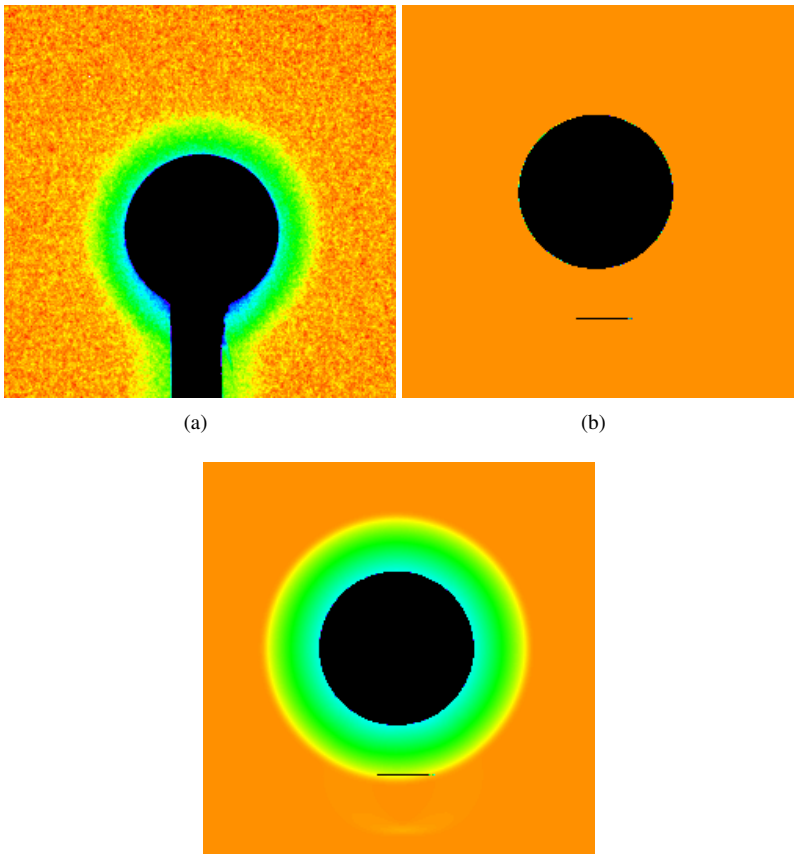

(a) (b)

(c)

Figure 5.17: The halo caused by the secondary spot is clearly visible in the real transmission image (a). The simulated transmission without (b) and with (c) spot correction is also shown. The black vertical artefact in (b) and (c) is from the holder of the real sample.

Table 5.7: Deviation between the simulated and real transmission data for the performed corrections calculated according to Equation 5.20.

Correction	Deviation from real scan (%)
no corr	7.74
constant	3.96
gaussian	2.94
polynomial	3.60
20% gaussian	2.66
50% gaussian	2.35

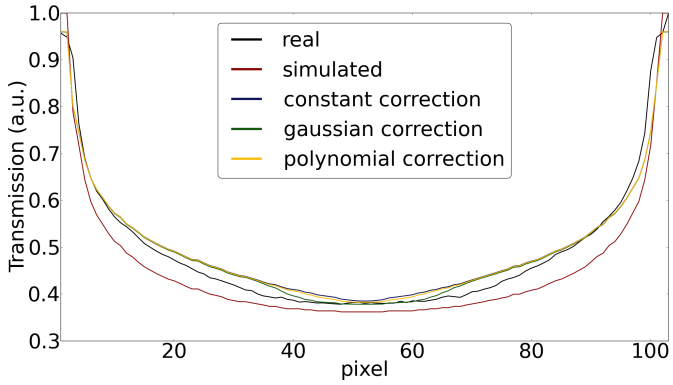

(a)

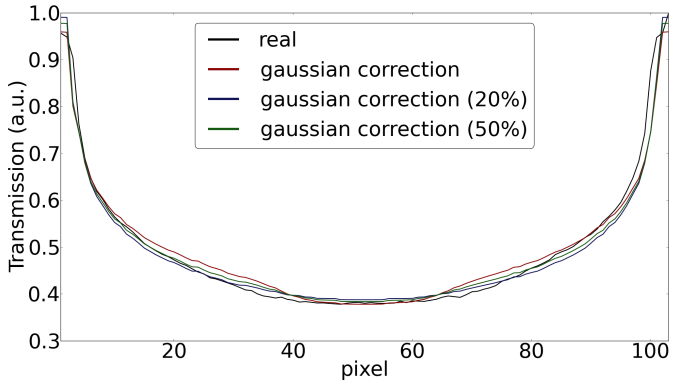

(b)

Figure 5.18: Transmission profiles of the measured and simulated secondary spot correction for different profiles (a) and with only a fraction of the gaussian correction applied (b).

5.4.2 CT scans

This section discusses the results of the reconstructed CT scans. For Nanowood, the sample described in [1] is also examined.

CT scans obtained at Nanowood

Section B.2.1 shows figures of line profiles of a reconstructed slice of a real and simulated CT scan of the Al sphere and POM cylinder at tube voltages of 30, 60, 90 and 120 kV. The scanner parameters were the same as described for the transmission profiles. A rotation of 360° was performed during the CT scan, and 901 projection images were obtained. The measured and simulated linear attenuation coefficient at the centre of each reconstructed slice is shown in Table 5.8. There is a large difference in the noise calculated by the simulations and measured in the real scans. This is probably because the MTF of the detector was not taken into account during the simulation process. The MTF causes smoothing in the projection images and reduces the noise in the final reconstructed volume. Of course, this smoothing also introduces a loss in resolution in these CT volumes. The influence of the MTF on the simulation is discussed below for the results obtained with HECTOR.

Table 5.8: Measured (M) and simulated (S) linear attenuation coefficients for different samples at different energies at Nanowood.

Filter	μ_M(1/cm)	μ_S(1/cm)	σ_{μ_M}	σ_{μ_S}
Al sphere @ 30 kV	3.59	6.03	0.42	0.33
Al sphere @ 60 kV	1.996	2.190	0.024	0.045
Al sphere @ 90 kV	1.334	1.423	0.021	0.044
Al sphere @ 120 kV	1.083	1.132	0.015	0.040
POM cylinder @ 30 kV	1.04	0.97	0.16	0.14
POM cylinder @ 60 kV	0.556	0.507	0.022	0.055
POM cylinder @ 90 kV	0.425	0.386	0.024	0.062
POM cylinder @ 120 kV	0.367	0.337	0.023	0.061

Table 5.9 presents the deviation between the line profiles of the reconstructed slices of the Al sphere and POM cylinder. The deviations are rather high, especially for the cylinder. This deviation is, however, caused by the large noise level in the scans. For the simulated data, the percentage of noise compared to the reconstructed attenuation coefficient is of the same magnitude as the error between both profiles.

Furthermore, a cylindrical phantom filled with water and containing five tubes (Fig. 5.19) with different aqueous solutions was used to test the performance of

Table 5.9: The deviation between the line profiles of the reconstructed slices for Nanowood of the Al sphere and POM cylinder calculated based on Equation 5.20.

Profile	Error (%)
Al Sphere @ 30 kV	45.36
Al Sphere @ 60 kV	9.07
Al Sphere @ 90 kV	5.16
Al Sphere @ 120 kV	4.00
POM cylinder @ 30 kV	15.80
POM cylinder @ 60 kV	10.91
POM cylinder @ 90 kV	15.32
POM cylinder @ 120 kV	15.14

the projection simulator. The solutions were barium chlorate, potassium bromide, calcium chloride, lead nitrate and phosphotungstic acid (PTA). For this scan, the directional tube mounted on Nanowood and the Varian detector were used. The mass fractions and densities of the used solutions are listed in Table 5.10. The phantom was scanned at a tube voltage of 100 kV with a tube power of 16 W. The beam was filtered with an aluminium filter of 0.45 mm thickness. The SOD and SDD were 287.6 and 689.9 mm, respectively. The detector was set to binning 2 with an integration time of 0.8 s.

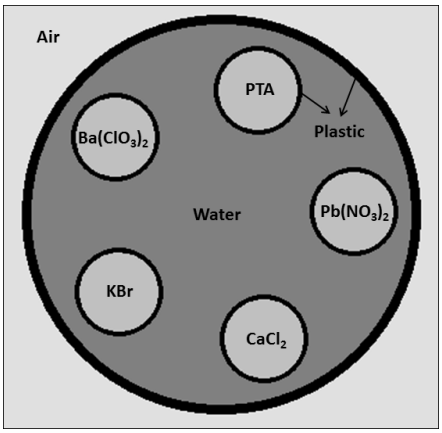

Figure 5.19: Model of the phantom containing five different aqueous solutions. [1]

Both simulated and real data were compared. Figure 5.20 shows a reconstructed slice from the real and simulated data. Artefacts induced by the polychromatic nature of the X-ray beam are clearly visible in both reconstructions. Streaking artefacts, which are the result of beam hardening, are equally strongly present and show a similar pattern in the slices. The linear attenuation coefficients and their

Table 5.10: Mass fractions of the solutes and water and the density for each solution used in the phantom (Fig. 5.19).

Material	Mass fraction solute	Mass fraction H_2O	density (g/cm^3)
$Ba(ClO_3)_2$	0.103	0.897	1.115
KBr	0.115	0.885	1.13
$CaCl_2$	0.412	0.588	1.32
$Pb(NO_3)_2$	0.078	0.922	1.085
PTA	0.074	0.926	1.08

standard errors for each solution and material present in the sample are compared for the real and simulated data in Table 5.11. A maximum deviation of 3.9% for the $CaCl_2$ solution was found. The fact that the deviation was the largest for this solution probably stems from the difficulty in determining the density of the solution, as the mass fraction of the solute in the $CaCl_2$ solution is much bigger than in the other solutions. In this case, contrary to the other solutions used here, this resulted in an increase in the volume of the mixture.

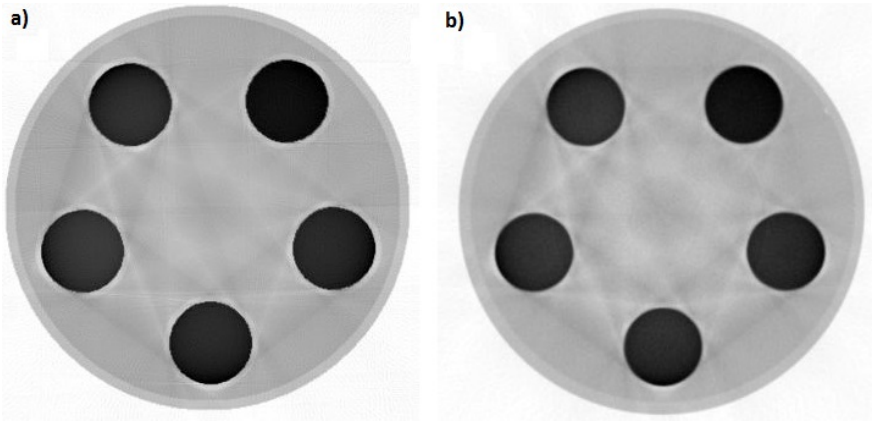

Figure 5.20: A reconstructed slice of the simulated (a) and real phantom (b). [1]

CT scans obtained at HECTOR

Section B.2.2 shows figures with the linear attenuation coefficient along a line profile in the reconstructed slices of the Al sphere and POM cylinder at different tube voltages. The parameters for these scans were the same as those for the radiographs of the Al sphere and POM cylinder taken at HECTOR as discussed previously. A total of 801 projections were taken for the full CT scan. Table 5.12 lists the deviation between the line profiles obtained from the real scans and simulated scans. The deviations lie in the range of the noise levels present in the images. Overall, the simulated and real profiles correspond very well in terms of

Table 5.11: Measured (M) and simulated (S) reconstructed attenuation values and corresponding standard deviations(σ_M and σ_S) at 100 keV for the different materials in the phantom. Deviations(Dev) between real and simulated data are listed as well.

Material	$\mu_M(\text{cm}^{-1})$	$\mu_S(\text{cm}^{-1})$	Dev(%)	$\sigma_{\mu_M}(\text{cm}^{-1})$	$\sigma_{\mu_S}(\text{cm}^{-1})$
$Ba(ClO_3)_2$	0.853	0.859	0.7	0.015	0.015
KBr	0.745	0.754	1.2	0.023	0.022
$CaCl_2$	0.748	0.720	3.9	0.021	0.023
$Pb(NO_3)_2$	0.769	0.776	0.9	0.022	0.022
PTA	0.776	0.777	0.1	0.021	0.020
H_2O	0.268	0.262	-2.2	0.026	0.022

attenuation coefficients. The attenuation and noise measured in the reconstructed slices at tube voltages of 60, 120 and 180 kV can be found in Table 5.13. The simulated and real attenuation coefficients correspond very well, but the noise in the real scans σ_{μ_M} is significantly lower than the noise σ_{μ_S} predicted by the simulations. This deviation was probably caused by the fact that the MTF of the detector was neglected during the simulations. For the reconstructions listed in the table, the noise for simulations adjusted with the MTF correction described in section 4.3.3 is included. These values correspond much better to the real noise levels in the images. This shows that adding an MTF correction can drastically improve the noise levels predicted by the simulations.

Table 5.12: The deviation between the line profiles of the reconstructed slices for HECTOR of the Al sphere and POM cylinder calculated based on Equation 5.20.

Profile	Error(%)
Al sphere @ 30kV	11.31
Al sphere @ 60kV	4.92
Al sphere @ 90kV	4.32
Al sphere @ 120kV	4.92
Al sphere @ 150kV	5.17
Al sphere @ 180kV	5.55
Al sphere @ 210kV	5.80
POM cylinder @ 30kV	7.34
POM cylinder @ 60kV	6.90
POM cylinder @ 90kV	7.43
POM cylinder @ 120kV	10.83
POM cylinder @ 150kV	11.06
POM cylinder @ 180kV	11.46
POM cylinder @ 210kV	12.19

Table 5.13: Measured (M) and simulated (S) linear attenuation coefficients for different samples at different energies at Hector.

Filter	μ_M(1/cm)	μ_S(1/cm)	σ_{μ_M}	σ_{μ_S}	$\sigma_{\mu_{S_{MTF}}}$
Al sphere @ 60kV	2.182	2.201	0.069	0.096	0.034
Al sphere @ 120kV	1.180	1.138	0.040	0.059	0.029
Al sphere @ 180kV	0.946	0.914	0.033	0.053	0.029
POM cylinder @ 60kV	0.542	0.529	0.024	0.035	0.012
POM cylinder @ 120kV	0.358	0.3438	0.019	0.029	0.014
POM cylinder @ 180kV	0.311	0.301	0.017	0.028	0.015

CT scans obtained at Medusa

Figure 5.21 shows the line profiles of a real and simulated reconstructed slice of the Al sphere. Different simulations are also shown next to the real profile. Figure 5.21(a) shows the line profile of the simulation without any corrections and the line profiles of the simulations with constant, Gaussian and polynomial spot corrections described by Equation 5.19. Figure 5.21(b) also shows line profiles of reconstructed data in which only a fraction of the Gaussian spot correction was applied. The deviation between these different simulations and the real data is given in Table 5.14. While adding a complete contribution of the secondary spot to the image does not result in a big improvement, adding only a fraction of the corrected spot (done here for the Gaussian correction) does reduce the deviation between the simulated and the real profile. This can be due either to an incorrect prediction of the secondary spot by the Monte Carlo simulations or to a shielding of a fraction of the X-ray beam produced in the secondary spot that cannot escape the tube in the real scan.

Table 5.14: Deviation between the simulated and real reconstructed data for the performed corrections based on Equation 5.20.

Correction	Deviation from real scan (%)
no corr	12.1
constant	10.8
gaussian	10.7
polynomial	10.9
20% gaussian	6.9
50% gaussian	7.1

5.4.3 Discussion

In general, the real and simulated data are in agreement within 5% and often better over a wide range of spectra and detectors. However, at low X-ray tube voltages, the relative difference between simulated and real data is substantially

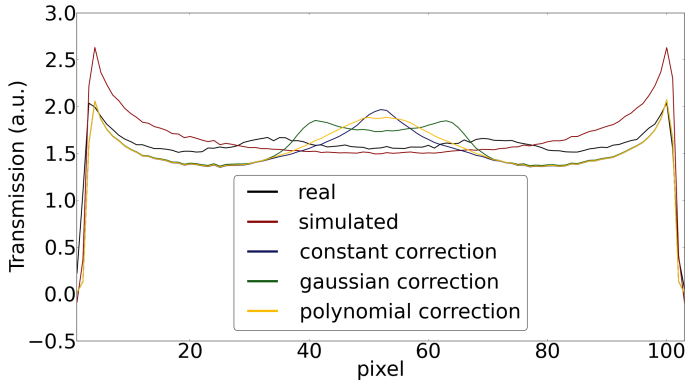

(a)

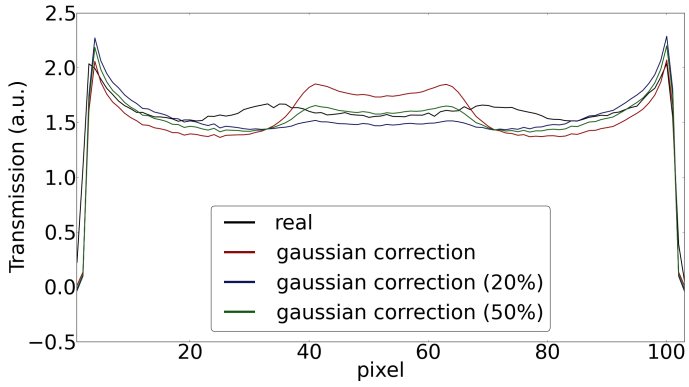

(b)

Figure 5.21: Measured and simulated data with a secondary spot implementation for different profiles (a) and with only a fraction of the gaussian correction applied (b).

higher. The absolute difference is in the low energy range not necessarily bigger than in the other energy ranges, but because the transmission is much lower it will cause a large relative error. There are thus some systematic deviations in the simulations which become of relevance at low transmissions. These deviations can be caused by incorrect modelling at low X-ray energies in the Monte Carlo simulations performed in chapter 4. Furthermore, detector ghosting (section 3.5.5) and X-ray scattering should be modelled and included in the simulation to study their behaviour during the X-ray imaging process and their effect on the simulated radiographs to draw further conclusions in this regard.

5.5 Applications of Arion

This section demonstrates the value of Arion to optimise scanning parameters. When a CT scanner is used to scan similar samples repeatedly, it can be practically feasible to optimise scanning conditions by running test scans and determining which parameters best fit the needs of the user. However, at a research facility such as UGCT, a wide variety of samples are scanned, and it is not feasible to run many tests for each sample that needs to be scanned. Using simulations to determine the optimal settings reduces not only the time and cost of a CT scan, but the simulator is also able to include a much broader parameter space in the simulations than what is practically feasible with real scans. This section discusses the optimisation of SNR and CNR. Afterwards, some scan results obtained in the context of the TomFood project are shown.

5.5.1 Optimising SNR

The easiest way to determine an optimal scanning setup is by using the SNR (Equation 5.17). This value is a good indication of how well features in a sample can be distinguished. Tables 5.15 and 5.16 show the linear attenuation, the standard deviation on this linear attenuation and the SNR of a 6-mm-diameter aluminium sphere for a real and simulated setup, respectively. As mentioned before, the noise in the simulated images is (with the exception of 30 kV) slightly higher than the noise in the real ones. This results in a lower SNR in the simulated images. Nevertheless, the general trend of the SNR in function of the tube voltage is the same in both cases, which makes the simulator a useful tool to optimise the SNR of a given scan.

The prediction of the linear attenuation coefficient μ and its error σ_μ can be calculated by the Setup Optimiser by using Equations 5.14 and 5.16. Table 5.17 shows the ratios of these values for a slab of aluminium with a thickness of 6 mm. Note that this is not the same as Equation 5.17, as the error obtained by the Setup Optimiser is the error on μ itself and is not the pixel-to-pixel variation. The way μ is calculated in the Setup Optimiser and in a reconstruction algorithm is different and this will lead to different errors σ_μ. Nevertheless, the ratio obtained by the Setup Optimiser behaves similarly to the SNR in the reconstructed slice and can thus be used for optimisation. This can clearly be seen in Figure 5.23 in which all SNR ratios are plotted as a function of the tube voltages on a log scale. The parallel behaviour of the curves indicates that the SNR ratio's show a similar behaviour for the different methods. The Setup Optimiser can thus be used as a fast method to determine the scanning conditions that give the best SNR for a given sample.

Table 5.15: Attenuation coefficient measured in the real data of the Al sphere.

Voltage (kV)	μ_{real} (cm^{-1})	$\sigma_{\mu_{real}}$ (cm^{-1})	SNR_{real}
30	5.897	0.710	8.311
60	2.194	0.067	32.533
90	1.462	0.045	32.561
120	1.185	0.039	30.676
150	1.033	0.035	29.718
180	0.949	0.034	28.011
210	0.894	0.032	27.636

Table 5.16: Attenuation coefficient measured in the simulated data of the Al sphere.

Voltage (kV)	μ_{Sim} (cm^{-1})	$\sigma_{\mu_{Sim}}$ (cm^{-1})	SNR_{Sim}
30	6.133	0.469	13.088
60	2.217	0.098	22.664
90	1.436	0.069	20.680
120	1.143	0.060	19.101
150	1.003	0.056	17.962
180	0.919	0.053	17.183
210	0.862	0.052	16.562

The same results were found for the real and simulated SNRs in the POM cylinder (Tables 5.18 and 5.19). Again, the same trend in SNR behaviour is predicted by the Setup Optimiser (Table 5.20). In addition to an estimate for the optimal SNR parameters, an estimate for the amount of beam hardening present in the sample can be given by the Setup Optimiser (Fig. 5.22).

Table 5.17: Attenuation coefficient as predicted by the Setup Optimiser in the Al sphere.

Voltage (kV)	μ_{SO} (cm^{-1})	$\sigma_{\mu_{SO}}$ (cm^{-1})	SNR_{SO}
30	7.215	0.060	121.170
60	2.709	0.012	232.557
90	1.7413	0.0082	212.5520
120	1.3695	0.0070	194.6160
150	1.1893	0.0065	181.9890
180	1.0831	0.0063	172.1420
210	1.0111	0.0062	164.2860

Table 5.18: Attenuation coefficient measured in the real data of the POM cylinder.

Voltage (kV)	μ_{real} (cm^{-1})	$\sigma_{\mu_{real}}$ (cm^{-1})	SNR_{real}
30	1.036	0.050	20.773
60	0.542	0.024	22.497
90	0.413	0.020	20.282
120	0.358	0.019	19.014
150	0.327	0.018	18.179
180	0.311	0.018	17.768
210	0.300	0.017	17.543

Table 5.19: Attenuation coefficient measured in the simulated data of the POM cylinder.

Voltage (kV)	μ_{Sim} (cm^{-1})	$\sigma_{\mu_{Sim}}$ (cm^{-1})	SNR_{Sim}
30	1.042	0.064	16.225
60	0.531	0.036	14.682
90	0.399	0.031	12.766
120	0.344	0.029	11.791
150	0.317	0.029	11.108
180	0.301	0.028	10.600
210	0.290	0.028	10.345

Table 5.20: Attenuation coefficient as predicted by the Setup Optimiser in the POM cylinder.

Voltage (kV)	μ_{SO} (cm^{-1})	$\sigma_{\mu_{SO}}$ (cm^{-1})	SNR_{SO}
30	1.1250	0.0066	170.9430
60	0.5610	0.0038	147.4320
90	0.4120	0.0033	123.7570
120	0.3506	0.0031	111.7250
150	0.3199	0.0031	104.7660
180	0.3017	0.0030	99.7872
210	0.2897	0.0030	96.0366

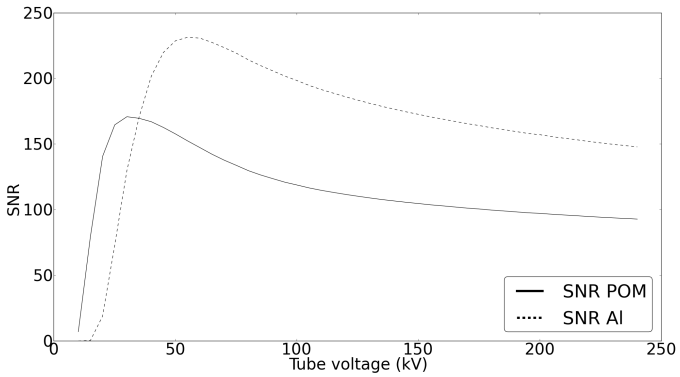

(a)

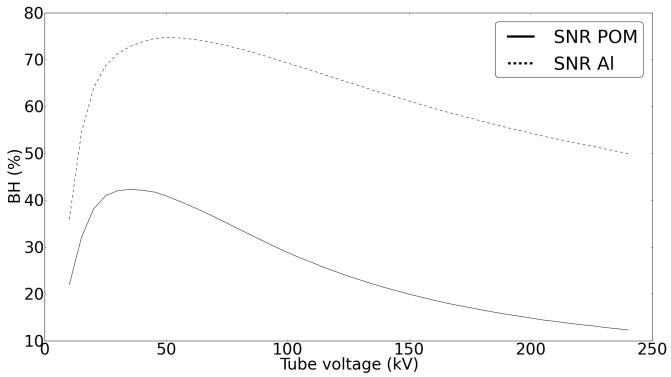

(b)

Figure 5.22: SNR and BH obtained by using the Setup Optimiser.

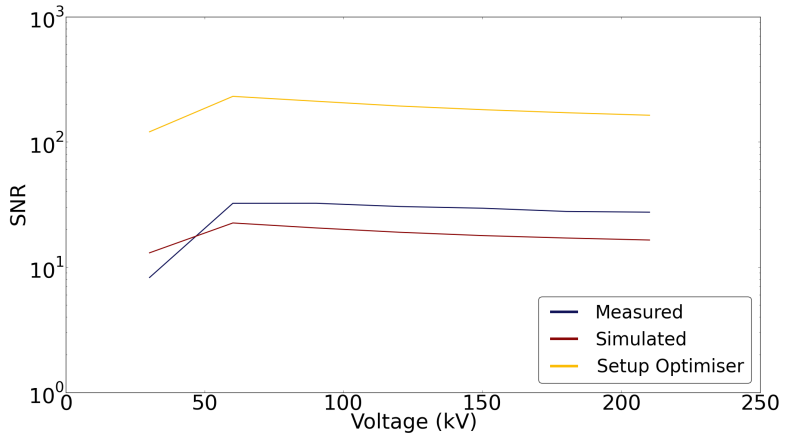

(a)

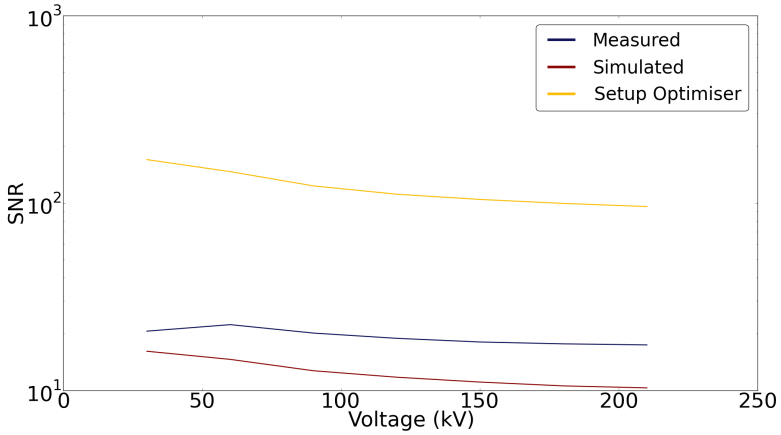

(b)

Figure 5.23: SNR for the Al sphere (a) and POM cylinder (b) obtained with different methods plotted on a log scale.

5.5.2 Optimising CNR

The method discussed above often has shortcomings when multiple materials of interest are present in the sample the user wants to scan. Optimising the SNR is useful in the case when a sample scanned only contains one material, for example, an aluminium foam. In most cases however, the user wants to distinguish two or more materials in a sample. Instead of using the SNR, which indicates how well a material can be distinguished in air, the CNR (Equation 5.18) can be used. This indicates how well two materials can be distinguished from each other.

How this is done is shown with an example in which an optimal scanning condition for a butter sample containing water is sought. Figure 5.24 shows a virtual phantom used for the simulations. This sample consists mainly of butter and is contained in a plastic cylinder. The butter contains air and water bubbles. The goal of the simulations is to find the optimal scanning parameters to distinguish the water from the butter. Figure 5.25 shows reconstructed slices of the simulation compared to a real scan of a butter sample. Table 5.21 shows the reconstructed attenuation coefficients and the noise for the butter and water in the reconstructed slices. The determined CNRs in the simulated scans correspond well with those observed in the real data. The deviation between the CNR obtained in the real and simulated data at 120 kV is probably due to the noise calculation in the simulated data, where the MTF of the detector was not taken into account.

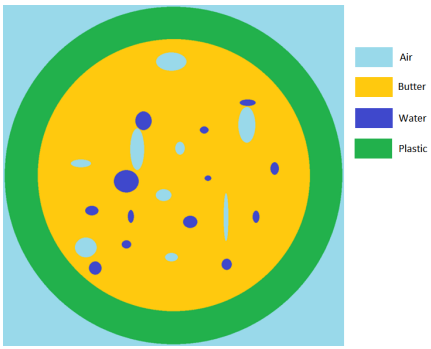

Figure 5.24: A virtual butter phantom containing water and air bubbles in a plastic container.

Figure 5.26 shows the CNR predicted by the Setup Optimiser. Again, just as for the optimisation of the SNR, it is much higher than those predicted by Arion or in the real scans due to how the error is calculated. Nevertheless, the behaviour is the same as in the real data, which means that this easy method can be used to determine the optimal scanning conditions. The maximum beam hardening in the

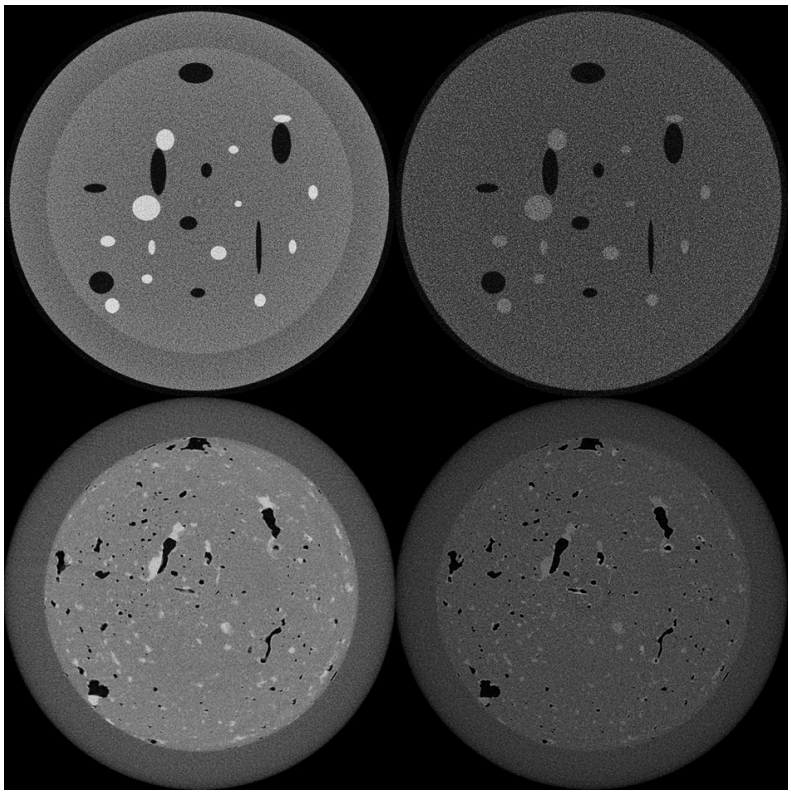

Figure 5.25: Reconstructed slices of the simulated phantom (top) and real sample (bottom) at 30 kV (left) and 120 kV (right).

Table 5.21: Reconstructed attenuation coefficients and CNR for butter and water in the simulated and real data.

Image	μ_B (cm^{-1})	σ_{μ_B} (cm^{-1})	μ_W (cm^{-1})	σ_{μ_W} (cm^{-1})	CNR
30k kV	0.69	0.13	1.06	0.14	1.86
120 kV	0.238	0.060	0.300	0.060	0.74
30 kV - SIM	0.63	0.22	1.17	0.23	1.70
120 kV - SIM	0.22	0.13	0.31	0.14	0.45

sample is also given (Fig. 5.27). Note that the maximal beam hardening is lower than predicted, as the sample has a cylindrical form and not a conical one.

5.5.3 Optimizing dual-energy CT

The use of Arion for optimising dual-energy CT (DECT) is extensively discussed in [18] and is therefore not examined here. Just as for optimising SNR and CNR, it has been proven that Arion is a successful tool for optimising the scanning

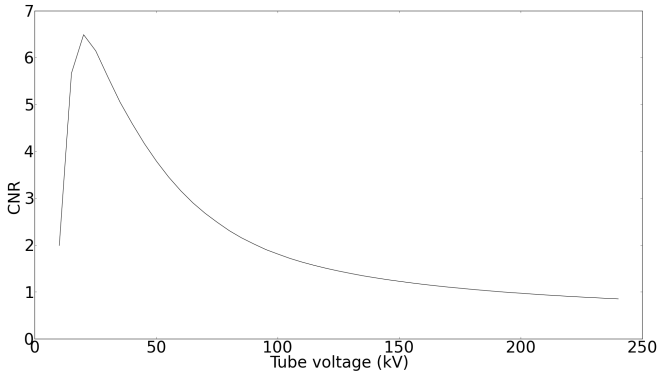

Figure 5.26: CNR determined by the Setup Optimiser for a range of tube voltages.

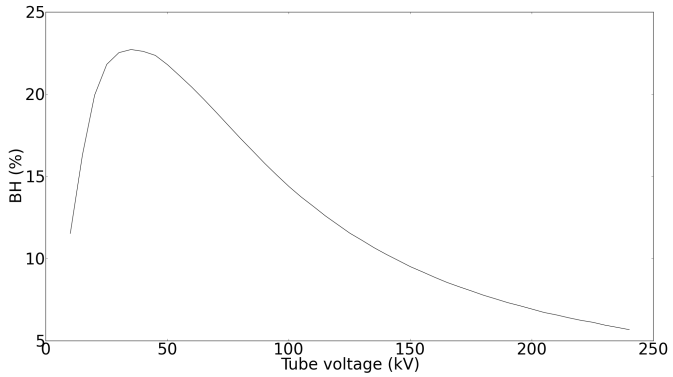

Figure 5.27: Maximum beam hardening in the reconstructed butter sample predicted by the Setup Optimiser.

parameters for DECT applications. More information about DECT can be found in chapter 6.

5.5.4 Results obtained in the context of the TomFood project

A selection of samples scanned in the context of the IWT/SBO TomFood project are shown below. These samples show what can be achieved when a sample is scanned under the right, optimised scanning conditions. Furthermore, the simulator was used in the context of the TomFood project to simulate and study a conveyer belt setup geometry for the detection of browning in apples [13], but this will not be discussed in this work.

Figures 5.28(a) and 5.28(b) show reconstructed slices of a chocolate mousse sample. The former was taken a day after the preparation of the mousse and was kept in the fridge during that day. The latter scan was taken after the sample was kept in the freezer for a month at a temperature of -20°. Figure 5.28(c) shows the rendering of a chocolate mousse sample.

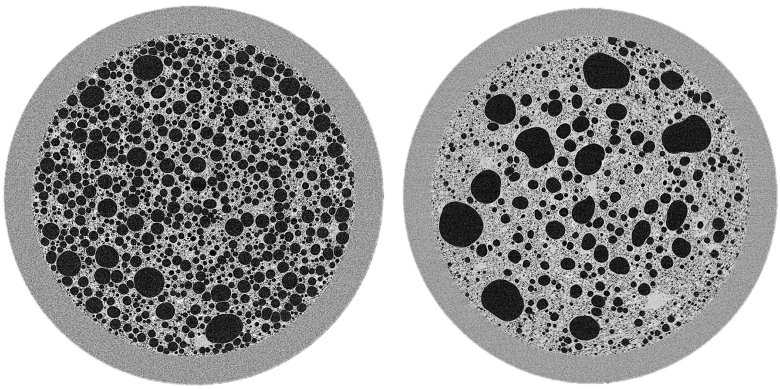

(a) (b)

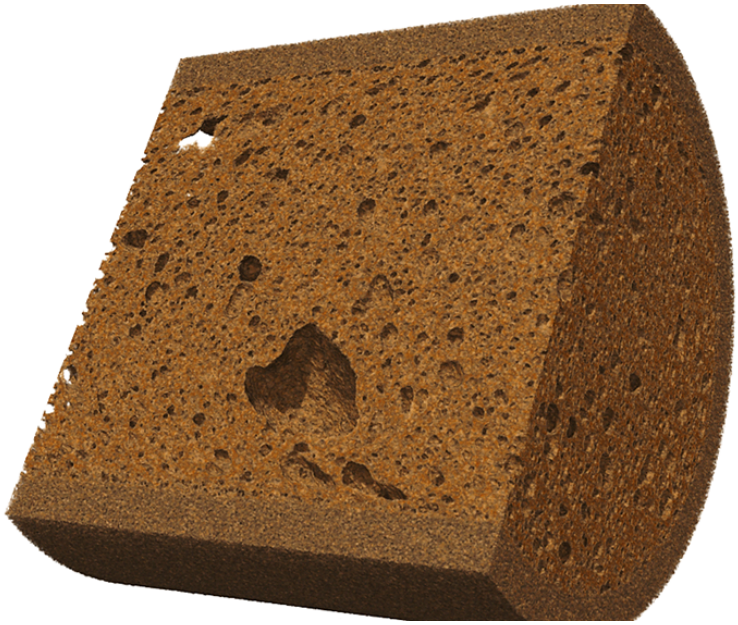

(c)

Figure 5.28: Reconstructed slices of chocolate mousse (a, b) and a rendering of chocolate mousse (c).

Another study performed in the context of TomFood concerned the development of eyes (holes) during the ripening process of cheese. During a period of a month, scans of cheese wheels at time intervals of a week were performed. Figures 5.29(a) and 5.29(b) show a reconstructed slice of a cheese wheel on the first and last day of the experiment. Figure 5.29(c) shows a rendering of a cheese wheel.

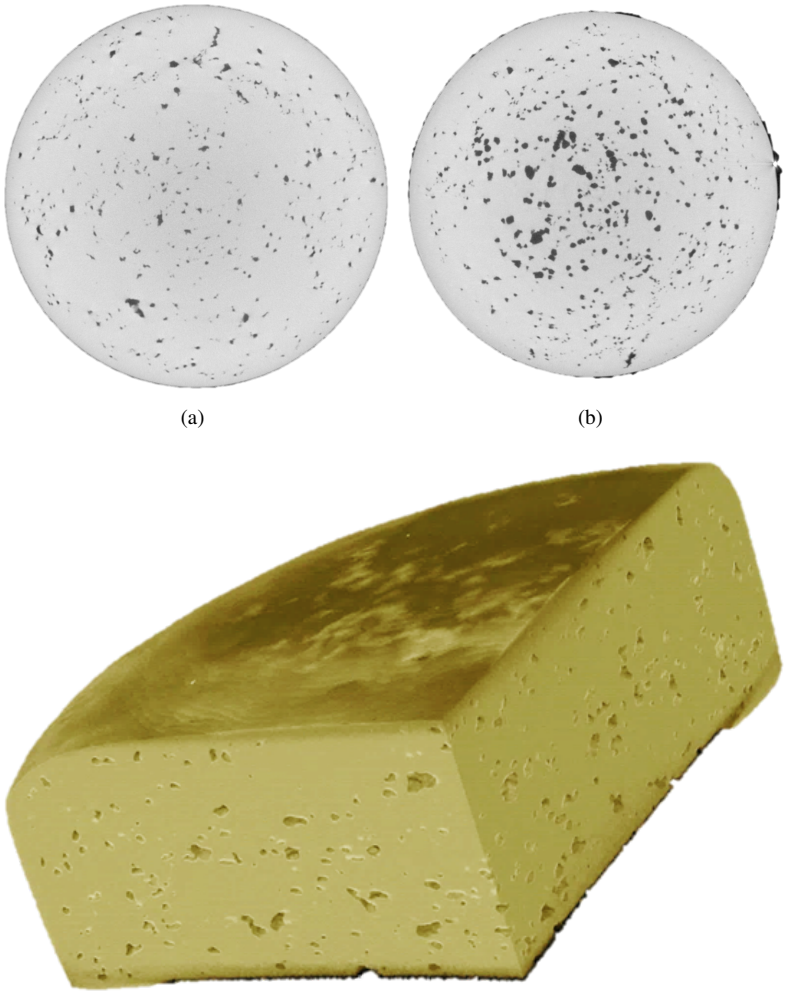

(a) (b)

(c)

Figure 5.29: Reconstructed slices of a cheese wheel (a, b) at different times during the ripening process and a rendering of the wheel (c).

One of the main goals of the TomFood project was to develop an inline CT system [13] to determine if apples have internal disorders such as browning or holes. In order to characterise these disorders, high-quality scans of apples containing disorders were performed. Figure 5.30 shows a reconstruction of a healthy apple next to apples with different disorders. In Figure 5.31, a rendering of the internal vessel structure of a healthy apple is shown. The rendered volume consists of 8 gigavoxels.

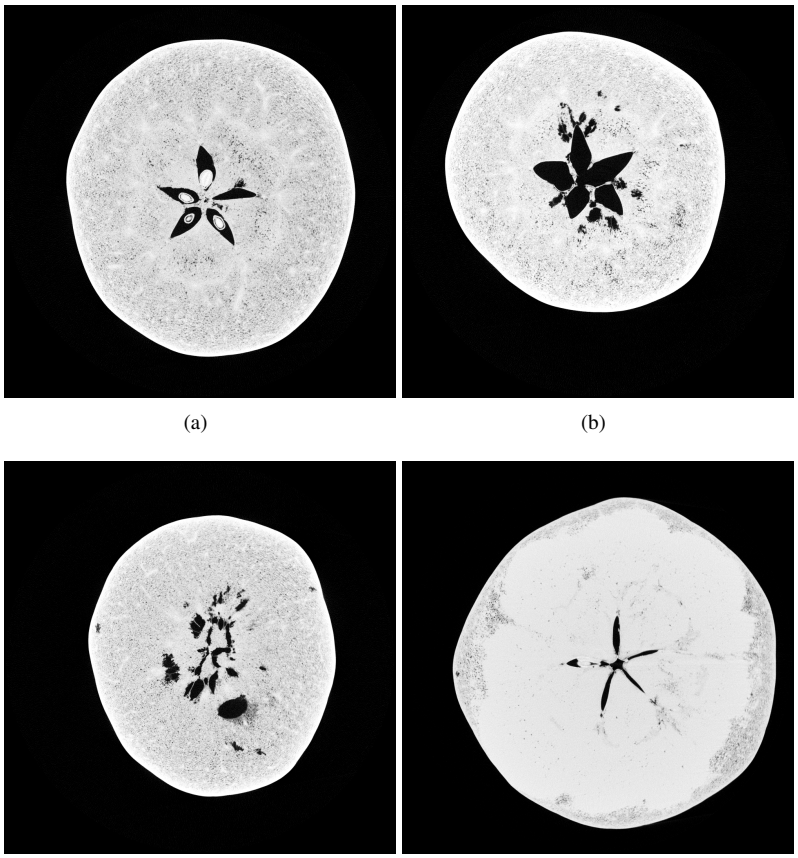

(a) (b)

(c) (d)

Figure 5.30: A healty apple (a) is compared with apples with different internal disorders. Apples can either contain holes (b, c) or dens brown spots (d).

A rendering of the butter samples discussed in section 5.5.2 is shown in Figure 5.32(c). The water inside the sample is shown in blue and the butter itself in yellow. In addition to the optimisation of the butter and water fraction inside

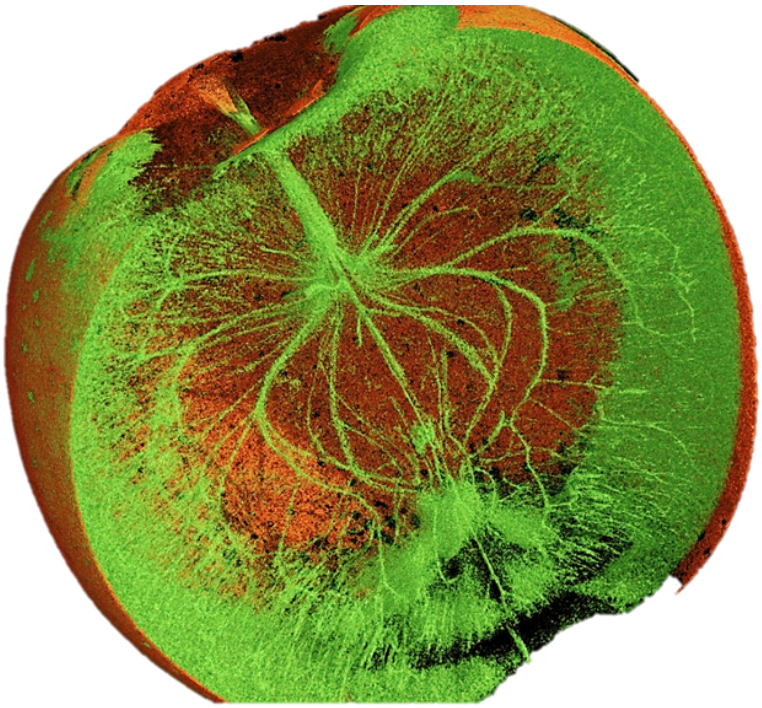

Figure 5.31: Rendering of an apple.

the sample, another problem arose during the reconstruction: phase artefacts were clearly visible (section 3.2.7). Figures 5.32(a) and 5.32(b) show the same reconstructed slice in the scanned butter sample before and after phase correction of the data.

A similar sample to the butter was also studied-a cake sample-with the intention of visualising the distribution of its internal fat structures and air bubbles. Again, phase artefacts were present in the reconstructed volume of the cake (Fig. 5.33(a)). By performing a phase correction (Fig. 5.33(b)), a correct analysis and segmentation could be conducted. Figure 5.33(c) shows a rendering in which the fat structures inside the cake sample are clearly visible.

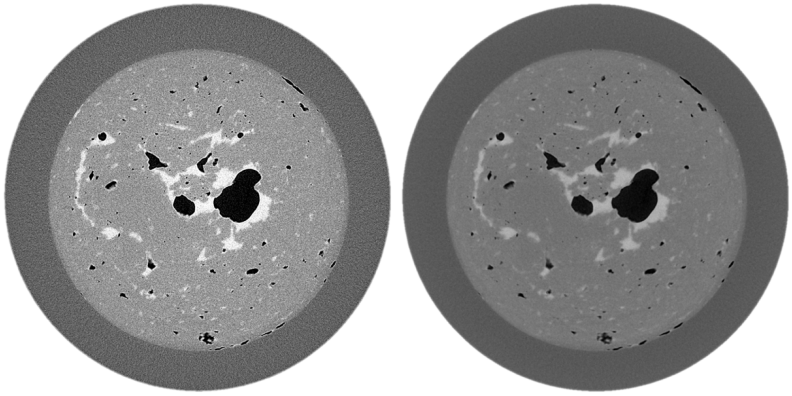

(a) (b)

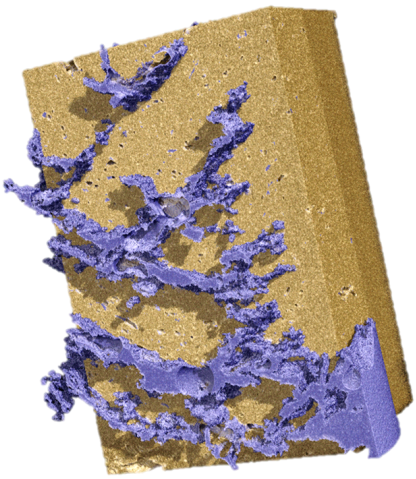

(c)

Figure 5.32: A slice in the reconstructed volume of the butter sample before (a) and after (b) phase correction. The water (blue) and butter (yellow) are clearly visible in the 3D rendering (c) of the sample.

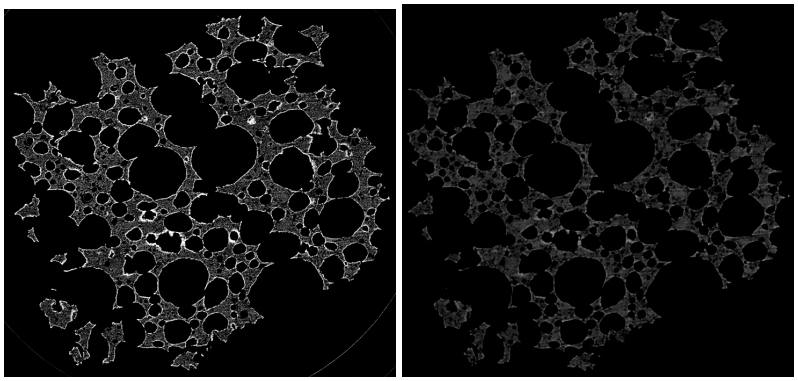

(a) (b)

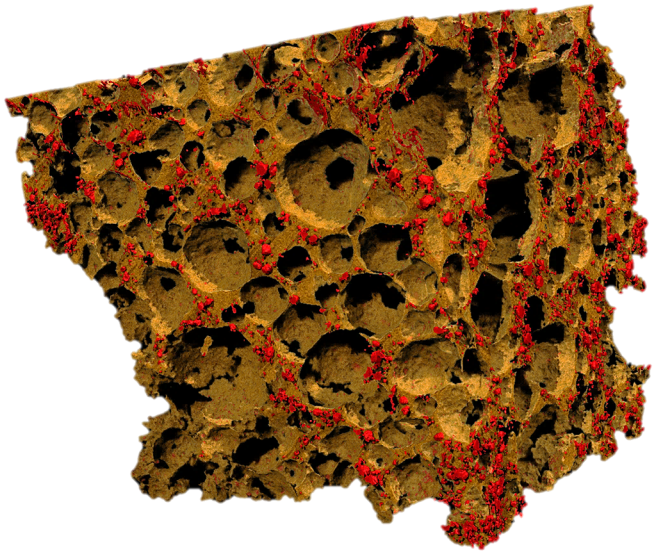

(c)

Figure 5.33: A slice in the reconstructed volume of the cake sample before (a) and after (b) phase correction. The fat (red) and cake (brown) are clearly visible in the 3D rendering (c) of the sample.

5.6 Other uses for Arion and future improvements

In this chapter, the polychromatic projection simulator, Arion, was extensively discussed and tested. The general conclusion is that in general the scans performed at real scanners can be simulated with an accuracy that only deviates around a few percent from the real scans. Only at low tube voltages higher deviations were found, this is probably because of the low transmission values, scattering effects will play a role in the measured transmission. Arion includes the physical properties of the real scanner, such as the polychromaticity of the beam and the polychromatic behaviour of the detector and sample. Further, it was shown how Arion can be used to optimise scanning conditions. However, the use of the simulator is not only limited to this purpose; some other uses are described below. Chapter 6 shows that the simulator can also be used to determine more physical parameters in a reconstructed volume.

Although the accuracy of the simulator is sufficient for the applications discussed in this chapter, some further improvements are discussed below. Some benchmarks of the program are also shown. The program really benefits from the GPU implementation, which allows for massive parallel computations that can never be achieved when implementing the program on the CPU.

5.6.1 Testing reconstruction algorithms

The most important aspect of the polychromatic projection simulator Arion is that it simulates the physical aspects of an X-ray CT scan very well. It can thus be used to study in detail the physical properties of a scan, such as beam hardening, which is clearly visible in the examples shown in this chapter. In addition, for the development of reconstruction algorithms, either analytical or iterative, Arion can be used to verify the quality of reconstructions, as a ground truth is perfectly known.

Another application mentioned earlier is the use of the projection simulator to explore new X-ray CT trajectories, such as the conveyer belt [13]. For industrial purposes, circular and helical CT are often not feasible for inline applications in an industrial environment. These inline solutions do not have to be limited to a conveyer belt setup, but can describe random trajectories. Arion's random trajectory module can be used to determine which trajectories are feasible to build and offer sufficient angular range and number of projections to reconstruct a qualitative 3D volume. This saves the cost of verifying different setups by building mock-up systems, while the physical properties of the scan are modelled very accurately.

5.6.2 Benchmarks

Table 5.22 shows some benchmarks for the simulator performed with a TITANX GPU. Choosing a variable bin size as shown in Figure 5.3 drastically reduces the computation time. Two benchmarks are listed for the Al sphere. The first column shows the computation time when the sample covers every pixel of the detector, which was obtained by selecting an SOD at which the sample covered the complete detector. The second column shows the simulations actually performed in this chapter. The total computation time is almost halved in the second case. This is because when a ray from the source to detector pixel does not traverse the virtual sample, the pixel value is calculated analytically as if there is only air between the source and detector. This also reduces the scan time compared to a ray-tracing being applied for each pixel. Further, two other simulations are listed. The third column shows the simulation time for a $1000 \times 1000 \times 1000$ virtual phantom that covers the whole detector. The last column shows a phantom that is typically used for the applications described in section 5.5. For these applications, it is sufficient to simulate only a couple of slices of the phantom to get an accurate view of how a real scan would look. The use of such a thin phantom provides enough information and reduces the computation time drastically for optimisation processes that require multiple setups to be simulated.

Table 5.22: Benchmarks for Arion, performed on a TITAN-X GPU, with a binned spectrum with 100 bins.

Parameter	Al sphere	Al sphere	phantom 1	phantom 2
Phantom dimension x	400	400	1000	1000
Phantom dimension y	400	400	1000	1000
Phantom dimension z	390	390	1000	40
Detector dimensions (y,z)	(600,600)	(500,500)	(600,600)	(600,600)
Number of projections	601	501	601	601
Time for 1 projections (ms)	$\sim$1000	$\sim$700	$\sim$2500	$\sim$90
Total simulation time (s)	663	314	1687	63

5.6.3 Future improvements

Although it was shown in this chapter that the Setup Optimiser and Arion are useful tools for accurately predicting and simulating X-ray CT behaviour and data, further improvements are always possible. It was shown that the corrections performed for effects like the MTF or secondary spot improve the simulated data when compared to the real scan. Especially the prediction of noise in the simulated images was much better when the MTF was taken into account. However, a more detailed model for both these effects should be developed over the whole energy range of the components. For most applications, these corrections are not

necessary, but if very accurate and detailed simulations or predictions are needed, these corrections would be the most likely to increase the accuracy of the simulations.

Wave effects are neglected in Arion but can play a very important role in X-ray CT. In order to simulate these effects, the simulator can be improved by taking the wave behaviour of X-rays into account. Additionally, scattering and 'ghosting' are neglected. All these effects can be useful additions to the program to make it have an even broader range of applications. The implementation of the scattering contribution to the measured intensity on the detector should improve the results of the simulated radiographs, especially, for low transmission values, where scattering effects can play an important role.

References

[1] Jelle Dhaene, Elin Pauwels, Thomas De Schryver, Amélie De Muynck, Manuel Dierick, and Luc Van Hoorebeke. *A realistic projection simulator for laboratory based X-ray micro-CT*. Nuclear Instruments and Methods in Physics Research, Section B, 342:170–178, 2015.

[2] J. A. Seibert and J. M. Boone. *X-ray imaging physics for nuclear medicine technologists. Part 2: X-ray interactions and image formation*. Journal of Nuclear Medicine Technology, 33(1):3–18, 2005.

[3] S. Kasperl, J. Hiller, and M. Krumm. *Computed tomography metrology in industrial research and development*. Materials Testing, 51(6):405–411, 2009.

[4] P. Duvauchelle, N. Freud, V. Kaftandjian, and D. Babot. *A computer code to simulate X-ray imaging techniques*. Nuclear Instruments and Methods in Physics Research, Section B, 170(1-2):245–258, 2000.

[5] N. Freud, P. Duvauchelle, S. A. Pistrui-Maximean, J.-M. Letang, and D. Babot. *Deterministic simulation of first-order scattering in virtual X-ray imaging*. Nuclear Instruments and Methods in Physics Research, Section B, 222(1-2):285–300, 2004.

[6] N. Freud, J.-M. Létang, and D. Babot. *A hybrid approach to simulate multiple photon scattering in X-ray imaging*. Nuclear Instruments and Methods in Physics Research, Section B, 227(4):551–558, 2005.

[7] N. Freud, P. Duvauchelle, J.-M. Létang, and D. Babot. *Fast and robust ray casting algorithms for virtual X-ray imaging*. Nuclear Instruments and Methods in Physics Research, Section B, 248(1):175–180, 2006.

[8] A. Peterzol, J. Berthier, P. Duvauchelle, C. Ferrero, and D. Babot. *X-ray phase contrast image simulation*. Nuclear Instruments and Methods in Physics Research, Section B, 254(2):307–318, 2007.

[9] D. Lazos, K. Bliznakova, Z. Kolitsi, and N. Pallikarakis. *An integrated research tool for X-ray imaging simulation*. Computer Methods and Programs in Biomedicine, 70(3):241–51, 2003.

[10] K. Bliznakova, Z. Kolitsi, and N. Pallikarakis. *Dual-energy mammography: simulation studies*. Physics in Medicine and Biology, 51(18):4497–4515, 2006.

[11] K. Bliznakova, R. Speller, J. Horrocks, P. Liaparinos, Z. Kolitsi, and N. Pallikarakis. *Experimental validation of a radiographic simulation code using*

breast phantom for X-ray imaging. Computers in Biology and Medicine, 40(2):208–14, 2010.

[12] F. Inanc. *Scattering and its role in radiography simulations*. NDT and E International, 35(8):581–593, 2002.

[13] Thomas De Schryver, Jelle Dhaene, Manuel Dierick, Matthieu N. Boone, Eline Janssens, Jan Sijbers, Mattias van Dael, Pieter Verboven, Bart Nicolai, and Luc Van Hoorebeke. *In-line NDT with X-Ray CT combining sample rotation and translation*. NDT and E International, 84:89 – 98, 2016.

[14] `http://www.nvidia.co.uk/`.

[15] `http://www.qt.io/`.

[16] `http://wccftech.com/nvidia-pascal-gpu-analysis/`.

[17] M. N. Boone, J. Vlassenbroeck, S. Peetermans, D. Van Loo, M. Dierick, and L. Van Hoorebeke. *Secondary radiation in transmission-type X-ray tubes: Simulation, practical issues and solution in the context of X-ray microtomography*. Nuclear Instruments and Methods in Physics Research, Section A, 661(1):7–12, 2012.

[18] E. Pauwels. *Optimal use of the polychromaticity in X-ray microtomography for dual energy methods and contrast agent imaging*. Phd thesis, Ghent University, 2017.

6

Material characterisation by using dual-energy CT

This chapter addresses the use of dual-energy CT (DECT) and its possibilities for performing a material characterisation in each voxel of a reconstructed volume by combining reconstructed data obtained at different energies or, as in the case of laboratory-based X-ray CT, this comes down to using different tube spectra which can be obtained by adjusting the tube voltage or by filtering the tube spectrum.

First, the chapter starts with a historical overview of DECT and the most important theories described in literature. Next, the theories implemented and developed at UGCT are explained. A new method is presented which is a new approach to an existing technique used to characterise the material in a voxel by means of its composition and its density. This method is applied on simulated and real samples, and it is shown that it can also be used for densitometry in CT. Finally, an outlook on the further development of this new method is given.

6.1 History of Dual energy CT

The reconstructed 3D volume that is obtained by performing an X-ray CT scan contains a linear attenuation coefficient in each voxel. This reconstructed linear attenuation coefficient μ is the product of the local mass attenuation coefficient μ/ρ and the local density ρ of the material. Each chemical element has its own unique

energy-dependent behaviour for its mass attenuation coefficient with respect to photon energy. This results in the fact that a distinction between two elements can be made by using a tuneable monochromatic X-ray energy.

In laboratory X-ray CT, two materials of different composition can have a very similar grey value in a reconstructed volume, making them practically indistinguishable. This is because the reconstructed linear attenuation coefficient is the product of the local mass attenuation coefficient, which is both energy and material dependent, and the local density of the material.

If only two materials are present in the sample, or if the user only wants to separate two materials, optimised parameters for a single scan can be found which will yield the best contrast-to-noise (CNR) ratio between the two materials (Section 5.5.2). If more materials are present in the sample, it is always possible that there will be two materials showing similar behaviour while scanning with certain scan parameters. In such cases, dual-energy CT (DECT) can offer a solution. The combination of CT scans at different X-ray energies can provide the information necessary to make a distinction between materials with otherwise very similar reconstructed attenuation coefficients. A special case of DECT is K-edge imaging, where scanning energies are chosen just below and above the K-edge of a selected element. Doing so allows for easy visualisation of the given element [1]. This technique is especially useful at synchrotron facilities where quasi-monochromatic X-ray beams are available.

The first articles about DECT date back to 1976. In this year Alvarez and Macovski [2] and Rutherford [3] published their theories about this technique. While Alvarez and Macovski's theory is a pre-reconstruction method, Rutherford's theory is applied post-reconstruction. An even more remarkable fact about the publication of these theories is that the first CT scanner was developed only five years earlier in 1971. Experimental validation, however, was not easy in those days because of the many shortcomings inherent to the first CT scanners. Since the development of the first CT system, there had already been interest in a method to extract more information from the CT scans by combining multiple scans at different energies/spectra. Ten years later, in the 1980s, new life was breathed into DECT techniques; more recently, dual-energy systems started to be used for medical purposes [4].

The use and applications of dual-energy CT are evolving rapidly, but the implementations of the techniques are essentially extensions of the theories proposed in 1976. Both principles of these theories are discussed below. A more thorough discussion on DECT techniques can be found in [5].

6.2 DECT theories in literature

In this section, three methods for DECT are explained. To begin with, the first method published by Alvarez and Macovski [2] is described, followed by that published by Rutherford et al. [3] several months later. A third method for three-material decomposition proposed by Vinegar and Wellington [6] is discussed as well, as this method is used at UGCT [5].

6.2.1 Alvarez and Macovski

Alvarez and Macovski published their technique [2] in February 1976, which was probably the first DECT theory. This method is a pre-reconstruction method, as it performs a correction on the radiographic images taken during the CT scan. As mentioned before, the reconstructed volume consists of linear attenuation coefficients and is calculated from 2D projections which contain the measurement of the intensity of a polychromatic beam, integrated over its whole spectrum. The attenuation coefficient determined in the reconstructed 3D volume is thus a linear attenuation coefficient at some kind of single average energy. Therefore, all information contained in the energy-dependent attenuation coefficient is lost. It is possible, however, to express the attenuation coefficient as a linear combination of energy-dependent basis functions:

$$\mu(x,y,E) = a_1(x,y)\frac{1}{E^3} + a_2(x,y)f_{KN}(E), \tag{6.1}$$

in which $f_{KN}(E)$ is the Klein-Nishina function:

$$f_{KN} = \frac{1+\alpha}{\alpha^2}\left[\frac{2(1+\alpha)}{1+2\alpha} - \frac{1}{\alpha}\ln(1+2\alpha)\right] + \frac{1}{2\alpha}\ln(1+2\alpha) - \frac{1+3\alpha}{(1+2\alpha)^2} \tag{6.2}$$

with $\alpha = E/510.975$ keV. The first part of Equation 6.1 is an approximation for the photoelectric effect, while the second part (Klein-Nishina) represents the energy dependence of Compton scattering (section 3.2). The basis set consists of two equations that describe the two main interaction processes in the typical energy range for X-ray CT. The coefficients of these equations can be expressed as follows:

$$\begin{aligned} a_1 &\approx K_1\frac{\rho}{A}Z^n, n \approx 4 \\ a_2 &\approx K_2\frac{\rho}{A}Z \end{aligned} \tag{6.3}$$

with K_1 and K_2 constants. While the photoelectric effect is strongly dependent on the atomic number, the Compton scattering depends on electron density, which is proportional to the mass density of a material. The coefficient a_2 thus provides information about the local density of the material. During a CT scan, a measurement of the line integral of the attenuation coefficient through the scanned object

is performed. The line integral through the sample can be expressed as:

$$\int \mu(x,y;E)ds = A_1 \frac{1}{E^3} + A_2 f_{KN}(E) \tag{6.4}$$

in which A_1 and A_2 are the line integrals over the coefficients a_1 and a_2:

$$\begin{aligned} A_1 &= \int a_1(x,y)ds, \\ A_2 &= \int a_2(x,y)ds. \end{aligned} \tag{6.5}$$

The purpose of this DECT technique is to reconstruct the coefficients $a_1(x,y)$ and $a_2(x,y)$. This requires two independent sources of information to determine A_1 and A_2, such as radiographies obtained with two different spectra. These equations can be written as:

$$\begin{aligned} I_1(A_1,A_2) &= T\int S_1(E)\exp\left[-\frac{A_1}{E^3} - A_2 f_{KN}(E)\right]dE \\ I_2(A_1,A_2) &= T\int S_2(E)\exp\left[-\frac{A_1}{E^3} - A_2 f_{KN}(E)\right]dE \end{aligned} \tag{6.6}$$

in which I_1 and I_2 represent the energy measured in a detector pixel, T is the total measurement time and $S_1(E)$ and $S_2(E)$ are different X-ray spectra. This set of line integrals can be solved as long as the Jacobian

$$J = det\begin{pmatrix} \partial I_1/\partial A_1 & \partial I_1/\partial A_2 \\ \partial I_2/\partial A_1 & \partial I_2/\partial A_2 \end{pmatrix} \tag{6.7}$$

is nonzero. Once the set of line integrals A_1 and A_2 are known for all projections, the functions a_1 and a_2 can be computed with a standard reconstruction algorithm.

This theory can be modified to be applied to radiographic projections as shown in Lehmann et al. [7]. Due to the superposition of different materials along the ray-path, this is not straightforward to do. The method shown in [7] allows a material to be removed from the image and the vacancy to be 'filled in' with a different material. The article also shows an experimental verification of the theory.

6.2.2 Rutherford's DECT theory

In the same year, in May 1976, a second DECT technique was presented by Rutherford et al. [3]. This second method allows for extraction of information on the electron density and the effective atomic number of the materials present in the sample. This is also achieved by combining two CT images obtained at two different X-ray beam spectra. The main difference with respect to the previous

technique is that this one is a post-reconstruction method. The image operations are thus performed on the reconstructed data and not on the radiographic projections. The disadvantage of this technique is that there can be a loss of accuracy due to artefacts such as streaking artefacts caused by beam hardening [8].

Rutherford showed that the linear attenuation coefficient for a particular material in function of photon energy can be expressed as:

$$\mu(E) = AE^{-B}Z^{C}N + \sigma(E)ZN + DE^{-F}Z^{G}N, \tag{6.8}$$

in which A, B, C, D, F and G are constants and N is the particle density and NZ thus represents the electron density. $\sigma(E)$ represents the Klein-Nishina cross section. The equation consists of three parts. The first part describes the photoelectric effect, the second part represents Compton scattering and the third part takes a correction for Rayleigh scattering and binding energy effects into account. Values for these constants were determined in [9]. With these coefficients, this equation becomes:

$$\mu(E) = 21.7E^{-3.30}Z^{4}.62N + \sigma(E)ZN + 1.17E^{-1.86}Z^{2}.92N. \tag{6.9}$$

By dividing the reconstructed attenuation coefficients obtained from two CT scans at different energies yields:

$$\frac{\mu(E_1)}{\mu(E_2)} = \frac{AE_1^{-B}Z^{C} + \sigma(E_1)Z + DE_1^{-F}Z^{G}}{AE_2^{-B}Z^{C} + \sigma(E_2)Z + DE_2^{-F}Z^{G}}. \tag{6.10}$$

Once the effective atomic number Z_{eff}, which fulfills Equation 6.10 is determined, Equation 6.8 can be used to calculate the particle density N of the material.

6.2.3 Three-material image-based decomposition

Another post-reconstruction method was developed by Vinegar and Wellington [6]. This method was also successfully applied by Granton et al. [10] and at UGCT. Each voxel in a reconstructed CT image contains a linear attenuation coefficient which can be expressed as a linear combination of the attenuation coefficients of each basis material in that voxel. The total attenuation in such a voxel can be expressed as

$$\mu = \mu_1 f_1 + \mu_2 f_2, \tag{6.11}$$

with f_1 and f_2 representing the volume fraction of materials 1 and 2, respectively. When CT scans are performed at two energies, a system of two equations is obtained

$$\begin{aligned} \mu_{E_1} &= \mu_{1,E_1} f_1 + \mu_{2,E_1} f_2 \\ \mu_{E_2} &= \mu_{1,E_2} f_1 + \mu_{2,E_2} f_2 \end{aligned} \tag{6.12}$$

with E_1 and E_2 representing the energies of the X-ray spectra used for the CT scans. μ_1 and μ_2 can be obtained from the images by measuring them in voxels consisting solely of materials 1 and 2, respectively.

In the case of a mix of two materials, a decomposition based on the set of equations shown in 6.12 can be carried out. An extension of this technique can be performed for a three-material decomposition. This can be done by adding a volume conservation constraint, and can be expressed as

$$f_1 + f_2 + f_3 = 1, \tag{6.13}$$

which means that the total volume of all fractions present in the volume is the volume of the voxel itself. For the three materials, Equations 6.12 can be rewritten as

$$\begin{aligned} \mu_{E_1} &= \mu_{1,E_1} f_1 + \mu_{2,E_1} f_2 + \mu_{3,E_1} f_3 \\ \mu_{E_2} &= \mu_{1,E_2} f_1 + \mu_{2,E_2} f_2 + \mu_{3,E_2} f_3. \end{aligned} \tag{6.14}$$

These three equations can be combined with a constraint that prevents the volume fractions from having negative values, as demonstrated in [10]. A scan at a third energy E_3 can be added to the set of equations

$$\mu_{E_3} = \mu_{1,E_3} f_1 + \mu_{2,E_3} f_2 + \mu_{3,E_3} f_3. \tag{6.15}$$

Together with this last fourth equation, the system is overdetermined but can still be solved by applying a minimisation of the mean squared difference between the calculated μ_c and measured μ_m attenuation coefficient at the three energies for all possible outcome fractions of the material. This squared difference can be written as

$$\Delta = \sum_{i=1}^{3} (\mu_{c,E_i} - \mu_{m,E_i})^2. \tag{6.16}$$

However, this method suffers from the same disadvantages as Rutherford's method. It is sensitive to beam hardening effects such as cupping and streaks because these effects cause a certain material to have different reconstructed attenuation coefficients in the same image, depending on the position in the sample.

6.2.4 Other DECT methods

Other methods such as raw data-based decomposition [8] and K-edge imaging [1] are extensively discussed by Pauwels [5] and will not be examined or used in the context of this work. Furthermore, an overview of dual-energy system setups [11] and practical applications are discussed there as well.

6.3 Dual energy at UGCT

Two methods are currently used at UGCT. The first technique is an implementation of three-material image-based decomposition (section 6.2.3). The second is an adaptation of Rutherford's method and is described extensively below. This second method uses simulated data of the tube and detector to characterise materials inside the scanned sample without the need for a calibration.

6.3.1 Decomposition method

The theoretical background of this method is described in section 6.2.3. By performing two CT scans, the following system of equations can be obtained and needs to be solved:

$$\begin{aligned} f_1 + f_2 + f_3 &= 1 \\ \mu_{E_1} &= \mu_{1,E_1} f_1 + \mu_{2,E_1} f_2 + \mu_{3,E_1} f_3 \\ \mu_{E_2} &= \mu_{1,E_2} f_1 + \mu_{2,E_2} f_2 + \mu_{3,E_2} f_3. \end{aligned} \tag{6.17}$$

Additionally, the non-negative constraint is also taken into account. Therefore, it is not straightforward to solve the set of equations. Originally, Granton et al. [10] used a matrix factorisation. At UGCT, a method proposed by Kacmarz [12] and further explained in [13] is used. By using this technique, even overdetermined systems can be solved.

This technique is implemented in a software tool developed at UGCT. The exact implementation and an explanation of the software tool can be found in [5].

6.3.2 Material characterisation with DECT

For a polychromatic beam that travels through a slab of a certain material with thickness d, the Lambert-Beer law can be written as

$$I = \sum_{i=0}^{E_{max}} I_i = \sum_{i=0}^{E_{max}} I_{0,i} exp(-\frac{\mu_i}{\rho}\rho d), \tag{6.18}$$

with μ_i/ρ representing the mass attenuation coefficient in energy bin i of the material and ρ signifying the density of the material. Furthermore, the reconstructed linear attenuation coefficient of the material in the slab can be expressed as

$$\mu = -\frac{1}{d} \ln\left(\frac{I}{I_0}\right). \tag{6.19}$$

Replacing I with Equation 6.18 and I_0 by $\sum_i I_{0,i}$, this equation can be rewritten as

$$\mu = -\frac{1}{d} \ln \left(\frac{\sum_i I_{0,i} \exp -\frac{\mu_i}{\rho} \rho d}{\sum_i I_{0,i}} \right). \tag{6.20}$$

By approximating the exponential function and the logarithmic function by its series expansion of the first order and taking into account that $I_{0,i}$ can be written in function of the emitted spectrum $S_i^{''}$ and detector efficiency $D_{inc,i}$, it is possible to rewrite this equation as (appendix C)

$$\mu = \rho \frac{\sum_i S_i^{''} D_{inc,i} \mu/\rho(E_i)_z}{\sum_i S_i^{''} D_{inc,i}}. \tag{6.21}$$

In this equation, i represents an energy bin. The mass attenuation coefficient of the material z in energy bin i is given by $\mu/\rho(E_i)_z$. $S_i^{''}$ and $D_{inc,i}$ represent the photons emitted by the source (with filtration) and mean energy detected per incident photon by the detector in energy bin i, respectively. All information about the tube parameters (voltage and power/current) and filtration are thus processed in $S^{''}(E)$ (appendix C) and the information about the detector in $D_{inc}(E)$ (section 4.3). When a material, represented here by $\mu/\rho(E)_z$ and its density are known, the reconstructed attenuation can thus be calculated.

The mass attenuation coefficient $\mu/\rho(E)_z$ is only dependent on the energy E and the composition of the material, represented here by z. Contrary to conventional DECT techniques, here z is not a numerical value that represents the effective atomic number of the composition, but is instead an index that corresponds to the energy dependent attenuation coefficient $\mu/\rho(E)_z$ of the material. These attenuation coefficient data is obtained from the XCOM database of NIST [14].

When a sample is scanned at a certain scanner, a reconstructed attenuation coefficient can be determined in each voxel of the reconstructed volume. Now, it is possible to search for a material that corresponds to this reconstructed attenuation coefficient. This material is characterised by two elements: its composition and its density. This means that in Equation 6.21, two unknowns ρ and z are present if the emitted spectrum and the detector sensitivity are known. This also means that a set of (at least) two linear independent equations is needed to obtain a unique solution for ρ and $\mu/\rho(E)_z$. Performing a CT scan at two different energies yields the following equations:

$$\mu_1 = \rho \frac{\sum S_{1,i}^{''} D_{inc,1,i} \mu/\rho(E_i)_z}{\sum S_{1,i}^{''} D_{inc,1,i}} \tag{6.22}$$

and

$$\mu_2 = \rho \frac{\sum S''_{2,i} D_{inc,2,i} \mu/\rho(E_i)_z}{\sum S''_{2,i} D_{inc,2,i}}. \tag{6.23}$$

With this system of equations, a solution for ρ and $\mu/\rho(E)_z$ can be found. Mathematically, this can be done when both equations are linear independent; physically, this comes down to using two spectra which differ significantly. Typically, a low-energy spectrum with a thin filter to reduce beam hardening can be combined with a heavily filtered high-energy spectrum. Dividing both reconstructed linear attenuation coefficients results in an equation that is only dependent on the composition z and thus $\mu/\rho(E)_z$,

$$\frac{\mu_1}{\mu_2} = \frac{\sum S''_{1,i} D_{inc,1,i} \mu/\rho(E_i)_z}{\sum S''_{1,i} D_{inc,1,i}} \Big/ \frac{\sum S''_{2,i} D_{inc,2,i} \mu/\rho(E_i)_z}{\sum S''_{2,i} D_{inc,2,i}}. \tag{6.24}$$

By minimising the following equation for each voxel in the reconstructed volume,

$$\frac{\mu_1}{\mu_2} - \frac{\sum S''_{1,i} D_{inc,1,i} \mu/\rho(E_i)_z}{\sum S''_{1,i} D_{inc,1,i}} \Big/ \frac{\sum S''_{2,i} D_{inc,2,i} \mu/\rho(E_i)_z}{\sum S''_{2,i} D_{inc,2,i}} \tag{6.25}$$

for all materials present, the composition of the material can be found. Practically, equation 6.25 is calculated for a series of materials labelled by the index $z = 1, 2, 3, ...$ The material for which the equation has a minimal value is taken as a solution and is characterised as the material inside the corresponding voxel.

Furthermore, from Equations 6.22 and 6.23, ρ can be determined. In addition to Equation 6.25, ρ and z can be determined simultaneously by adding the following two expressions to the minimisation:

$$\mu_1 - \rho_z \frac{\sum S''_{1,i} D_{inc,1,i} \mu/\rho(E_i)_z}{\sum S''_{1,i} D_{inc,1,i}} \tag{6.26}$$

and

$$\mu_2 - \rho_z \frac{\sum S''_{2,i} D_{inc,2,i} \mu/\rho(E_i)_z}{\sum S''_{2,i} D_{inc,2,i}} \tag{6.27}$$

in which ρ_z is used instead of ρ. Here ρ_z is linked to the composition z. A density which is likely to occur for a certain composition is used in this second method. For example, the density for H_2O is 1.00 g/cm^3 when using this method because water is very unlikely to occur with a density which differs considerably from this one. Note that in this method only the composition is fitted for the material in the voxel. Afterwards, Equations 6.22 and 6.23 are still used to fit a density to the material. This fitted density can deviate from the density used during the fit of the composition.

By using this technique, it is possible to change the parameter space of the reconstructed values. This means that instead of the reconstructed attenuation coefficients μ_1 and μ_2 obtained from DECT, a transformation can be made to the composition z and density ρ in each voxel. These latter parameters are, in contrast to the former, physical properties of the material inside that voxel; μ_1 and μ_2 are also dependent on the scanner system used, while z and ρ do not depend on the scanner. Applications of this technique on simulated and real data are shown in the next section.

Note that to use this technique, the spectrum $S^{''}(E)$ and the mean deposited energy per incident photon in the detector $D_{inc}(E)$ need to be known. These parameters can be simulated as described in Chapter 4.

Densitometry

When the composition of the material is known in a reconstructed volume, but the density can cover a range of values, Equation 6.21 can be solved for each voxel in the reconstructed volume. This way, a density map of the reconstructed sample can be obtained. One application of this technique on a wood sample with unknown density is shown in the next section.

6.4 Applications of DECT technique

In this section, the practical use of the DECT technique discussed in section 6.3.2 is tested on the basis of simulations performed with Arion and on a real sample scanned at HECTOR. Densitometry is performed with a wood sample. Where not specifically mentioned in this section, Equations 6.25, 6.26 and 6.27 are used to fit a material.

6.4.1 A virtual phantom

To test the DECT technique, a virtual phantom described in Figure 6.1 is used. This phantom contains nine materials in addition to air, and contains mainly liquid water. Two scans of this phantom were simulated for the HECTOR scanner at a tube voltage of 50 and 160 kV. For both scans, a filtration of 1 mm aluminium was used. For both spectra, a scan with and without noise was performed. This was done to test how well the technique can work in the ideal and real case. In the case of simulated data, the spectra and detector efficiency used in Equation 6.21 are exactly known. In reality, there will always be a slight difference between these simulated spectra and efficiencies and those of a real scan system.

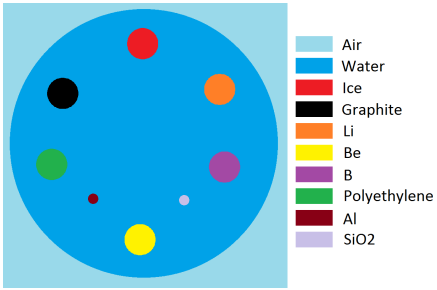

Figure 6.1: A slice of the virtual phantom used for testing the proposed DECT technique.

Figure 6.2 shows a reconstructed slice of the noiseless and normal simulation, with noise, performed for both spectra. It can be seen that the aluminium and silicon dioxide cause weak streaking artefacts in the reconstructions performed for the simulated data using the low-energy spectrum. Two methods are used to reconstruct the composition and density. In the first method, the material in a pixel is determined by only using Equation 6.25 and a corresponding density is then calculated. In the second method, Equations 6.26 and 6.27 are added to the optimisation process in addition to Equation 6.25. The possible density and composition of the material is thus taken into account when a material is fitted.

Figure 6.3 shows the reconstructed composition for the noiseless and realistic data for both methods. For the noiseless data, the first method already yields a very good result. For the realistic data, the inclusion of estimated densities for different compositions can significantly improve the correctness of the material characterisation. The material characterisation can thus benefit from this prior knowledge. Furthermore, the Al is still falsely labelled as SiO_2. Table 6.1 lists the percentages of incorrectly labelled voxels for the different scans and methods.

Table 6.1: Percent of pixels labelled incorrectly by the different methods to perform the material characterisation.

Scan and method	Wrongly labeled pixels (%)
Noiseless (Z)	2.73
Noiseless (Zρ)	0.48
With noise (Z)	30.57
With noise (Zρ)	3.93

Figure 6.4 shows the density map corresponding with Figures 6.3(b) and 6.3(d). In Table 6.2, the densities corresponding to the compositions fitted for the realistic reconstructions are shown. Note that although an expected density is used to fit the

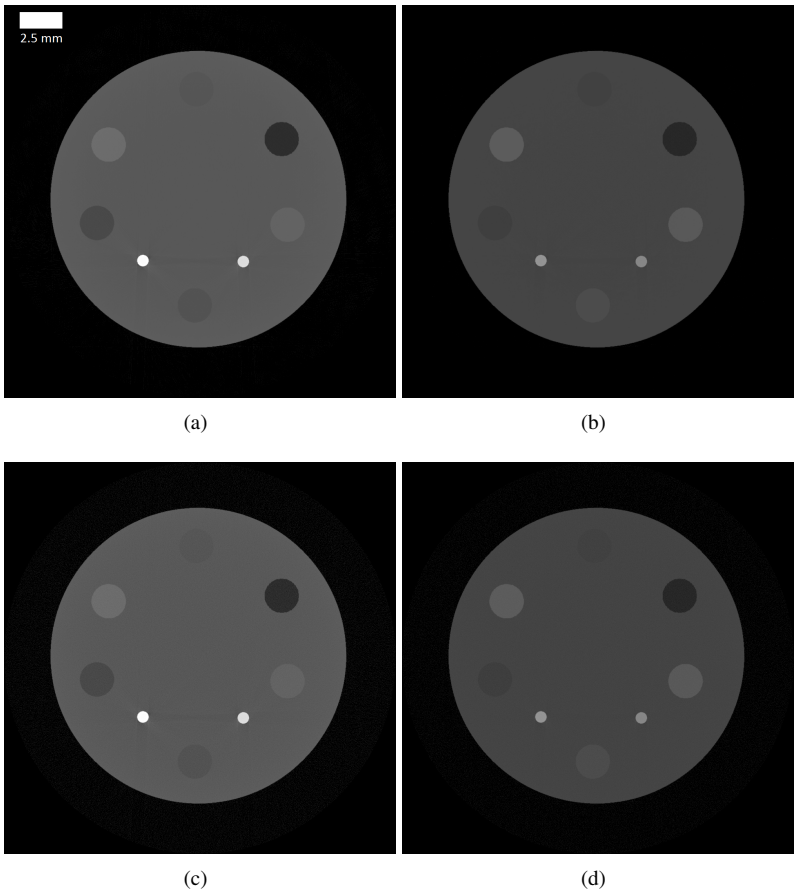

Figure 6.2: Reconstructed slices of the simulated phantom. Noiseless (top) and simulations that include noise (bottom) were performed at 50 kV (left) and 160 kV (right), both with a filtration of 1 mm Al.

materials, a density is still fitted once the composition inside a voxel is determined.

The previous results shown are not able to fit the Al correctly. This is because the Al inclusion present in the phantom is surrounded by water. The used method assumes that a spectrum $S^{''}(E)$ reached each voxel inside the sample and thus treats each voxel as if it is not surrounded by the sample. A more correct estimation for the attenuation coefficient for Al can be obtained by adding an extra filtration to the spectrum. Figure 6.5 shows the results of the material characterisation when an extra filter of 9 mm of H_2O is added to the spectrum used in the fitting process.

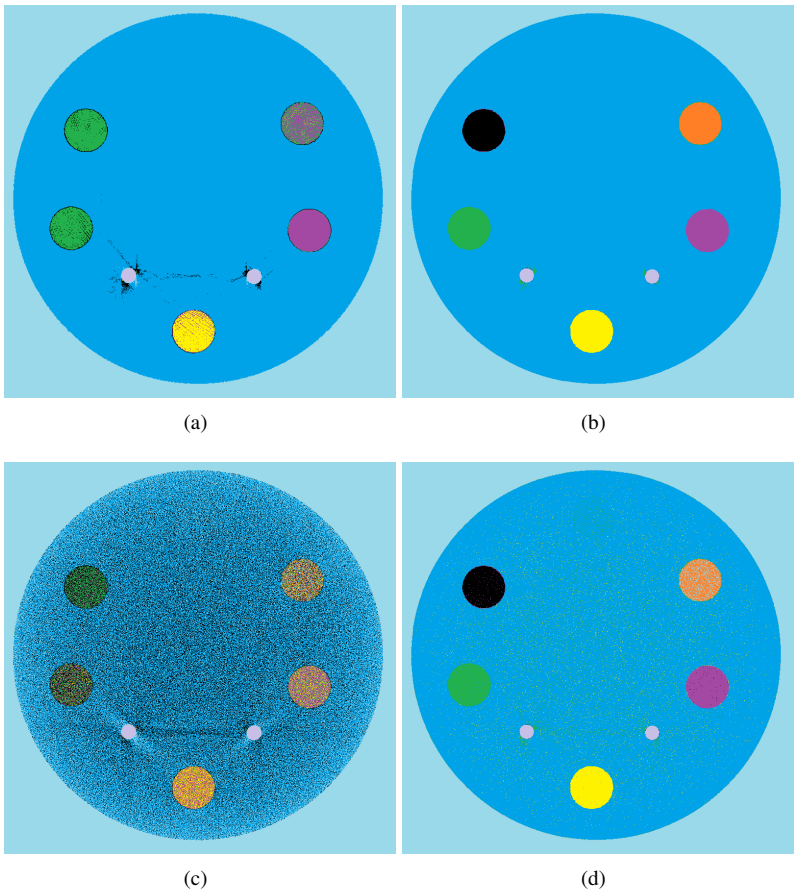

Figure 6.3: Reconstructed slices of the simulated phantom. The noiseless data (top) and data containing noise (bottom) are compared. Once only Equation 6.25 was used (left) and once Equation 6.26 and 6.27 were taken into account as well (b).

By doing this, the aluminium inclusion is labelled correctly and it does not affect the labelling of the other materials. The percentage of incorrectly labelled voxels when using this filtration is 1.41%. The densities determined from the density map corresponding with this method are listed in Table 6.3. On average the deviations of the measured density with this method is smaller than when the spectrum is not filtered, 4.04% against 4.64%, but when the individual deviations are compared, 6 out of 9 are 'better' without the filtered spectrum. However, the difference in the determination of the density is minimal between both methods. The main advantage of applying the filtered spectrum is that the correct composition inside a voxel can be determined more easily.

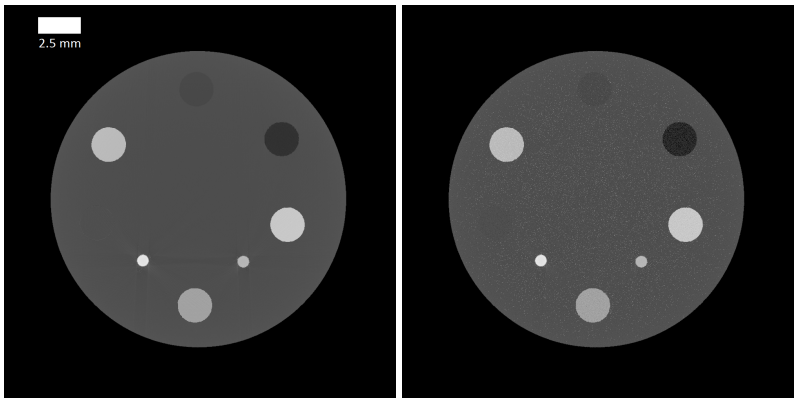

(a) (b)

Figure 6.4: Density maps corresponding with the noiseless (a) and realistic data (b).

Table 6.2: Densities measured in the density map of the realistic data. On average a deviation of 4.64% is found.

Material	Real	measured ρ (g/cm^3)	measured σ_ρ (g/cm^3)	dev(%)
H_2O	1.000	0.96	0.15	4.00
Ice(H_2O)	0.917	0.90	0.11	1.85
Graphite	2.267	2.223	0.074	1.94
Li	0.534	0.48	0.21	10.11
Be	1.848	1.920	0.079	3.75
B	2.370	2.373	0.072	0.13
Polyethylene	0.930	0.936	0.060	0.65
Al	2.699	2.675	0.026	0.89
SiO_2	2.648	2.158	0.024	18.50

Table 6.3: Densities measured in the density map of the realistic data when an extra filter is applied to the calculation of the spectrum $S''(E)$. On average a deviation of 4.04% is found.

Material	Real	measured ρ (g/cm^3)	measured σ_ρ (g/cm^3)	dev(%)
H_2O	1.000	1.015	0.086	1.50
Ice(H_2O)	0.917	0.955	0.062	4.14
Graphite	2.267	2.333	0.059	2.91
Li	0.534	0.49	0.20	8.24
Be	1.848	1.93	0.13	4.44
B	2.370	2.38	0.12	0.42
Polyethylene	0.930	0.956	0.079	2.80
Al	2.699	2.512	0.025	6.93
SiO_2	2.648	2.517	0.027	4.95

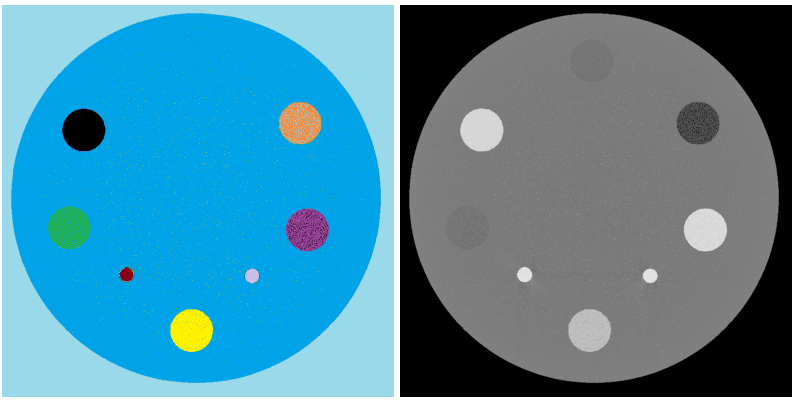

(a) (b)

Figure 6.5: Composition map (a) and density map (b) obtained for the realistic data when an extra water filter is applied in the calculation of the spectrum $S^{''}(E)$.

6.4.2 Organic samples

Figure 6.6 shows the reconstructed slices of a mouse leg of two scans taken at HECTOR. These scans were both performed at a tube voltage of 50 kV and with a filtration of 1 mm Al and 3 mm Al. Note that these are two different spectra due to the different filtration used. The composition map can be found in Figure 6.6(c). During the fitting procedure an extra filtration of 5 mm muscle was added to the spectrum $S^{''}(E)$.

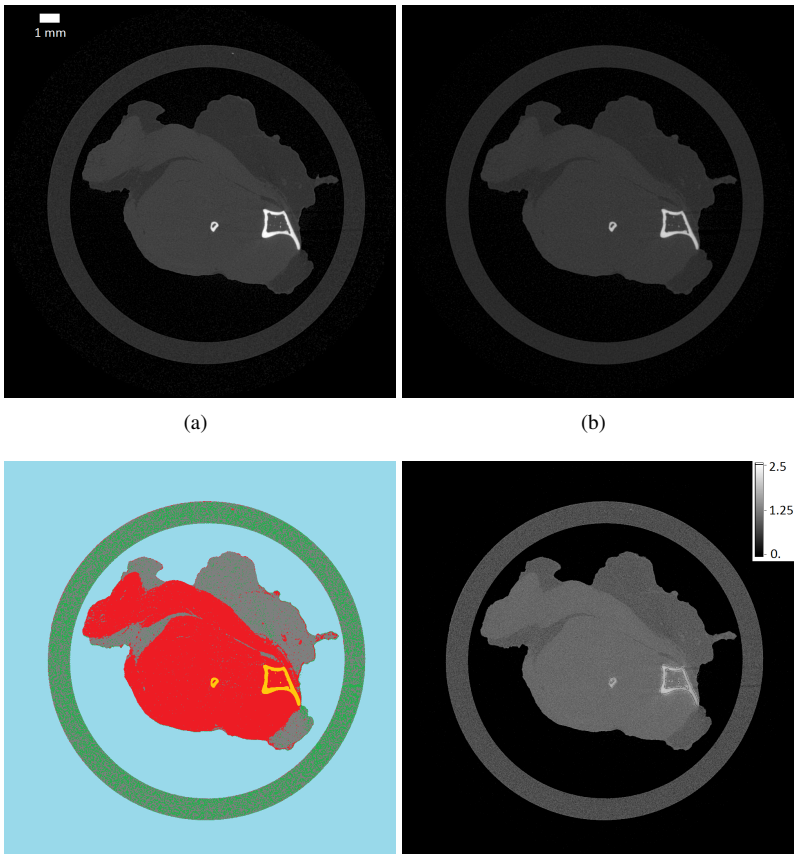

(a) (b)

(c) (d)

Figure 6.6: Reconstructed slices of a mouse leg taken at HECTOR using 50 kV with a filtration of 1 mm (a) and 3 mm (b) aluminium. The material characterisation method results in a composition map (c) and density map (d). Adipose tissue is represented in grey, muscle in red, cortical bone in yellow , polyethylene in green and air in light blue.

Figure 6.7 presents the reconstructed slices of a butter sample taken at HECTOR. The scans were performed at a tube voltage of 40 kV and 160 kV with a filtration of 1 mm aluminium. The composition map can be seen in Figure 6.7(c). An extra filtration of 7 mm butter was applied for the spectrum $S^{''}(E)$ used during the fitting procedure.

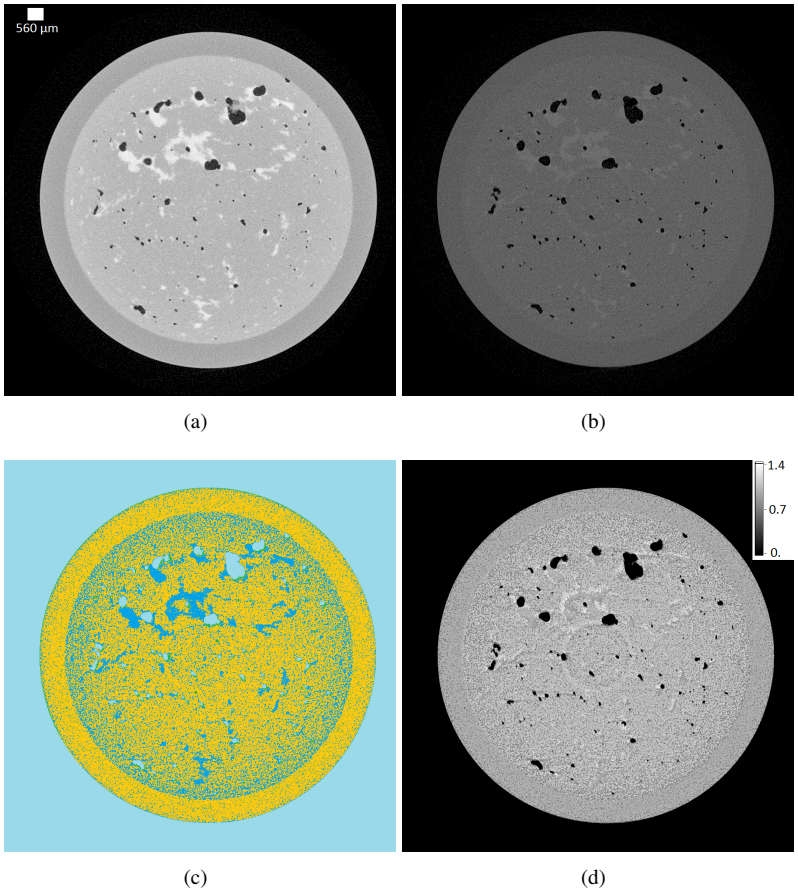

(a) (b)

(c) (d)

Figure 6.7: Reconstructed slices of a butter sample with taken at HECTOR at a tube voltage of 40 kV (a) and a tube voltage of 160 kV with a filtration of 1 mm aluminium (b). Applying the material characterisation method results in a composition map (c) and density map (d). Air is represented in light blue, water in dark blue and butter in yellow.

6.4.3 Densitometry

In Figure 6.8 two reconstructed slices of two different wood samples can be observed. The first sample, containing six different wood samples and a piece of POM, was scanned in a POM cylinder with holes drilled in it. The second sample, containing different wood and POM pieces, was scanned in a cylindrical floral foam. In both samples, pieces of POM are inserted in one or more holes next to different pieces of wood. The POM has the same composition as wood and is normally used as a calibration material to determine the density of the wood samples [15–17]. The samples were scanned at HECTOR with a tube voltage of 140 kV and a filtration of 0.5 mm Al was used for both.

Both scanned samples were reconstructed with and without a standard beam hardening correction of the reconstruction package Octopus. Figure 6.8(a) and 6.8(b) show a reconstructed slice of both samples for which a beam hardening correction was applied. By using Equation 6.22 with the prior knowledge that the composition of all materials present in the sample is POM, a fit for the density can be made with the use of a single scan. Figures 6.8(c) and 6.8(d) show the density maps for a beam hardening corrected reconstructed slice of both scans taken at HECTOR.

The density of the POM present in the samples could be determined for the four reconstructions and is given in Table 6.4. Although it is not a straightforward process to apply a 'correct' beam hardening in a reconstructed volume, these results show clearly that such a correction can drastically improve the results obtained with this method. No density for the wood inside these samples was determined as a density estimation of the wood is based on the POM scanned in this sample. The correctness of the wood densities will thus be of the same order as the ones determined for POM.

Table 6.4: Densities obtained from the reconstructed data for POM (ρ = 1.40 g/cm^3) without and with beam hardening correction (BHC).

Slice	Density (g/cm^3)	Error on density (g/cm^3)
Scan 1	1.31	0.04
Scan 2	1.30	0.02
Scan 1 with BHC	1.42	0.05
Scan 2 with BHC	1.39	0.02

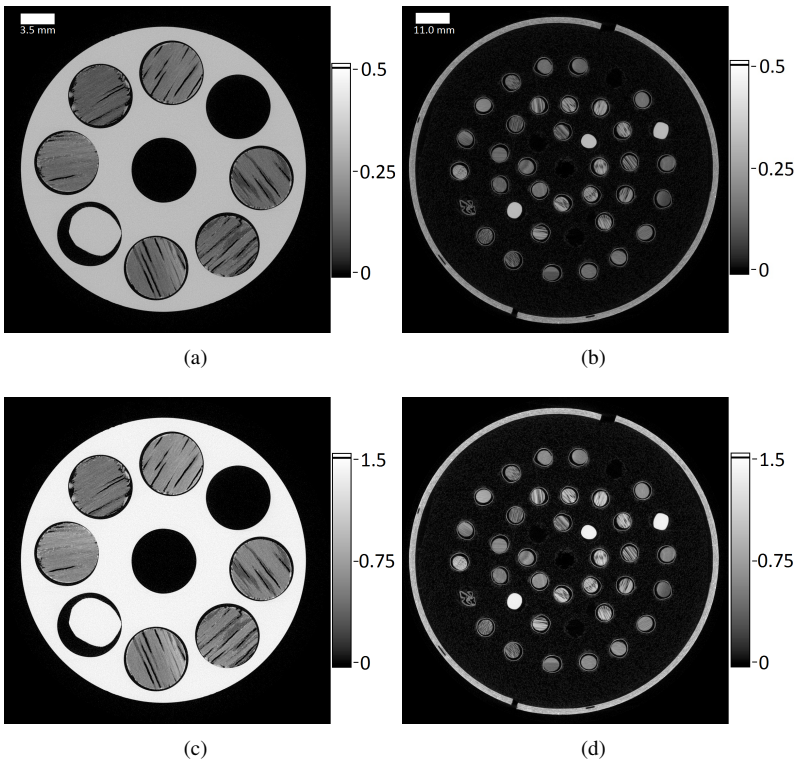

Figure 6.8: Reconstructed slices of the wood sample in a POM container (a) and a floral foam container (b) are shown. The corresponding reconstructed density maps of these samples are shown in (c) and (d).

6.5 Outlook

A new DECT method based on Rutherford's theory was proposed in this chapter. The method uses a simulated tube spectrum $S^{''}(E)$ and a simulated mean energy deposited in the detector per incident photon $D(E)$. The method was successfully applied on virtual and real samples and could be used for densitometry by CT as well. Although the initial results shown here are promising, the method can be further improved.

The DECT method assumes that a voxel is passed through with the initial spectrum $S^{''}(E)$ as if that voxel is not surrounded by the rest of the sample. As shown in this chapter, the method works better when the mean ray-path through the sample is taken into account. This is done by filtering the spectrum $S^{''}(E)$ with a filter with the composition and density of the bulk of the material and a thickness roughly equal the mean ray-path through the bulk of the material. This problem can be coped with by including this method, together with the forward projection simulator, Arion, in an iterative reconstruction algorithm. Furthermore, this should also address the issue of other beam hardening artefacts such as cupping or streaking artefacts, as well as the reconstructed volume containing materials characterised by composition and densities instead of reconstructed attenuation coefficients, which are not physical parameters of a material. A disadvantage of the method presented in this chapter is that partial volume effects are not taken into account, and thus only one material can be labelled to a pixel. This can especially be a problem for samples with a microstructure which cannot be resolved at the resolution of the CT scan.

The work presented in this chapter, in combination with the previous chapters, is thus a first step in the direction of direct material characterisation during the reconstruction step of laboratory-/industrial-based CT data obtained with an energy-integrating detector without the need for calibration materials. An iterative reconstruction algorithm that attempts to achieve this material characterisation benefits from a correct model for the possible tube spectra and detector efficiencies (chapter 4), a realistic forward projection simulator (chapter 5) and a dual-energy method to determine the composition and density in a voxel of the reconstructed volume.

References

[1] A. Sarnelli, H. Elleaume, A. Taibi, M. Gambaccini, and A. Bravin. *K-edge digital subtraction imaging with dichromatic x-ray sources: SNR and dose studies*. Physics in Medicine and Biology, 51(17):4311–28, 2006.

[2] R. E. Alvarez and A. Macovski. *Energy-selective reconstructions in X-ray computerized tomography*. Physics in Medicine and Biology, 21(5):733–744, 1976.

[3] R. A. Rutherford, B. R. Pullan, and I. Isherwood. *Measurement of Effective Atomic Number and Electron-Density Using an Emi Scanner*. Neuroradiology, 11(1):15–21, 1976.

[4] T. G. Flohr, C. H. McCollough, H. Bruder, M. Petersilka, K. Gruber, C. Suss, M. Grasruck, K. Stierstorfer, B. Krauss, R. Raupach, A. N. Primak, A. Kuttner, S. Achenbach, C. Becker, A. Kopp, and B. M. Ohnesorge. *First performance evaluation of a dual-source CT (DSCT) system*. European Radiology, 16(2):256–268, 2006.

[5] E. Pauwels. *Optimal use of the polychromaticity in X-ray microtomography for dual energy methods and contrast agent imaging*. Phd thesis, Ghent University, 2017.

[6] H. J. Vinegar and S. L. Wellington. *Tomographic imaging of three-phase flow experiments*. Review of Scientific Instruments, 58(1):96–107, 1987.

[7] L. A. Lehmann, R. E. Alvarez, A. Macovski, W. R. Brody, N. J. Pelc, S. J. Riederer, and A. L. Hall. *Generalized image combinations in dual KVP digital radiography*. Medical Physics, 8(5):659–67, 1981.

[8] W. A. Kalender, W. H. Perman, J. R. Vetter, and E. Klotz. *Evaluation of a prototype dual-energy computed tomographic apparatus. I. Phantom studies*. Medical Physics, 13(3):334–9, 1986.

[9] W. H. Payne, W. D. McDavid, R. G. Waggener, M. J. Dennis, and V. J. Sank. *Extrapolation of linear attenuation coefficients of biological materials from diagnostic-energy x-ray levels to the megavoltage range*. Medical Physics, 4(6):505–7, 1977.

[10] P. V. Granton, S. I. Pollmann, N. L. Ford, M. Drangova, and D. W. Holdsworth. *Implementation of dual- and triple-energy cone-beam micro-CT for postreconstruction material decomposition*. Medical Physics, 35(11):5030–42, 2008.

[11] Cynthia H. McCollough, Shuai Leng, Lifeng Yu, and Joel G. Fletcher. *Dual- and Multi-Energy CT: Principles, Technical Approaches, and Clinical Applications*. Radiology, 276(3):637–653, 2015. PMID: 26302388.

[12] S. Kacmarz. *Angenäherte auflösung von systemen linearer gleichungen*. Bulletin International de l'AcadÃ©mie Polonaise des Sciences et des Lettres, 35:355–357, 1937.

[13] K. Tanabe. *Projection method for solving a singular system of linear equations and its applications*. Numerische Mathematik, 17(3):203–214, 1971.

[14] `http://www.nist.gov/pml/data/xcom/`.

[15] Maaike De Ridder, Jan Van den Bulcke, Dries Vansteenkiste, Denis Van Loo, Manuel Dierick, Bert Masschaele, Yoni De Witte, David Mannes, Eberhard Lehmann, Hans Beeckman, Luc Van Hoorebeke, and Joris Van Acker. *High-resolution proxies for wood density variations in Terminalia superba*. Annals of Botany, 107(2):293–302, 2011.

[16] Jan Van den Bulcke, Erik LG Wernersson, Manuel Dierick, Denis Van Loo, Bert Masschaele, Loes Brabant, Matthieu Boone, Luc Van Hoorebeke, Kristof Haneca, Anders Brun, Cris L Luengo Hendriks, and Joris Van Acker. *3D tree-ring analysis using helical X-ray tomography*. Dendrochronologia, 32(1):39–46, 2014.

[17] Tom De Mil, Astrid Vannoppen, Hans Beeckman, Joris Van Acker, and Jan Van den Bulcke. *A field-to-desktop toolchain for X-ray CT densitometry enables tree ring analysis*. Annals of Botany, 2016.

7
Conclusion and outlook

In X-ray μCT, numerous parameters and physical properties of the scanner influence the reconstructed attenuation coefficient obtained in each voxel of the 3D volume. Optimising these scanner parameters is therefore a problem that is anything but simple. In order to cope with this challenge, a method was developed to predict and simulate the physical properties of such scanners as accurately as possible.

After discussing all physical processes that occur during a CT, such as photon and electron interactions with matter and the wave properties of X-rays, Monte Carlo simulations of the main components of a CT scanner were described to model their behaviour. For the sources available at UGCT, spectra could be simulated and a model for the secondary spot in the transmission tube mounted at Medusa could also be proposed. Furthermore, the detectors could be modelled as well, and their efficiency and energy deposition in the scintillator were successfully simulated. In addition to these Monte Carlo simulations, the Line Spread Profile (LSF) for the Perkin Elmer detector was measured and a model was fitted to the measured data that could be included in the CT simulations later on.

In chapter 5, the developed projection simulator, Arion, was thoroughly discussed. A geometry is included in Arion that allows the user to describe any possible trajectory for the source, sample and detector imaginable during a CT scan, which makes it particularly useful for exploring the possibilities of industrial CT setups in which only a limited angular range and number of projections are

available. These simulations have much to offer in terms of practically feasible solutions for specific problems. Furthermore, the simulation tool is implemented on a GPU, which drastically reduces the computation time of the simulations.

Apart from the simulator itself, various other useful tools are available which make it easier to handle the data (Material Creator and Image Handler) and to provide additional information about the physical properties of a CT scan (Setup Optimiser). Furthermore, Arion was comprehensively tested for three scanners available at UGCT: Nanowood, Medusa and HECTOR. Simulated and real data are in good agreement with each other in terms of reconstructed attenuation and noise measured in reconstructed slices at the different scanners. Deviations of a few percentage points were found between the simulated and real data, which is overall a very satisfactory result.

Additionally, a method to model a secondary spot and the MTF was described. These models were applied to the simulated data to include a secondary spot or MTF in the simulated projections. Although the initial results are promising, a great deal of work still needs to be performed in order to achieve more accurate models of these effects.

Next, it was shown how Arion can be used to optimise scanning conditions for different applications. By using a simulator to optimise scanning parameters, it is not only possible to take a much larger parameter space into account, but the real scanner operation time, and thus cost, can be reduced drastically. This feature of Arion was used extensively for the samples that needed to be scanned in the context of the TomFood project at UGCT.

In the last chapter, a new DECT method was proposed to perform material characterisation in the voxels of a reconstructed volume. In each voxel of the volume, a composition and density can be calculated based on simulated spectra and detector efficiencies. Furthermore, this method was successfully applied to simulated and real data obtained at HECTOR.

Outlook

Although Arion is able to predict real CT scans in a highly accurate manner, further improvements are still possible. It was shown here that including a secondary spot, if present, and the MTF of the detector in the simulation can further improve the results; nevertheless, further research is needed to model and include them in the simulator in a more feasible way than achieved here. In addition, wave

effects are neglected in Arion, but as seen in various samples scanned in the context of TomFood, this effect can play a very important role in X-ray CT. In order to improve the physical correctness, a method to include these can be added. Also, scattering is neglected during the simulations. Including scattered photons in the simulations can improve its physical correctness.

The initial results obtained with the proposed DECT method are promising, though much work can still be done to improve this method. Obtaining better simulations of the tube spectra and detector efficiencies can be a first step in this process. Unfortunately, many manufacturers are not eager to share the specific details of their developed tubes or detectors, which can make accurate simulations difficult since the correct parameters and geometry of these components are not always available.

The proposed DECT method also suffers from the polychromatic behaviour of X-ray CT, e.g. beam hardening can influence the results. Including the method together with the developed projection simulator, Arion, in an iterative reconstruction algorithm can help to tackle this problem and solve or at least reduce all beam hardening artefacts present in polychromatic X-ray CT. Furthermore, this iterative algorithm should be able to reconstruct the composition and density of a material inside a voxel of a reconstructed 3D volume. The work presented in this thesis is thus a first step in this direction, which will hopefully be further explored.

A

Tait-Bryan angles and coordinate transformations

Tait-Bryan angles are used to describe the transformation of an object around three axes. The difference between these angles and Euler angles is the use of the rotation axes. The Tait-Bryan angles describe a rotation about three distinct axes (x, y, z), while Euler angles use the same axis for the first and third rotation. This appendix describes the rotation around three axes and the complete coordinate transformation used in Arion. The reason why Tait-Bryan angles are chosen over Euler angles here is that it is more intuitive for a user to describe a rotation around the initial axes of an object rather than to make a rotation around an axis that turns along with each rotation. A mathematical model to describe such a rotation is described below.

A.1 Rotation around one axis

A rotation around an angle α around the x-axis can be written as:

$$X(\alpha) = \begin{bmatrix} 1 & 0 & 0 \\ 0 & \cos(\alpha) & -\sin(\alpha) \\ 0 & \sin(\alpha) & \cos(\alpha) \end{bmatrix} \tag{A.1}$$

A rotation around an angle β around the y-axis can be written as:

$$Y(\beta) = \begin{bmatrix} \cos(\beta) & 0 & \sin(\beta) \\ 0 & 1 & 0 \\ -\sin(\beta) & 0 & \cos(\beta) \end{bmatrix} \tag{A.2}$$

A rotation around an angle γ around the z-axis can be written as:

$$Z(\gamma) = \begin{bmatrix} \cos(\gamma) & -\sin(\gamma) & 0 \\ \sin(\gamma) & \cos(\gamma) & 0 \\ 0 & 0 & 1 \end{bmatrix} \tag{A.3}$$

A.2 3D rotation matrix

The 3D rotation matrix depends on which order the three rotations are performed. For every application in this work, the same rotation order is used. The rotation around the y-axis is performed first, followed by the rotation around the x-axis, and the rotation around the z-axis is performed last. The final rotation matrix is then obtained by multiplying the three separate matrices:

$$R(\alpha,\beta,\gamma) = Z(\gamma)X(\alpha)Y(\beta) = \begin{bmatrix} c_\beta c_\gamma - s_\alpha s_\beta s_\gamma & -c_\alpha s_\gamma & c_\gamma s_\beta + c_\alpha s_\alpha s_\beta \\ c_\beta s_\gamma + c_\gamma s_\alpha s_\beta & c_\alpha c_\gamma & s_\beta s_\gamma - c_\beta c_\gamma s_\alpha \\ -c_\alpha s_\beta & s_\alpha & c_\alpha c_\beta \end{bmatrix}. \tag{A.4}$$

The cosines and sines are shortened as c and s, respectively, with the angle as an index. This rotation matrix can be created for each component, resulting in R_{source}, R_{sample} and $R_{detector}$.

A.3 Coordinate transformations

In Arion, the user can define a position and orientation for all three main components of a CT scanner. This makes this geometry an overdetermined system. For the ease of calculations, a coordinate transformation is performed such that the sample is always placed in the origin of the main coordinate system with base $\{\vec{e_x}, \vec{e_y}, \vec{e_z}\}$, and it does not rotate during a complete CT scan, regardless of which geometry is used.

For each projection, a position of the source ($\vec{r}_{source}$), sample ($\vec{r}_{sample}$) and detector ($\vec{r}_{detector}$) can be given as input. In addition to these vectors, the initial orientations of the source and detector are determined by

$$\begin{aligned} \vec{n}_{source} &= (0,1,0) \\ \vec{n}_{detector} &= (0,-1,0) \end{aligned} \tag{A.5}$$

which are the normal vectors of both components. $\vec{n}_{source}$ points in the direction of the central axis of the conical beam emitted from the source, and $\vec{n}_{detector}$ is defined perpendicular to the surface of the detector. These initial directions of source and detector are rotated with the corresponding rotation matrices, determined from the rotation angles for each component, which can also be given as input in the GUI of Arion.

The transformed positions of the source ($\vec{r'}_{source}$), sample ($\vec{r'}_{sample}$) and detector ($\vec{r'}_{source}$) detector are then given by:

$$\begin{aligned} \vec{r'}_{sample} &= \vec{0} = [\vec{r}_{sample} - \vec{r}_{sample}], \\ \vec{r'}_{source} &= R^{-1}_{sample}[\vec{r}_{source} - \vec{r}_{sample}], \\ \vec{r'}_{detector} &= R^{-1}_{sample}[\vec{r}_{detector} - \vec{r}_{sample}], \end{aligned} \tag{A.6}$$

and the transformed directions of the source ($\vec{n'}_{source}$) and detector ($\vec{n'}_{detector}$) are given by:

$$\begin{aligned} \vec{n'}_{source} &= R^{-1}_{sample} R_{source} \vec{n}_{source}, \\ \vec{n'}_{detector} &= R^{-1}_{sample} R_{detector} \vec{n}_{detector}. \end{aligned} \tag{A.7}$$

The centre of the sample is then located at $\vec{0}$, and the grid of the voxelised virtual volume aligns with the coordinate system $\{\vec{e_x}, \vec{e_y}, \vec{e_z}\}$. Figure A.1 shows a schematic representation of the transformed positions and orientations.

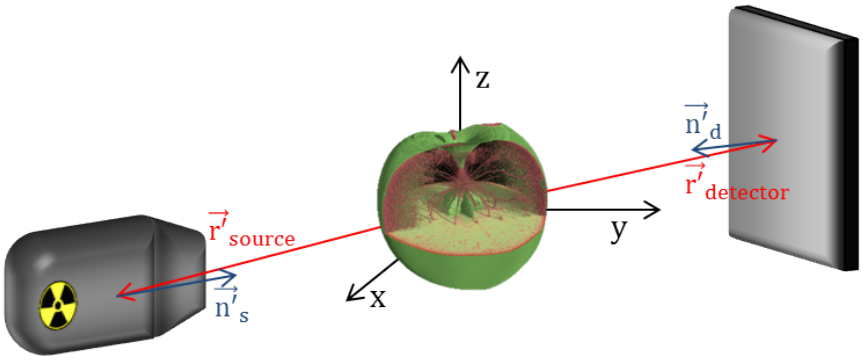

Figure A.1: Schematic representation of the transformed positions and normal vectors of tube and detector.

B

Comparison of simulated and real data

This appendix shows the line profiles of transmission and reconstructed images of the scans and simulations performed in chapter 5.

B.1 Transmission data

B.1.1 Nanowood

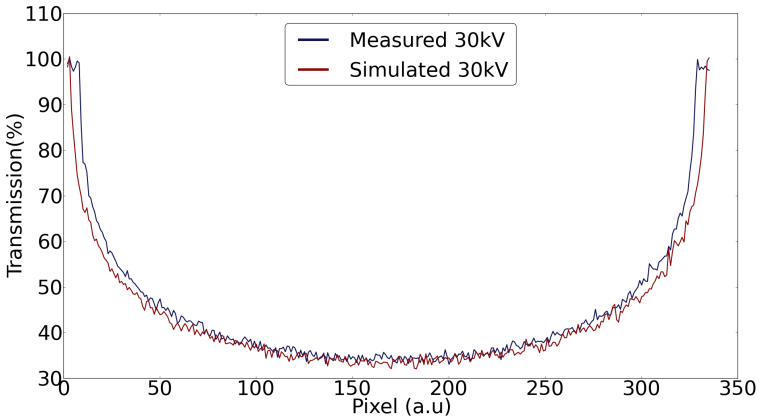

Figure B.1: Line profile of the transmission through the POM cylinder at 30 kV at Nanowood.

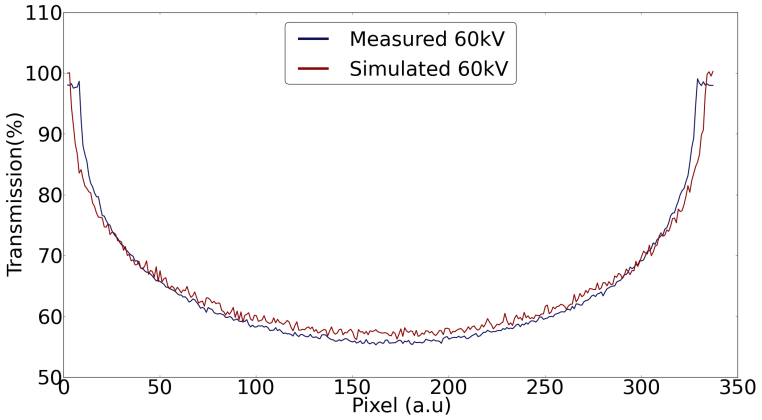

Figure B.2: Line profile of the transmission through the POM cylinder at 60 kV at Nanowood.

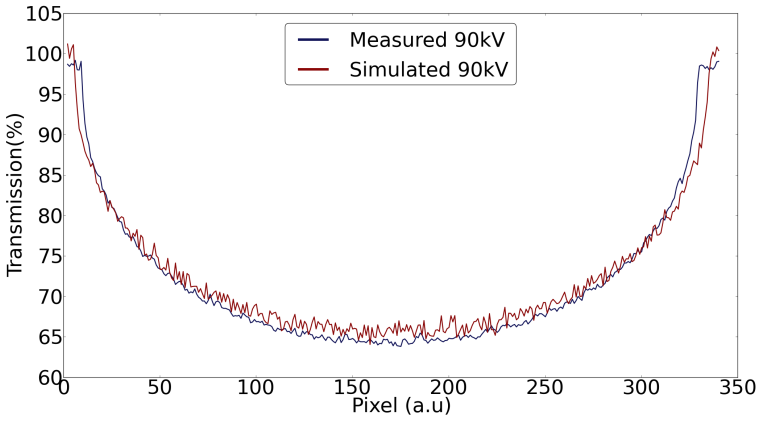

Figure B.3: Line profile of the transmission through the POM cylinder at 90 kV at Nanowood.

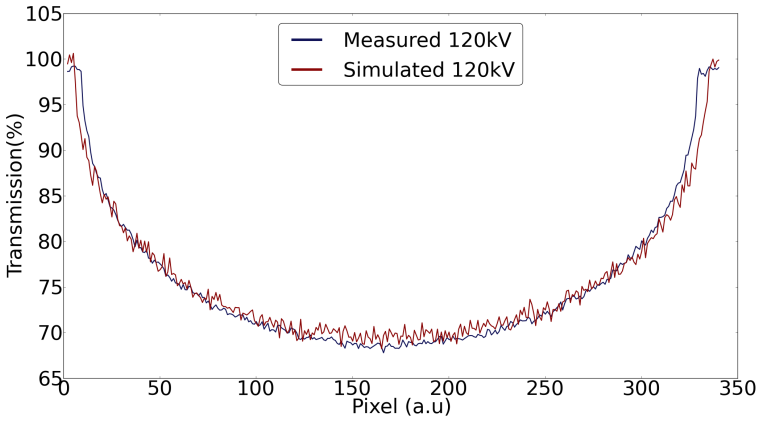

Figure B.4: Line profile of the transmission through the POM cylinder at 120 kV at Nanowood.

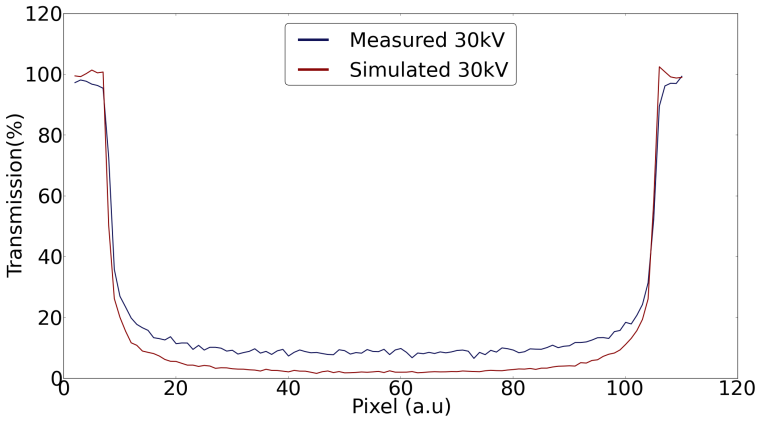

Figure B.5: Line profile of the transmission through the Al sphere at 30 kV at Nanowood.

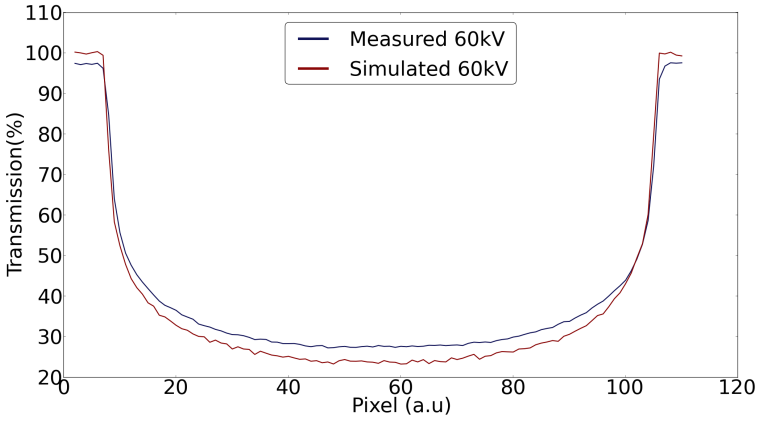

Figure B.6: Line profile of the transmission through the Al sphere at 60 kV at Nanowood.

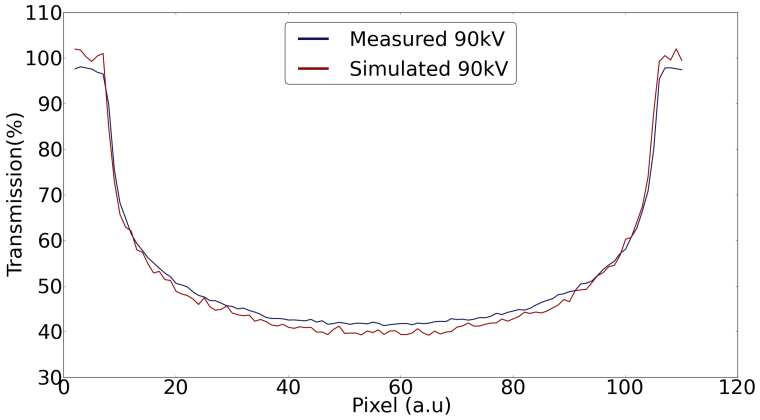

Figure B.7: Line profile of the transmission through the Al sphere at 90 kV at Nanowood.

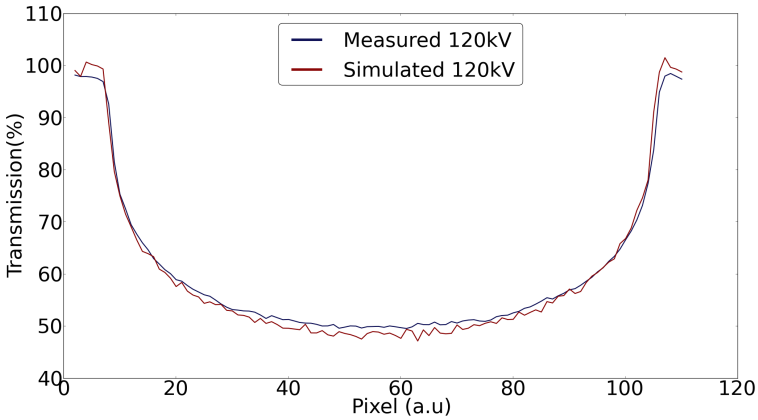

Figure B.8: Line profile of the transmission through the Al sphere at 120 kV at Nanowood.

B.1.2 HECTOR

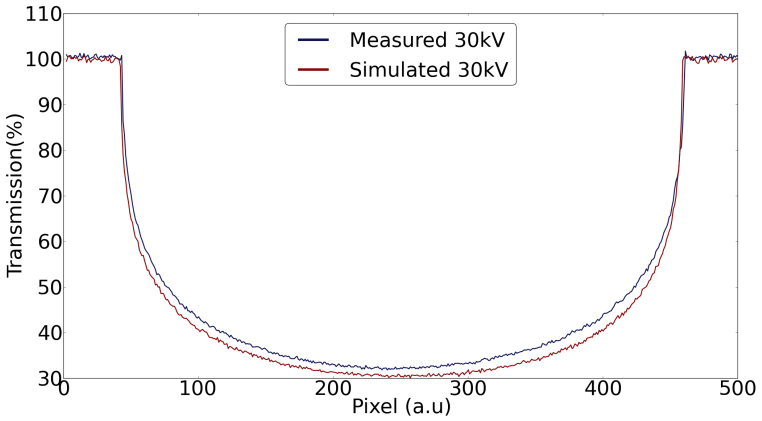

Figure B.9: Line profile of the transmission through the POM cylinder at 30 kV at HECTOR.

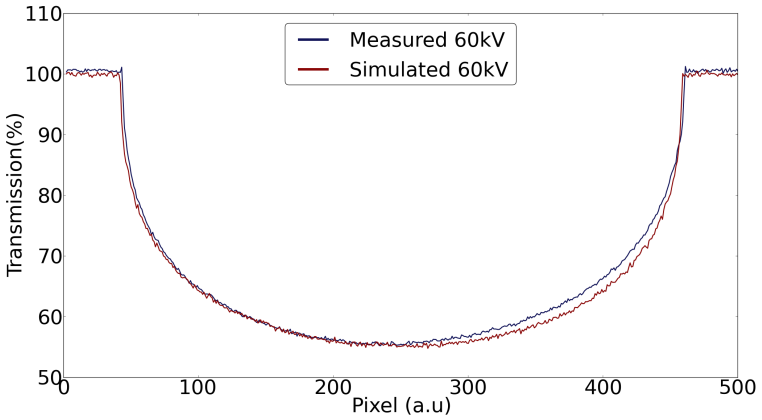

Figure B.10: Line profile of the transmission through the POM cylinder at 60 kV at HECTOR.

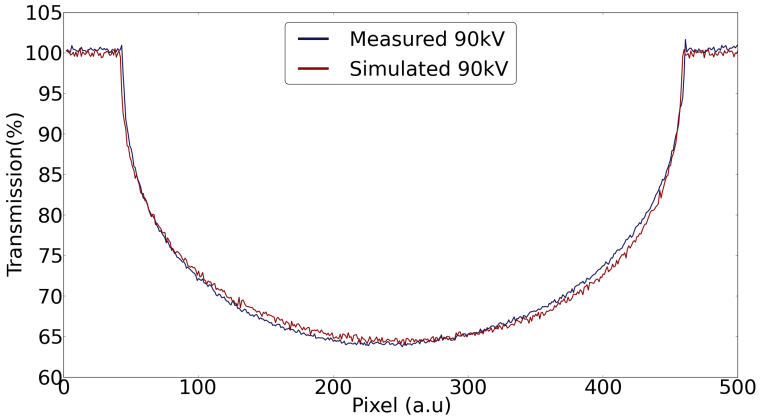

Figure B.11: Line profile of the transmission through the POM cylinder at 90 kV at HECTOR.

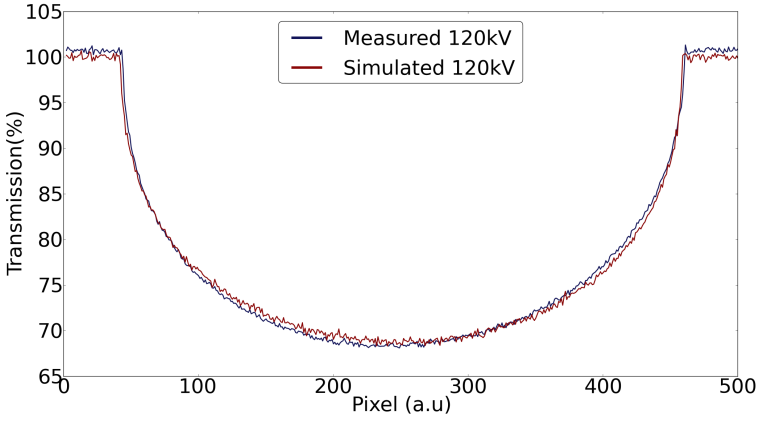

Figure B.12: Line profile of the transmission through the POM cylinder at 120 kV at HECTOR.

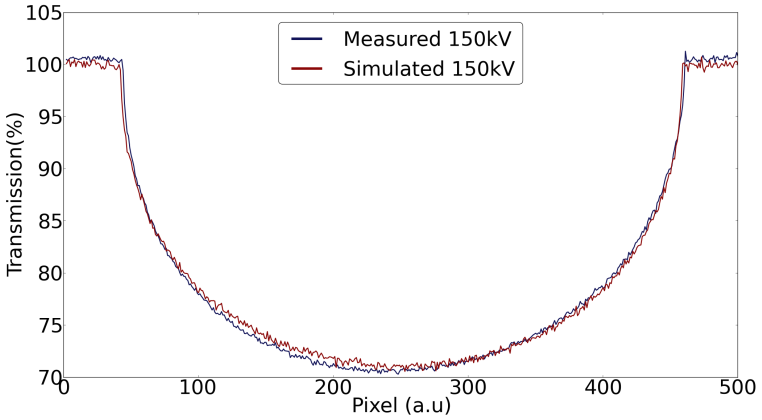

Figure B.13: Line profile of the transmission through the POM cylinder at 150 kV at HECTOR.

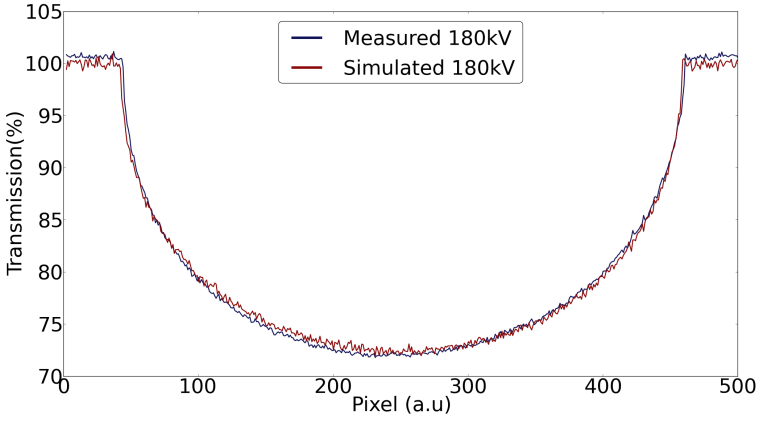

Figure B.14: Line profile of the transmission through the POM cylinder at 180 kV at HECTOR.

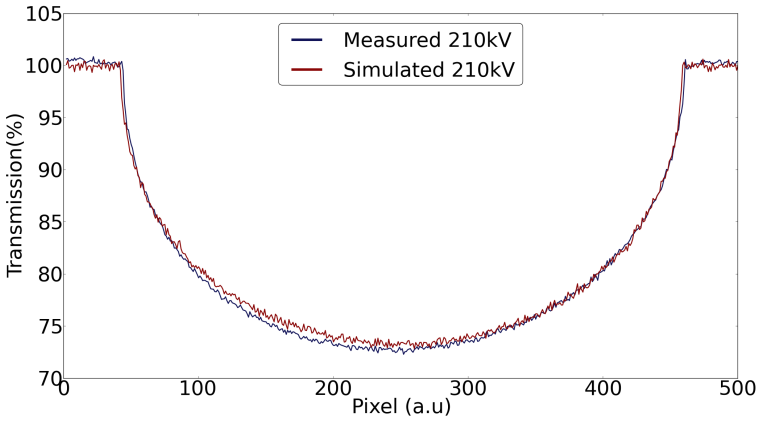

Figure B.15: Line profile of the transmission through the POM cylinder at 210 kV at HECTOR.

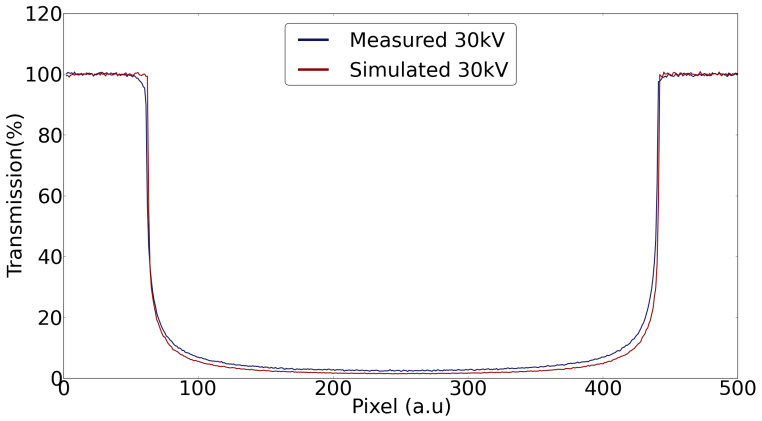

Figure B.16: Line profile of the transmission through the Al sphere at 30 kV at HECTOR.

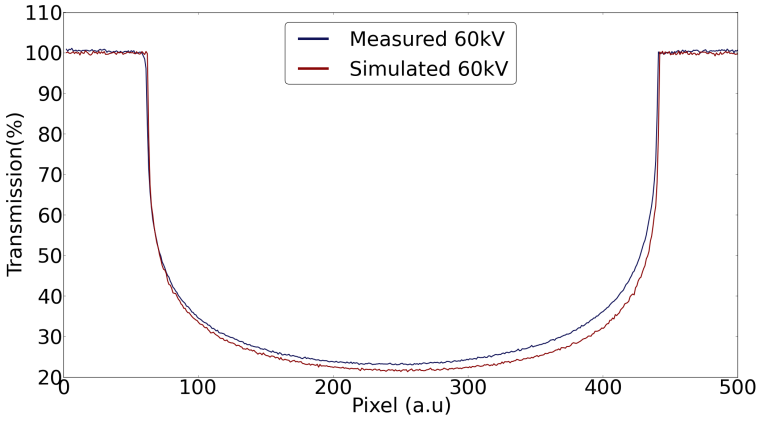

Figure B.17: Line profile of the transmission through the Al sphere at 60 kV at HECTOR.

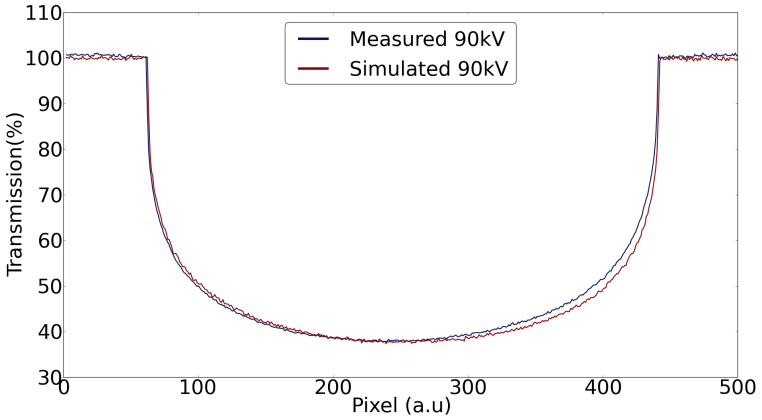

Figure B.18: Line profile of the transmission through the Al sphere at 90 kV at HECTOR.

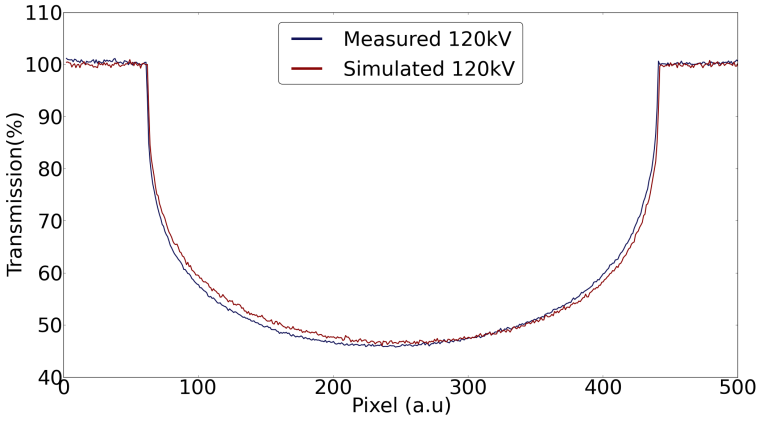

Figure B.19: Line profile of the transmission through the Al sphere at 120 kV at HECTOR.

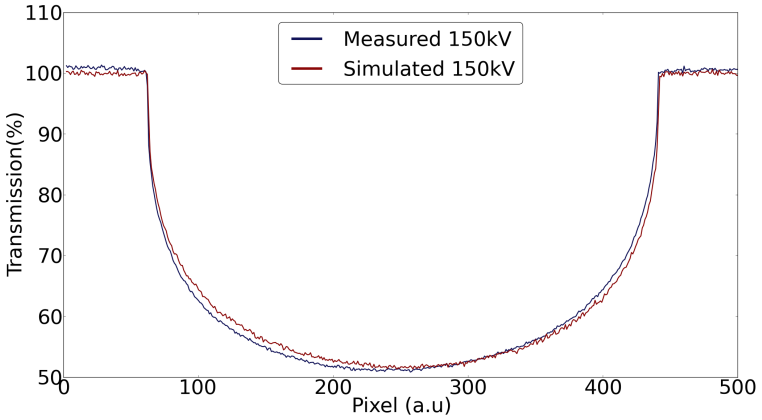

Figure B.20: Line profile of the transmission through the Al sphere at 150 kV at HECTOR.

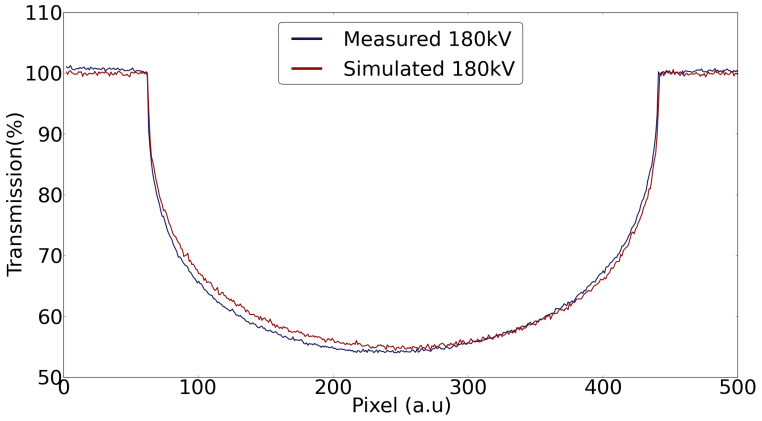

Figure B.21: Line profile of the transmission through the Al sphere at 180 kV at HECTOR.

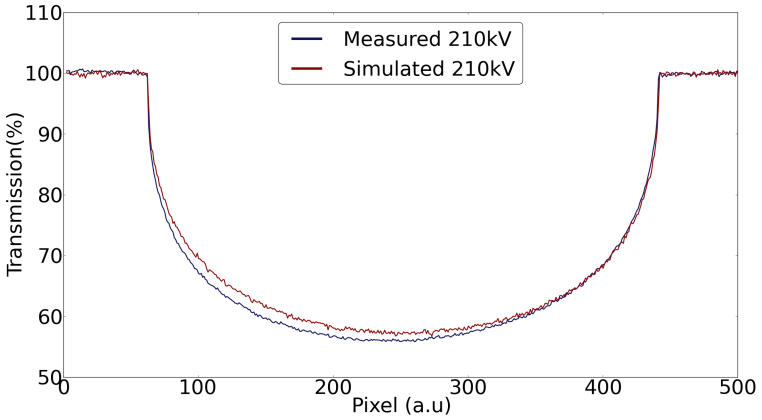

Figure B.22: Line profile of the transmission through the Al sphere at 210 kV at HECTOR.

B.2 Reconstructed data

B.2.1 Nanowood

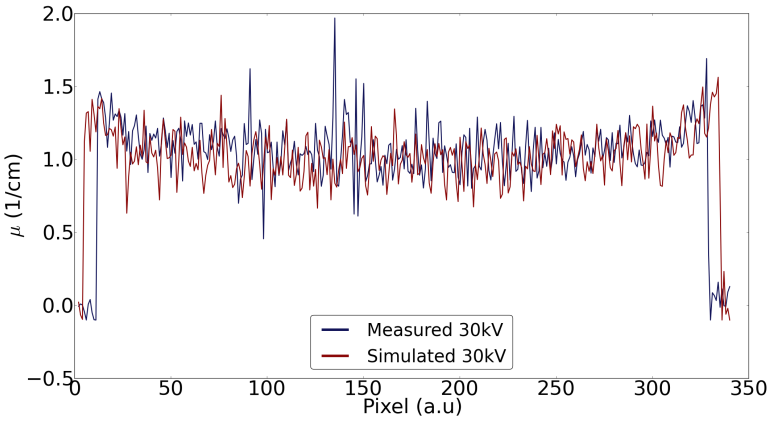

Figure B.23: Line profile in a reconstructed slice of the POM cylinder at 30 kV at Nanowood.

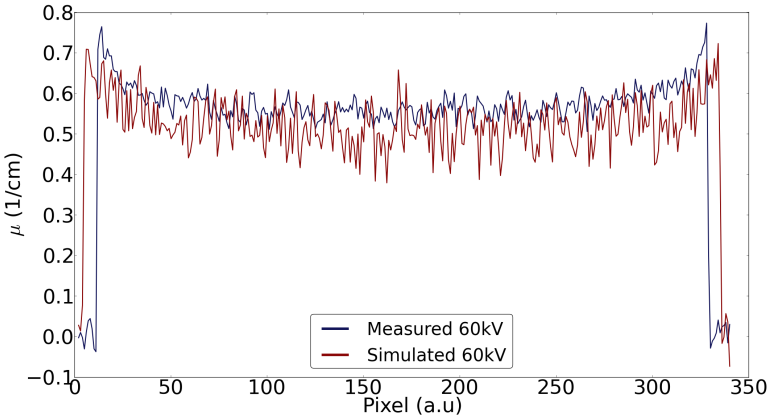

Figure B.24: Line profile in a reconstructed slice of the POM cylinder at 60 kV at Nanowood.

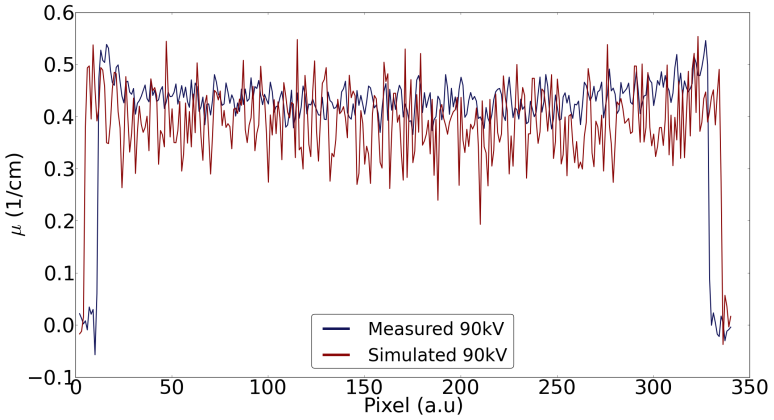

Figure B.25: Line profile in a reconstructed slice of the POM cylinder at 90 kV at Nanowood.

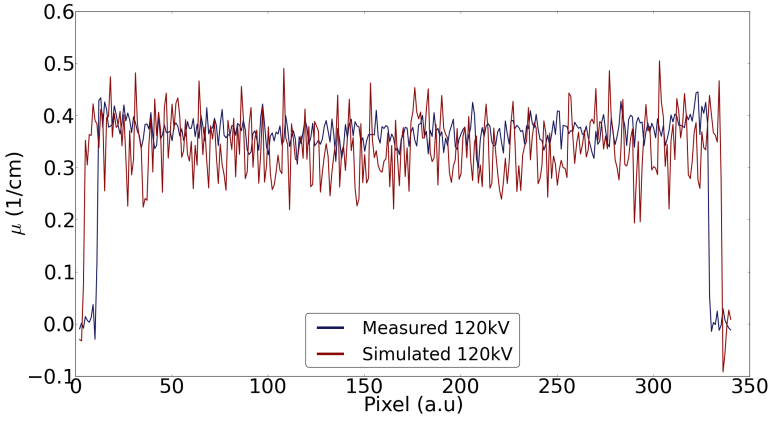

Figure B.26: Line profile in a reconstructed slice of the POM cylinder at 120 kV at Nanowood.

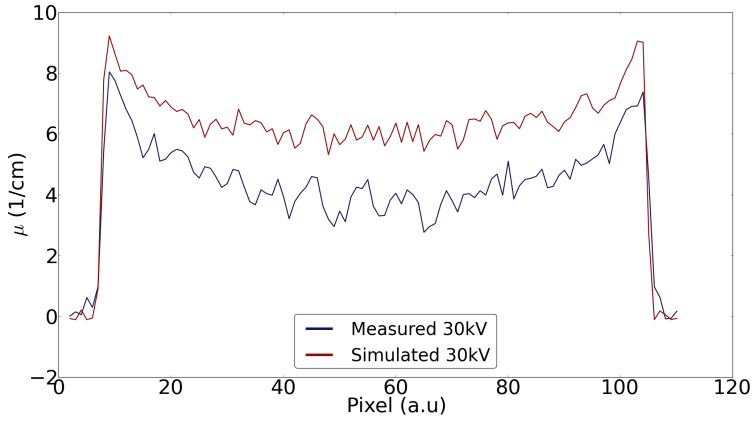

Figure B.27: Line profile in a reconstructed slice of the Al sphere at 30 kV at Nanowood.

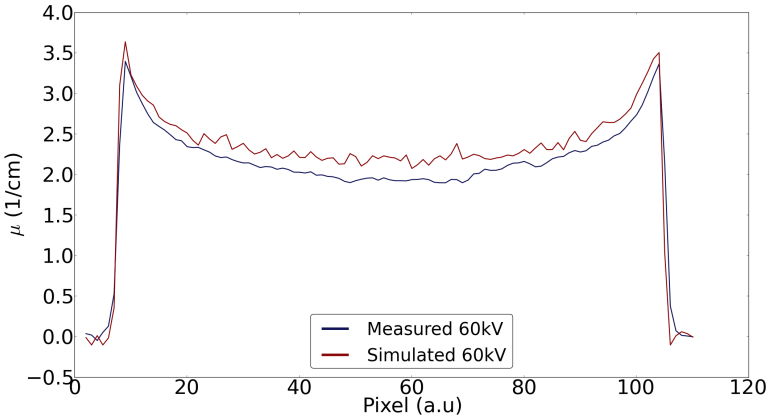

Figure B.28: Line profile in a reconstructed slice of the Al sphere at 60 kV at Nanowood.

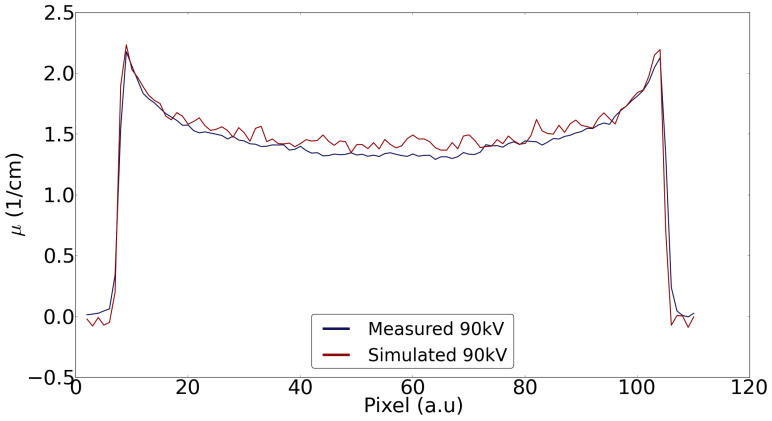

Figure B.29: Line profile in a reconstructed slice of the Al sphere at 90 kV at Nanowood.

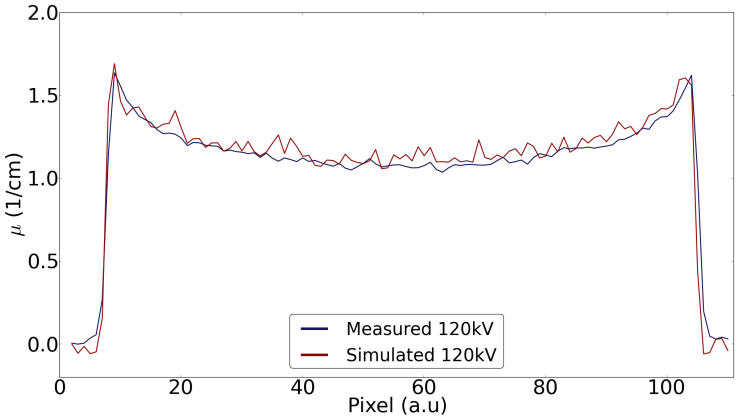

Figure B.30: Line profile in a reconstructed slice of the Al sphere at 120 kV at Nanowood.

B.2.2 HECTOR

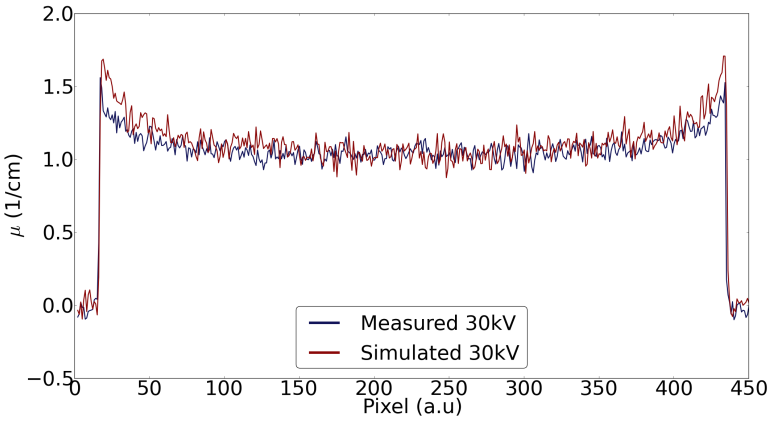

Figure B.31: Line profile in a reconstructed slice of the POM cylinder at 30 kV at HECTOR.

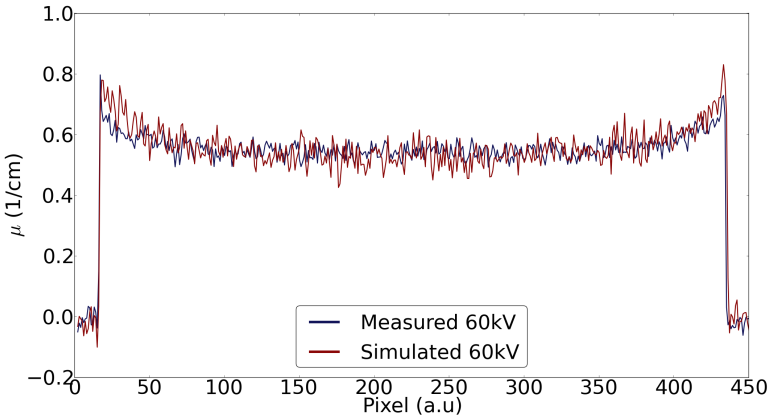

Figure B.32: Line profile in a reconstructed slice of the POM cylinder at 60 kV at HECTOR.

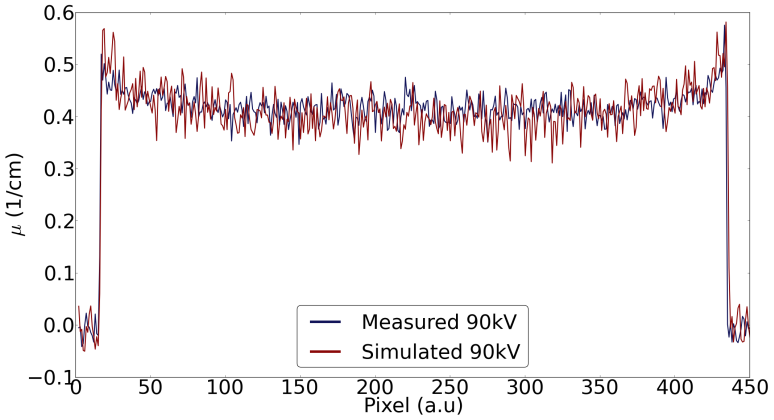

Figure B.33: Line profile in a reconstructed slice of the POM cylinder at 90 kV at HECTOR.

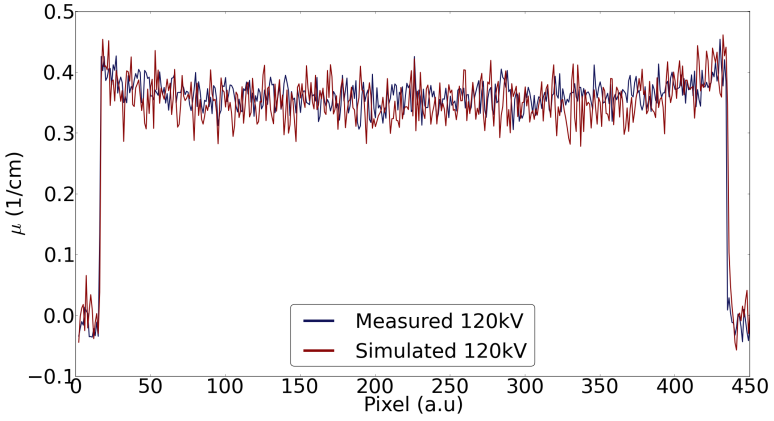

Figure B.34: Line profile in a reconstructed slice of the POM cylinder at 120 kV at HECTOR.

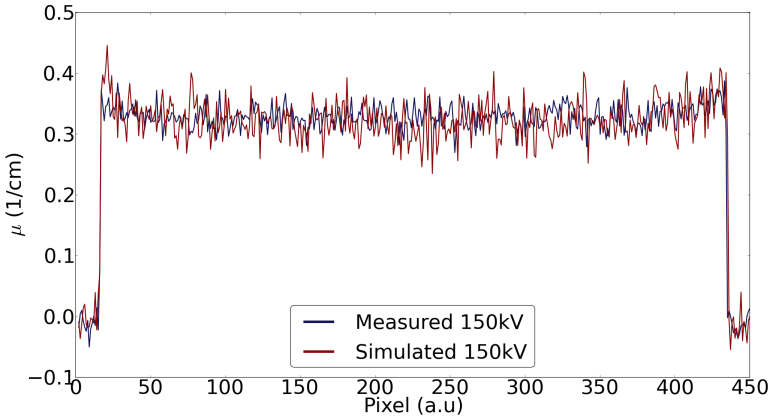

Figure B.35: Line profile in a reconstructed slice of the POM cylinder at 150 kV at HECTOR.

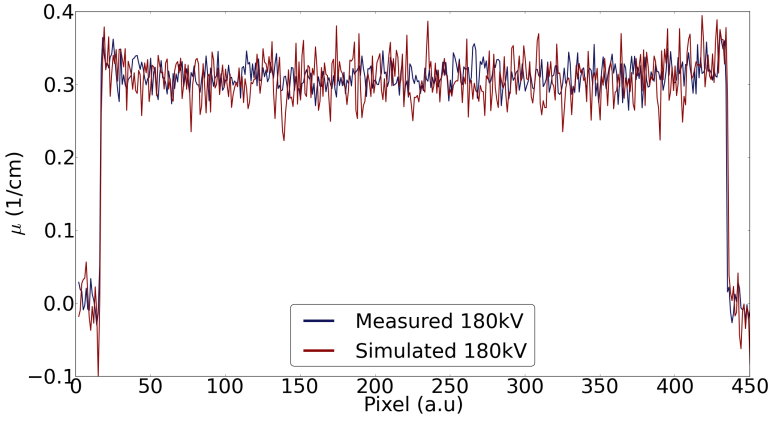

Figure B.36: Line profile in a reconstructed slice of the POM cylinder at 180 kV at HECTOR.

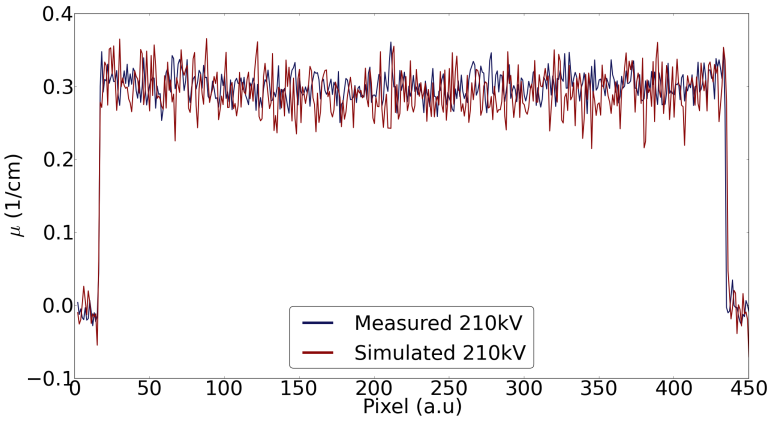

Figure B.37: Line profile in a reconstructed slice of the POM cylinder at 210 kV at HECTOR.

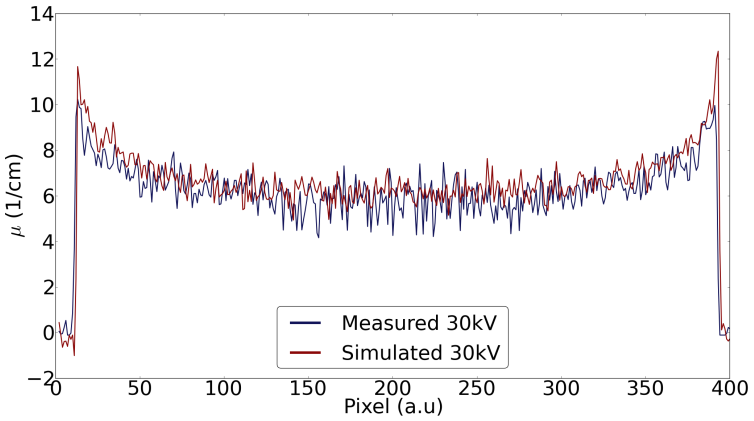

Figure B.38: Line profile in a reconstructed slice of the Al sphere at 30 kV at HECTOR.

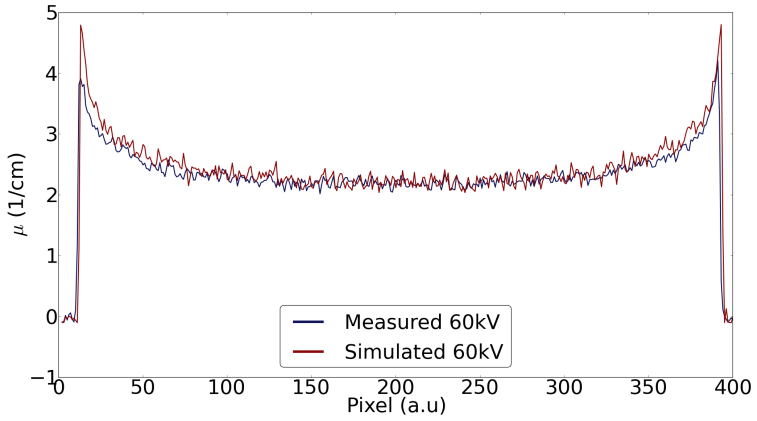

Figure B.39: Line profile in a reconstructed slice of the Al sphere at 60 kV at HECTOR.

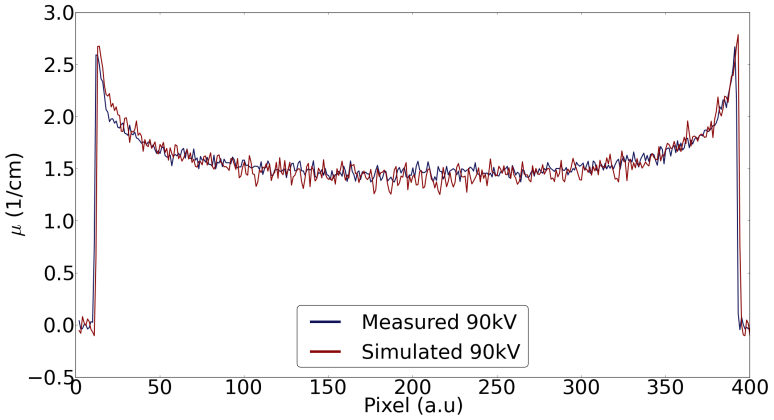

Figure B.40: Line profile in a reconstructed slice of the Al sphere at 90 kV at HECTOR.

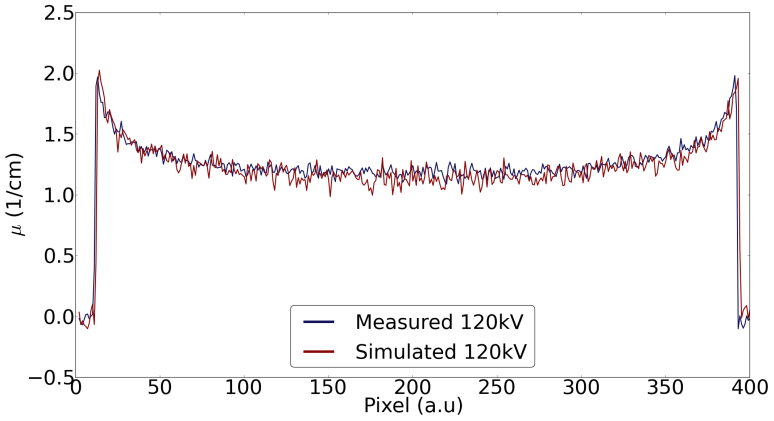

Figure B.41: Line profile in a reconstructed slice of the Al sphere at 120 kV at HECTOR.

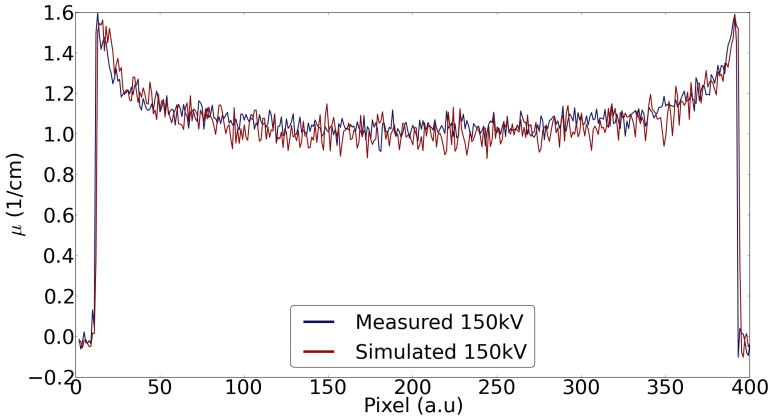

Figure B.42: Line profile in a reconstructed slice of the Al sphere at 150 kV at HECTOR.

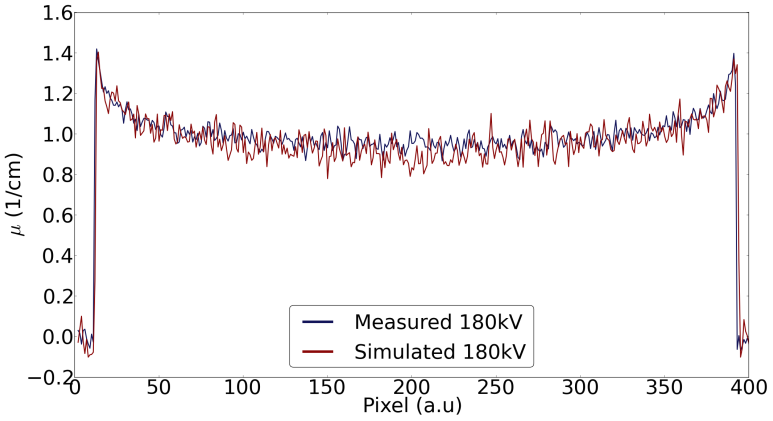

Figure B.43: Line profile in a reconstructed slice of the Al sphere at 180 kV at HECTOR.

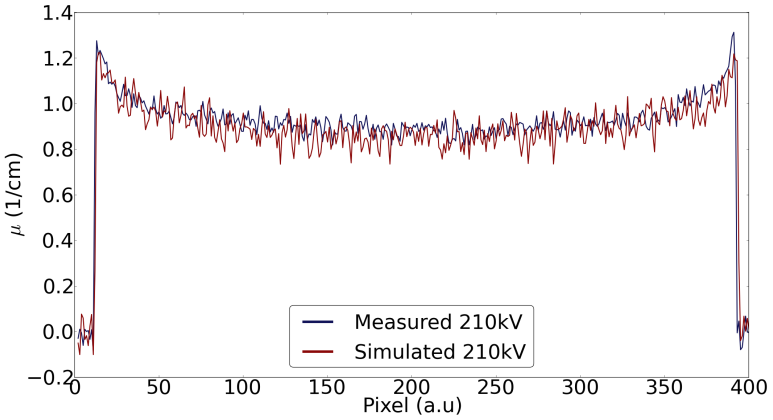

Figure B.44: Line profile in a reconstructed slice of the Al sphere at 210 kV at HECTOR.

C

Calculating reconstructed attenuation coefficients

The Lambert-Beer law for a monochromatic beam that travels through a material with thickness d can be written as

$$I = I_0 exp(-\frac{\mu}{\rho}\rho d), \tag{C.1}$$

with μ/ρ representing the mass attenuation coefficient of the material and ρ signifying the density of the material. For a polychromatic beam, this equation becomes:

$$I = \sum_{i=0}^{E_max} I_i = \sum_{i=0}^{E_{max}} I_{0,i} exp(-\frac{\mu_i}{\rho}\rho d). \tag{C.2}$$

The reconstructed linear attenuation coefficient of the material in the slab can be expressed as

$$\mu = -\frac{1}{d} \ln \left(\frac{I}{I_0} \right). \tag{C.3}$$

Replacing I with Equation C.2 and I_0 by $\sum_i I_{0,i}$, this equation can be rewritten as

$$\mu = -\frac{1}{d} \ln \left(\frac{\sum_i I_{0,i} \exp -\frac{\mu_i}{\rho}\rho d}{\sum_i I_{0,i}} \right). \tag{C.4}$$

$$\mu = -\frac{1}{d} \left[\ln \left(\sum_i I_{0,i} \exp -\frac{\mu_i}{\rho}\rho d \right) - \ln \left(\sum_i I_{0,i} \right) \right] \tag{C.5}$$

The exponential function can be approximated by its series expansion of the first order.

$$\mu = -\frac{1}{d}\left[\ln\left(\sum_i I_{0,i} - \sum_i I_{0,i}\frac{\mu_i}{\rho}\rho d\right) - \ln\left(\sum_i I_{0,i}\right)\right] \tag{C.6}$$

$$\mu = -\frac{1}{d}\left[\ln\left(\sum_i I_{0,i}\left(1 - \frac{\sum_i I_{0,i}\frac{\mu_i}{\rho}\rho d}{\sum_i I_{0,i}}\right)\right) - \ln\left(\sum_i I_{0,i}\right)\right] \tag{C.7}$$

$$\mu = -\frac{1}{d}\left[\ln\left(\sum_i I_{0,i}\right) + \ln\left(1 - \frac{\sum_i I_{0,i}\frac{\mu_i}{\rho}\rho d}{\sum_i I_{0,i}}\right) - \ln\left(\sum_i I_{0,i}\right)\right] \tag{C.8}$$

$$\mu = -\frac{1}{d}\left[\ln\left(1 - \frac{\sum_i I_{0,i}\frac{\mu_i}{\rho}\rho d}{\sum_i I_{0,i}}\right)\right] \tag{C.9}$$

Furthermore, a series expansion for the natural logarithm can be performed

$$\mu = -\frac{1}{d}\left(-\frac{\sum_i I_{0,i}\frac{\mu_i}{\rho}\rho d}{\sum_i I_{0,i}}\right) \tag{C.10}$$

$$\mu = \rho\frac{\sum_i I_{0,i}\frac{\mu_i}{\rho}}{\sum_i I_{0,i}} \tag{C.11}$$

in which $\frac{I_{0,i}}{\sum_i I_{0,i}}$ is the weight factor w_i in the ith bin. The factor $I_{0,i}$ can be calculated as (section 5.2)

$$I_{0,i} = \frac{P\Delta t}{UQ_{e^-}}\Delta\Omega_{pixel}\Delta E_i S_i^{'} D_{inc,i} \tag{C.12}$$

and the filtered spectrum $S_i^{'}$ can be expressed as

$$S_i^{'} = S_i \prod_{j=1}^{l} \exp\left(-\mu_{ij} d_j\right). \tag{C.13}$$

The weight factor $\frac{I_{0,i}}{\sum_i I_{0,i}}$ can then be expressed as

$$\frac{I_{0,i}}{\sum_i I_{0,i}} = \frac{\frac{P\Delta t}{UQ_{e^-}}\Delta\Omega_{pixel}\Delta E_i S_i^{'} D_{inc,i}}{\sum_i \frac{P\Delta t}{UQ_{e^-}}\Delta\Omega_{pixel}, \Delta E_i S_i^{'} D_{inc,i}} \tag{C.14}$$

$$\frac{I_{0,i}}{\sum_i I_{0,i}} = \frac{\Delta E_i S_i^{'} D_{inc,i}}{\sum_i \Delta E_i S_i^{'} D_{inc,i}}, \tag{C.15}$$

$$\frac{I_{0,i}}{\sum_i I_{0,i}} = \frac{S_i^{''} D_{inc,i}}{\sum_i S_i^{''} D_{inc,i}}. \tag{C.16}$$

D
Bibliography

A1 Publications

[1] Jelle Dhaene, Elin Pauwels, Thomas De Schryver, Amélie De Muynck, Manuel Dierick, and Luc Van Hoorebeke. *A realistic projection simulator for laboratory based X-ray micro-CT*. Nucl. Instrum. Methods Phys. Res., Sect. B, 342:170–178, 2015.

[2] Thomas De Schryver, Jelle Dhaene, Manuel Dierick, Matthieu N. Boone, Eline Janssens, Jan Sijbers, Mattias van Dael, Pieter Verboven, Bart Nicolai, and Luc Van Hoorebeke. *In-line NDT with X-Ray CT combining sample rotation and translation*. {NDT} & E International, 84:89 – 98, 2016.

[3] Wanzhao Li, Jan Van den Bulcke, Imke De Windt, Nele Defoirdt, Jelle Dhaene, Manuel Dierick, Hugo Sol, and Joris Van Acker. *Relating MOE decrease and mass loss due to fungal decay in plywood and MDF using resonalyser and X-ray CT scanning*. International Biodeterioration & Biodegradation, 110:113 – 120, 2016.

[4] Wanzhao Li, Jan Van den Bulcke, Imke De Windt, Jelle Dhaene, and Joris Van Acker. *Moisture behavior and structural changes of plywood during outdoor exposure*. European Journal of Wood and Wood Products, 74(2):211–221, 2016.

[5] Vladimirs Biziks, Jan Van den Bulcke, Juris Grinins, Holger Militz, Bruno Andersons, Ingeborga Andersone, Jelle Dhaene, and Joris Van Acker. *Assessment of wood microstructural changes after one-stage thermo-hydro treatment (THT) by micro X-ray computed tomography*. HOLZFORSCHUNG, 70(2):167–177, FEB 2016.

[6] Jeroen Van Stappen, Tom Bultreys, Francisco A. Gilabert, Xander K.D. Hillewaere, David Garoz Gomez, Kim Van Tittelboom, Jelle Dhaene, Nele De Belie, Wim Van Paepegem, Filip E. Du Prez, and Veerle Cnudde. *The microstructure of capsule containing self-healing materials: A micro-computed tomography study*. Materials Characterization, 119:99 – 109, 2016.

[7] Raf Claes, Pieter G. G. Muyshondt, Luc Van Hoorebeke, Jelle Dhaene, Joris J. J. Dirckx, and Peter Aerts. *The effect of craniokinesis on the middle ear of domestic chickens (Gallus gallus domesticus)*. Journal of Anatomy, pages n/a–n/a, 2016.

Conference contributions

[1] Jelle Dhaene, Thomas De Schryver, Manuel Dierick, Sofie De Man, Johan Claes, and Luc Van Hoorebeke. *Optimizing laboratory and industrial micro-CT for food appllications*. In 30th EFFoST International Conference: Targeted Technologies for Sustainable Food Systems, 2016.

[2] Thomas De Schryver, Jelle Dhaene, Manuel Dierick, Matthieu Boone, Eline Janssens, Jan Sijbers, Pieter Verboven, Bart Nicolai, and Luc Van Hoorebeke. *In-line 3D X-ray CT inspection of food on a continuous high throughput conveyor belt system*. In 30th EFFoST International Conference: Targeted Technologies for Sustainable Food Systems, 2016.

[3] Sofie De Man, Jelle Dhaene, Geertrui Vlaemynck, Luc Van Hoorebeke, and Jan De Block. *Influence homogenization cheese milk on textural and sensorial properties of cheese*. In 30th EFFoST International Conference: Targeted Technologies for Sustainable Food Systems, 2016.

[4] Sofie De Man, Jelle Dhaene, Geertrui Vlaemynck, Luc Van Hoorebeke, and Jan De Block. *Influence of homogenization of cheese milk on process and textural properties of cheese.* In Cheese Science & Technology Symposium, 2016.

[5] Jelle Dhaene, Elin Pauwels, Thomas De Schryver, Amélie De Muynck, Manuel Dierick, and Luc Van Hoorebeke. *Arion: a realistic projection simulator for optimizing laboratory and industrial micro-CT*. In Bernard Long, editor, Tomography of Materials and Structures, 2nd International conference, Proceedings, pages 60–64, 2015.

[6] Sofie De Man, Jelle Dhaene, Thomas De Schryver, Luc Van Hoorebeke, and Jan De Block. *Use of X-ray tomography in aerated dairy food and cheese research*. In Matthieu Boone and Jan Van den Bulcke, editors, 2nd UGCT seminar : book of abstracts. Ghent University. Centre for X-ray Tomography (UGCT), 2015.

[7] Jolien Delepierre, Jelle Dhaene, Matthieu Boone, Manuel Dierick, and Luc Van Hoorebeke. *Modelling of X-ray tube spot size and heel effect in Arion*. In Bernard Long, editor, Tomography of Materials and Structures, 2nd International conference, Proceedings, pages 82–86, 2015.

[8] Elin Pauwels, Jelle Dhaene, Amélie De Muynck, Manuel Dierick, and Luc Van Hoorebeke. *Optimization of scanner parameters for dual energy micro-CT*. In Bernard Long, editor, Tomography of Materials and Structures, 2nd International conference, Proceedings, pages 87–91, 2015.

[9] Amélie De Muynck, Stijn Bonte, Jelle Dhaene, Manuel Dierick, Klaus Bacher, and Luc Van Hoorebeke. *Evaluation of the absorbed dose in X-ray microtomography*. In Bernard Long, editor, Tomography of Materials and Structures, 2nd International conference, Proceedings, pages 100–103, 2015.

[10] Gabriele Chiesura, Geert Luyckx, Eli Voet, Wim Van Paepegem, Joris Degrieck, Matthieu Boone, Jelle Dhaene, and Luc Van Hoorebeke. *Micro-CT as a well-established technique to investigate the internal damage state of a composite laminate subjected to fatigue*. In Emerging Technologies in Non-Destructive Testing, 6th Conference, Papers, page 6, 2015.

[11] Matthieu Boone, Bert Masschaele, Manuel Dierick, Denis Van Loo, Thomas De Schryver, Elin Pauwels, Jelle Dhaene, Amélie De Muynck, Marjolein Heyndrickx, and Luc Van Hoorebeke. *Latest technical developments at UGCT: an overview*. In Matthieu Boone and Jan Van den Bulcke, editors, 2nd UGCT seminar : book of abstracts. Ghent University. Centre for X-ray Tomography (UGCT), 2015.

[12] Jelle Dhaene, Elin Pauwels, Thomas De Schryver, Amélie De Muynck, Loes Brabant, Manuel Dierick, and Luc Van Hoorebeke. *Realistic projection simulator for laboratory based X-ray micro-CT*. In Industrial Computed Tomography, 5th Conference, Abstracts, 2014.

[13] Jelle Dhaene, Elin Pauwels, Thomas De Schryver, Amélie De Muynck, Manuel Dierick, and Luc Van Hoorebeke. *Accurate projection simulator for laboratory based X-ray micro-CT*. In 12th International conference on X-Ray Microscopy : conference program handbook, 2014.

[14] Elin Pauwels, Jelle Dhaene, Amélie De Muynck, Thomas De Schryver, Manuel Dierick, and Luc Van Hoorebeke. *Optimization of scanner parameters for dual energy micro-CT*. In 12th International conference on X-Ray Microscopy : conference program handbook, 2014.

[15] Amélie De Muynck, Jelle Dhaene, Elin Pauwels, Thomas De Schryver, Manuel Dierick, and Luc Van Hoorebeke. *A modular approach to generate spectral characteristics of X-ray micro-CT scanner components*. In 12th International conference on X-Ray Microscopy : conference program handbook, pages 107–107, 2014.

[16] Amélie De Muynck, Jelle Dhaene, Elin Pauwels, Manuel Dierick, and Luc Van Hoorebeke. *Modelling scattering contributions in X-ray micro-CT scanners with variable geometry*. In Industrial Computed Tomography, 5th Conference, Abstracts, 2014.